이학박사 학위논문

우리 은하 중심 10 파섹 내부의 구조와 동역학 연구

Structure and Dynamics at the Central 10 Parsecs of the Galaxy

2005년 8월

서울대학교 대학원
지구환경과학부 천문학 전공
이 성 호

Structure and Dynamics at the Central 10 Parsecs of the Galaxy

지도교수 이 상 각

이 논문을 이학박사 학위논문으로 제출함
2005년 4월

서울대학교 대학원
지구환경과학부 천문학 전공
이 성 호

이성호의 이학박사 학위논문을 인준함
2005년 6월

위 원 장 ______________________

부위원장 ______________________

위　　원 ______________________

위　　원 ______________________

위　　원 ______________________

Structure and Dynamics at the Central 10 Parsecs of the Galaxy

A dissertation submitted in satisfaction of the final requirement for the degree of

Doctor of Philosophy

Sungho Lee

School of Earth and Environmental Sciences

Seoul National University

August 2005

To My Little Daughter

ABSTRACT

The Galactic center influences the current nature as well as the formation, the evolution and the future fate of the Milky Way. The Galactic nucleus stands for the galactic nuclei of other galaxies and provides an opportunity to study the environment around a super-massive black hole (SMBH) at high spatial resolution. The central 10 pc of the Galaxy, the Sgr A region, contains several principal components; the SMBH candidate (Sgr A*), the Central cluster, the circum-nuclear disk (CND), Sgr A West, a powerful supernova-like remnant (Sgr A East), and surrounding molecular clouds. Developing a consistent picture of the interactions between these components will improve our understanding of the Galaxy and the nature of galactic nuclei in general. Previous studies on the spatial and dynamical relationships between the various objects are mostly based on indirect and qualitative evidence and leave many unsolved questions, which need more robust evidence. Molecular hydrogen (H_2) emission has been used as an excellent tracer and diagnostic for interactions between dense molecular clouds and hot, powerful sources.

We observed the H_2 $1-0$ $S(1)$ ($\lambda = 2.1218\mu m$) and H_2 $2-1$ $S(1)$ ($\lambda = 2.2477\mu m$) emission line spectra from the interaction regions between Sgr A East, the CND, and the surrounding molecular clouds. Using the long-slit Cooled Grating Spectrometer 4 (CGS4) with an echelle grating at the 3.8 m United Kingdom Infrared Telescope (UKIRT) on Mauna Kea, we scanned 56 positions in the interaction regions. We reduced 2-D spectral images using IRAF and analyzed a 3-D data cube using MIRIAD. The data cube has the H_2 information both in space (with a resolution of $\sim 2''$) and in velocity (with a resolution of ~ 18 km s^{-1}). The H_2 $1-0$ $S(1)$ data cube was directly compared with the NH_3(3,3) data cube from McGary, Coil, & Ho (2001, ApJ, 559, 326) to investigate the gas kinematics.

Based on the H_2 1–0 $S(1)$ and 2–1 $S(1)$ line intensities and gas kinematics, we concluded that the H_2 excitation can be explained by two mechanisms; a combination of fluorescence and C-shocks in very strong magnetic fields, or a mixture of slow C-shocks and fast J-shocks. We estimated shock velocities (~ 100 km s^{-1}) of Sgr A East by comparing H_2 line profiles with those of NH_3. From the distribution of the shocked H_2 emission, we determined the interacting boundary of Sgr A East in projection as an ellipse with the center at ~ 1.5 pc offset from Sgr A* and the dimension of 10.8 pc $\times$ 7.6 pc. We also determined the positional relationship between Sgr A East and the molecular clouds along the line-of-sight and suggested a revised model for the 3-D structure of the central 10 pc. From the estimated shock velocities, we deduced the initial explosion energy (0.2–4×10^{53} ergs) of Sgr A East. This extremely large energy excludes the hypothesis of a single, typical, supernova (SN) for the origin of Sgr A East. We examined other hypotheses (tidal disruption of a star by the SMBH, multiple supernovae, and a hypernova) and we concluded that a hypernova (collapsar or microquasar) is the most probable origin of Sgr A East.

Based on the energy, we investigated the influences of the Sgr A East-like explosions (hypernovae) and normal SNe on the mass inflow to the Galactic nucleus. We suggest a scenario that the continuous mass inflow into the Galactic nucleus makes it active by igniting the SMBH or stimulating a starburst every $\sim 10^8$ yr, but each active phase continues only $\lesssim 10^7$ yr since a large number of SNe resulting from newly born massive stars cease the mass supply soon. The Galactic nucleus is likely to spend only about $1/10$ of its life in active. As for the recent history of the central 10 pc, the mass inflow restarted several 10^6 yr ago after a quiescent phase for $\sim 10^8$ yr. In its usual schedule, the Galactic nucleus would continue its activity for a few 10^6 yr more from now before a huge number of SNe occur. However, the active phase was unexpectedly ceased $\sim 10^4$ yr ago, by Sgr A East.

Keywords: Galactic center, ISM, infrared, supernovae, supernova remnants

Student Number: **99304-804**

Contents

List of Figures

List of Tables

Chapter 1

An Overview of the Central 10 Parsecs

1.1 Introduction

The Galactic center is a unique place. As the heart of the galaxy, it influences the current nature, the formation and growth, the evolution and the future fate of the Milky Way (Figure 1.1). The Galactic nucleus is also a standard when trying to understand the galactic nuclei of other galaxies, as the sun is for studies of other stars. Since Lynden-Bell & Rees (1971) suggested that massive black holes may exist in most galaxies, including our own Galaxy, many observations have concentrated on the Galactic center in order to understand active galactic nuclei (AGNe). The nucleus of our Galaxy is obviously much closer than those of other galaxies and therefore provides an excellent opportunity to study the environment around a super-massive black hole (SMBH) at high resolution.

Hidden behind a thick veil of dust and gas, the center of our Galaxy cannot be seen in visible light. In order to study the Galactic center, astronomers must observe it in other wavelengths, such as gamma-rays, X-rays, infrared (IR), and radio. The Galactic Center region is filled with high-speed electrons and magnetic fields which produce strong radio emission (see Figure 1.2). The nucleus is marked by the most prominent radio source, Sagittarius (Sgr) A, which probably contains a SMBH (Sgr A*) deep within it. There are a number of other interesting features in Figure 1.2; the star-forming regions Sgr B1 and B2 where hot young stars are heating the gas, a number of supernova remnants (SNRs) which have evolved from short-lived massive stars, and the radio arc and non-thermal filaments which must be associated with the structure of the strong magnetic field in the Galactic center.

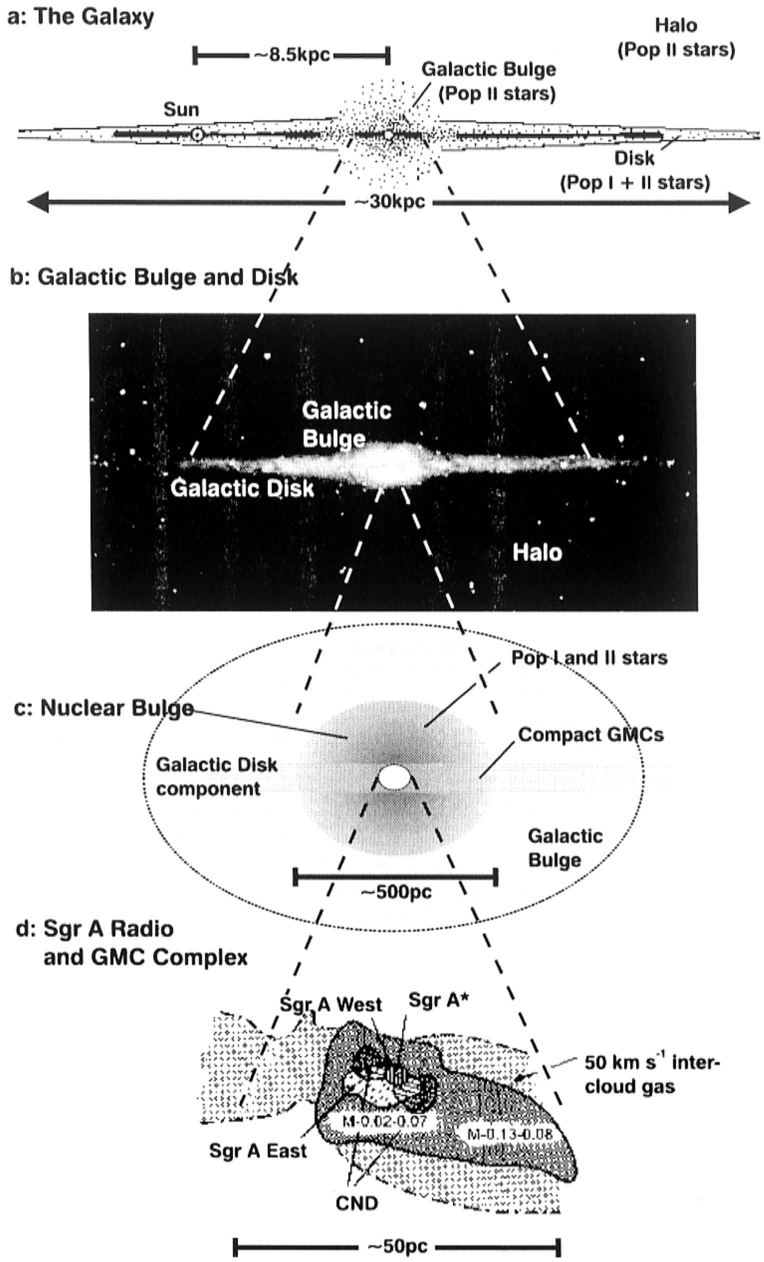

FIG. 1.1: A hierarchical picture of the galaxy (from Mezger, Duschl, & Zylka 1996). (a) Schematic cross section of the Galaxy. (b) DIRBE image of the Galactic Bulge, created from observations at wavelengths of 1.25, 2.2, and 3.5 μm. Most of the emission here comes from low and medium mass stars; dust emission is negligible. (c) A schematic representation of the Galactic and Nuclear Bulge and the thin layer of interstellar medium. (d) A schematic representation of the Sgr A and giant molecular cloud (GMC) complex. Note that our knowledge of the structure in this scale has been significantly changed since Mezger, Duschl, & Zylka (1996)'s review.

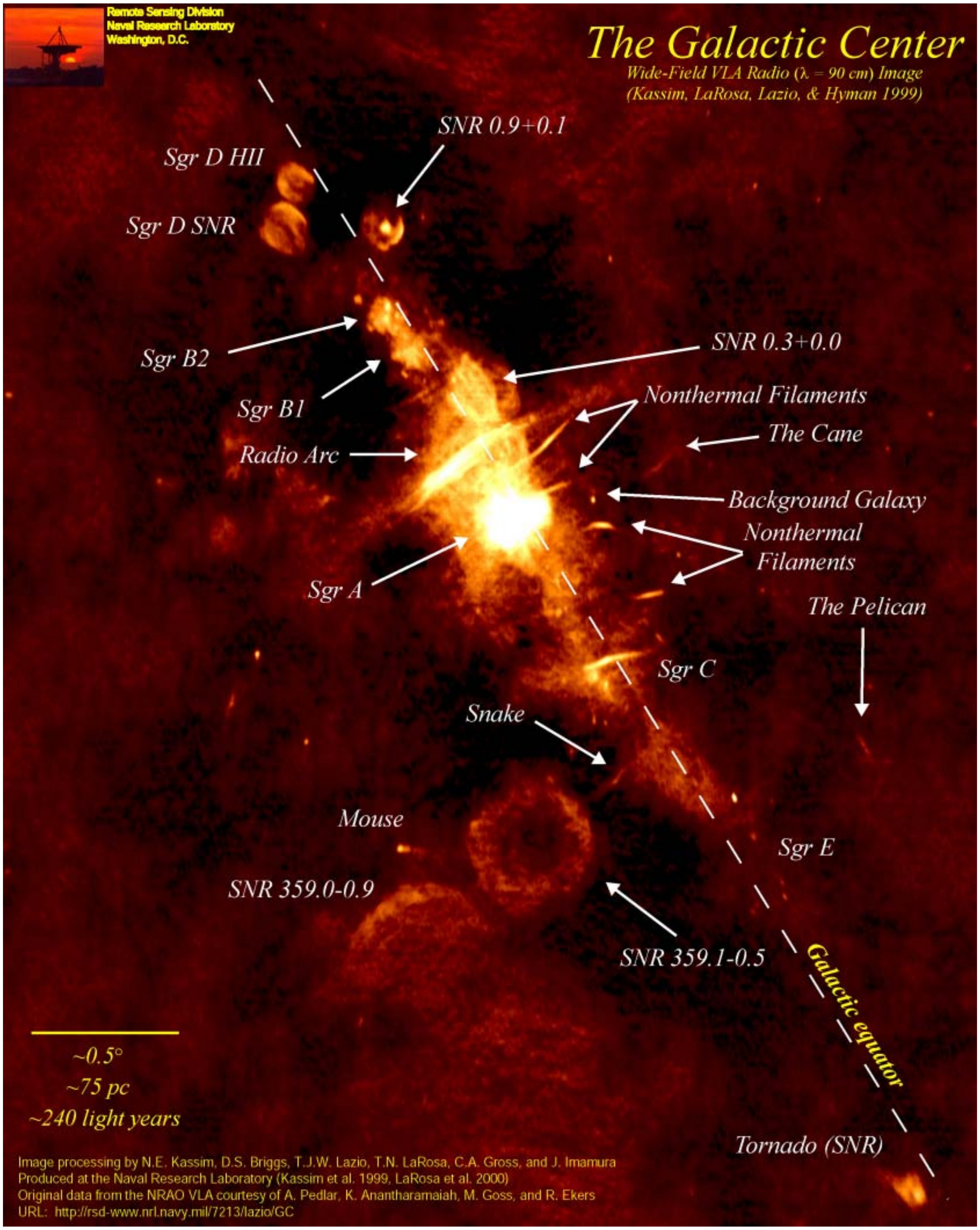

FIG. 1.2: Central $2\overset{\circ}{.}6 \times 3\overset{\circ}{.}3$ of the Galaxy at Wavelength of 90 cm (from Kassim et al. 1999). It was produced from data obtained by Pedlar et al. (1989) and Anantharamaiah et al. (1991) using the Very Large Array (VLA). The resolution is $43'' \times 23''$. The peak brightness is 8.5 Jy beam^{-1} and the RMS noise level is 5.9 mJy beam^{-1}.

The inner 10 pc at the center of our Galaxy, the Sgr A region in Figures 1.1 & 1.2, contains several principal components which will be described in more detail in the following sections; a SMBH candidate (Sgr A*) of about 4×10^6 $M_\odot$, a surrounding cluster of stars (the Central cluster; see Table 6.2 for its properties), molecular and ionized gas clouds (the circum-nuclear disk (CND) and Sgr A West, respectively), a powerful supernova-like remnant (Sgr A East), and the surrounding molecular structures including two giant molecular clouds (GMCs) M-0.02-0.07 and M-0.13-0.08. The interaction between these components is responsible for many of the phenomena occurring in this complicated and unique portion of the Galaxy. Developing a consistent picture of the primary interactions between the components at the Galactic center will improve our understanding of the nature of galactic nuclei in general.

1.2 Sagittarius A Complex and Super-Massive Black Hole

Since Piddington & Minnett (1951)'s discovery of a strong radio source, Sgr A, there has been dramatic progress in observational technology which has led to a better understanding of this source. The multiple nature of Sgr A became evident in the early 1970's. The eastern part of it (Sgr A East) has a non-thermal spectrum, while Sgr A West is predominantly a thermal source which is associated with IR sources and radio recombination lines (see the review of Goss et al. 1983 and references therein). The bright and very compact radio source, Sgr A*, was discovered by Balick & Brown (1974) within Sgr A West using the National Radio Astronomy Observatory (NRAO) interferometer.

Sgr A East surrounds Sgr A West in projection (Figure 1.3). Sgr A East has frequently been interpreted as a SNR due to its shell structure and non-thermal spectrum (e.g. Jones 1974; Goss et al. 1983). Alternatively, Sgr A East may be a bubble driven by several supernovae or a very low-luminosity example of a radio component associated with the active nucleus of a spiral galaxy (see Melia & Falcke 2001 and references therein). Observations of Sgr A East show it to be associated with the GMC M-0.02-0.07. Such an association may require more than 10^{52} ergs of explosive energy to account for the origin of Sgr A East (Mezger et al. 1989). It may be the remnant of an extreme phenomenon, such as a star that has been tidally disrupted by the SMBH (Khokhlov & Melia 1996). On the other hand, Sgr A East is also associated with diffuse X-ray emission (Figure 1.4). The large temperature and pressure of the emitting region producing the hard X rays suggest that this gas is prob-

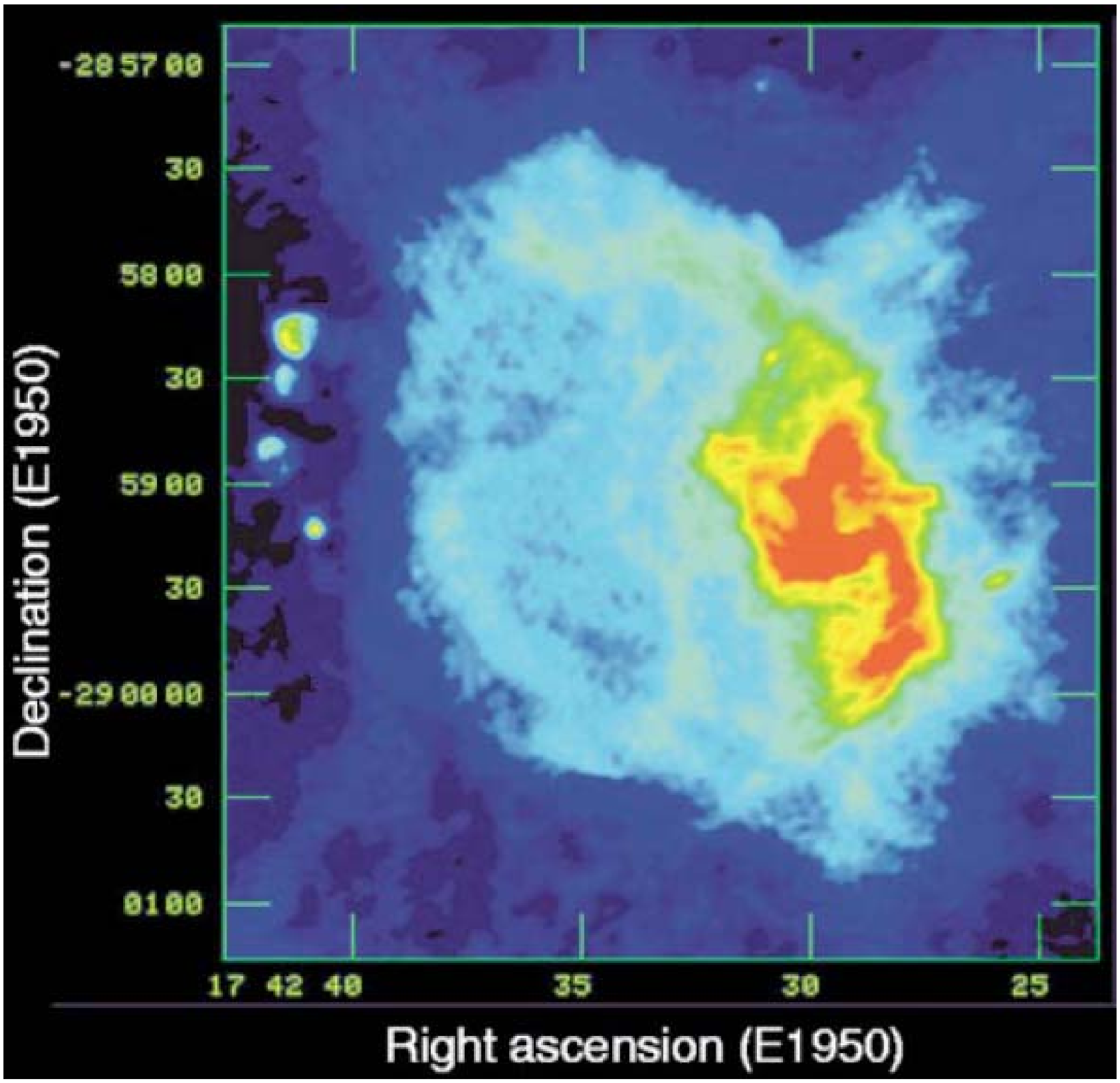

FIG. 1.3: A 6 cm continuum image of the Sgr A complex (from Yusef-Zadeh, Melia, & Wardle 2000) showing the shell-like structure of the non-thermal Sgr A East (light blue and green) and the spiral-shaped structure of the thermal Sgr A West (red) at a resolution of $3''.4 \times 2''.9$. A cluster of HII regions apparently associated with Sgr A East is also evident to the east of the shell. The weak extended features (dark blue) surrounding the shell are part of the Sgr A East halo.

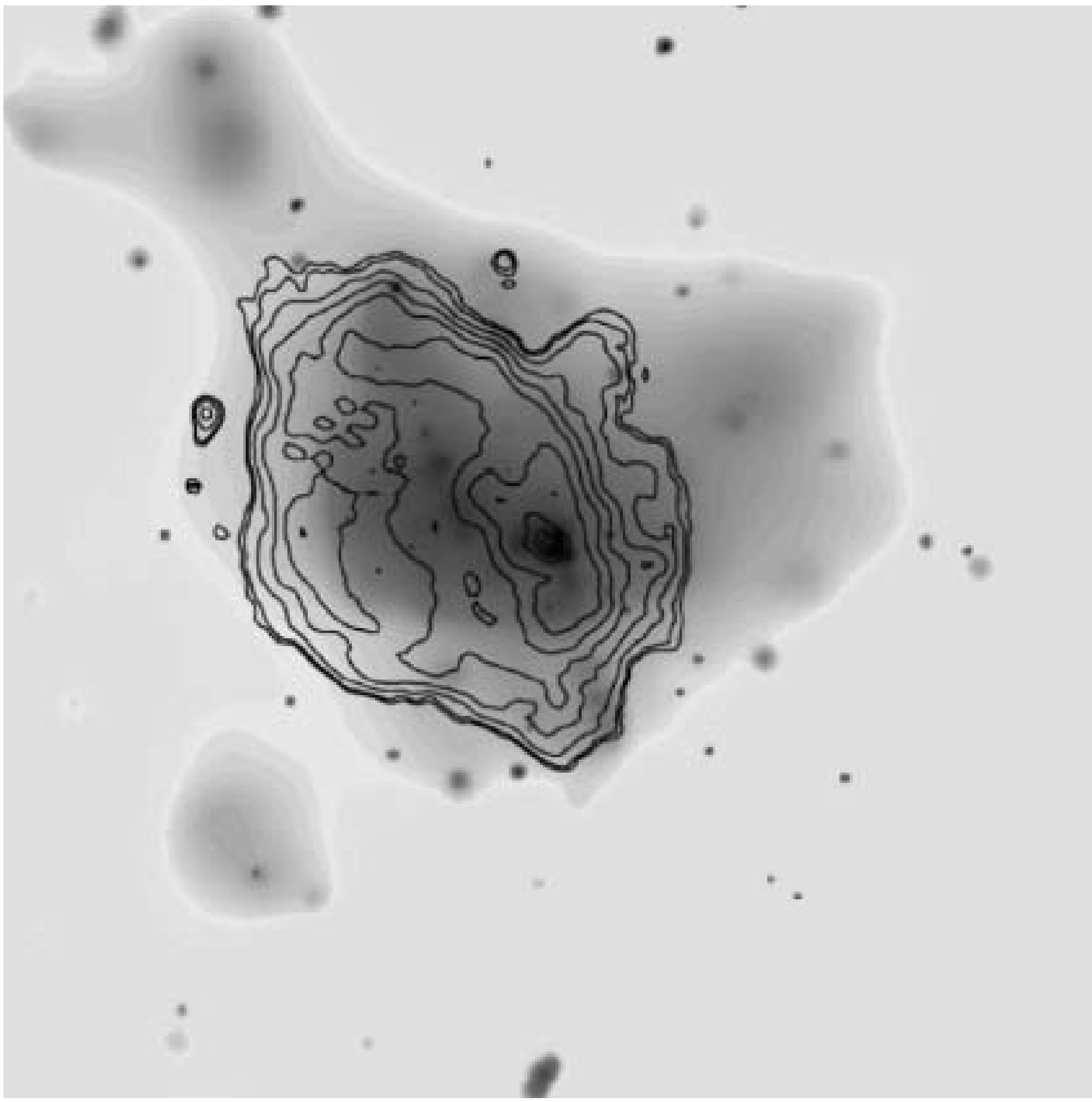

FIG. 1.4: *Chandra* X-ray image (1.5–7.0 keV) of the Sgr A region with 20 cm radio contours overlaid (from Maeda et al. 2002).

ably unbound (Melia & Falcke 2001 and references therein). The X-ray observations may favor a classification as a young ($\sim 10^4$ yr) metal-rich mixed-morphology SNR (Maeda et al. 2002). Thus, the origin of Sgr A East is still an open question.

Sgr A West, also known as the "Mini-spiral" due to the three-arm spiral configuration of ionized gas and dust, is thought to lie within a large central cavity that is surrounded by the circum-nuclear disk (CND) at a radius of ~ 2 pc from the Galactic center (Figure 1.5). The name, CND, was inspired by early observations of HCN and HCO+ that showed signatures of a single rotating disk with the center swept clear of material (Güsten 1987). However, recent observations with increased sensitivity and resolution show that, with a distinct outer edge at $\sim 45''$ from Sgr A*, the CND resembles a ring more than a disk, that is composed of at least three distinct clouds that are orbiting the SMBH (e.g., Wright et al. 2001). In fact, the CND is composed of many clumps with an average density of $\sim 10^5\ \mathrm{cm}^{-3}$ (McGary, Coil, & Ho 2001).

The superposition of the radio continuum emission from Sgr A West due to free-free radiation with the surrounding molecular gas (Figure 1.5) suggests that the central cavity is filled with a bath of ultraviolet radiation heating the dust and gas (Yusef-Zadeh et al. 1999b). For instance, the western arc of the Mini-spiral traces the ionized inner edge of the CND (see the references in McGary, Coil, & Ho 2001). Sgr A West probably derives its heat from the central distribution of hot and luminous stars (some of them are thought to have been formed as recently as a few million years ago) rather than from a single point source (such as Sgr A*) (see the review of Melia & Falcke 2001). We therefore see a sprinkling of several IR-bright sources throughout Sgr A West that are probably embedded luminous stars (e.g., see Figure 1.6). Spectroscopy of the hot gas in the mini-spiral structure and the Very Large Array (VLA) proper motion studies suggest that it is rotating with a velocity of a few hundreds $\mathrm{km\ s^{-1}}$ around Sgr A* and possibly feeding the SMBH (Melia & Falcke 2001 and references therein).

Sgr A*, the bright and very compact radio point at the intersection of the arms of the Mini-spiral (more exactly, at $\alpha = 17^{\mathrm{h}}45^{\mathrm{m}}40\overset{\mathrm{s}}{.}0,\ \delta = -29°00'26\overset{''}{.}6$; J2000) is now known to be the very center of the Galactic gravitational potential well and the highly probable candidate of a SMBH. Since Lacy et al. (1980) suggested a concentration of matter with a point-like object of mass several $\times 10^6\ \mathrm{M_\odot}$ at the Galactic center, many observational efforts have been made to understand this mass concentration better, including spectroscopic studies on radial velocities of late-type giants, AGB stars, and emission line stars within a few arcsec

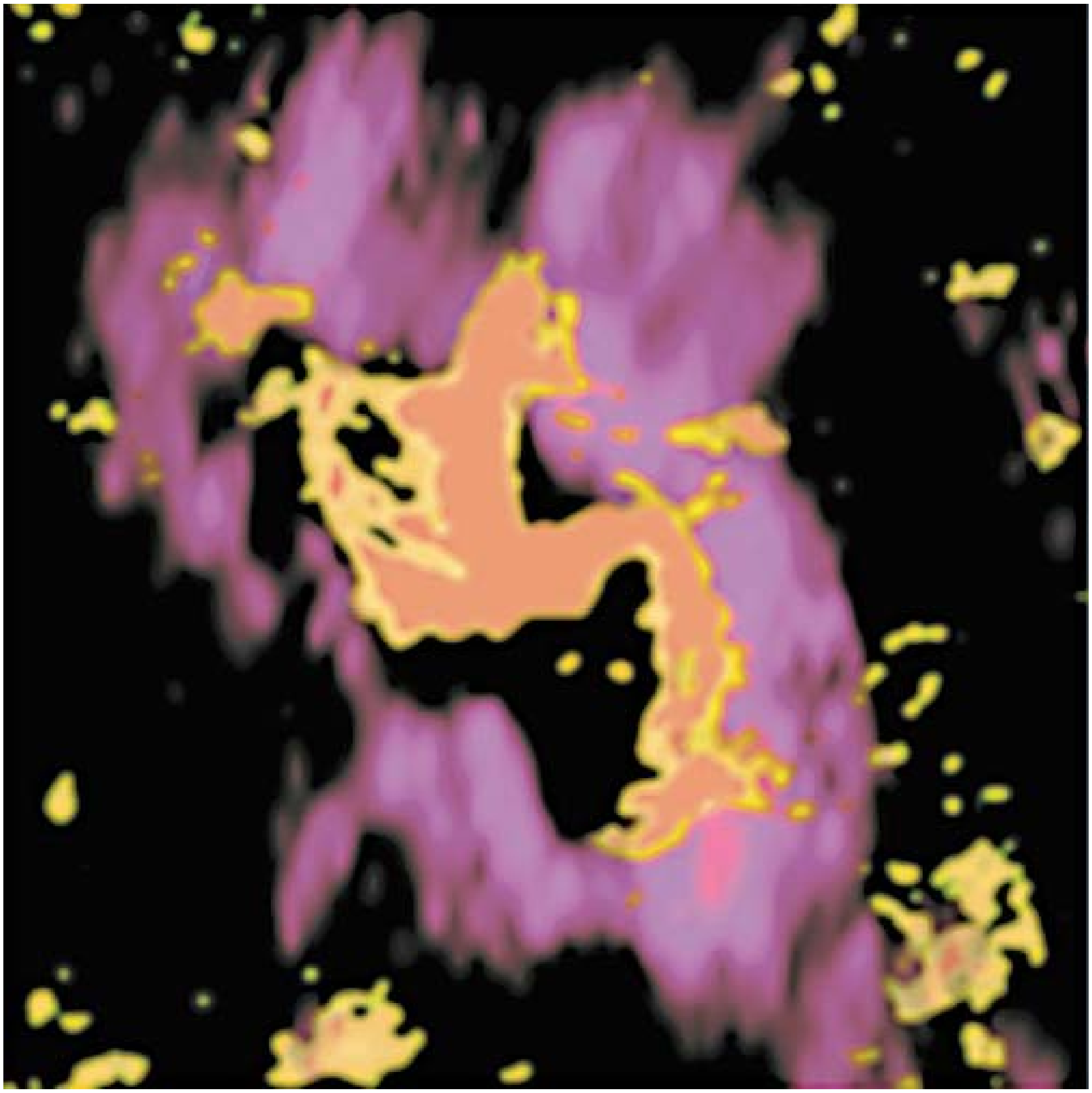

FIG. 1.5: A radio image of Sgr A West (ionized gas) at $\lambda = 1.2$ cm, showing its three-arm appearance (orange), and the circum-nuclear disk (CND) in HCN emission (purple) (from Yusef-Zadeh, Melia, & Wardle 2000). Most of the ionized gas is distributed in the molecular cavity. At the distance to the Galactic center (8.0 kpc; Reid 1993), this image corresponds to a size of ~ 4 pc on each side.

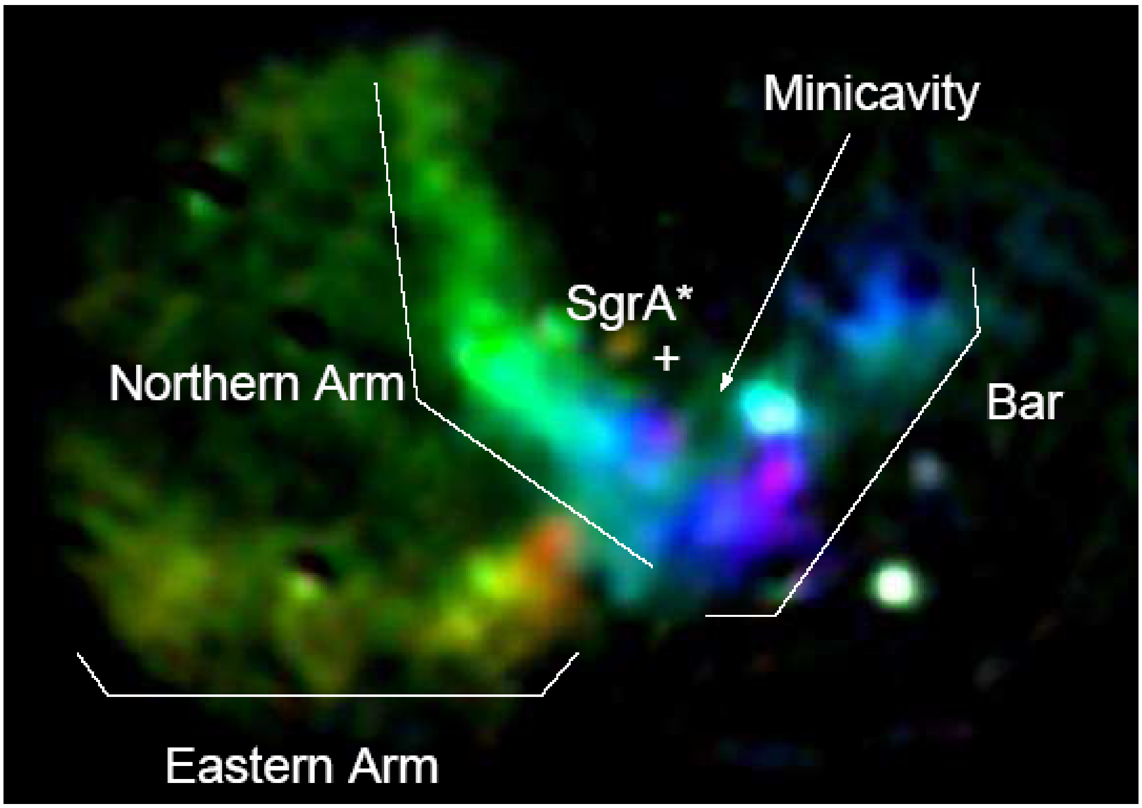

FIG. 1.6: Sgr A West observed in Brγ (from Paumard, Maillard, & Morris 2004) between -350 $\mathrm{km\ s^{-1}}$ (purple) and +350 $\mathrm{km\ s^{-1}}$ (red). The standard bright features, Northern and Eastern Arms, Bar, and the Mini-cavity, are indicated. Also, a few emission line stars show up as bright points in the image.

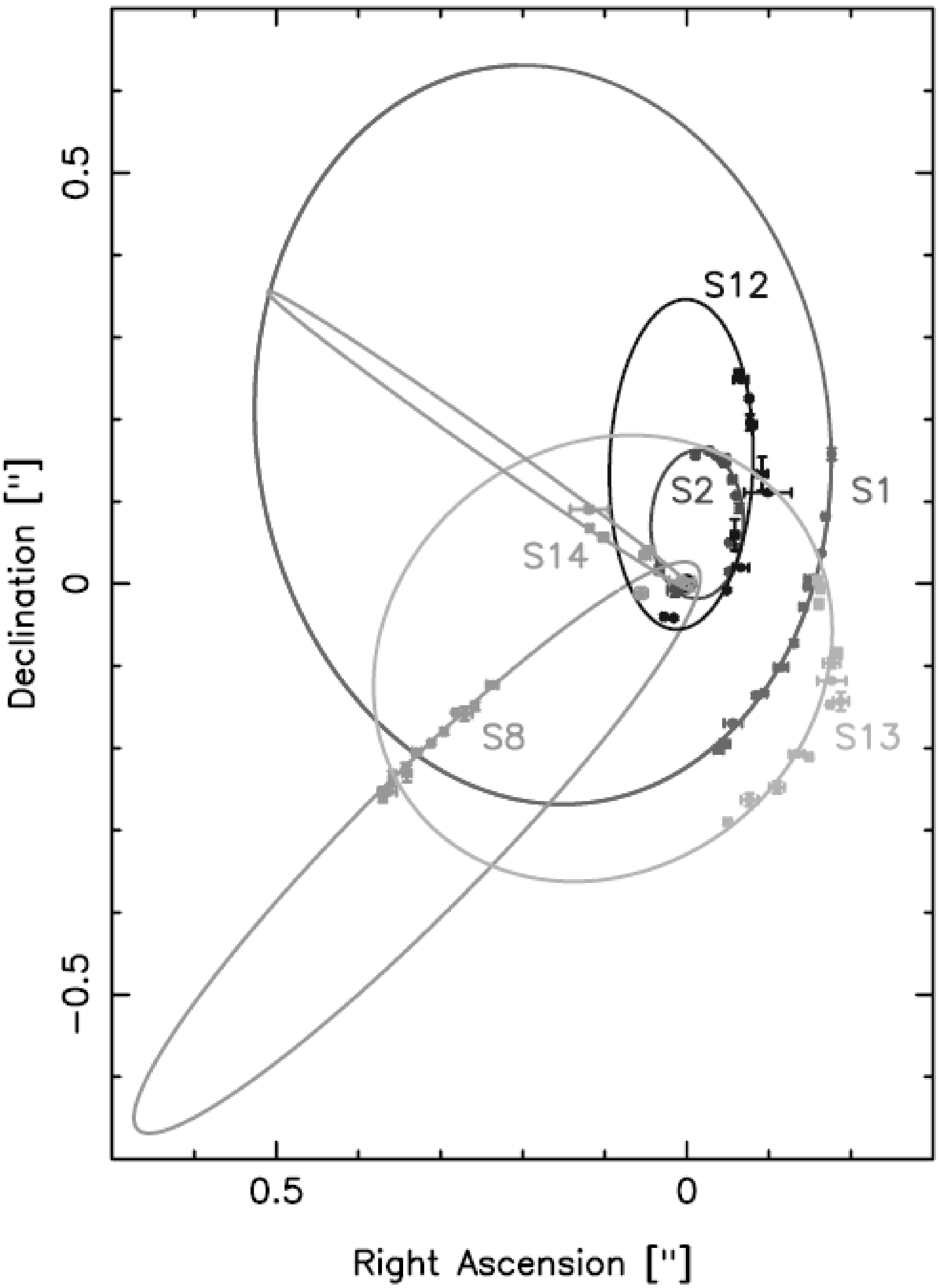

FIG. 1.7: Proper motions of stars around Sgr A* (from Schödel et al. 2003). Measured time-dependent positions with their errors are presented with the determined projected orbits.

from Sgr A* (see the review of Melia & Falcke 2001). The most important observations that demonstrated the presence of the SMBH are those of the proper motions of stars near Sgr A*. With the proper motion data for stars at projected distances $\lesssim 1$ arcsec or 0.04 pc from Sgr A* (assuming the distance to the Galactic center as 8.0 kpc; Reid 1993), acquired over a period of last decade with the W. M. Keck telescope, the ESO New Technology Telescope (NTT), and the ESO Very Large Telescope (VLT), the mass of this SMBH candidate is determined to be $\simeq 4 \times 10^6\ \mathrm{M}_\odot$ (see Ghez et al. 2003; Schödel et al. 2003 and references therein; see Figure 1.7 for example).

1.3 Molecular Clouds Surrounding the Sgr A Complex

A number of dissipative processes lead to a strong concentration of gas in a "Central Molecular Zone" (CMZ) of about 200-pc radius, in which the molecular medium is characterized by high densities ($n \sim 10^4\ \mathrm{cm}^{-3}$), large velocity dispersions (15–30 $\mathrm{km\ s}^{-1}$), high temperatures ($T_K \sim 50$–70 K), and strong magnetic fields (of order milliGauss) (see Figures 1.8 & 1.2). The physical state of the gas and the resultant processes of star formation and evolution occurring in this environment are therefore quite unlike those occurring in the large-scale disk. Gas not consumed by star formation either enters a hot X ray-emitting halo and is lost as a thermally driven galactic wind, or continues moving inward through the domain of the Galactic nucleus, which is defined to be composed of Sgr A*, Sgr A West, and the CND in this thesis, and eventually into the SMBH (see the reviews of Morris & Serabyn 1996 and Güsten & Philipp 2004).

The two GMCs, M-0.02-0.07 and M-0.13-0.08, found within a few arcminutes of Sgr A* (see Figure 1.8) are known to be physically located at the Galactic center and are seen connected to the nuclear region (composed of Sgr A*, Sgr A West, and the CND). The GMC M-0.13-0.08 (also known as the "$20\ \mathrm{km\ s}^{-1}$ cloud"), lying ~ 9 pc directly south of Sgr A* in projection, appears to be connected to the CND via its northern extensions called the "southern streamer" (Coil & Ho 1999, 2000; see Figure 1.9).

The GMC M-0.13-0.08 is also connected to the other nearby GMC, M-0.02-0.07 (the "$50\ \mathrm{km\ s}^{-1}$ cloud"), by a ridge of gas and dust named as the "molecular ridge" (see Coil & Ho 2000 and references therein). This ridge appears to be compressed gas that wraps around Sgr A East and continues to the core of the $50\ \mathrm{km\ s}^{-1}$ cloud (see Figures 1.10 & 1.11). The molecular ridge is long and narrow, roughly 3 pc across and extending well over 10 pc north

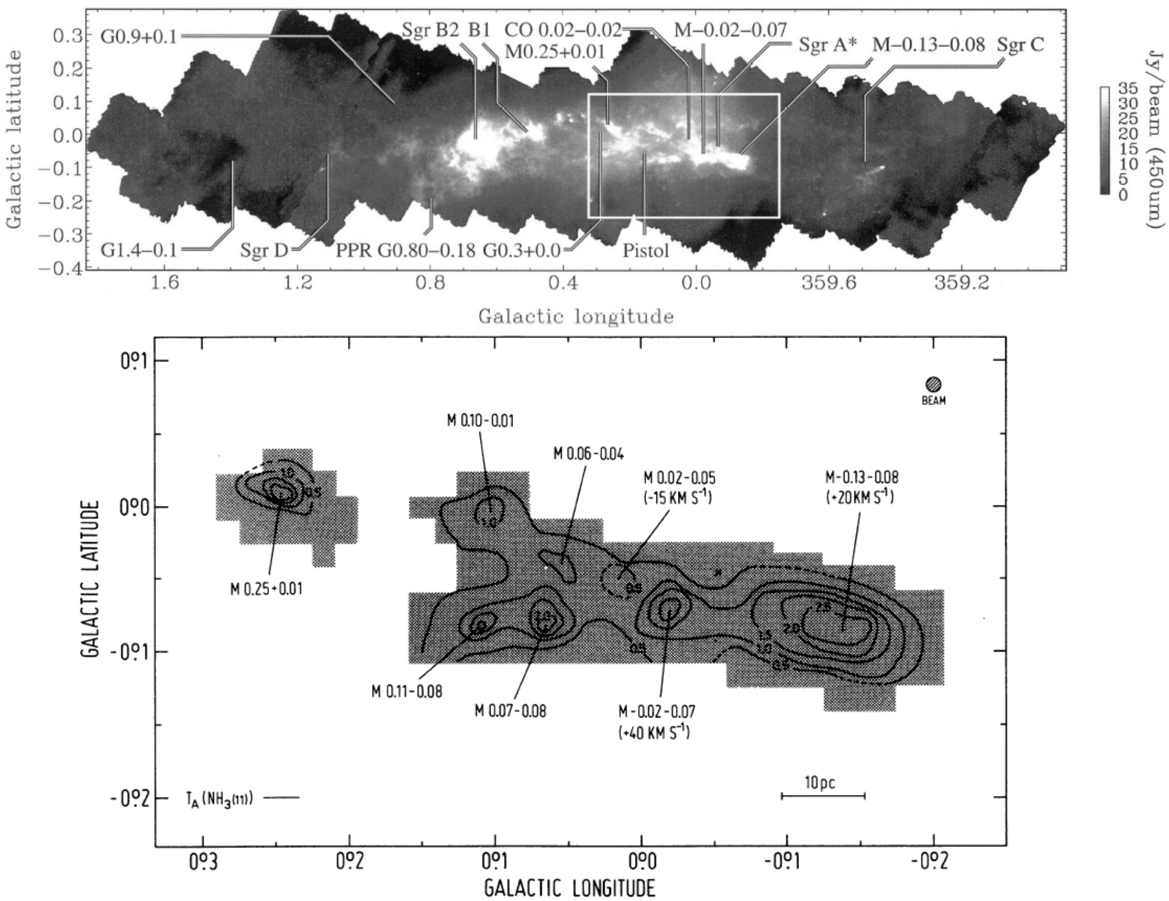

FIG. 1.8: Molecular features in the Central Molecular Zone (CMZ). (top) 450 $\mu\mathrm{m}$ map of the Galactic center CMZ made with the Sub-millimeter Common-User Bolometer Array (SCUBA) (from Pierce-Price et al. 2000). The size of this map is approximately $2^\circ\!.8 \times 0^\circ\!.5$ (400×75 pc). (bottom) Map of the NH_3(1,1) line emission (from Güsten, Walmsley, & Pauls 1981) in the region indicated by a box in the SCUBA map. Various molecular clouds shown as NH_3 concentrations are labelled with 'M' followed by the galactic coordinates of the peak in NH_3(1,1). Antenna temperatures are indicated on the contours where 0.4 K antenna temperature $\simeq 1$ K main beam brightness temperature. Note that M-0.02-0.07 is more known as the "+50 $\mathrm{km\ s^{-1}}$ cloud" nowadays.

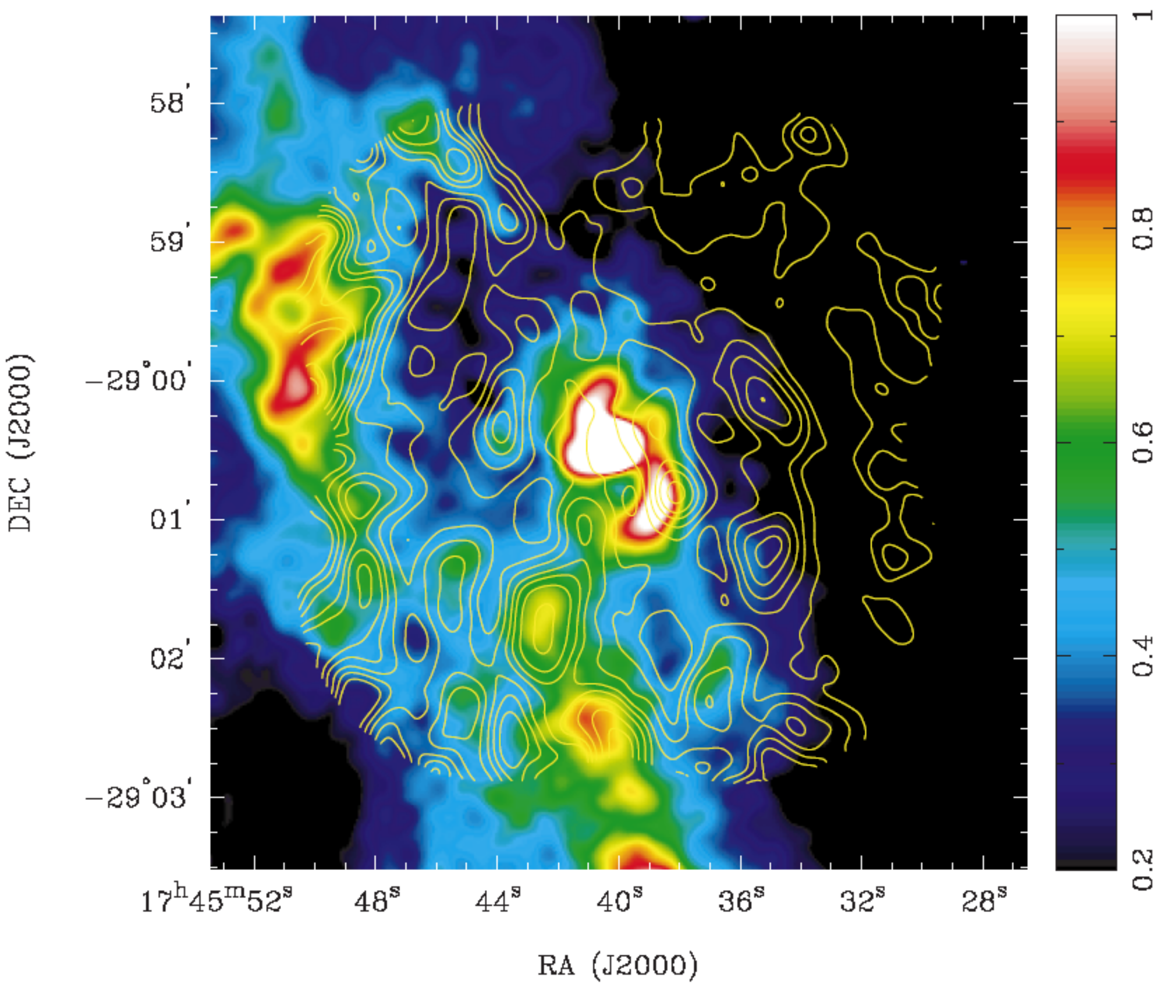

FIG. 1.9: 1.2 mm continuum emission and NH_3(3,3) emission maps of the central 10 pc (from Figure 9 of McGary, Coil, & Ho 2001). Primary beam-corrected NH_3(3,3) contours are overlaid on 1.2 mm emission of Zylka et al. (1998). Contour levels are 3, 6, 10, 15, 23, 30, 40, 55, 70, 90, and 110 σ where $\sigma = 0.33 \text{ Jy beam}^{-1} \text{ km s}^{-1}$ (the beam size is $\sim 15'' \times 13''$), and the color scale runs from 0.3 to 1 Jy beam^{-1} (the beam size is $11''$). Spiral-shaped bright feature at the center is thermal emission from Sgr A West. Bright 1.2 mm emission in the north-eastern and southern parts is from dust in the giant molecular clouds (GMCs) M-0.02-0.07 and M-0.13-0.08, respectively.

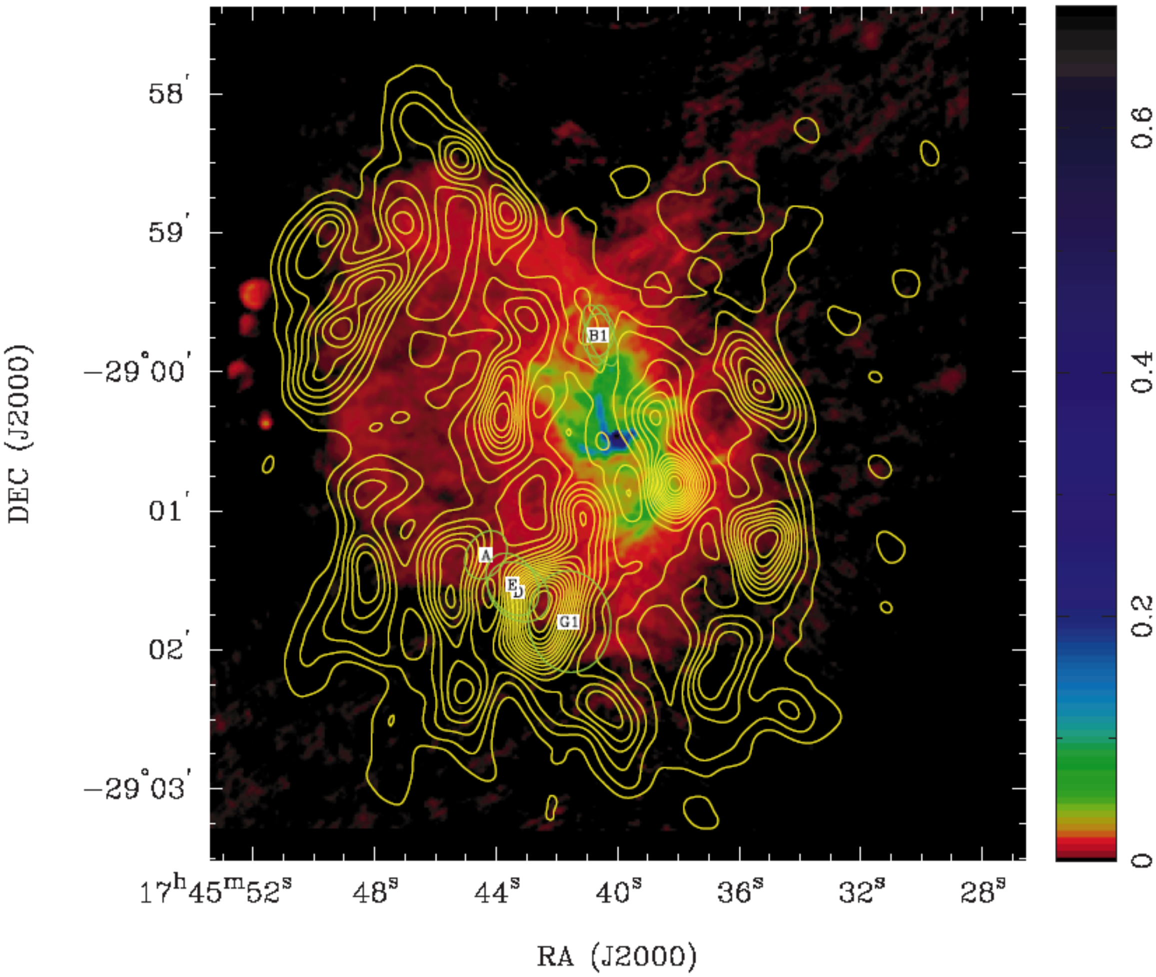

FIG. 1.10: 6 cm continuum and NH_3(3,3) emission maps of the central 10 pc (from McGary, Coil, & Ho 2001). Velocity-integrated NH_3 (3,3) emission in yellow contours is overlaid on 6 cm continuum emission showing Sgr A* (black dot in the center), Sgr A West (mini-spirals in green and blue), and Sgr A East (red shell) (Yusef-Zadeh & Morris 1987). Contour levels are in intervals of $4\,\sigma$ where $\sigma = 0.33$ Jy beam^{-1} km s^{-1} (the beam size is $\sim 15'' \times 13''$), and the color scale ranges from 0 to 0.7 Jy beam^{-1} (the beam size is $3.''4 \times 3.''0$). The positions of the 1720 MHz OH masers from Yusef-Zadeh et al. (1999a) are labeled with green error ellipses scaled up in size by a factor of 15.

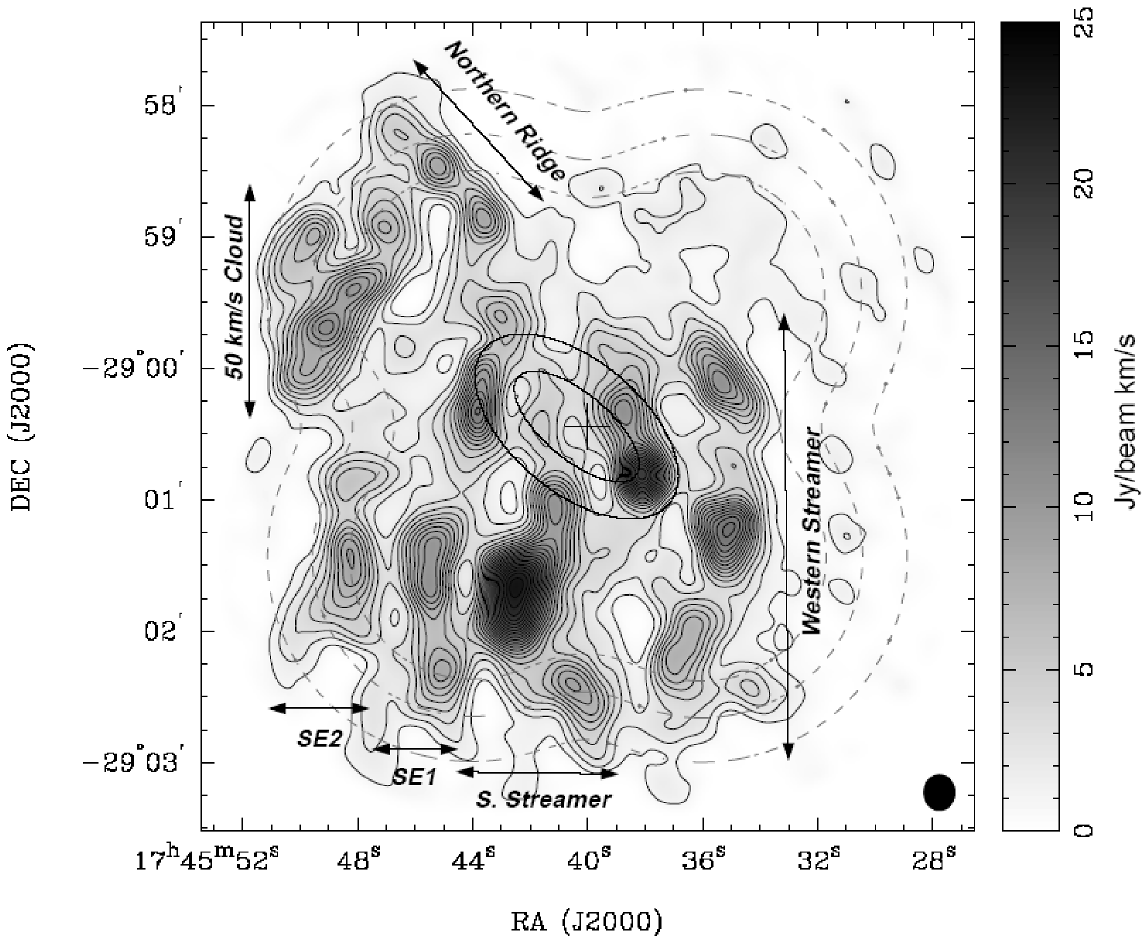

FIG. 1.11: Velocity-integrated NH_3 (3,3) emission with the main features labeled (from McGary, Coil, & Ho 2001). The approximate location of the CND is represented by two ellipses, and the location of Sgr A* is marked by a cross. SE1 and SE2 are the parts of the "molecular ridge" discussed by Coil & Ho (2000). The RMS noise of the map is $\sigma = 0.33\ \mathrm{Jy\ beam^{-1}\ km\ s^{-1}}$ (the beam size is $\sim 15'' \times 13''$) and the contour levels are in intervals of $3\ \sigma$. Primary-beam responses of 10%, 30%, and 50% are shown in dashed contours.

to south. Along the length of the entire ridge, there is a roughly north-south velocity gradient of $0.1~\mathrm{km~s^{-1}}$ arcsec^{-1} (Coil & Ho 2000).

With a better spatial resolution than previous observations, McGary, Coil, & Ho (2001) found new molecular features in NH_3 emission including a "western streamer" and a "northern ridge" (Figures 1.10 & 1.11). The western streamer has a long, filamentary structure, and its curvature matches closely the western edge of Sgr A East. McGary, Coil, & Ho (2001) reported a large velocity gradient of $1~\mathrm{km~s^{-1}}$ arcsec^{-1} ($25~\mathrm{km~s^{-1}}$ pc^{-1}) covering $150''$ (6 pc) along the western streamer. At the southern end, NH_3 emission is at $-70~\mathrm{km~s^{-1}}$, but the velocity smoothly shifts toward the red until it reaches $\sim +90~\mathrm{km~s^{-1}}$ at the northern end. Molecular gas in the western streamer has the largest average NH_3 line width ($20~\mathrm{km~s^{-1}}$) and highest temperatures ($T_K = 46$) in the central 10 pc (Herrnstein & Ho 2005).

The northern ridge is also a linear feature, roughly $90''$ in length, that lies along the northern edge of Sgr A East. This cloud has a similarly large average NH_3 line width ($17~\mathrm{km~s^{-1}}$) and high temperature (37 K) as the western streamer. However, McGary, Coil, & Ho (2001) found no velocity gradient larger than their spectral resolution of $9.8~\mathrm{km~s^{-1}}$ along the northern ridge.

1.4 Relationships between the Various Components in the Central 10 Parsecs

A number of observational efforts have been made to determine whether these various components (the Galactic nucleus, Sgr A East, and the surrounding molecular clouds) in the central 10 pc in projection are really residing in the Galactic center or are just seen overlapped in that direction. Observers have sought to reveal the relative positions along the line-of-sight and the physical relationships between the components. Studies concerning the structure and dynamics of the central 10 pc (e.g., Mezger et al. 1989; Coil & Ho 1999, 2000; Herrnstein & Ho 2005) have reached a few agreements, but still leave many unresolved contradictions, as follows.

1.4.1 Interaction between Sgr A East and the Molecular Clouds

Based on the morphology and dynamics of the molecular clouds, an interaction between the eastern part of Sgr A East and the GMC M-0.02-0.07 (the $50~\mathrm{km~s^{-1}}$ cloud) has been inferred (e.g. Mezger et al. 1989; Genzel et al. 1990; Ho et al. 1991; Serabyn, Lacy, & Achtermann 1992; Mezger, Duschl, & Zylka 1996; Novak 1999; Coil & Ho 2000). Recent observations of NH_3(3,3) emission in the region show that Sgr A East impacts material to the northern ridge and to the western streamer as well (McGary, Coil, & Ho 2001; Herrnstein & Ho 2005; see Figure 1.10). However, the relationships between Sgr A East and the GMC M-0.13-0.08, the southern streamer, and the molecular ridge are unclear, and the degree to which Sgr A East influences the $50\ \mathrm{km\ s^{-1}}$ cloud is still in debate.

From their observational studies on molecular abundance variations, Min et al. (2005) found enhancement of HNCO and SiO (tracers for high-temperature, probably shocked, regions) toward the GMC M-0.13-0.08 and suggested that this may be caused by the interaction with Sgr A East. Several 1720 MHz OH masers, which are a good diagnostic of continuous shock (or C-shock) excitation (Frail et al. 1996; Wardle, Yusef-Zadeh, & Geballe 1999), have been detected along the southern edge of Sgr A East (Yusef-Zadeh et al. 1996; see Figure 1.10). There may thus be evidence that Sgr A East is also driving shocks into the southern streamer and the molecular ridge, which are extensions of M-0.13-0.08. However, there is an alternative interpretation for these southern OH masers; that they may result from the impact of the SNR G 359.92-0.09 on Sgr A East (Coil & Ho 2000; Herrnstein & Ho 2005).

Kinematics of the molecular ridge indicate that the gas in the $50\ \mathrm{km\ s^{-1}}$ cloud is being pushed both to the east and behind Sgr A East along the line of sight, which would place the $50\ \mathrm{km\ s^{-1}}$ cloud adjacent to and partially behind Sgr A East. The velocity shift resulting from this expansion is reported as 20–40 $\mathrm{km\ s^{-1}}$ (Genzel et al. 1990; Ho et al. 1991; Serabyn, Lacy, & Achtermann 1992). The line width in the core of the $50\ \mathrm{km\ s^{-1}}$ cloud is FWHM$=$ $40\ \mathrm{km\ s^{-1}}$, which is unusually broad for molecular cloud cores (see the review of Coil & Ho 2000). However, Herrnstein & Ho (2005) argue that the molecular gas in the $50\ \mathrm{km\ s^{-1}}$ cloud does not appear to be strongly affected by the impact of Sgr A East, based on the results from their NH_3 observations; the estimated kinetic temperature of this cloud (25 K) is the lowest value of any molecular feature in the central 10 pc, and no significant velocity gradient is observed in this cloud.

1.4.2 Mass Inflow from the GMCs to the Galactic Nucleus

For the past two decades, the origin of the dense gas and dust in the CND and Sgr A West has remained unclear. Many attempts have been made to detect kinematic connections between two nearby GMCs and the CND (see the review of Herrnstein & Ho 2005). The southern streamer extends northward from the $20\ \mathrm{km\ s^{-1}}$ GMC, which is located in front of the Galactic nucleus along the line-of-sight, toward the south-eastern edge of the CND (see Figure 1.11). Increased line widths and evidence of heating as the southern streamer approaches the Galactic center indicate that gas may be flowing from the $20\ \mathrm{km\ s^{-1}}$ GMC toward the nuclear region, since the line broadening and the heating could result from shocks as the gas merges with the CND or from high-energy photons escaping from the nuclear region (Coil & Ho 2000; McGary, Coil, & Ho 2001). Supporting morphological evidence for this connection has come from observations of HCN, ^{13}CO, and 1 mm continuum emission (e.g., see Figure 1.9). However, Herrnstein & Ho 2005 argue that the southern streamer shows no significant velocity gradient, as would be expected for a cloud infalling toward the nucleus.

Having examined three additional connections – the western streamer, the molecular ridge and the northern ridge – based on the velocity and temperature gradients observed in NH_3 emission, McGary, Coil, & Ho (2001) discarded the western streamer while accepted the northern ridge and the south-western part of the molecular ridge as the possible connections. However, Herrnstein & Ho (2005) suggested that the very high velocity gradient of the western streamer is consistent with a ridge of gas highly inclined to the line-of-sight that is being pushed outward by expansion of Sgr A East. They interpreted the fact that the western streamer radiates strong NH_3 (6,6) emission (thus some fraction of the gas may have kinetic temperatures of $\gtrsim 100$ K) as supporting evidence that the western streamer was cleared out of the central parsecs by Sgr A East.

1.4.3 Influence of Sgr A East on the Activity of the Galactic Nucleus

According to studies of the mass inflow to the Galactic center, the time-averaged rate of total mass flow seems high enough for the nucleus to emit at the Eddington rate, making the Milky Way a Seyfert galaxy (Morris & Serabyn 1996). However, the current accretion rate and luminosity of Sgr A* are many orders of magnitude smaller than this. The efficiency of mass transfer from the nearby GMCs into the nuclear region through the passages introduced above is thought to be significantly responsible for this low activity of the Galactic center.

The Galactic nucleus generally thought to lie in front of Sgr A East along the line-of-sight considering the absorption of 90 cm continuum from Sgr A East by Sgr A West (Yusef-Zadeh & Morris 1987; Pedlar et al. 1989). However, many arguments suggest that the Galactic nucleus is possibly embedded within the hot cavity of the Sgr A East shell (see the review in Maeda et al. 2002). For example, Yusef-Zadeh et al. (1996) detected 1720 MHz OH masers to the north of the CND (see Figure 1.10 for the position) and argued that this is the evidence that Sgr A East is driving shocks into the CND. It is thus likely that Sgr A East really is an object situated in the Galactic center, so physical interactions between Sgr A East and the Galactic nucleus is inevitable. Sgr A East may indeed be a key to understanding the activity in the nucleus of our Galaxy (Yusef-Zadeh, Melia, & Wardle 2000).

The expansion of the Sgr A East shell appears to be a dominating force in the central 10 pc, possibly pushing much of the molecular gas away from the nucleus as seen above (McGary, Coil, & Ho 2001; Herrnstein & Ho 2005). Thus, explosive events like Sgr A East are generally expected to obstruct the mass inflow from surrounding material into the SMBH at the Galactic center and, as a result, suppress the activity of the nucleus. The main issues are: how strong and how frequent this kind of explosion is, and how long and how effective are they at maintaining an expanding hot cavity against infalling material, thereby starving the SMBH. If the explosions are very strong and frequent, our Galaxy could spend most of its life in a quiescent phase (with occasional short periods of AGN events). In the opposite case, the evolution of the Galactic nucleus could be dominated by an active phase due to a high rate of mass inflow (with occasional breaks by infrequent explosions). Therefore, the explosion that made Sgr A East may be a clue to what our Galaxy was like in the past, and to what it will be like in the future. As seen in Section 1.2, however, we have little knowledge about the nature and origin of Sgr A East.

1.5 Observations of Near-IR H_2 Emission from the Central 10 Parsecs

It should be noted that the arguments in the previous section on the relationships between the various objects are mostly based on indirect and qualitative evidence, e.g. morphology, kinematics of molecular clouds, absorption of background radiation, etc. They were generally not based on direct evidence nor on the physical properties of the interactions between the objects. Therefore, to solve the remaining open questions in the central 10 pc, more robust evidence from observations toward the interaction regions is needed.

Molecular hydrogen (H_2) is the most abundant molecule in the interstellar medium (ISM). We cannot, however, observe H_2 directly in cold, dense molecular clouds because the lowest energy levels of H_2 are too high to be excited in these environments, where $T <$ 50 K. Instead, H_2 emission is observed in more active regions, for example in warm regions heated by shocks or in the surfaces of clouds illuminated by far-ultraviolet (far-UV) radiation fields. H_2 emission has been found associated with star-forming regions, SNRs, planetary nebulae, and active galactic nuclei. H_2 emission is an excellent tracer and diagnostic for interactions between dense molecular clouds and other hot and powerful sources, like Sgr A East.

The first detection of H_2 emission from the Galactic center was made by Gatley et al. (1984) (Figure 1.12). They observed the rotational-vibrational H_2 lines in transitions $1-0$ S(1) (2.122 μm), $2-1$ S(1) (2.248 μm), and $1-0$ S(0) (2.223 μm) from the CND. They concluded that the H_2 molecules are excited by shocks based on the measured line ratios. After two years, Gatley et al. (1986) mapped the CND in $\mathrm{H_2}\ 1-0\ \mathrm{S}(1)$ emission with an angular resolution of $18''$, using a Fabry-Perot etalon with $130\ \mathrm{km\ s^{-1}}$ resolution at the United Kingdom Infrared Telescope (UKIRT). They found that the CND has a broken and clumpy appearance and rotates at about $100\ \mathrm{km\ s^{-1}}$.

Burton & Allen (1992) obtained images of various line emission (He I 2.058 μm, Brγ 2.166 μm, and $\mathrm{H_2}\ 1-0\ \mathrm{S}(1)\ 2.122$ μm), together with broad band K' (2.1 μm) image from the nuclear region using the Anglo-Australian Telescope (AAT) (see Figure 1.13). The line images were constructed by scanning the telescope perpendicular to the slit (with $20''$ length $\times 1.4''$ width), covering spatially an area of $103'' \times 145''$ and spectrally the entire K window (2.0–2.4 μm) with a resolution of $\lambda/\Delta\lambda = 400$. This technique is superior to narrow-band imaging using a filter in crowded regions like the Galactic center where seeing changes prohibit accurate continuum subtraction (Burton & Allen 1992).

On larger scale, Pak, Jaffe, & Keller (1996a,b) surveyed the Galactic plane in $\mathrm{H_2}$ 1–0 $\mathrm{S}(1)$ emission along a 400 pc-long strip and found that H_2 emission exists throughout the surveyed region and peaks toward Sgr A. They also mapped the central 50 pc with a beam size of $3\rlap{.}'3$ in diameter (Figure 1.14). Based on the absolute intensity of $\mathrm{H_2}\ 1-0\ \mathrm{S}(1)$ emission and comparisons with far-IR intensities measured in the Galactic center, they concluded that the observed H_2 emission is from UV-excitation. They also argued that the H_2 emission from the

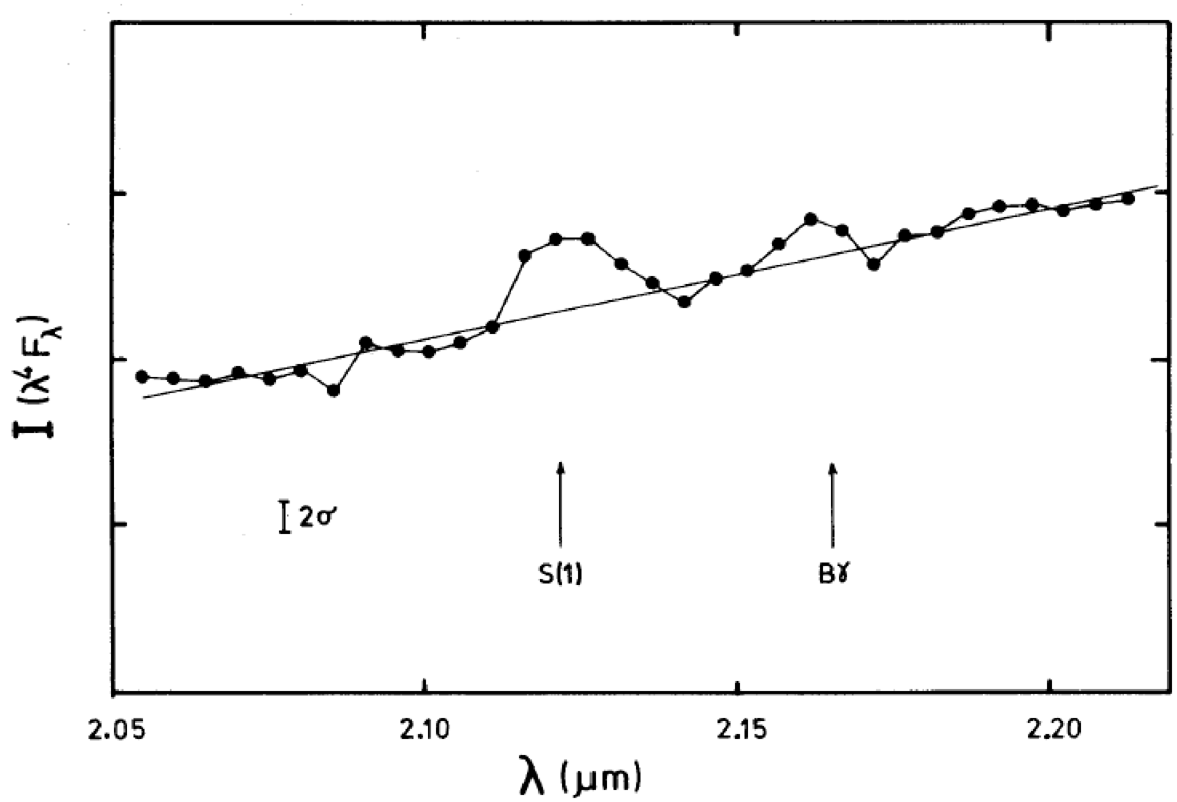

FIG. 1.12: The first H_2 spectrum observed from the Galactic center. Gatley et al. (1984) observed the $\mathrm{H_2}\ 1-0\ \mathrm{S}(1)$ line from the CND with the United Kingdom Infrared Telescope (UKIRT) using a circular variable filter wheel (CVF) of 1 per cent spectral resolution. A typical error bar is shown.

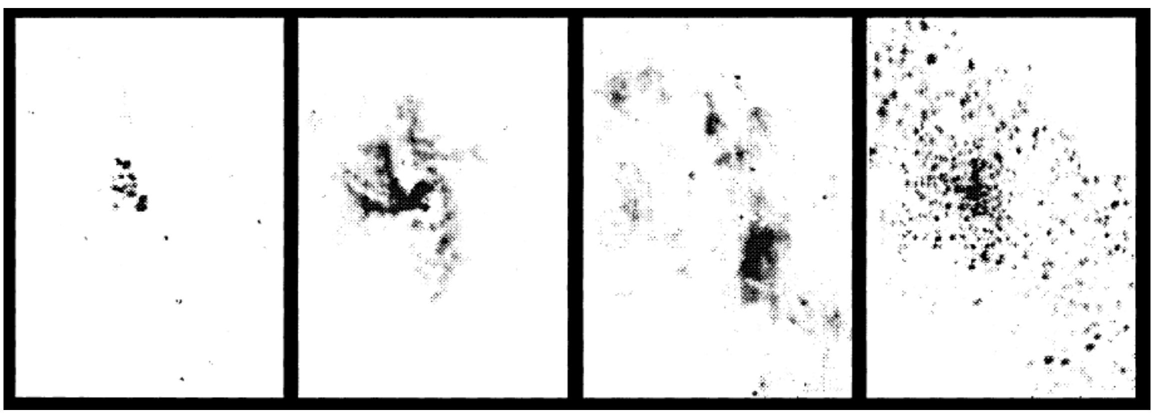

FIG. 1.13: K-band images of the Galactic nuclear region observed by Burton & Allen (1992) From the left, He I ($2.058\ \mu$m), Brγ ($2.166\ \mu$m), $H_2\ 1-0\ S(1)$ ($2.122\ \mu$m), and broad band K' ($2.1\ \mu$m) images covering $103'' \times 145''$ of the Galactic center. The He I shows the cluster of massive stars around Sgr A*, the Brγ the ionized streamers of Sgr A West, the H_2 the surrounding CND, and K' the stellar distribution along the Galactic plane. North is at the top and east to the left.

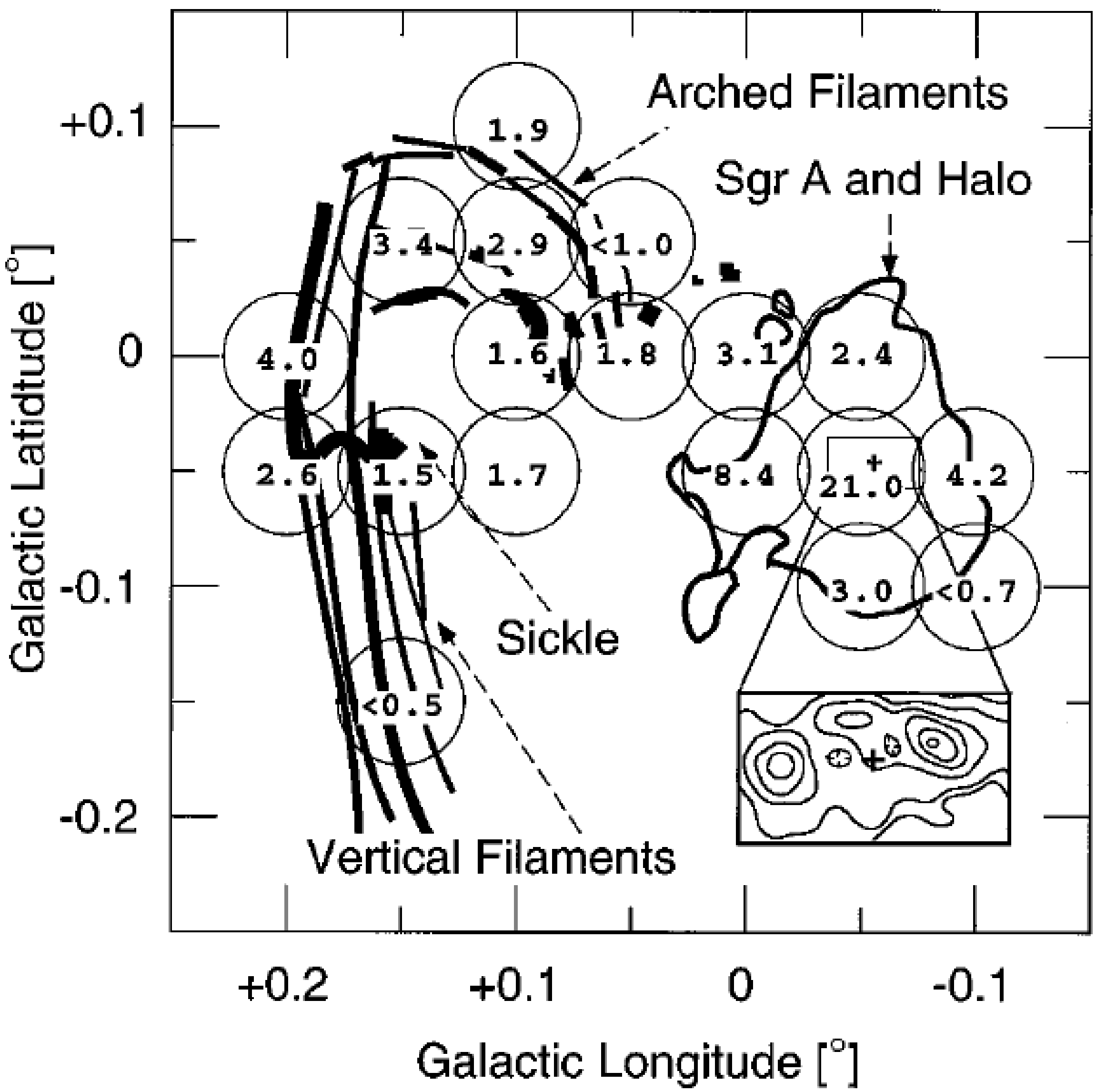

FIG. 1.14: Large-scale distribution of $\mathrm{H_2}\ 1-0\ \mathrm{S(1)}$ emission in the inner 50 pc of the Galaxy (from Pak, Jaffe, & Keller 1996a) with positions (circles with a diameter of the telescope beam size, $3\farcm3$) and measured $\mathrm{H_2}$ intensities (numbers inside the circles in units of 10^{-6} ergs s^{-1} cm^{-2} sr^{-1}). Typical measurement uncertainties are 0.7×10^{-6} ergs s^{-1} cm^{-2} sr^{-1}. The heavy lines show a schematic version of the radio continuum distribution (Yusef-Zadeh, Morris, & Chance 1984). The small box and inset show the $\mathrm{H_2}\ 1{-}0\ \mathrm{S(1)}$ distribution in the CND (Gatley et al. 1986). The plus sign marks the position of Sgr A* ($l = -0\fdg0558$, $b = -0\fdg0462$).

CND, which was suggested to be shock-excited by Gatley et al. (1984), can be explained by UV-excitation in the environment around the Galactic center where the UV field is intense and the gas density is high.

Using the Cooled Grating Spectrometer 4 (CGS4) at the UKIRT, Wardle, Yusef-Zadeh, & Geballe (1999) detected the $\mathrm{H_2}$ $1\text{–}0\ \mathrm{S}(1)$, $2\text{–}1\ \mathrm{S}(1)$, and $1\text{–}0\ \mathrm{S}(0)$ lines at the position 'A' of the 1720 MHz OH maser detection in Figure 1.10. They measured line ratios marginally, but could not constrain the H_2 excitation mechanisms with these ratios. Based on the positional coincidence with the OH maser, they suggested that the H_2 emission is originated from the shocks driven by Sgr A East.

Yusef-Zadeh et al. (1999b, 2001) also surveyed H_2 line emission around the regions where the OH masers have been detected, and imaged the CND and most of the Sgr A East region using NICMOS on the *Hubble Space Telescope (HST)* (Figure 1.15). Despite of the difficulty in continuum subtraction using 1% band-width filters (F212N for line + continuum, F215N for continuum), their H_2 image has the highest spatial resolution ($0\farcs2035$) so far. The brightest H_2 features around Sgr A*, which consist of a partial ring-like structure, trace the CND very well. They found a filamentary structure near the north-west of the CND, where the OH maser is also detected. Based on the morphological coincidence with the western edge of the Sgr A East shell in 20 cm continuum, they suggest that the H_2 feature originates in shocks driven by Sgr A East (see Figure 1.15). To study the kinematics of the CND, they also observed this field using the University of New South Wales Infrared Fabry-Perot (UNSWIRF) etalon at the AAT, with a FWHM spectral resolution of $\sim 75\ \mathrm{km\ s^{-1}}$ and a pixel size of $0\farcs77$. In addition, highly redshifted gas of up to $140\ \mathrm{km\ s^{-1}}$ close to the eastern edge of the Sgr A East shell is detected. Based on their results, combined with the OH detection, they suggest that the H_2 gas is shocked and accelerated by the expansion of Sgr A East into the $50\ \mathrm{km\ s^{-1}}$ cloud and the CND.

As seen so far, the H_2 observations toward the central 10 pc has been dramatically advanced during the past two decades. However, there are still many remaining unsolved questions and limitations. The H_2 excitation mechanism is still in debate (UV-heated vs. shock-heated), particularly between studies using line ratios and those based on the relationships with OH masers. The previous observations were concentrated on the CND, the brightest H_2 feature, rather than the regions where interactions between Sgr A East and the surrounding molecular clouds are expected. Although the spatial resolution has greatly increased, the spectral resolution is not yet high enough to investigate the detailed kinematics

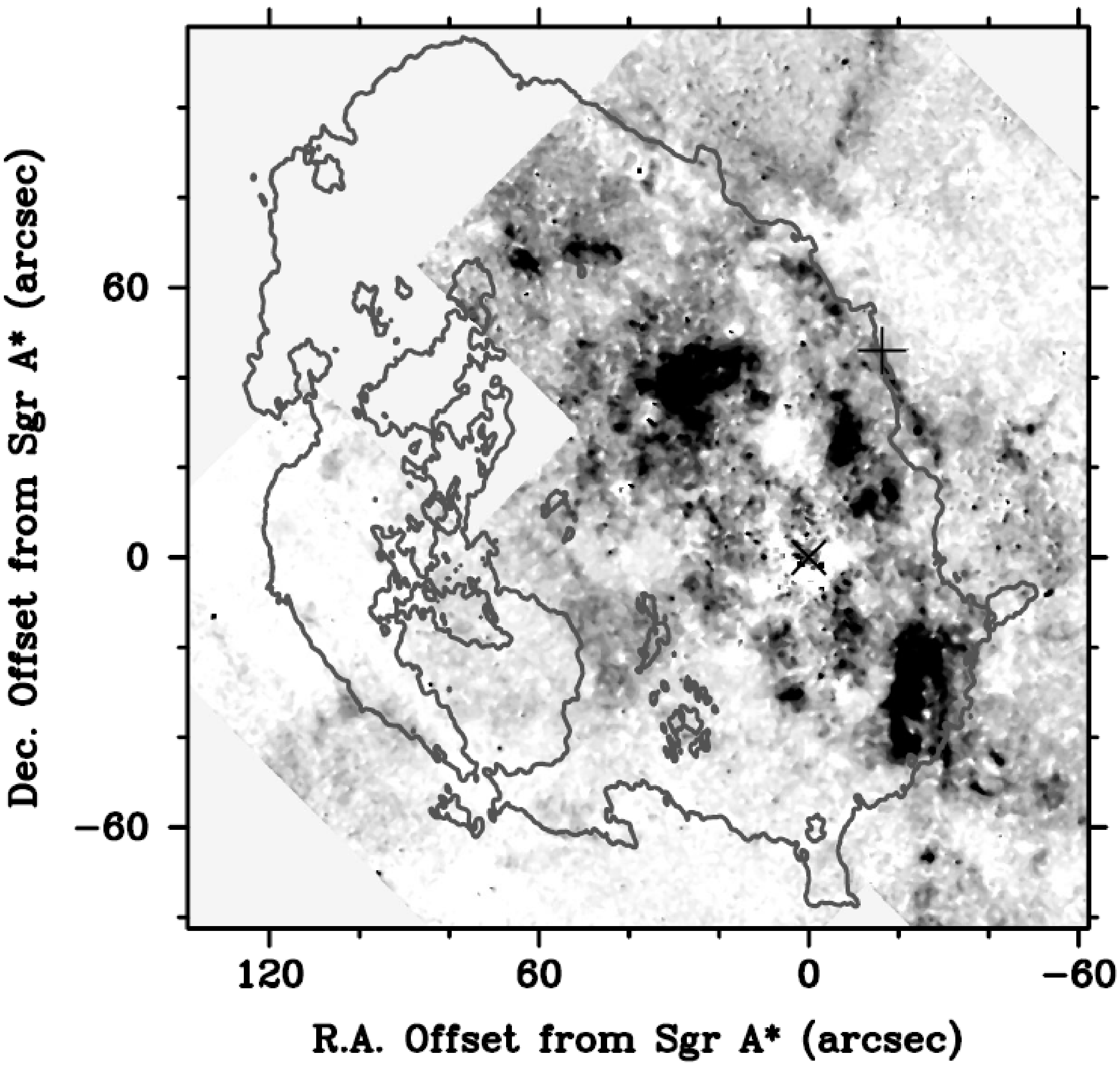

FIG. 1.15: *HST*/NICMOS image of the $2.12\ \mu\mathrm{m}\ \mathrm{H}_2\ 1-0\ \mathrm{S}(1)$ line emission from the CND and Sgr A East (from Yusef-Zadeh et al. 2001). The reverse gray scale ranges from -0.05 to 1.5×10^{-16} ergs s^{-1} cm^{-2} pixel^{-1} (1 pixel = $0.''2035$). The noise level is of the order of 0.02×10^{-16} ergs s^{-1} cm^{-2} pixel^{-1}. Contour of 20 cm continuum emission outlining the Sgr A East shell is shown at 0.75 mJy pixel^{-1}, pixel scale $0.''5$ and resolution $3.''1 \times 1.''6$. The plus sign shows the position of 1720 MHz OH maser source from Yusef-Zadeh et al. (1996), and the cross shows the position of Sgr A*. Despite the high spatial resolution of the *HST* image, and the stability of the point-spread function, this image illustrates the extreme difficulty in obtaining a line image in a crowded region when only low (1%) spectral resolution is used. The white patches in the H_2 image are the results of imperfect continuum subtraction.

(e.g., line profiles) in the interaction regions. Therefore, in order to study the spatial and dynamical relationships between the various components in the central 10 pc, it is necessary to observe additional interaction regions other than the CND in H_2 emission at high spatial and spectral resolution.

In this thesis, we observed the $\mathrm{H_2}\ 1-0\ \mathrm{S}(1)$ and $\mathrm{H_2}\ 2-1\ \mathrm{S}(1)$ lines from the interaction regions between Sgr A East and the other members in central 10 pc, the Galactic nucleus (the CND) and the molecular clouds. We describe the observations using CGS4 at UKIRT in chapter 2 and the reduction of the spectroscopic data in chapter 3. The excitation mechanism of the observed H_2 emission is investigated and the velocities of shocks from Sgr A East are estimated in chapter 4. Based on the directions of the shocks, we construct a three-dimensional model for the structure of the central 10 pc in chapter 5. Finally in chapter 6, we estimate the explosion energy and age of Sgr A East, from which we constrain its origin. We also discuss the influence of Sgr A East-like explosions and SNe on the mass inflow to the nuclear region, and suggest scenarios for the long-time-scale variation and the recent history of the activity of the Galactic nucleus.

REFERENCES

Anantharamaiah K.R., Pedlar A., Ekers R.D., & Goss W.M., 1991, MNRAS, 249, 262

Balick B., & Brown R.L., 1974, ApJ, 194, 265

Burton M., & Allen D., 1992, Proc. Ast. Soc. Australia, 10, 55

Coil A.L., & Ho P.T.P., 1999, ApJ, 513, 752

Coil A.L., & Ho P.T.P., 2000, ApJ, 533, 245

Frail D.A., Goss W.M., Reynoso E.M., Green A.J., & Otrupcek R., 1996, AJ, 111, 1651

Gatley I., Jones T.J., Hyland A.R., Beattie D.H., & Lee T.J., 1984, MNRAS, 210, 565

Gatley I., Jones T.J., Hyland A.R., Wade R., Geballe T.R., & Krisciunas K., 1986, MNRAS, 222, 299

Genzel R., Stacey G.J., Harris A.I., Geis N., Graf U.U., Poglitsch A., & Sutzki J., 1990, ApJ, 356, 160

Ghez A.M., et al., 2003, ApJ, 586, L127

Goss W.M., Schwarz U.J., Ekers R.D., & van Gorkom J.H., 1983, in Danziger J., Gorenstein P., eds, Proc. IAU Symp. 101, Supernova Remnants and Their X-Ray Emission. Dordrecht, Reidel, p. 65

Güsten R., Genzel R., Wright M.C.H., Jaffe D.T., Stutzki J., & Harris A.I., 1987, ApJ, 318, 124

Güsten R., & Philipp S.D., 2004, in Pfalzner S., Kramer C., Staubmeier C., & Heithausen A., eds, Springer proceedings in physics, Vol. 91, Proc. of the 4th Cologne-Bonn-Zermatt Symp., The Dense Interstellar Medium in Galaxies, Berlin, Heidelberg: Springer, p. 253

Güsten R., Walmsley C.M., & Pauls T., 1981, A&A, 103, 197

Herrnstein R.M., & Ho P.T.P., 2005, ApJ, 620, 287

Ho P.T.P., Ho L.C., Szczepanski J.C., Jackson J.M., Armstrong J.T., & Barrett A.H., 1991, Nature, 350, 309

Jones T.W., 1974, A&A, 30, 37

Kassim N.E., La Rosa T.N., Lazio T.J.W., & Hyman S.D., 1999, in Falcke H. et al., eds, ASP Conf. Ser. Vol. 186, The Central Parsecs of the Galaxy. Astron. Soc. Pac., San Francisco, p. 403

Khokhlov A., & Melia F., 1996, ApJ, 457, L61

Lacy J.H., Townes C.H., Geballe T.R., & Hollenbach D.J., 1980, ApJ, 241, 132

Lynden-Bell D., & Rees M.J., 1971, MNRAS, 152, 461

Maeda Y. et al., 2002, ApJ, 570, 671

Marshall J., Lasenby A.N., & Harris A.I., 1995, MNRAS, 277, 594

McGary R.S., Coil A.L., & Ho P.T.P., 2001, ApJ, 559, 326

Melia F., & Falcke H., 2001, ARA&A, 39, 309

Mezger P.G., Duschl W.J., & Zylka R., 1996, ARA&A, 7, 289

Mezger P.G., Zylka R., Salter C.J., Wink J.E., Chini R., Kreysa E., & Tuffs R., 1989, A&A, 209, 337

Minh Y.C., Kim S.-J., Pak S., Lee S., Irvine W.M., & Nyman L.-A., 2005, New Astronomy, 10, 425

Morris M., & Serabyn E., 1996, ARA&A, 34, 645

Novak G., 1999, in Falcke H. et al., eds, ASP Conf. Ser. Vol. 186, The Central Parsecs of the Galaxy. Astron. Soc. Pac., San Francisco, p. 488

Pak S., Jaffe D.T., & Keller L.D., 1996a, ApJ, 457, L43

Pak S., Jaffe D.T., & Keller L.D., 1996b, in Gredel R., ed., ASP Conf. Ser. Vol. 102, The Galactic Center. Astron. Soc. Pac., San Francisco, p. 28

Paumard T., Maillard J.-P., & Morris M., 2004, A&A, 426, 81

Pedlar A., Anantharamaiah K.R., Ekers R.D., Goss W.M., van Gorkom J.H., Schwarz U.J., & Zhao J.-H., 1989, ApJ, 342, 769

Piddington J.H., & Minnett H.C., 1951, Australian J. Sci. Res., 4, 459

Pierce-Price D., et al., 2000, ApJ, 545, L121

Reid M.J., 1993, ARA&A, 31, 345

Serabyn E., Lacy J.H., & Achtermann J.M., 1992, ApJ, 395, 166

Schödel R., Ott T., Genzel R., Eckart A., Mouawad N., & Alexander T., 2003, ApJ, 596, 1015

Wardle M., Yusef-Zadeh F., & Geballe T.R., 1999, in Falcke H. et al., eds, ASP Conf. Ser. Vol. 186, The Central Parsecs of the Galaxy. Astron. Soc. Pac., San Francisco, p. 432

Wright M.C.H.W., Coil A.L., McGary R.S., Ho P.T.P., & Harris A.I., 2001, ApJ, 551, 254

Yusef-Zadeh F., Melia F., & Wardle M., 2000, Science, 287, 85

Yusef-Zadeh F., & Morris M., 1987, ApJ, 320, 545

Yusef-Zadeh F., Morris M., & Chance D., 1984, Nature, 310, 557

Yusef-Zadeh F., Roberts D.A., Goss W.M., Frail D.A., & Green A.J., 1996, ApJ, 466, L25

Yusef-Zadeh F., Roberts D.A., Goss W.M., Frail D.A., & Green A.J., 1999a, ApJ, 512, 230

Yusef-Zadeh F., Stolovy S.R., Burton M., Wardle M., & Ashley M.C.B., 2001, ApJ, 560, 749

Yusef-Zadeh F., Stolovy S.R., Burton M., Wardle M., Melia F., Lazio T.J.W., Kassim N.E., & Roberts D.A., 1999b, in Falcke H. et al., eds, ASP Conf. Ser. Vol. 186, The Central Parsecs of the Galaxy. Astron. Soc. Pac., San Francisco, p. 197

Zylka R., Mezger P.G., & Wink J.E., 1990, A&A, 234, 133

Zylka R., Philipp S., Duschl W.J., Mezger P.G., Herbst T., & Tuffs R., 1998, in Sofue Y., ed., IAU Symp. No. 184, The Central Regions of the Galaxy and Galaxies, Kluwer, Dordrecht, p. 291

Chapter 2

Observations

2.1 Observing Strategy

We observe H_2 emission lines in the interaction regions between Sgr A East and the other members within the central 10 pc, the Galactic nucleus (including the CND) and the molecular clouds. H_2 emission is a good tracer and diagnostic for interactions between hot, powerful, sources and molecular clouds. Among many rotational-vibrational H_2 lines at various wavelengths, H_2 $1-0$ $S(1)$ line is the strongest and so most likely to be detected at high signal-to-noise (S/N) ratio. The wavelength of this line is 2.1218 μm (Cox 2000), which is in the regime of near-infrared (near-IR; 1–5 μm) and so suffers much less interstellar extinction compared to visual or ultraviolet (UV) lights even toward the Galactic center; $A_K \sim 2.5$ mag while $A_V \sim 30$ mag (Catchpole, Whitelock, & Glass 1990). It is also in the K-band window (2.0–2.4 μm) of the Earth's atmosphere and shorter than the wavelength domain ($\gtrsim 2.3$ μm) of thermal radiation from room temperature, making this line easy to be observed on the ground (McLean 1997).

We have some requirements on the observation as follows.

(i) High spatial resolution: considering the complicated morphology and the close proximity between the objects in the central 10 pc, an angular resolution of at least several arcsec ($1'' = 0.04$ pc at the distance to the Galactic center of 8.0 kpc; Reid 1993) is required to distinguish the structure.

(ii) Large field-of-view (FOV): we need to cover the whole interaction region on the surface of a molecular cloud to understand the geometry. Looking at the previous H_2 surveys for the CND (Gatley et al. 1986; Burton & Allen 1992; Yusef-Zadeh et al. 1999b, 2001; see Section 1.5), H_2 emission may be observed over a whole clump in a molecular cloud, in projection. Considering that the typical size of a clump is $30''$ or 1.2 pc in the NH_3 map of the central 10 pc (Figure 1.10), a FOV as large as several tens of arcsec is required.

(iii) High spectral resolution: in order to investigate the detailed kinematics in the interaction regions, we need to obtain the profiles of H_2 line. Considering that the widths of observed H_2 lines are generally less than $45\ \mathrm{km\ s^{-1}}$, which is the critical velocity of shock dissociation in a condition of typical molecular clouds (e.g. Smith, Brand, & Moorhouse 1991), a spectral resolution less than a few tens of $\mathrm{km\ s^{-1}}$ is required. This requirement is much higher than the spectral resolutions (75–130 $\mathrm{km\ s^{-1}}$) of the previous spectroscopic observations using Fabry-Perot etalons for investigating the kinematics of H_2 gas in the central 10 pc (Gatley et al. 1986; Yusef-Zadeh et al. 1999b, 2001; see Section 1.5).

(iv) Measuring line ratio: to determine the excitation mechanism of the H_2 molecules in the interaction regions, we need to measure the strength ratios between different rotational-vibrational H_2 lines. Since the ratio between the $1-0\ \mathrm{S}(1)$ and $2-1\ \mathrm{S}(1)$ transitions is most popularly used in the excitation studies, we also observe $\mathrm{H_2}\ 2-1\ \mathrm{S}(1)$ line at the regions where the brightest $\mathrm{H_2}\ 1-0\ \mathrm{S}(1)$ emission is detected considering that $2-1\ \mathrm{S}(1)$ line is fainter than $1-0\ \mathrm{S}(1)$ line generally by several factors.

(v) Effective continuum subtraction: since the Galactic center is very crowded, it is extremely difficult to obtain a line-emission image with continuum subtracted using narrow-band filters (e.g., see Figure 1.15) due to the seeing changes (Burton & Allen 1992). Thus we need a spectroscopic observation which can obtain line and continuum simultaneously.

(vi) Avoiding telluric OH lines: the wavelength range of 1–2.5 $\mu\mathrm{m}$ is crowded by a dense forest of telluric OH lines. These emission lines come from a thin layer of the atmosphere at an altitude of about 90 km and the strength of the emission can vary rapidly; by a factor of 2 or more in half an hour due (McLean 1997). There are also very strong OH lines near to the objective H_2 lines; stronger than by orders of magnitude and as close as a few hundred $\mathrm{km\ s^{-1}}$ apart. Hence we need a high spectral resolution to resolve and discard the telluric lines, less than $\sim 100\ \mathrm{km\ s^{-1}}$ taking into account the possibility of broad H_2 lines.

The high spectral resolution ($\Delta\lambda/\lambda \gtrsim 10000$) required above can be achieved by using a spectrometer adopting an echelle grating. Then we need the observing technique of scanning using a long slit as Burton & Allen (1992) did with a low dispersion spectrometer (see also Lee et al. 2005 for an example of the similar implementation of slit scanning, but for an external galaxy) to obtain a large FOV. In most cases, however, echelle spectrometers are used and optimized for observing point sources and have very small FOV. One of a few exceptions is the Cooled Grating Spectrometer 4 (CGS4) at the 3.8 m United Kingdom Infrared Telescope (UKIRT) on the summit of Mauna Kea in Hawaii; it has an observing mode equipped with $90''$-length slit and with a high dispersion ($\Delta\lambda/\lambda \simeq 37000$ or $\sim 8 \mathrm{~km~s^{-1}}$) echelle grating at the same time. This instrument should be appropriate for our purpose.

In $\mathrm{H_2}\ 1-0\ \mathrm{S}(1)$ line emission, we survey largely four different fields around Sgr A East where the interactions between this hot, expanding, cavity and the molecular clouds in the central 10 pc are expected (see Figure 2.1). In the north-eastern field (hereafter field NE), there are the $50 \mathrm{~km~s^{-1}}$ GMC and the northern ridge overlapping with the NE edge of Sgr A East. The eastern field (field E) includes the northern portion of the molecular ridge which looks likely to be in contact with the eastern edge of Sgr A East. The southern field (field S) extends along the southern streamer, northern half of which is overlapped with Sgr A East and the 1720 MHz OH maser (the shock indicator) is also detected in this field. Finally, the western field (field W) includes some portion of the north-western part of the CND and the northern part of the western streamer.

By scanning these fields with the long slit of the CGS4 equipped with an echelle grating, we can build three-dimensional (3-D) data cubes which contain the kinematic information in high resolution at each position in the interaction regions. In real observations, each field is divided into 2 or 4 scanning blocks and the observing time is allocated to each block as an observation unit. We also observe $\mathrm{H_2}\ 2-1\ \mathrm{S}(1)$ line at a position in field NE-1, where $1-0\ \mathrm{S}(1)$ emission is brightest, to measure the line ratio and investigate the excitation mechanism of H_2 molecules (see Figure 2.1 and Section 2.3 for more detailed descriptions).

2.2 Telescope and Instrument

2.2.1 United Kingdom Infrared Telescope

The 3.8 m United Kingdom Infrared Telescope (UKIRT) is the largest telescope in the world dedicated solely to observations at infrared wavelengths between $1\ \mu\mathrm{m}$ and $30\ \mu\mathrm{m}$. UKIRT is a classical Cassegrain telescope with a thin primary mirror utilizing an “English” yoke mounting (see Figure 2.2). After the Cassegrain hole, a flat tertiary mirror directs beam to one of four focal stations of instruments. For the specifications and performance of UKIRT,

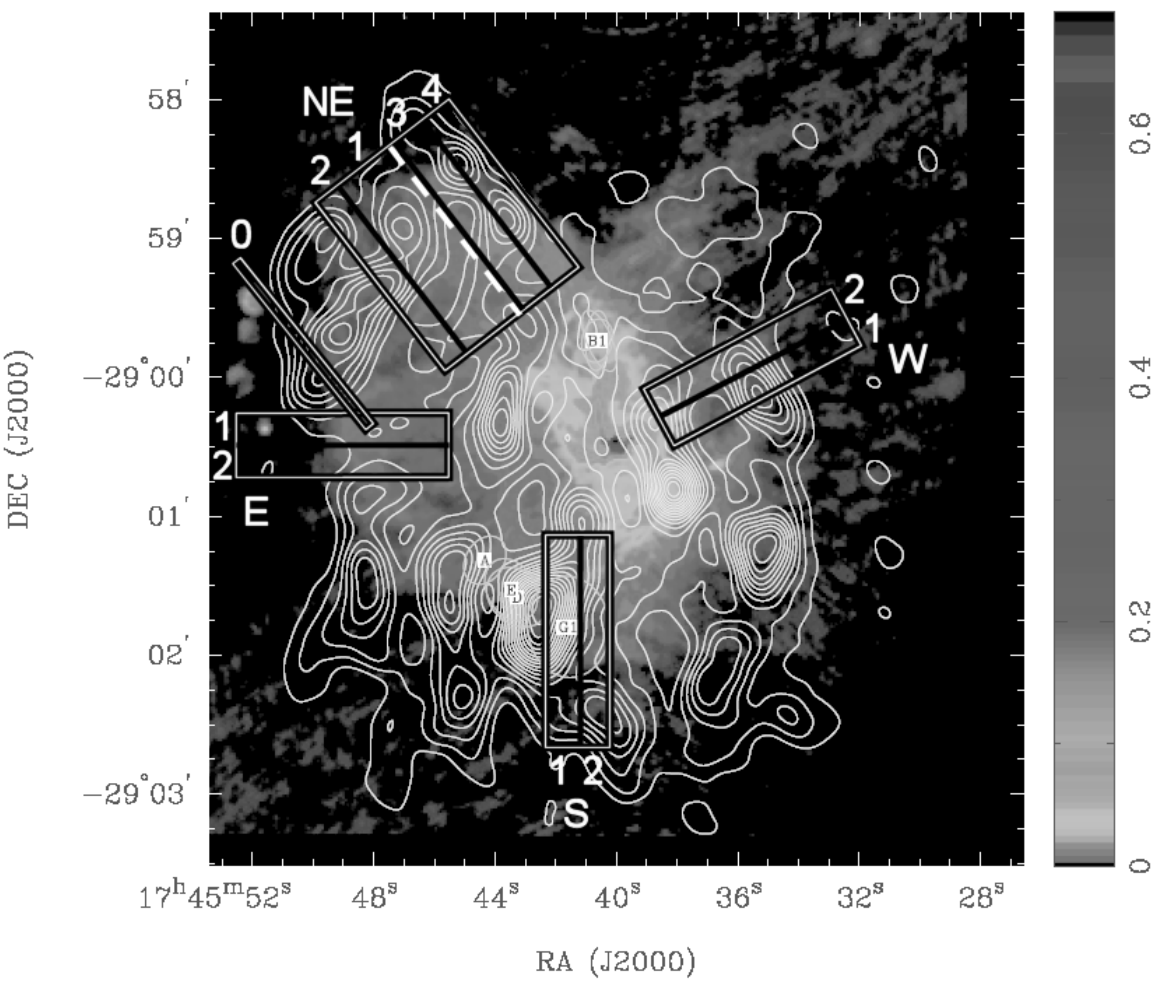

FIG. 2.1: Field positions of the H_2 observations. Four fields, which are observed in H_2 $1-0$ S(1) with the slit-scanning technique using the Cooled Grating Spectrometer 4 (CGS4) at the 3.8 m United Kingdom Infrared Telescope (UKIRT), are indicated by the labelled white boxes; the north-eastern (NE; composed of 24 parallel positions of the $90''$-length slit), eastern (E; 10 slit positions), southern (S; 10 slit positions), western (W; 10 slit positions) fields. Each field is divided by 2 or 4 scanning blocks (labelled by numbers) with black solid lines. The narrow box (labelled by '0') between field NE and field E is a supplementary field which is composed of only two slit positions and belongs to field E. The white dashed line in field NE-1 indicates the slit position where H_2 $2-1$ S(1) spectra are observed. The background image is a gray-scaled version of Figure 1.10.

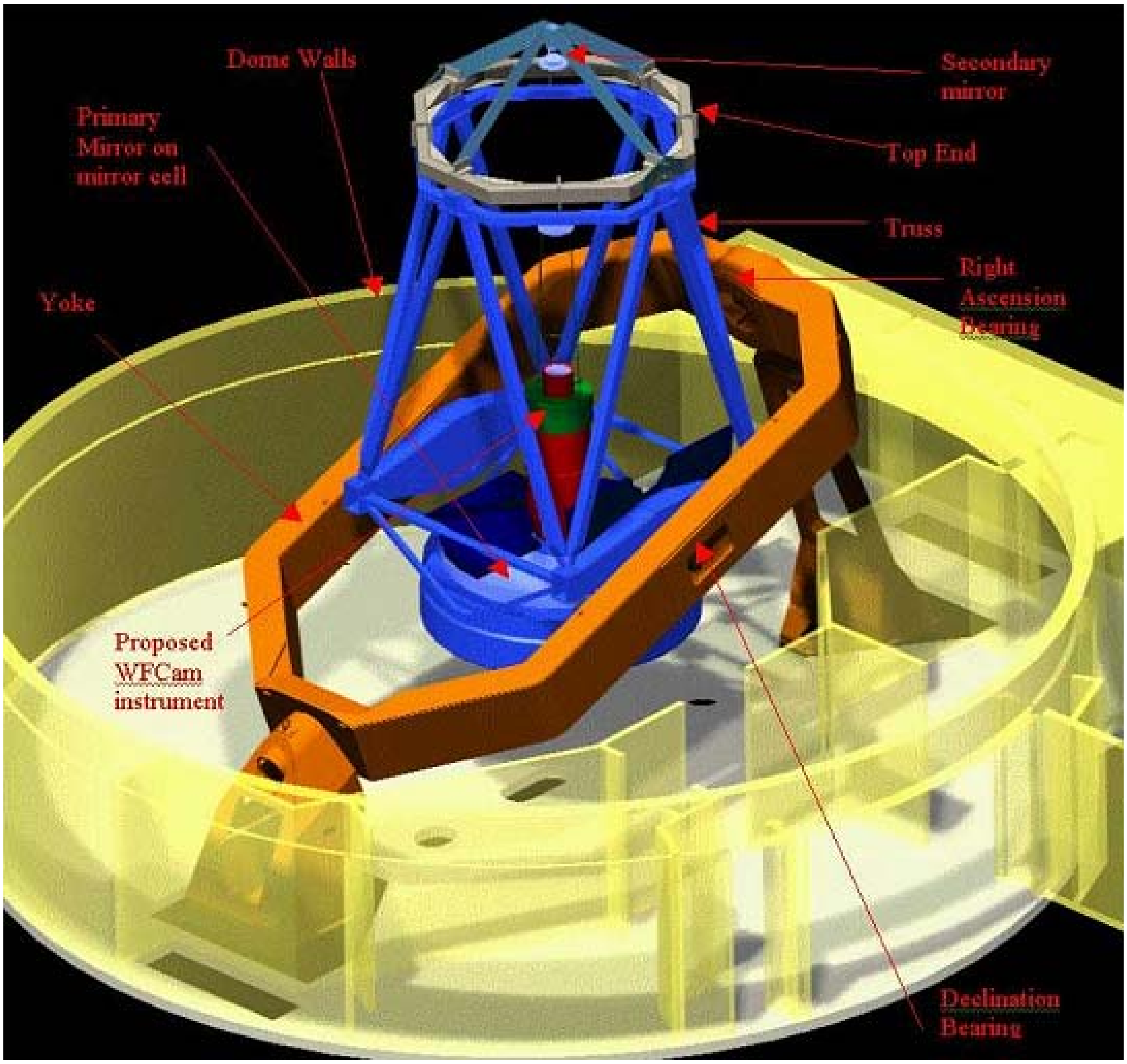

FIG. 2.2: Solid model image of UKIRT (from *http://www.jach.hawaii.edu/UKIRT*).

TABLE 2.1: Specifications and Performance of UKIRT

Longitude	$-155°28'23''.6 \pm 0''.2$
Latitude	$+19°49'32''.2 \pm 0''.2$
Altitude	4194 ± 6.0 m
Diameter of primary mirror	3802.5 ± 1.0 mm
Focal length of primary	9516 ± 10 mm
Diameter of secondary mirror	313.4 ± 0.1 mm
Radius of curvature of secondary	1725 ± 2 mm
Plate scale at Cassegrain focus	1.525 ± 0.001 arcsec mm^{-1}
Effective focal length	135256 ± 87 mm
Sky access	$+60°$ to $-40°$
All-sky absolute pointing	$\sim 1''.3$ (RMS errors)
K-band image quality (median FWHM)	$\sim 0''.433$ (on exposures $>$ tens of seconds)
Image stabilization	$< 0''.1$ (in winds < 45 mph)

From *http://www.jach.hawaii.edu/UKIRT*

refer to Table 2.1.

2.2.2 Cooled Grating Spectrometer 4

CGS4 is a 1–5 μm multi-purpose two-dimensional (2-D) grating spectrometer containing a 256×256 InSb array, installed in a cryostat which is cooled by liquid nitrogen and closed cycle coolers (Mountain et al. 1990; see Figure 2.3 for its optics layout). Four gratings are available, two of which are installed in the cryostat at any one time. They are a 40 line mm^{-1} (hereafter l/mm) grating which provides resolving powers ($R = \Delta\lambda/\lambda$) of 500–2200, a 75 l/mm grating, a 150 l/mm grating ($R \simeq 3000$–8500), and a 31 l/mm echelle ($R \simeq 37000$ or 8 km s^{-1}). The 75 l/mm grating is rarely used these days. These resolving powers are achieved with the 300 mm focal length camera optics and a one-pixel-wide slit, which provide a scale of 0.6 arcsec/pixel for the two moderate resolution gratings and roughly 0.41×0.90 arcsec/pixel for the echelle (0.41 arcsec/pixel in the direction of the dispersion). If a 150 mm focal length camera mirror is installed, the pixel scales and wavelength coverages

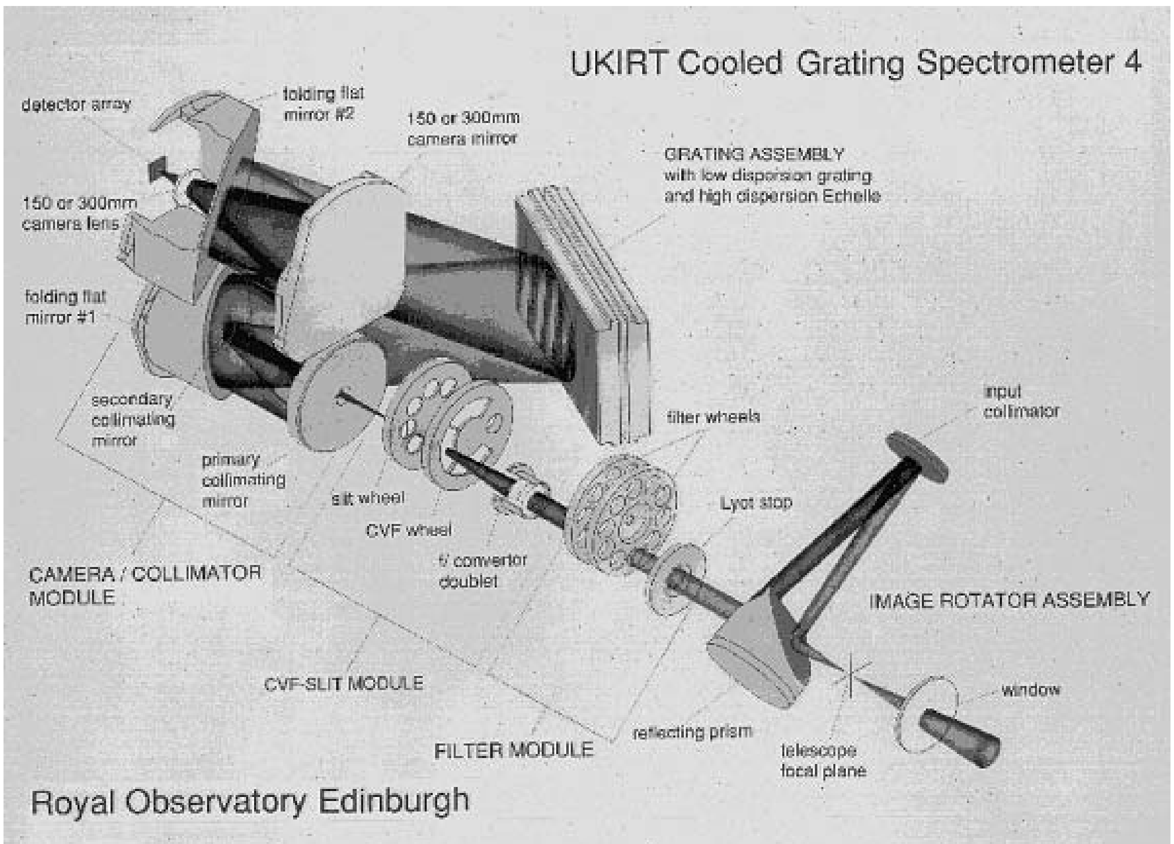

FIG. 2.3: Optics layout of CGS4 (from *http://www.jach.hawaii.edu/UKIRT*).

TABLE 2.2: Specifications and Performance of CGS4

Wavelength	1–5 μm			
Detector	256×256 InSb array			
Slit length	80–90 arcsec			
Slit width	1, 2, or 4 pixels			
Grating (line mm^{-1})	40	75[a]	150	31 (echelle)
Resolving power ($\Delta\lambda/\lambda$)[b]				
300 mm camera	500–2200	–	3000–8500	~ 37000
150 mm camera	300–2000	600–2000	2000–6000	~ 20000
Pixel scale (arcsec/pixel)				
300 mm camera	0.6	–	0.6	0.41×0.90[c]
150 mm camera	1.22	–	1.22	1.0×1.5[d]

From *http://www.jach.hawaii.edu/UKIRT*

[a] Rarely used these days.

[b] With a one-pixel-wide slit.

[c] 0.41 arcsec/pixel in the direction of the dispersion.

[d] 1.0 arcsec/pixel in the direction of the dispersion.

are doubled and resolving powers are halved (in principle).

CGS4 slit lengths are about 80–90 arcsec. It is possible to orient a slit at any angle on the sky. Slit widths of one pixel, two, and four pixels are available. The instrument has a calibration unit, containing a black-body source for flat-fielding and argon, krypton, and xenon arc lamps for wavelength calibration. Six broad band filters continuously cover the wavelength band 0.95–5.4 μm. Circular variable filters (CVFs) serve as order-blockers for the echelle. Spectro-polarimetry is available with CGS4 at all wavelengths but not with the echelle. Table 2.2 summarizes the specifications and performance of CGS4.

2.3 Observations at UKIRT

We observed the $\mathrm{H_2}$ 1–0 $\mathrm{S(1)}$ ($\lambda = 2.1218\mu\mathrm{m}$) and the $\mathrm{H_2}$ 2–1 $\mathrm{S(1)}$ ($\lambda = 2.2477\mu\mathrm{m}$) spectra at UKIRT in 2001 and 2003, using CGS4 with a 31 l/mm echelle grating, 300 mm focal length camera optics and a two-pixel-wide slit. The pixel scale along the slit was 0.90 arcsec for $\mathrm{H_2}\ 1-0\ \mathrm{S(1)}$ with the grating angle of $64.^{\circ}691$ and 0.84 arcsec for $\mathrm{H_2}\ 2-1\ \mathrm{S(1)}$ with $62.^{\circ}127$, respectively; the slit widths on the sky were 0.83 and 0.89 arcsec, respectively, for these two configurations. The slit length is $\sim$ 90 arcsec.

Seeing was less than 1 arcsec throughout the whole observations. The image quality is degraded, however, through the optical system of CGS4 and the final spatial resolution was about 2 arcsec (~ 0.1 pc at the distance to the Galactic center) according to the FWHM of the flux profile of the standard star along the slit. The instrumental resolutions, measured from Gaussian fits to telluric OH lines in our raw data, were $\sim 18\ \mathrm{km\ s^{-1}}$ for $\mathrm{H_2}\ 1-0\ \mathrm{S(1)}$ and $\sim 19\ \mathrm{km\ s^{-1}}$ for $\mathrm{H_2}\ 2-1\ \mathrm{S(1)}$, respectively.

In slit scanning, adjacent slit positions were separated by 3 arcsec perpendicular to the slit axis. Hereafter, we name each slit position "slit " + [scanning direction] + [separation from a "base position" in the scanning block it belongs to; in arcsec]. For example, in field NE-1, the slit position separated from the base position (called "slit 00") by 12 arcsec toward north-west is called "slit NW12".

The telescope was nodded between object and blank sky positions every 1200 seconds (one cycle for observing a single slit position; 1 sky exposure + 5 object exposures), to subtract the background and telluric OH line emission. The sky positions were offset by about $2.^{\circ}5$ ($\Delta\alpha = -2.^{\circ}03,\ \Delta\delta = 0.^{\circ}85$) from the on-source positions.

2.3.1 Observing Runs in 2001

On 2001 August 3 (UT), $\mathrm{H_2}$ $1-0$ $\mathrm{S(1)}$ spectra from 10 parallel slit positions (slits SE12–00–NW15) were observed in field NE-1. The coordinates of the base position (slit 00) in field NE-1 are $\alpha = 17^{\mathrm{h}}45^{\mathrm{m}}45.^{\mathrm{s}}95,\ \delta = -28^{\circ}59'5.''16$ (J2000). The slit was oriented 40° east of north for each measurement. For a standard star, we observed HR 6496 ($\mathrm{m_K} = 5.13$ mag, type F7V, $\alpha = 17^{\mathrm{h}}27^{\mathrm{m}}2.^{\mathrm{s}}1,\ \delta = -12^{\circ}30'45''$; J2000) before and after the slit scanning.

On August 4, the $\mathrm{H_2}\ 1-0\ \mathrm{S(1)}$ observation for one slit position, SE15, was added to field NE-1. Field NE-2, which is composed of three slit positions (SE18, SE21, and SE24), was observed in $\mathrm{H_2}\ 1-0\ \mathrm{S(1)}$ with a base position of $\alpha = 17^{\mathrm{h}}45^{\mathrm{m}}45.^{\mathrm{s}}86,\ \delta = -28^{\circ}59'6.''54$

(J2000). The supplementary observation of field E-0 was also made that night with a base position of $\alpha = 17^{\mathrm{h}}45^{\mathrm{m}}50\overset{\mathrm{s}}{.}60,\ \delta = -28°59'44''.30$ (J2000) and with the same position angle of slit ($40°$ east of north) as field NE-1 and NE-2.

The $\mathrm{H_2}\ 1{-}0\ \mathrm{S}(1)$ slit scanning on August 4 are different from those at other nights in the manner of observation. In order to get rid of bad pixels efficiently, we jittered the observing positions along the slit axis during the 5 exposures for object (Δp = 0, +1, +2, -1, and -2 pixel in sequence). Because of this difference, the reduction process of the $\mathrm{H_2}\ 1{-}0\ \mathrm{S}(1)$ data obtained on August 4 is also different from others as we will see in Chapter 3.

$\mathrm{H_2}$ 2–1 $\mathrm{S}(1)$ spectra was observed on August 4 only at the position slit NW12 in field NE-1, where the observed $\mathrm{H_2}\ 1{-}0\ \mathrm{S}(1)$ line emission is brightest and therefore the possibility of $\mathrm{H_2}\ 2{-}1\ \mathrm{S}(1)$ detection is highest. The total integration time for the $\mathrm{H_2}\ 2{-}1\ \mathrm{S}(1)$ observation was 2880 seconds (or 48 minutes) including the sky exposures.

2.3.2 Observing Runs in 2003

On 2003 May 23, $\mathrm{H_2}\ 1-0\ \mathrm{S}(1)$ spectra from 5 parallel slit positions (slits NW15–NW27) were observed in field NE-3. The coordinates of the base position in field NE-3 are $\alpha = 17^{\mathrm{h}}45^{\mathrm{m}}45\overset{\mathrm{s}}{.}87,\ \delta = -28°59'4''.16$ (J2000). The slit was oriented $40°$ east of north like the other observations in field NE.

On May 28, field NE-4 (slits NW30–NW42) was observed with a base position of $\alpha = 17^{\mathrm{h}}45^{\mathrm{m}}45\overset{\mathrm{s}}{.}95,\ \delta = -28°59'5''.16$ (J2000). From this night, we changed the standard star from HR 6496 to BS 6310 ($\mathrm{m_K} = 4.79$ mag, type F4V, $\alpha = 17^{\mathrm{h}}00^{\mathrm{m}}09\overset{\mathrm{s}}{.}5,\ \delta = -24°59'21''$; J2000) which is brighter and closer to the object fields than the previous one.

On May 29–31 and June 1, we observed fields E, W, and S. For the positions and detailed information, see Figure 2.1 and Table 2.3 which summarizes the observations.

TABLE 2.3: H_2 Observations with Echelle Grating CGS4 at UKIRT

Field[a]	Date (UT) (yyyy/mm/dd)	Base Position[b] (J2000) R.A.	Dec	Slit names[c] (number of slits)	P.A.[d]	Seeing[e] (FWHM)
			H_2 1−0 S(1) ($\lambda = 2.1218\mu$m)			
NE-1	2001/08/3–4[f]	$17^h45^m45\overset{s}{.}95$	$-28°59'05\overset{''}{.}16$	NW15, NW12...SE12, SE15 (11)	40°	2.0″
NE-2	2001/08/04[f]	$17^h45^m45\overset{s}{.}86$	$-28°59'06\overset{''}{.}54$	SE18, SE21, SE24 (3)	40°	2.1″
NE-3	2003/05/23	$17^h45^m45\overset{s}{.}87$	$-28°59'04\overset{''}{.}16$	NW15, NW18...NW24, NW27 (5)	40°	2.4″
NE-4	2003/05/28	$17^h45^m45\overset{s}{.}95$	$-28°59'05\overset{''}{.}16$	NW30, NW33...NW39, NW42 (5)	40°	1.8″
E-0	2001/08/04[f]	$17^h45^m50\overset{s}{.}60$	$-28°59'44\overset{''}{.}30$	00, SE03 (2)	40°	2.0″
E-1	2003/05/29	$17^h45^m48\overset{s}{.}30$	$-29°00'15\overset{''}{.}00$	00, S03...S09, S12 (5)	−90°	2.1″
E-2	2003/06/01	$17^h45^m48\overset{s}{.}60$	$-29°00'13\overset{''}{.}80$	S15, S18...S24, S27 (5)	−90°	1.7″
S-1	2003/05/30	$17^h45^m42\overset{s}{.}30$	$-29°01'53\overset{''}{.}00$	00, W03...W12, W15 (6)	0°	2.0″
S-2	2003/06/01	$17^h45^m42\overset{s}{.}27$	$-29°01'50\overset{''}{.}60$	W18, W21, W24, W27 (4)	0°	1.7″
W-1	2003/05/31	$17^h45^m34\overset{s}{.}69$	$-29°00'06\overset{''}{.}40$	00, NE03...NE09, NE12 (5)	−60°	2.2″
W-2	2003/05/31	$17^h45^m34\overset{s}{.}80$	$-29°00'05\overset{''}{.}00$	NE15, NE18...NE24, NE27 (5)	−60°	2.2″
			H_2 2−1 S(1) ($\lambda = 2.2477\mu$m)			
NE-1	2001/08/04	$17^h45^m45\overset{s}{.}95$	$-28°59'05\overset{''}{.}16$	NW12 (1)	40°	2.0″

[a] See Figure 2.1 for an outline.

[b] Base position for a slit-scanning block.

[c] Defined by [scanning direction] + [separation from the base position in arcsec].

[d] Position angle of slit (east of north).

[e] Final seeing on the detector which is degraded through the optical system of CGS4.

[f] H_2 1−0 S(1) observations on 2001 August 4 (slit SE15 in field NE-1, field NE-2, and field E-0) used the slit-jittering method (see text).

REFERENCES

Burton M., & Allen D., 1992, Proc. Ast. Soc. Australia, 10, 55

Catchpole R.M., Whitelock P.A., & Glass I.S., 1990, MNRAS, 247, 479

Cox A.N., 2000, Allen's astrophysical quantities (4th ed.). AIP press, New York

Gatley I., Jones T.J., Hyland A.R., Wade R., Geballe T.R., & Krisciunas K., 1986, MNRAS, 222, 299

Lee S., Pak S., Lee S.-G., Davis C.J., Kaufman M.J., Mochizuki K., & Jaffe D.T., 2005, MNRAS, in press (astro-ph/0410572)

McLean I., 1997, Electronic Imaging in Astronomy: Detectors and Instrumentation. Praxis publishing Ltd., Chichester

Mountain C.M., Robertson D.J., Lee T.J., & Wade R., 1990, in Crawford D.L., ed., Proc. SPIE Vol. 1235, Instrumentation in Astronomy VII. SPIE, Bellingham, p. 25

Reid M.J., 1993, ARA&A, 31, 345

Smith M.D., Brand P.W.J.L., & Moorhouse A., 1991, MNRAS, 248, 730

Yusef-Zadeh F., Stolovy S.R., Burton M., Wardle M., & Ashley M.C.B., 2001, ApJ, 560, 749

Yusef-Zadeh F., Stolovy S.R., Burton M., Wardle M., Melia F., Lazio T.J.W., Kassim N.E., & Roberts D.A., 1999b, in Falcke H. et al., eds, ASP Conf. Ser. Vol. 186, The Central Parsecs of the Galaxy. Astron. Soc. Pac., San Francisco, p. 197

Chapter 3

Data Reduction†

3.1 Reduction of Spectral Image Data Using IRAF

Initial data reduction steps, involving bias-subtraction and flat-fielding (using an internal blackbody lamp), were accomplished by the automated Observatory Reduction and Acquisition Control (ORAC) pipeline at the United Kingdom Infrared Telescope (UKIRT).

IRAF [1] was used for the remainder of the reduction of the two-dimensional (2-D; wavelength and position) spectral image obtained from each slit position. Unification of these 2-D spectral images into a three-dimensional (3-D) data cube and the reduction procedures after that are implemented using MIRIAD (Multichannel Image Reconstruction, Image Analysis and Display) as we will see in the next section. Note that the $\mathrm{H_2}\ 2-1\ \mathrm{S(1)}$ data is not included in the 3-D data reduction since $\mathrm{H_2}\ 2-1\ \mathrm{S(1)}$ is observed at only one slit position; we just extracted some spectra from the reduced spectral image.

Sequence of data reduction of 2-D spectral images using IRAF is shown in Figure 3.1. Some steps in the sequence will be described in more detail in the following subsections. As seen in Section 2.3, $\mathrm{H_2}\ 1-0\ \mathrm{S(1)}$ data obtained on 2001 August 4 (slit SE15 in field

†Part of this chapter are in publication; Lee S., Pak S., Lee S.-G., Davis C.J., Kaufman M.J., Mochizuki K., & Jaffe D.T., 2005, MNRAS, in press (astro-ph/0410572)

[1]IRAF is distributed by the National Optical Astronomy Observatories, which are operated by the Association of Universities for Research in Astronomy, Inc., under cooperative agreement with the National Science Foundation.

NE-1, field NE-2, and field E-0) were observed using the slit-jittering method while other data were not jittered. As a result, the reduction sequence for "2001/08/04 $1-0\ \mathrm{S}(1)$ data" is different from that for others (see Figure 3.1). For example, we must do the distortion correction before un-jittering (i.e. shifting) the images to combine, otherwise the distortions will spread out and become impossible to be corrected.

3.1.1 Multiple Extensions FITS Format

As a result of the initial data reduction, the ORAC pipeline at UKIRT makes WCE (Wavelength Calibrated by Estimation) files in the format of NDF for the STARLINK reduction system. We can convert the format of a WCE file into FITS for IRAF.

In the case of the 2001 data, every single WCE file is converted into a single FITS file so we can use it in IRAF directly. Since 2003, however, a WCE file is converted into a FITS file with Multiple Extensions (so called a MEF file; refer to 'IRAF FITS Kernel User's Guide' from *http://iraf.noao.edu/iraf/web/docs/fitsuserguide.html*). Each extension in a MEF file can be visualized as a single FITS file containing only a single kind of information. For example, the MEF files converted from the 2003 WCE files have two different FITS extensions; one for image data and the other for variance data.

MEF files can be processed by any IRAF tasks but with one extension at a time. However, since this may make things more complicated and we need only one extension for image data, we extracted only the image extension from a MEF file into a single FITS file using the IRAF task PROTO.IMEXTENSIONS. The resulting FITS files of the 2003 data are just like the 2001 data so can be processed by the same methods.

3.1.2 Cleaning Contaminations

By subtracting a blank sky image from an object image, not only the background level but also bad pixels and sky OH lines are diminished by a huge amount (see Figure 3.2 for example). However, a number of bad pixels still remain after the sky subtraction and some pixels are over subtracted. They are typically stronger than diffuse H_2 emission and should be serious sources of noise. Sky OH lines are not subtracted perfectly because of their nature of rapidly changing with time (McLean 1997). Owing to the high spectral resolving power ($\Delta\lambda/\lambda \simeq 18000$ or $\sim 16\ \mathrm{km\ s^{-1}}$ with the 300 mm focal length camera and two-pixel-wide slit) of the echelle grating of the Cooled Grating Spectrometer 4 (CGS4), the target

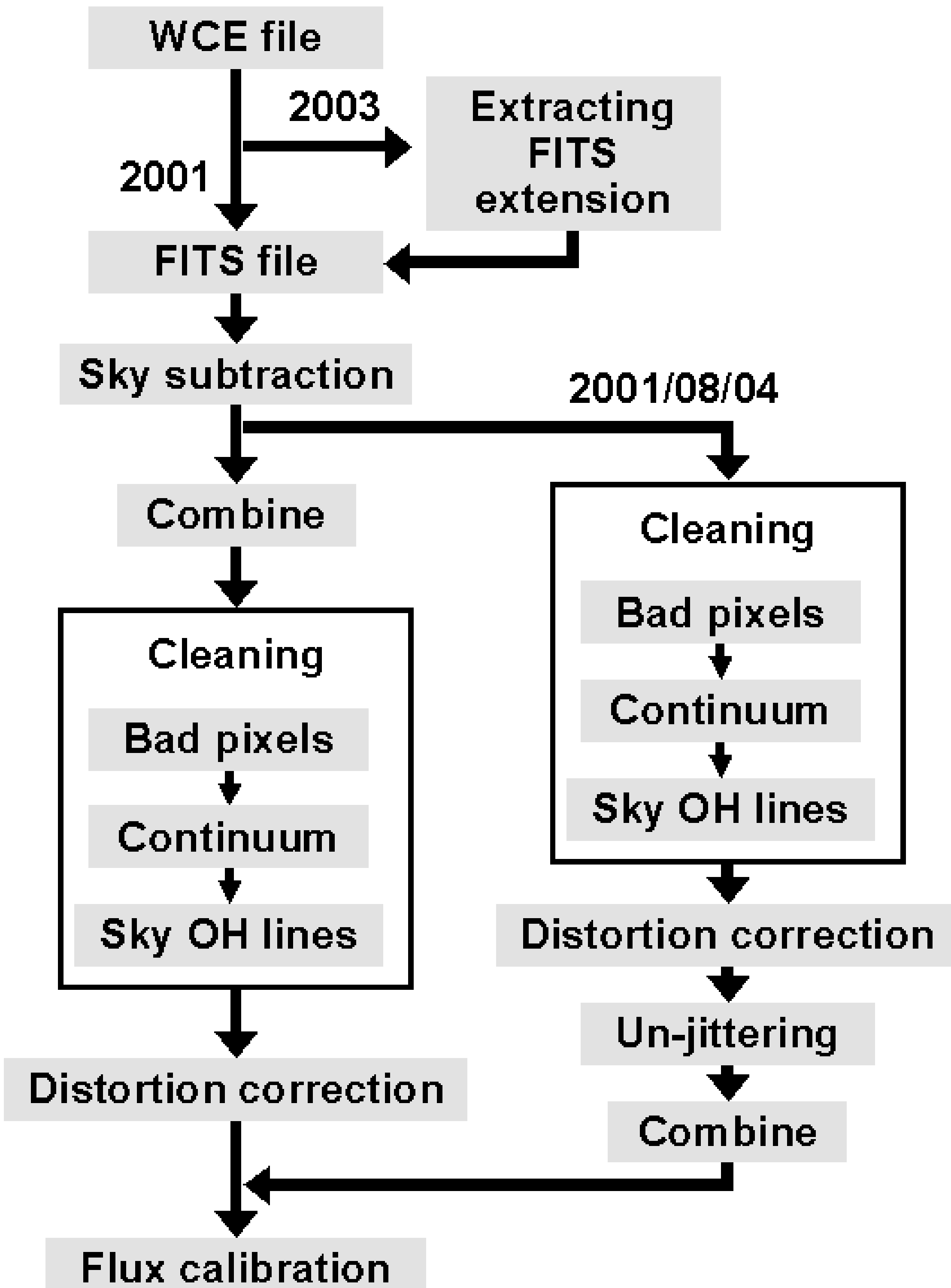

FIG. 3.1: Reduction sequence of the 2-D spectral image data using IRAF.

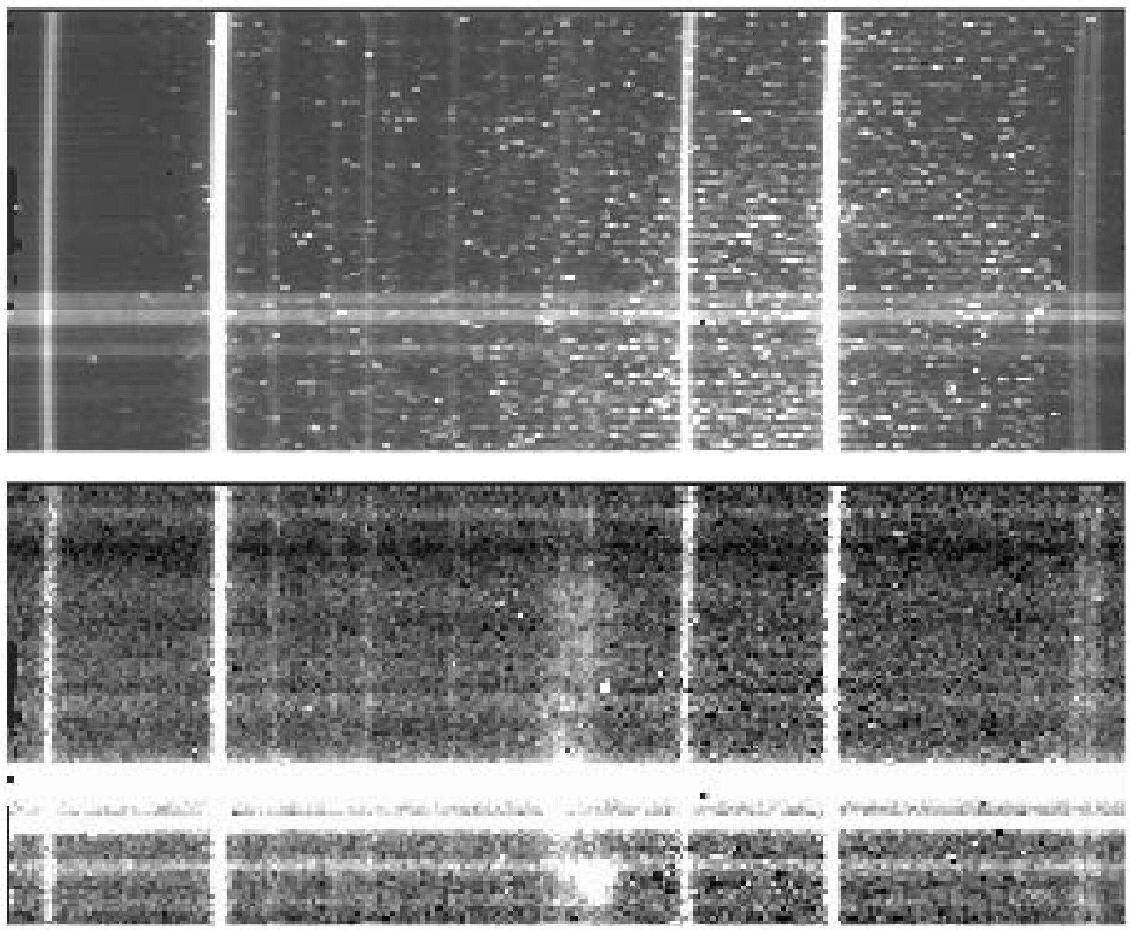

FIG. 3.2: Example of sky subtraction. (top) Raw spectral image of slit NW15 in field NE-3. The horizontal axis is along spectral dispersion and the vertical axis is along spatial position on the slit. Strong and weak vertical lines are telluric OH lines and horizontal lines are stellar continua. There are a huge number of bad pixels particularly in the right half of the image. (bottom) After subtracting blank sky image, diffuse H_2 emission becomes visible in the central part of the image. Since the background and strong OH lines are diminished, stellar continua look more prominent. Dark horizontal lines in upper part of the image are the scars due to the stellar continua in the sky image. The number of serious bad pixels are obviously decreased but many of them still remain and a lot of over-subtracted pixels newly appear as black points.

H_2 emission is probably well separated from the brightest residual OH lines. However, we found that the velocity dispersions of the H_2 lines observed from the Galactic center are so high that, in a few spectral images, the wings of $\mathrm{H_2}\ 1\text{–}0\,\mathrm{S}(1)$ lines are nearly overlapped with the nearest OH line which is separated by $\sim 200\ \mathrm{km\ s^{-1}}$ (at $\lambda = 2.1232424\ \mu\mathrm{m}$; Rousselot et al. 2000). On the other hand, since the Galactic center is an extremely crowded region, not surprisingly several number of stellar continua are included in a spectral image and typically a few of them are much brighter than the H_2 emission (see Figure 3.2). Therefore we should clean up these contaminations to obtain pure H_2 spectra with high signal-to-noise (S/N) ratios.

We clean up the residual bad pixels using NOAO.IMRED.CCDRED.COSMICRAYS, which detects cosmic rays or bad pixels and replaces them with the average of the four neighbor pixels. We implement this task two times for one image. First, we correct the bad pixels with positive values. Then to eliminate the bad pixels with negative values, which are by-products of the sky subtraction, we invert (i.e. multiply by -1) the once-corrected image and implement COSMICRAYS again. Inverting the resulting image again to its original state, we complete the cleaning process of bad pixels (see Figure 3.3 for example).

For removing stellar continua, we use NOAO.IMRED.GENERIC.BACKGROUND. For each line or column in an input image, this task fit a function to the background and subtracted it. We assume linear functions for the observed stellar continua and continuum levels are fitted on either side (short-ward and long-ward in wavelength) of H_2 emission for each row in images. As a result, stellar continua are subtracted successfully in most images (see Figure 3.4 for example).

In order to clean up the residual telluric OH lines, we need a template image of OH lines which will be scaled to have identical intensity levels with the residual OH lines and then subtracted from the object image. A blank sky image can be used as a template. However, it includes the dark and sky background which was already subtracted from the object image by the process of sky subtraction above. Thus, we make a template image of pure OH lines by subtracting a mode value of the background from the blank sky image (e.g., the upper image in Figure 3.5). This template image, however, still contains contaminations (bad pixels and stellar continua; even a blank sky image is difficult to be perfectly 'blank' near the Galactic center) like the raw image of object. Therefore we clean up the template image (see Figure 3.5) before we use it for removing the residual OH lines in the object image (see Figure 3.6 for example).

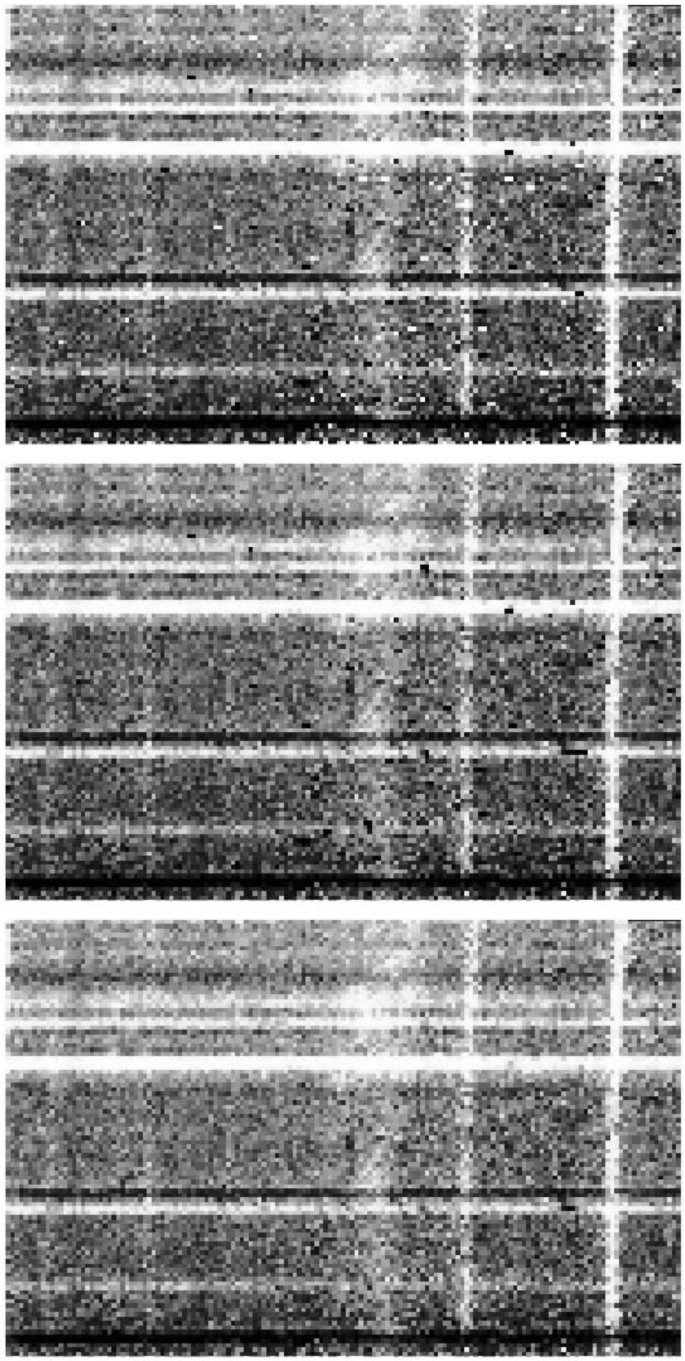

FIG. 3.3: Example of cleaning bad pixels. (top) Raw spectral image of slit SE09 in field NE-1. (middle) After the first correction for the bad pixels with positive values. (bottom) After the second correction for the negative bad pixels which were over-subtracted in the sky subtraction.

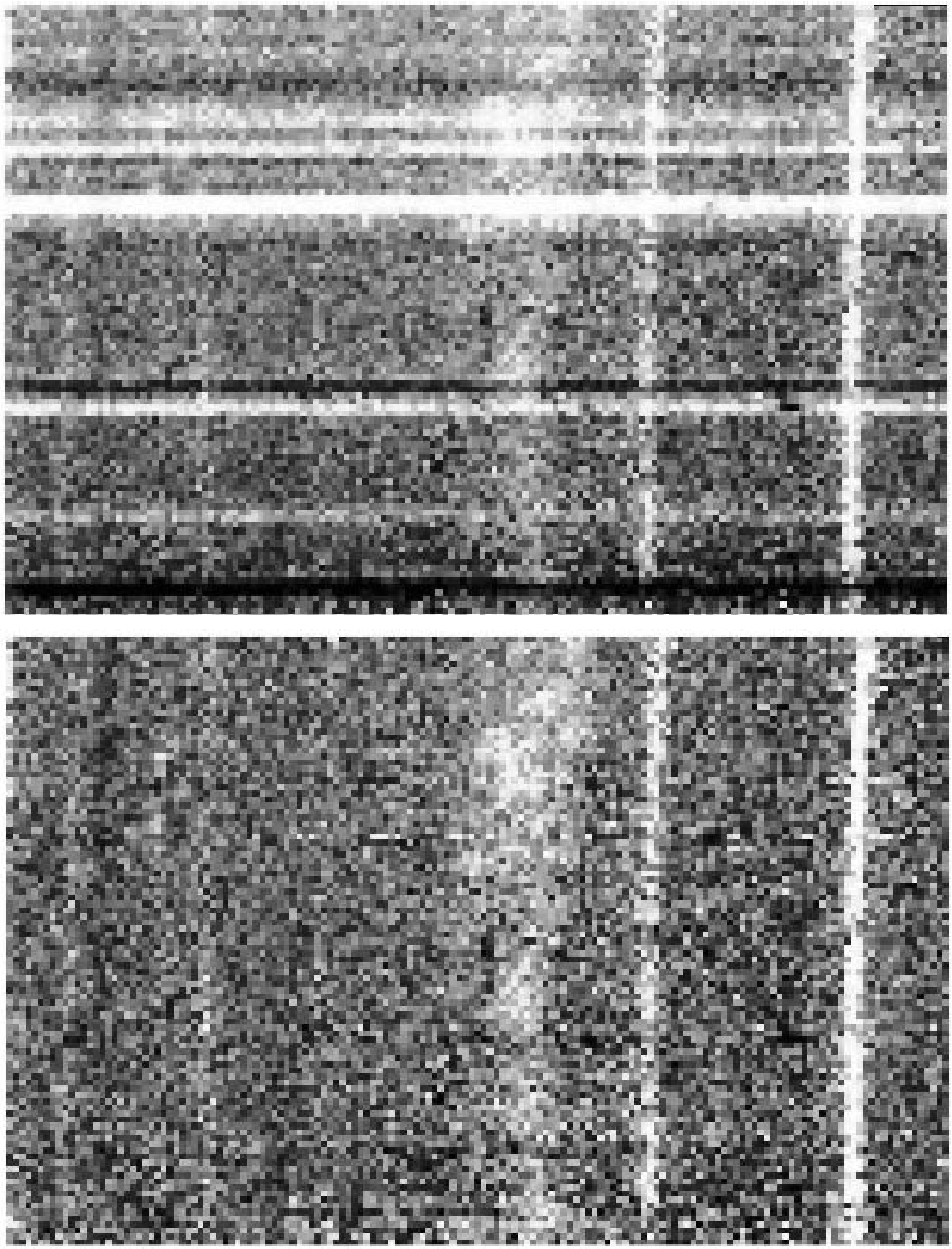

FIG. 3.4: Example of cleaning stellar continua. (top) The spectral image of slit SE09 in field NE-1 after the correction for bad pixels; the same image as Figure 3.3 (bottom). (bottom) After the correction for stellar continua.

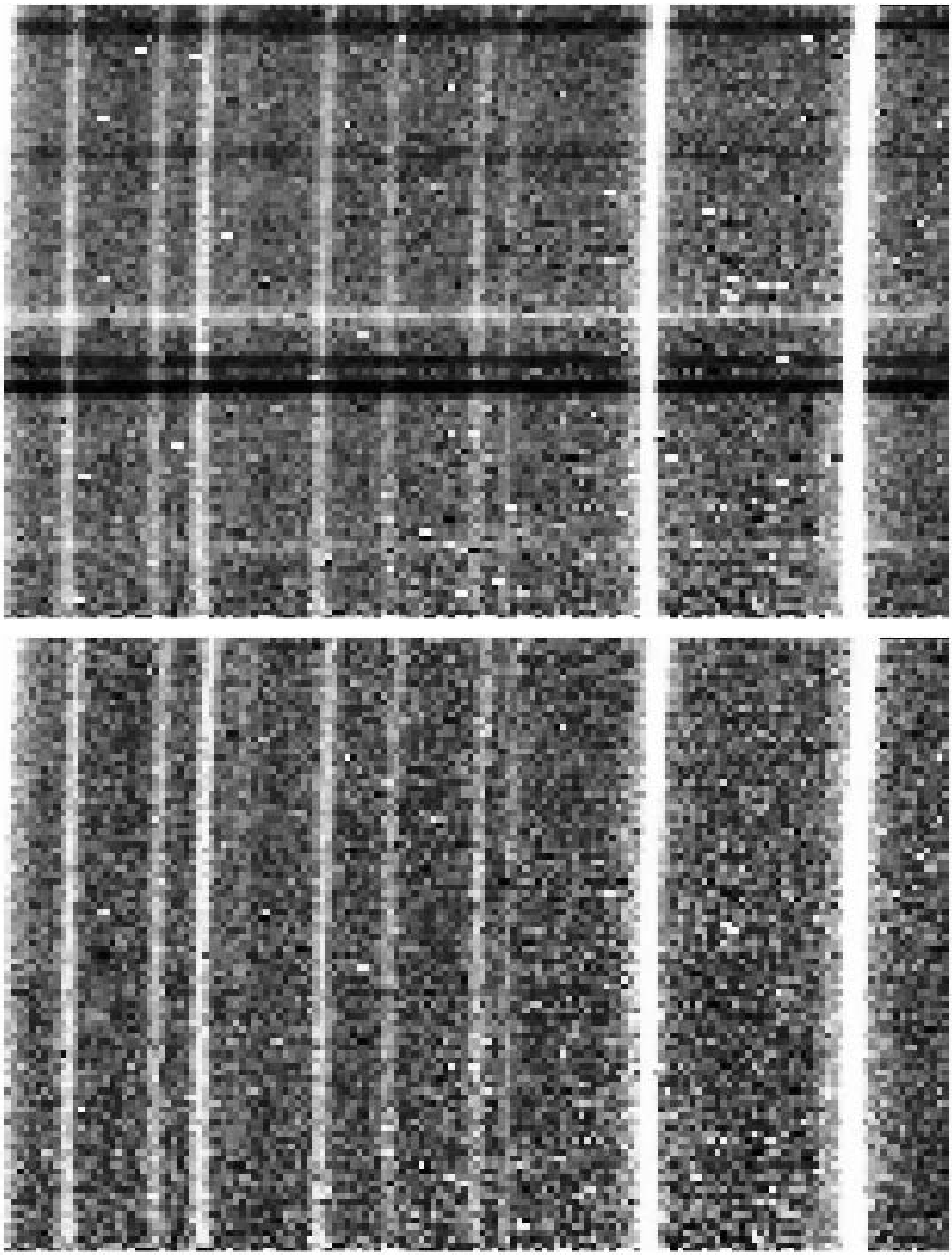

FIG. 3.5: Example of sky template for cleaning telluric OH lines. (top) The raw image of sky template. (bottom) After the correction for bad pixels and stellar continua.

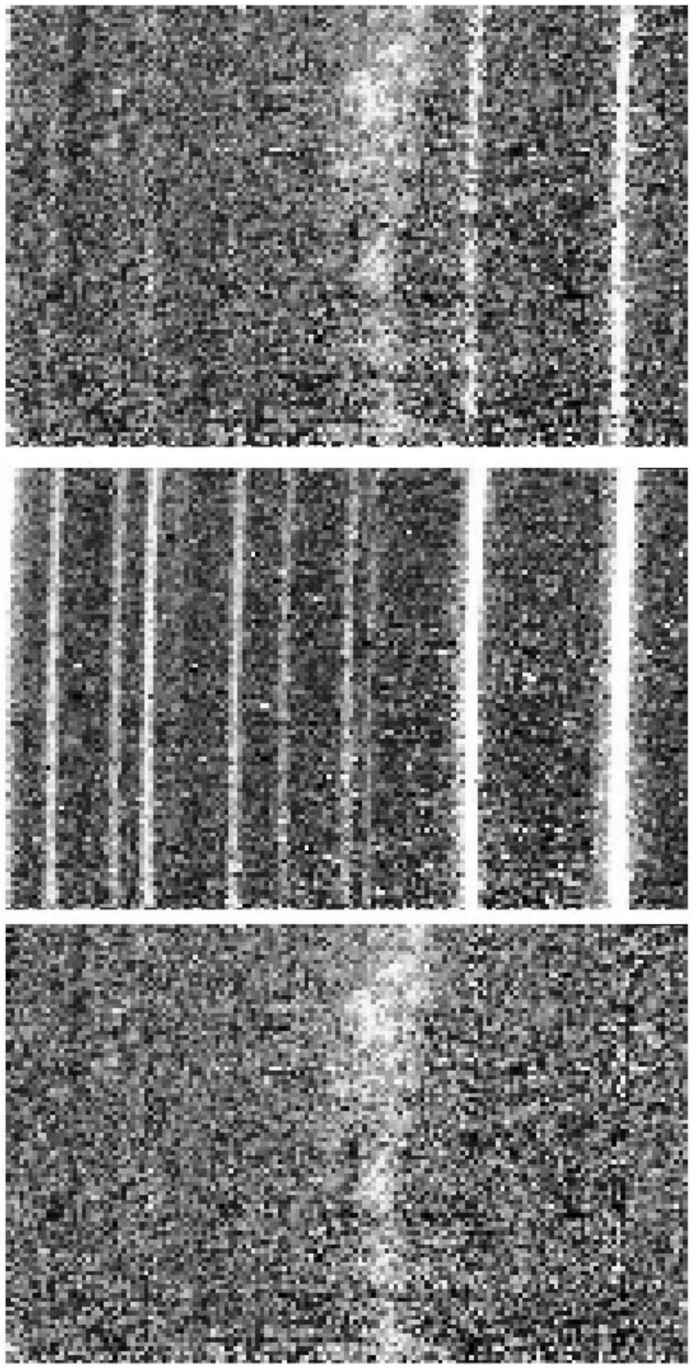

FIG. 3.6: Example of cleaning telluric OH lines. (top) The spectral image of slit SE09 in field NE-1 after the correction for bad pixels and stellar continua; the same image as Figure 3.4 (bottom). (middle) The sky template of telluric OH lines after the correction for bad pixels and stellar continua; the same image as Figure 3.5 (bottom). (bottom) After all the process of cleaning contaminations including the telluric OH lines.

The order in the cleaning process (bad pixel – stellar continuum – telluric OH lines) is determined exclusively. The correction for bad pixels should be done before removing OH lines, otherwise the bad pixels in the OH template will be added to the object image and we will lose or spoil more signals. Also the stellar continuum subtraction should be done before OH correction to scale the template accurately to the object image. We found that it is better to correct bad pixels before subtracting continuum. It probably makes the continuum fit better. The cleaning process should be done before correcting spatial and spectral distortions, which will be described in the next section, since the distortion correction 'distort' original features in images. Particularly it makes bad pixels larger and much more difficult to be identified and removed using COSMICRAYS.

3.1.3 Correction for Spatial & Spectral Distortions and Wavelength Calibration

We corrected the spectral distortion along the dispersion axis (i.e. curved stellar continuum) and the spatial distortion along the slit (i.e. tilted or curved arc or telluric OH lines) following the reduction guide 'Post-Reduction of CGS4 data with IRAF' by Dr. Chris J. Davis at UKIRT (*http://www.jach.hawaii.edu/~cdavis/cgs4_iraf.html*). In this works of correcting for geometrical distortions, the IRAF tasks, IDENTIFY, REIDENTIFY, FITCOORDS, and TRANSFORM in the NOAO.TWODSPEC.LONGSLIT package are used. Notably, in correcting for distortions in the spectral direction, we also carry out wavelength calibration.

For the correction of spectral distortion, we use the spectrum of the standard star (HR 6496 or BS 6310) as a template. To rectify for distortions in the spectral direction, you should ideally observe the standard star at different positions along the slit. Since we found that the spectral distortion of CGS4 with echelle grating is not serious (nearly negligible particularly around the wavelengths of the targeted H_2 lines), however, stellar spectra at two or three different positions are enough for making a template. Typically, stars are jittered along the slit in long-slit observations to directly subtract the sky background (e.g. by subtracting the jittered image from the original one). Thus we can make two templates (we call them template 1 and template 2) each of which contains one stellar spectrum at two different positions, respectively, from a normal observation for standard star.

The process of correcting for spectral distortion is as follows. First, we use IDENTIFY to mark the position of the standard spectrum along the central column in template 1. Second, we measure the position of the same standard spectrum along different columns in template 1 using REIDENTIFY. Then we repeat IDENTIFY and REIDENTIFY on template 2. We must next find the transformation parameters that will correct for the distortion in the dispersion direction evident in these standard spectra, using the task FITCOORDS. Finally, we transform first the standard star spectral images, and then the object images themselves using TRANSFORM.

In a very similar way we correct for distortions in the spatial direction. First, we run IDENTIFY on the sky OH spectra, though this time along the central line, and input the wavelength of each line. We use four OH lines (at $2.1156116\ \mu\mathrm{m}$, $2.1176557\ \mu\mathrm{m}$, $2.1232424\ \mu\mathrm{m}$, and $2.1249592\ \mu\mathrm{m}$) for the $\mathrm{H_2}\ 1-0\ \mathrm{S(1)}$ spectral images and three lines ($2.2460264\ \mu\mathrm{m}$, $2.2516727\ \mu\mathrm{m}$, and $2.2519211\ \mu\mathrm{m}$) for $\mathrm{H_2}\ 2-1\ \mathrm{S(1)}$. These telluric OH lines are strong enough for their positions along the dispersion axis to be measured with high accuracy and have known wavelengths in the literature (Rousselot et al. 2000). Next, we run REIDENTIFY, FITCOORDS, and TRANSFORM just like in the correction for spectral distortions. In Figure 3.7, we show an example for the effects of the distortion correction.

We also calibrate simultaneously wavelength of our data in the correction of spatial distortions, using the wavelength-known OH lines as standards. The information of calibrated wavelength is written in FITS headers as coordinate information along the axis of spectral dispersion. Then we converted wavelength into velocity relative to the rest wavelength of $\mathrm{H_2}$ line using NOAO.ONEDSPEC.DISPTRANS. We also corrected for the motions of the Earth and Sun using ASTUTIL.RVCORRECT in order to determine local standard of rest (LSR) velocities.

The reliability of the wavelength calibration was inferred by estimating its uncertainty and accuracy. For uncertainty, we measured the wavelengths of OH line in the calibrated sky images and compare them with the known values (Rousselot et al. 2000). Then the differences are about $\pm 0.5\ \mathrm{km\ s^{-1}}$. For accuracy, we measured the dispersion of measured wavelengths of the OH line at $2.1232424\ \mu\mathrm{m}$, which is nearest to the $\mathrm{H_2}\ 1-0\ \mathrm{S(1)}$ line at $2.1218\ \mu\mathrm{m}$, in the calibrated sky images. Then the estimated accuracy is about $\pm 1\ \mathrm{km\ s^{-1}}$.

3.1.4 Flux Calibration

Flux calibration for extended sources like diffuse $\mathrm{H_2}$ emission is converting instrumental pixel values in the unit of ADU into specific intensities (I_λ or I_V) in physical units

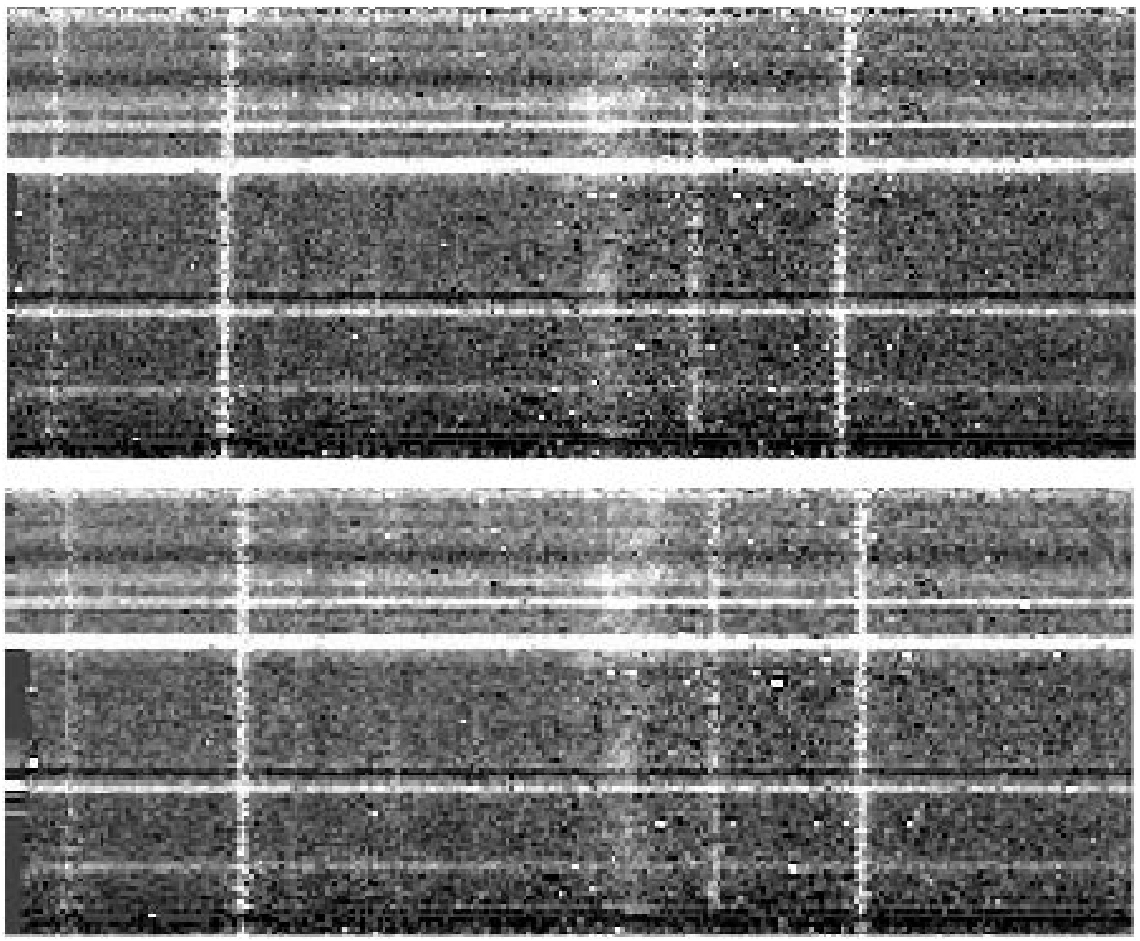

FIG. 3.7: Example of correction for spatial and spectral distortions. (top) The spectral image of slit SE09 in field NE-1 before the correction for distortions. (bottom) After correcting for both spatial and spectral distortions. Note that we present an example before cleaning the contaminations which are discussed in Section 3.1.2, since the stellar continua and the telluric OH lines in the image show the effects of distortions best.

(W m^{-2} arcsec^{-2} $\mu\mathrm{m}^{-1}$ or W m^{-2} arcsec^{-2} km^{-1} s). Given a pixel value, $S(\lambda)$, the specific intensity, $I(\lambda)$, is calculated by a linear equation,

$$I(\lambda) = C_{flux}(\lambda) \cdot S(\lambda). \tag{3.1}$$

Here the scaling factor of flux calibration, $C_{flux}(\lambda)$, can be calculated from

$$C_{flux}(\lambda) = \frac{F_{std}(\lambda)}{S_{std}(\lambda)} \cdot \frac{1}{\Omega_{pix}} \cdot \frac{t_{std}}{t_{obj}} \cdot \frac{1}{W_{slit} \cdot C_{slit}} \tag{3.2}$$

where $F_{std}(\lambda)$ is the flux density of a standard star in W m^{-2} $\mu\mathrm{m}^{-1}$, $S_{std}(\lambda)$ is the pixel value of the standard star in ADU, Ω_{pix} is the pixel field-of-view (FOV) in arcsec^2, t_{std} and t_{obj} are the exposure times of the standard star and the object, respectively, W_{slit} is the slit width in pixels, and C_{slit} is a correction factor for slit obscuration.

Since only part of the flux from the standard star is detected due to the narrow slit, the measured signal must be corrected for proper flux calibration. We assumed a circularly symmetric point-spread-function (PSF) for the star, based on the flux profile along the slit length, to estimate the missing flux. The correction factor, which varies with the seeing, ranged from 2.06 to 2.94 (see Appendix A for more detailed descriptions).

The scaling factor, $C_{flux}(\lambda)$, is a function of wavelength since the response function between the celestial object and the detector (through interstellar space, the atmosphere of Earth, telescope, and instrument including the detector itself) is a function of wavelength. Within a small range of wavelength, however, the variation is small and we can assume that the scaling factor is approximately constant. For example, $C_{flux}(\lambda) \simeq C_{flux}(2.1218\ \mu\mathrm{m})$ around the H_2 $1-0$ $\mathrm{S}(1)$ line. Since we observe only one H_2 line in a spectral image using the high-dispersion echelle grating, we can adopt this approximation when calibrating the spectral images. The calibration in a wavelength far from the H_2 line is not important. Thus hereafter we use an approximated equation for the scaling factor for an objective H_2 line as follows.

$$C_{flux} = \frac{F_{std}(\lambda_0)}{S_{std}(\lambda_0)} \cdot \frac{1}{\Omega_{pix}} \cdot \frac{t_{std}}{t_{obj}} \cdot \frac{1}{W_{slit} \cdot C_{slit}} \tag{3.3}$$

where λ_0 is the rest wavelength of the H_2 line.

The flux density of a standard star, $F_{std}(\lambda_0)$, can be calculated if we know its flux density at K-band (2.0–2.4 $\mu\mathrm{m}$). Since we observe the H_2 lines only in K-band, assuming that the spectral energy distribution of the standard is approximately Plankian in the small range of

TABLE 3.1: Standard Stars

Standard star	Observing date (UT)	$m_K{}^a$ (mag)	Type[a]	$T_{std}{}^a$ (K)	$F_{std}(\lambda_K)$ (W m^{-2} μm^{-1})
HR 6496	2001, 2003/05/23	5.13	F7V	6300	3.67×10^{-12}
BS 6310	2003	4.79[b]	F4V	6600	5.02×10^{-12}

[a] From Eyres et al. (1998).
[b] $m_K = m_H - (H - K)$ where $m_H = 4.83$ (Eyres et al. 1998) and $(H - K) = 0.04$ (Cox 2000).

wavelength, we can use a relation for flux densities like

$$F_{std}(\lambda_0) = F_{std}(\lambda_K) \cdot \frac{B(\lambda_0, T_{std})}{B(\lambda_K, T_{std})} \tag{3.4}$$

where the central wavelength of K-band, $\lambda_K = 2.179\ \mu\mathrm{m}$, T_{std} is the effective temperature of the standard star, and the Plank function is given by

$$B(\lambda, T_{std}) = \frac{1.1910 \times 10^8 \cdot \lambda_{\mu\mathrm{m}}^{-5}}{e^{14387.7/\lambda_{\mu\mathrm{m}}/T_{std}} - 1} \tag{3.5}$$

(Cox 2000). $F_{std}(\lambda_K)$ can be calculated from the K-band flux density of Vega;

$$F_{std}(\lambda_K) = F_{Vega}(\lambda_K) \cdot 10^{-\frac{m_K}{2.5}} \tag{3.6}$$

where $F_{Vega}(\lambda_K) = 4.14 \times 10^{-10}\ \mathrm{W\ m^{-2}}\ \mu\mathrm{m}^{-1}$ (Cox 2000) and m_K is the K-band magnitude of the standard star. We present the information of the standard stars we used in Table 3.1.

Now we can calculate $F_{std}(\lambda_0)$ using equation 3.4 and we can measure $S_{std}(\lambda_0)$ in the spectrum of a standard star. Therefore, with the known values of Ω_{pix} ($0''.90 \times 0''.41 = 0.369$ arcsec^2 for H_2 $1-0$ S(1) and $0''.84 \times 0''.41 = 0.344$ arcsec^2 for H_2 $2-1$ S(1)), t_{std}/t_{obj} ($7/100$ for H_2 $1-0$ S(1) and $7/60$ for H_2 $2-1$ S(1)), W_{slit} (2 pixels), and C_{slit} (see Appendix A), the scaling factors for flux calibration can be calculated using equation 3.3 as in Table 3.2.

For all the 2-D spectral images we observed, the raw (only sky-subtracted) and reduced images are presented together in Figures 3.8–3.18.

TABLE 3.2: Scaling Factors for Flux Calibration

Date (UT) (yyyy/mm/dd)	Standard star	$F_{std}(\lambda_0)$ (W m^{-2} $\mu\mathrm{m}^{-1}$)	$S_{std}(\lambda_0)$ (ADU)	C_{slit}[a]	C_{flux} (W m^{-2} arcsec^{-2} $\mu\mathrm{m}^{-1}$ ADU^{-1})
		H_2 $1-0$ S(1) ($\lambda = 2.1218\mu$m)			
2001/08/03-A[b]	HR 6496	4.01×10^{-12}	1600	2.56	9.27×10^{-17}
2001/08/03-B[c]	HR 6496	4.01×10^{-12}	1850	2.20	9.36×10^{-17}
2001/08/04-C[d]	HR 6496	4.01×10^{-12}	1480	2.52	1.02×10^{-16}
2001/08/04-D[e]	HR 6496	4.01×10^{-12}	1530	2.43	1.02×10^{-16}
2003/05/23	HR 6496	4.01×10^{-12}	2270	2.94	5.70×10^{-17}
2003/05/28	BS 6310	5.48×10^{-12}	3050	2.20	7.75×10^{-17}
2003/05/29	BS 6310	5.48×10^{-12}	2570	2.59	7.82×10^{-17}
2003/05/30	BS 6310	5.48×10^{-12}	3480	2.39	6.24×10^{-17}
2003/05/31	BS 6310	5.48×10^{-12}	1680	2.66	1.16×10^{-16}
2003/06/01	BS 6310	5.48×10^{-12}	3140	2.06	8.02×10^{-17}
		H_2 $2-1$ S(1) ($\lambda = 2.2477\mu$m)			
2001/08/04	HR 6496	4.12×10^{-12}	1030	2.32	1.76×10^{-16}

[a] Calculated from Appendix A using the seeing information from Table 2.3.

[b] Slits 00–NW12 in field NE-1.

[c] Slits NW15 and SE03–SE12 in field NE-1.

[d] Slit SE15 in field NE-1 and slits SE18–SE24 in field NE-2.

[e] Field E-0.

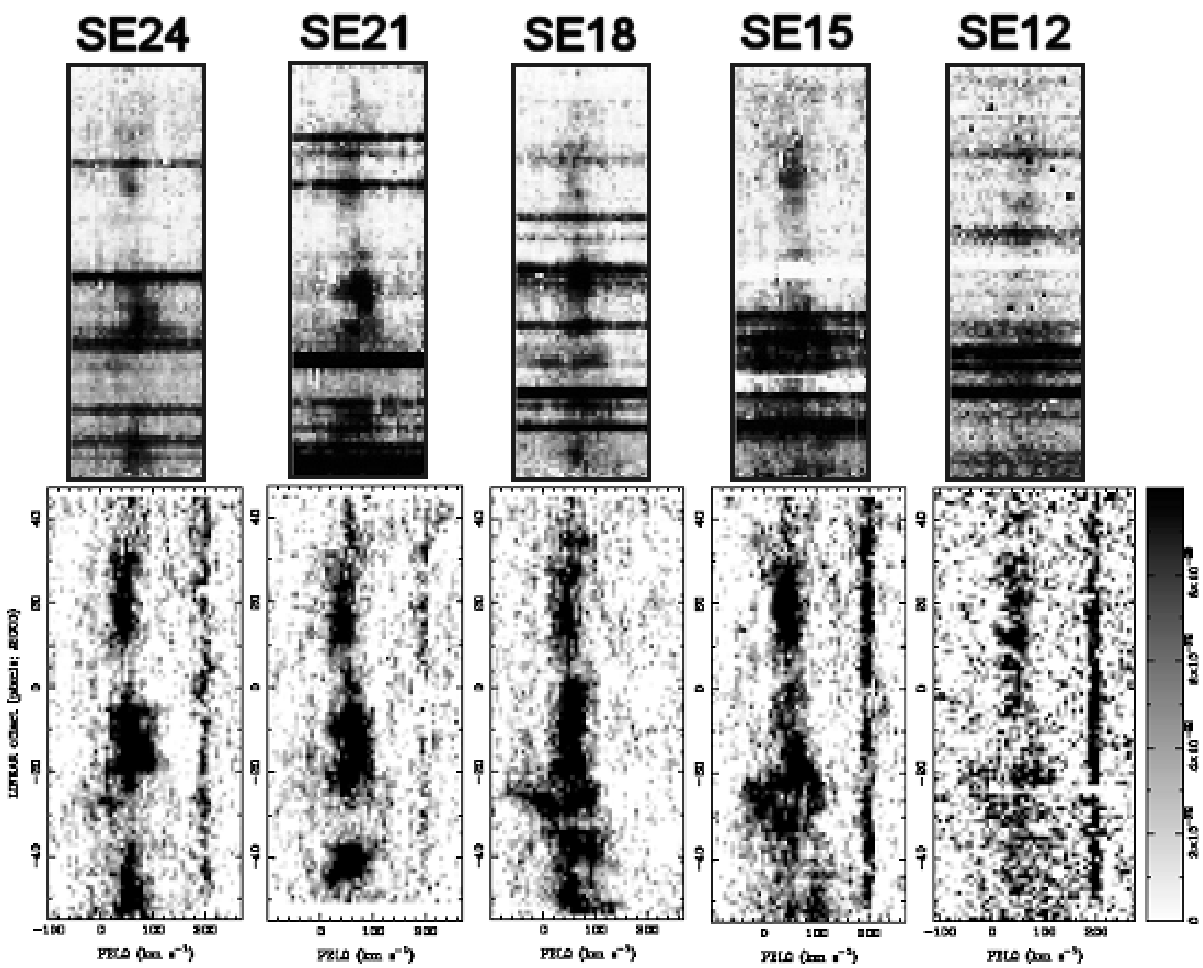

FIG. 3.8: Results of data reduction of the 2-D spectral images in field NE (part I). (top) The raw (only sky-subtracted) spectral image in field NE in negative. Slit name, which is defined by [scanning direction] + [separation from the base position in arcsec] is indicated on top of each image. (bottom) After reduction and calibrations. Vertical axis along the slit represents offset from a reference position in units of pixels. Horizontal axis along the spectral dispersion represents V_{LSR} relative to the rest wavelength of $\mathrm{H_2}$ $1-0$ S(1) line in units of $\mathrm{km\ s^{-1}}$. The gray scale runs from 0 to 10^{-21} W $\mathrm{m^{-2}}$ $\mathrm{arcsec^{-2}}$ $\mathrm{km^{-1}}$ s.

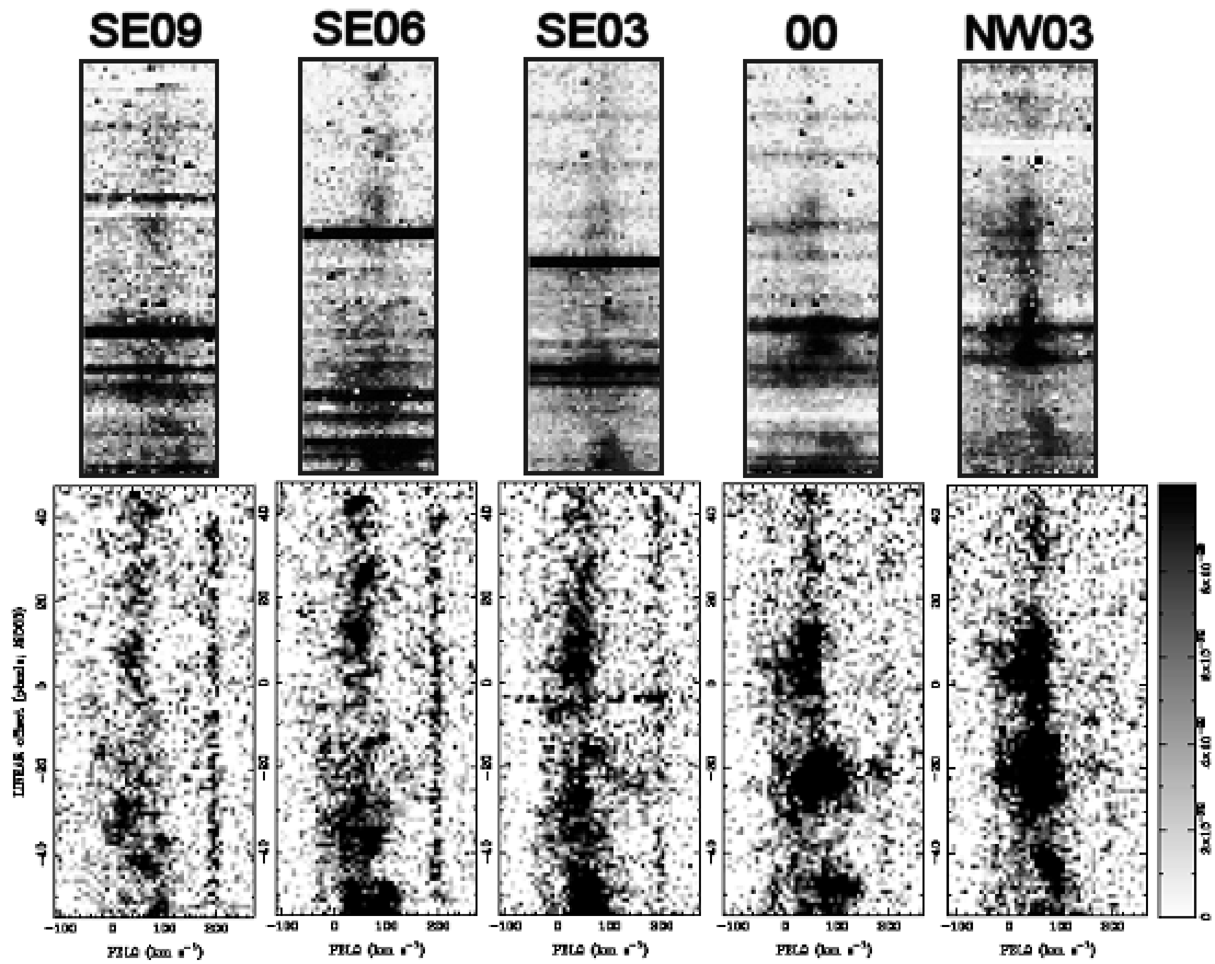

FIG. 3.9: Results of data reduction of the 2-D spectral images in field NE (part II). The same as in Figure 3.8.

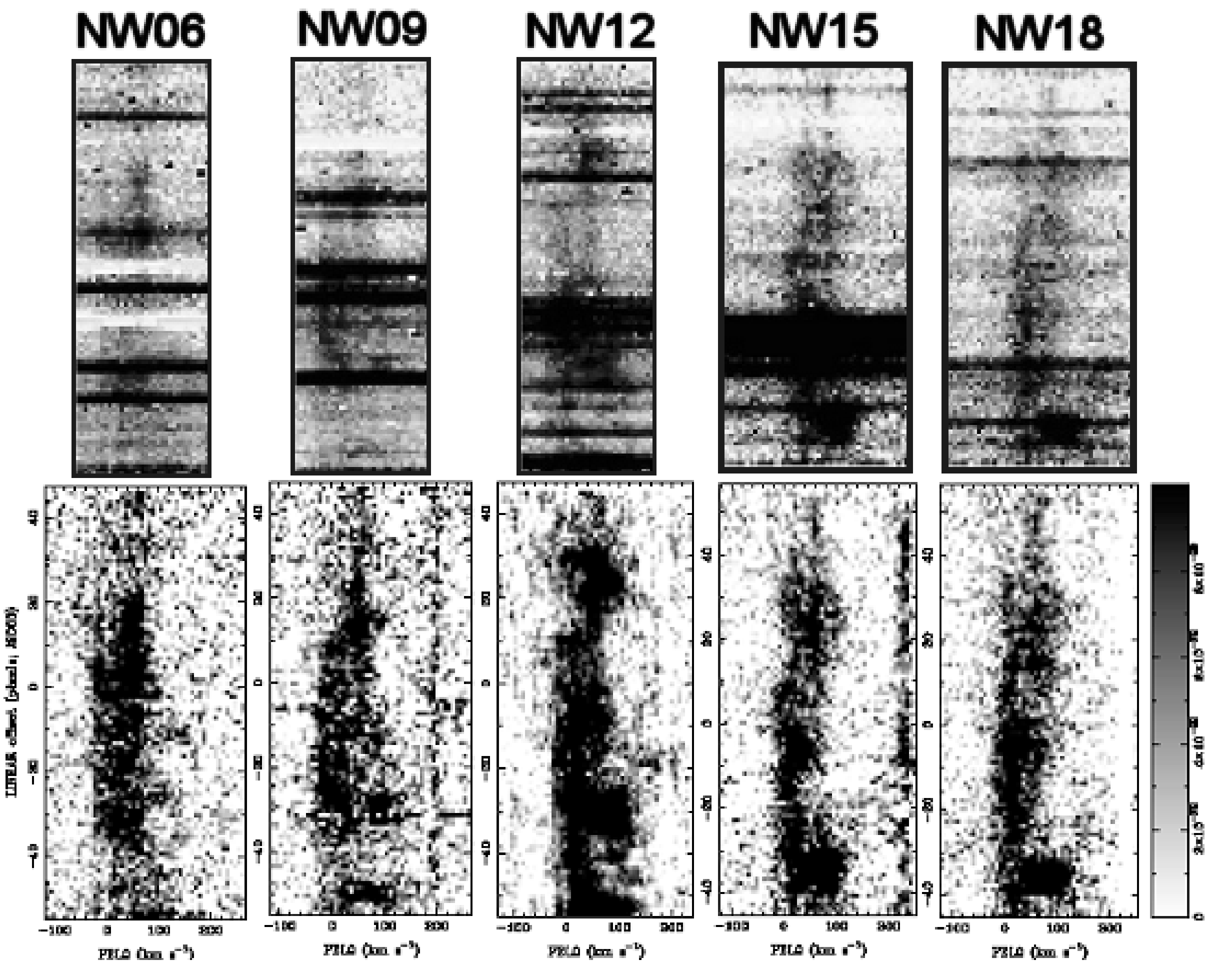

FIG. 3.10: Results of data reduction of the 2-D spectral images in field NE (part III). The same as in Figure 3.8.

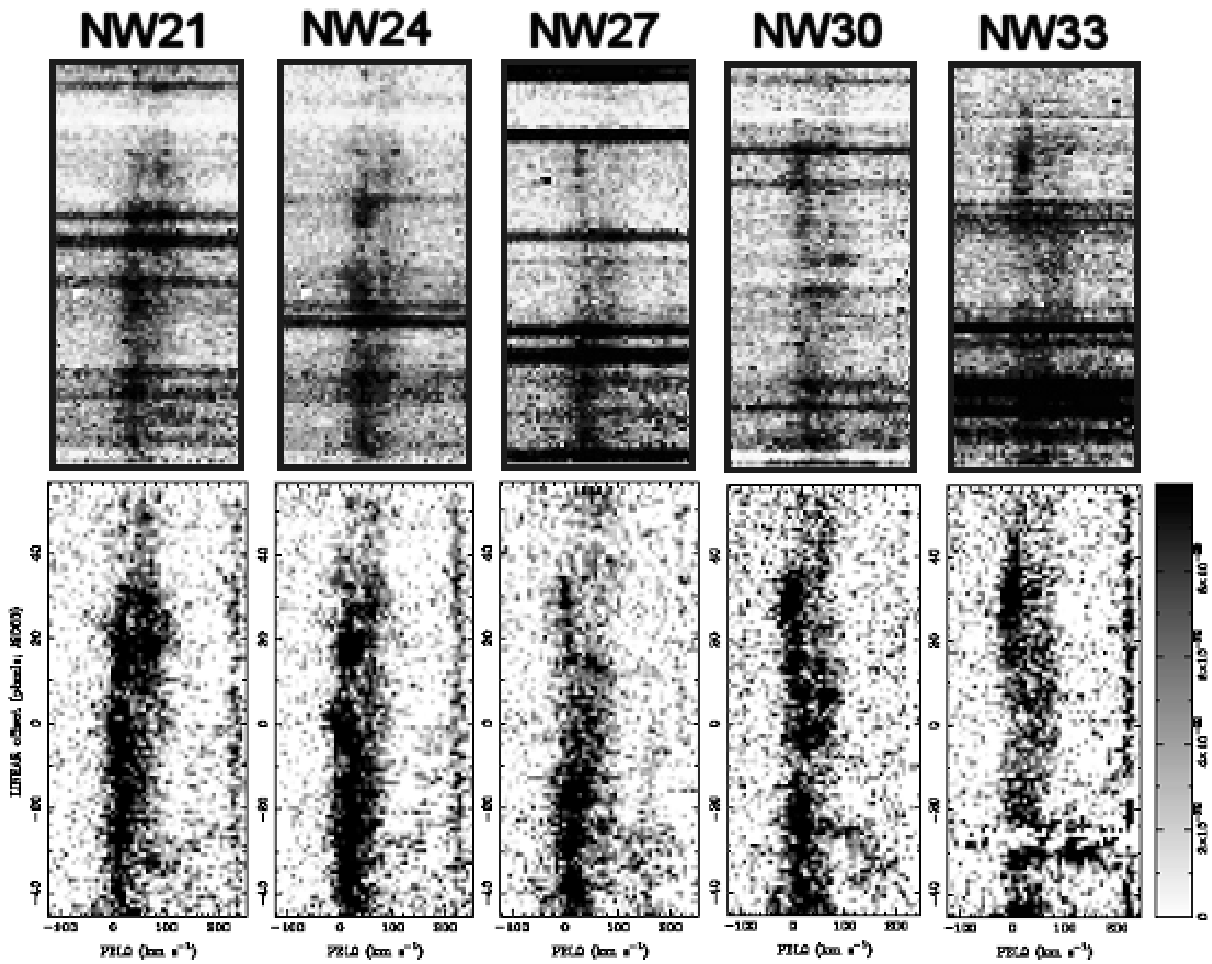

FIG. 3.11: Results of data reduction of the 2-D spectral images in field NE (part IV). The same as in Figure 3.8.

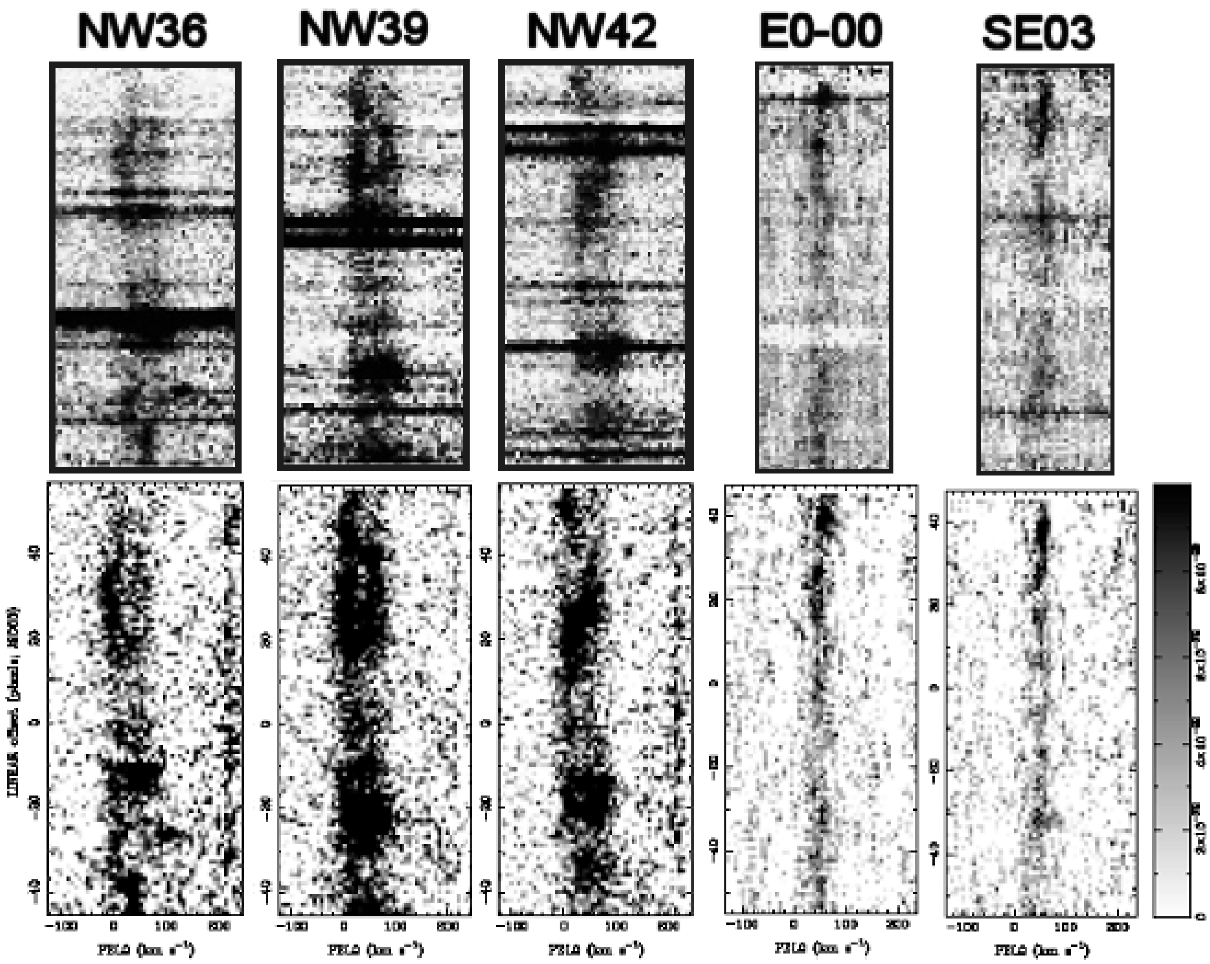

FIG. 3.12: Results of data reduction of the 2-D spectral images in field NE (part V) and field E-0. The same as in Figure 3.8.

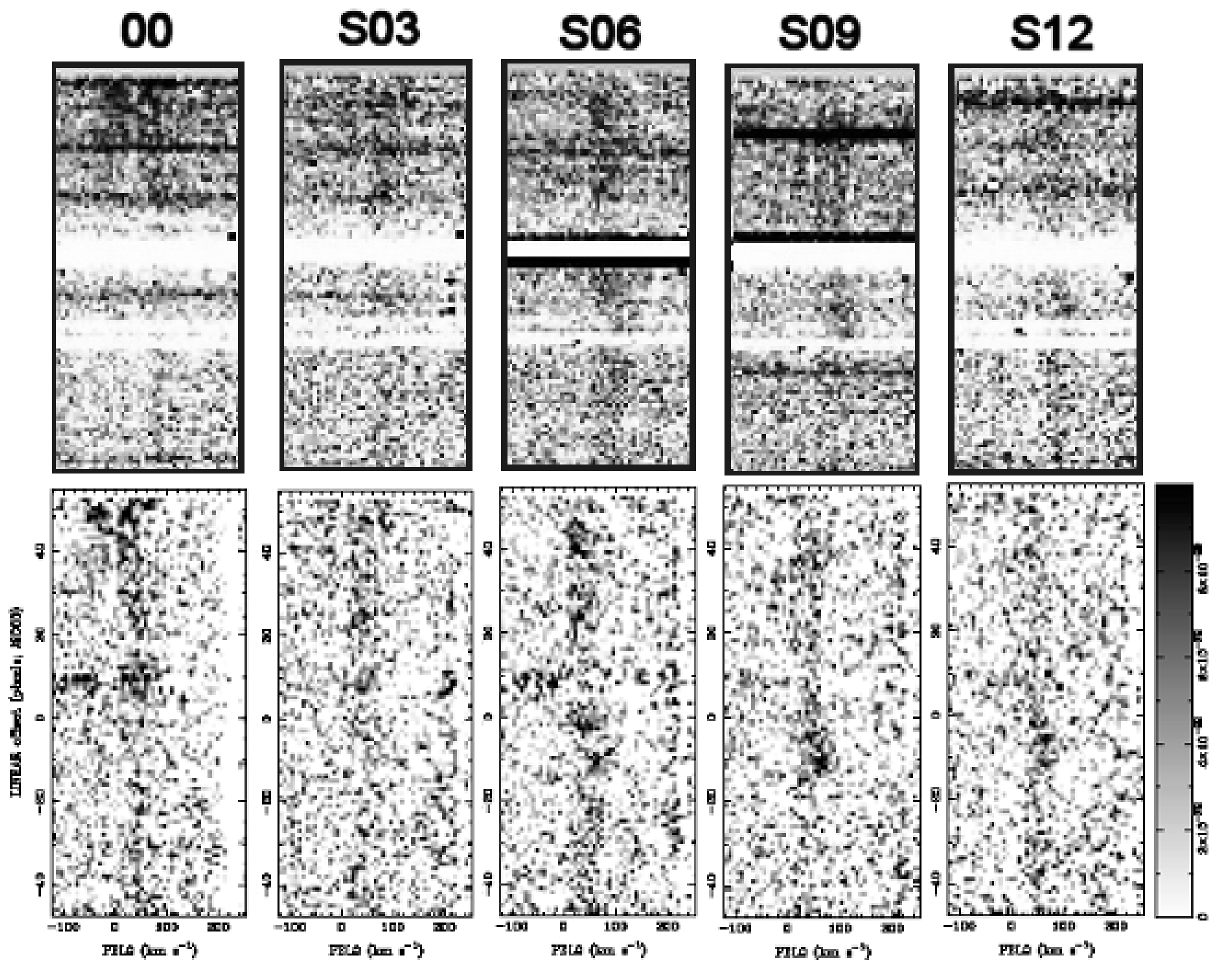

FIG. 3.13: Results of data reduction of the 2-D spectral images in field E (part I). The same as in Figure 3.8.

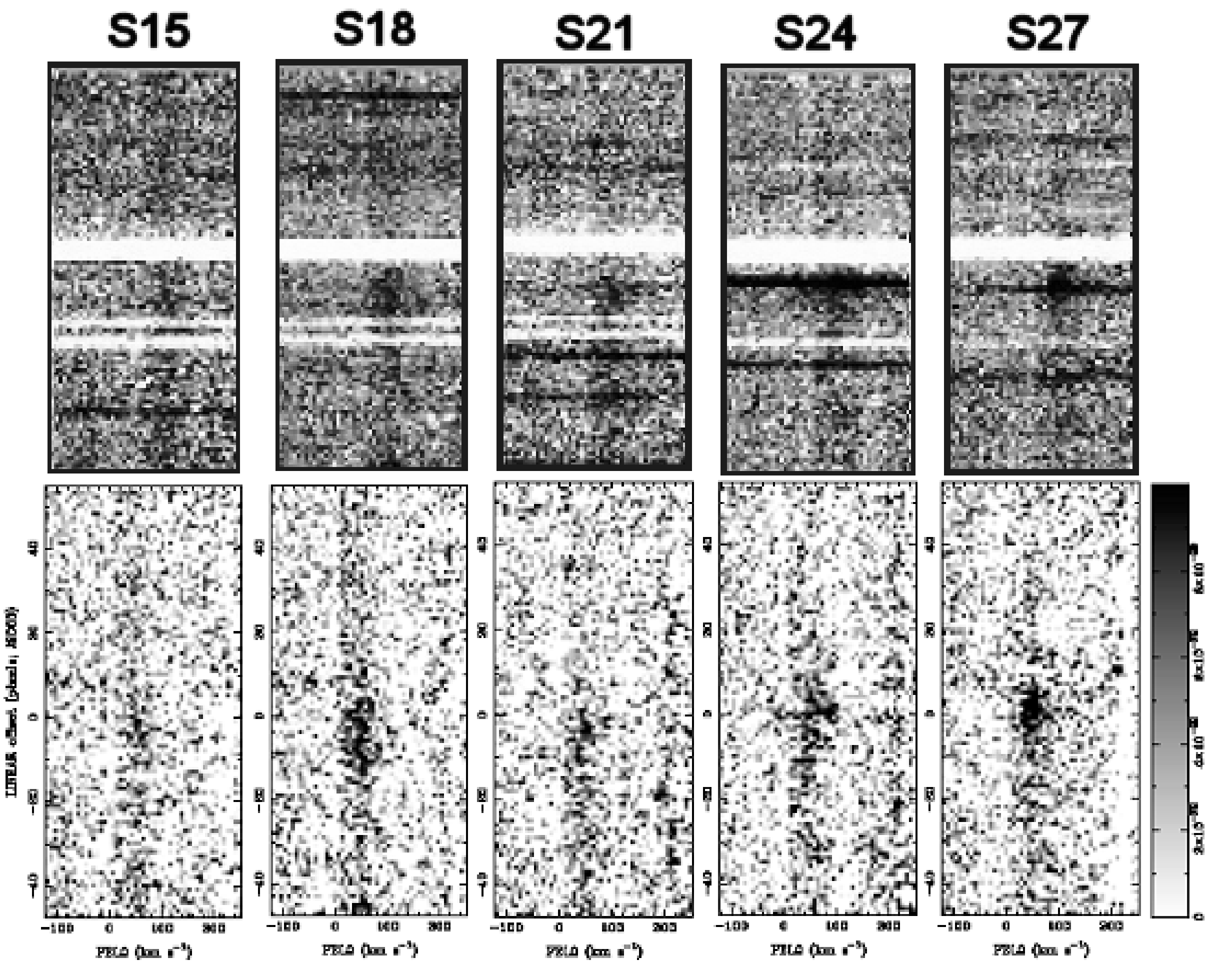

FIG. 3.14: Results of data reduction of the 2-D spectral images in field E (part II). The same as in Figure 3.8.

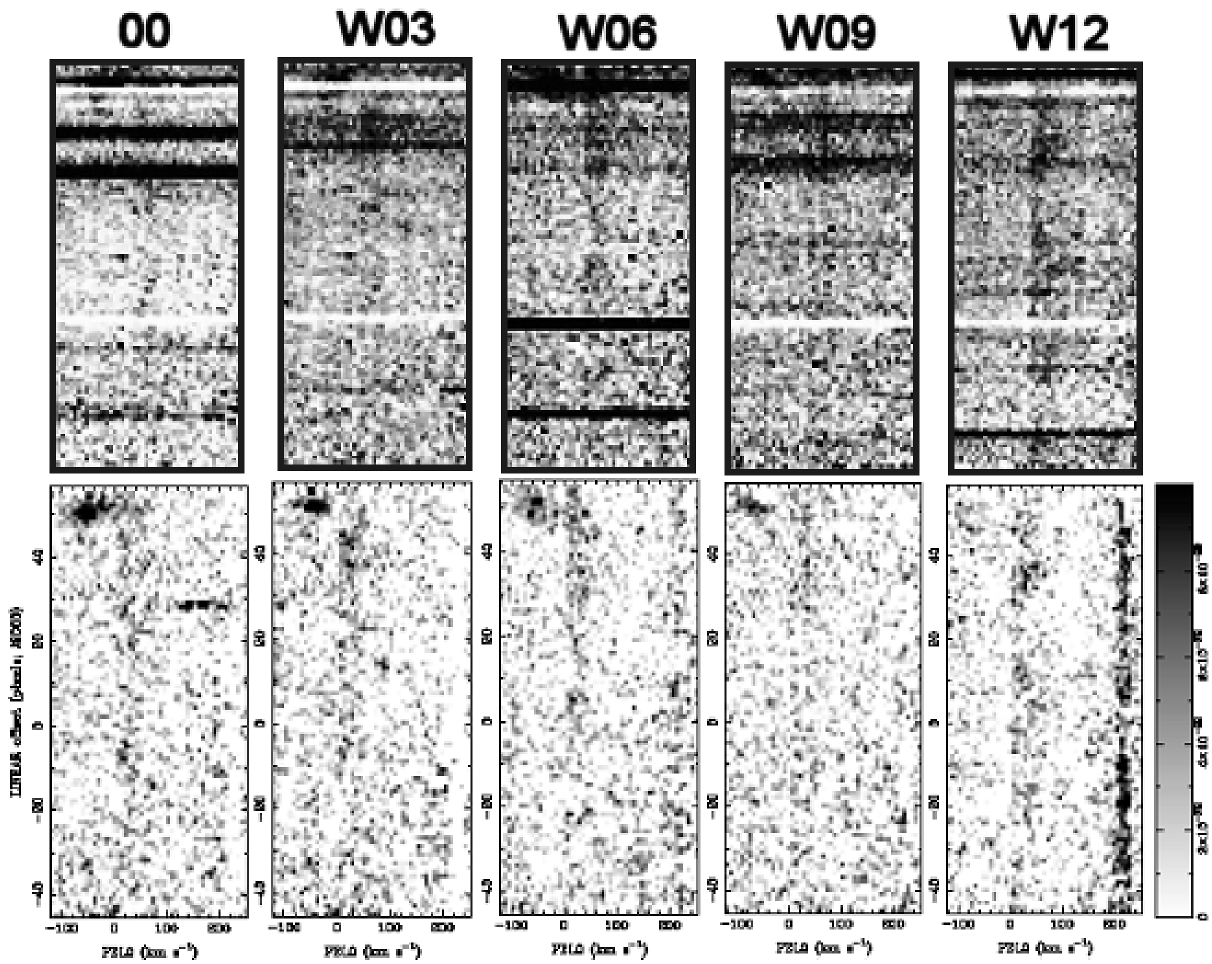

FIG. 3.15: Results of data reduction of the 2-D spectral images in field S (part I). The same as in Figure 3.8.

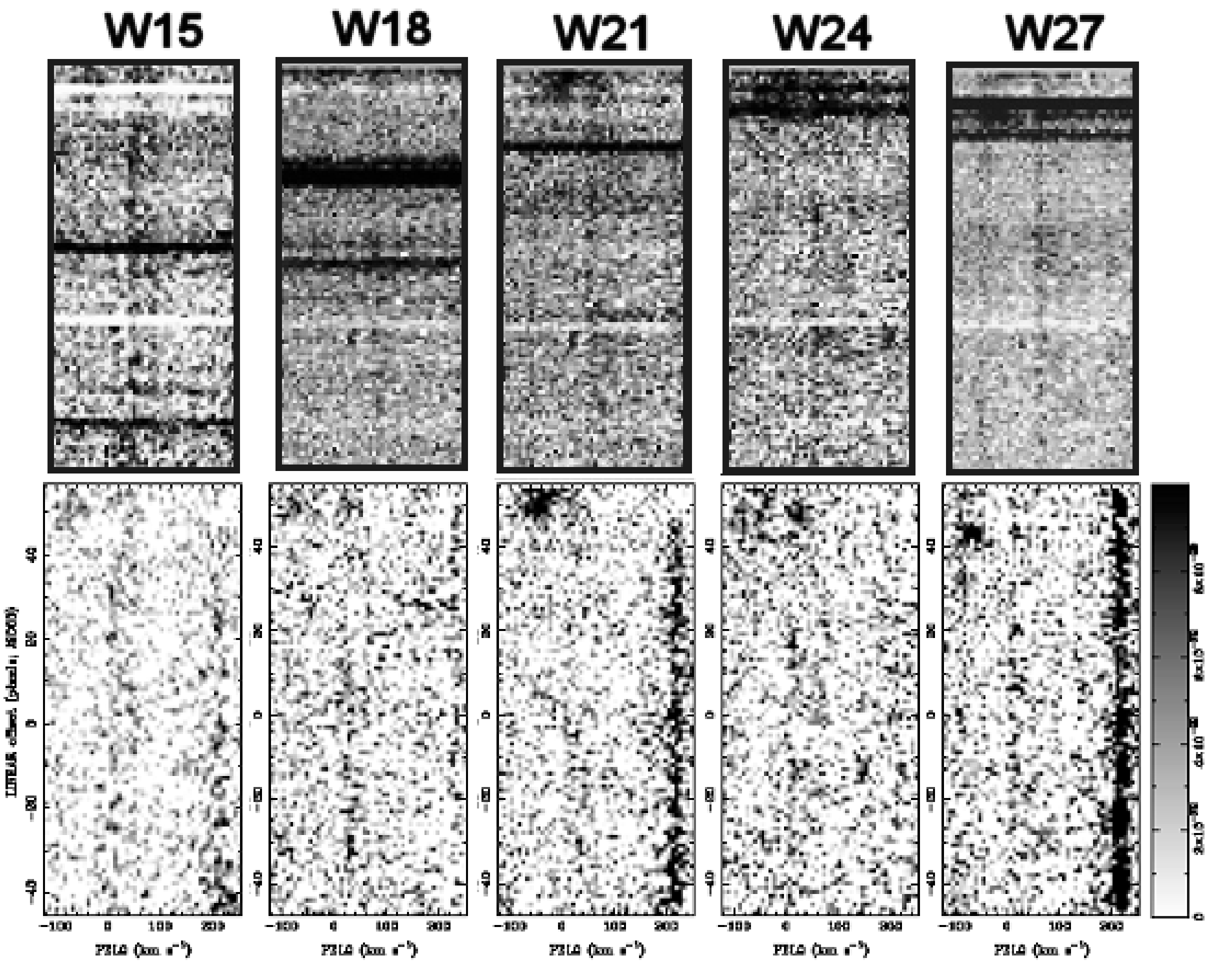

FIG. 3.16: Results of data reduction of the 2-D spectral images in field S (part II). The same as in Figure 3.8.

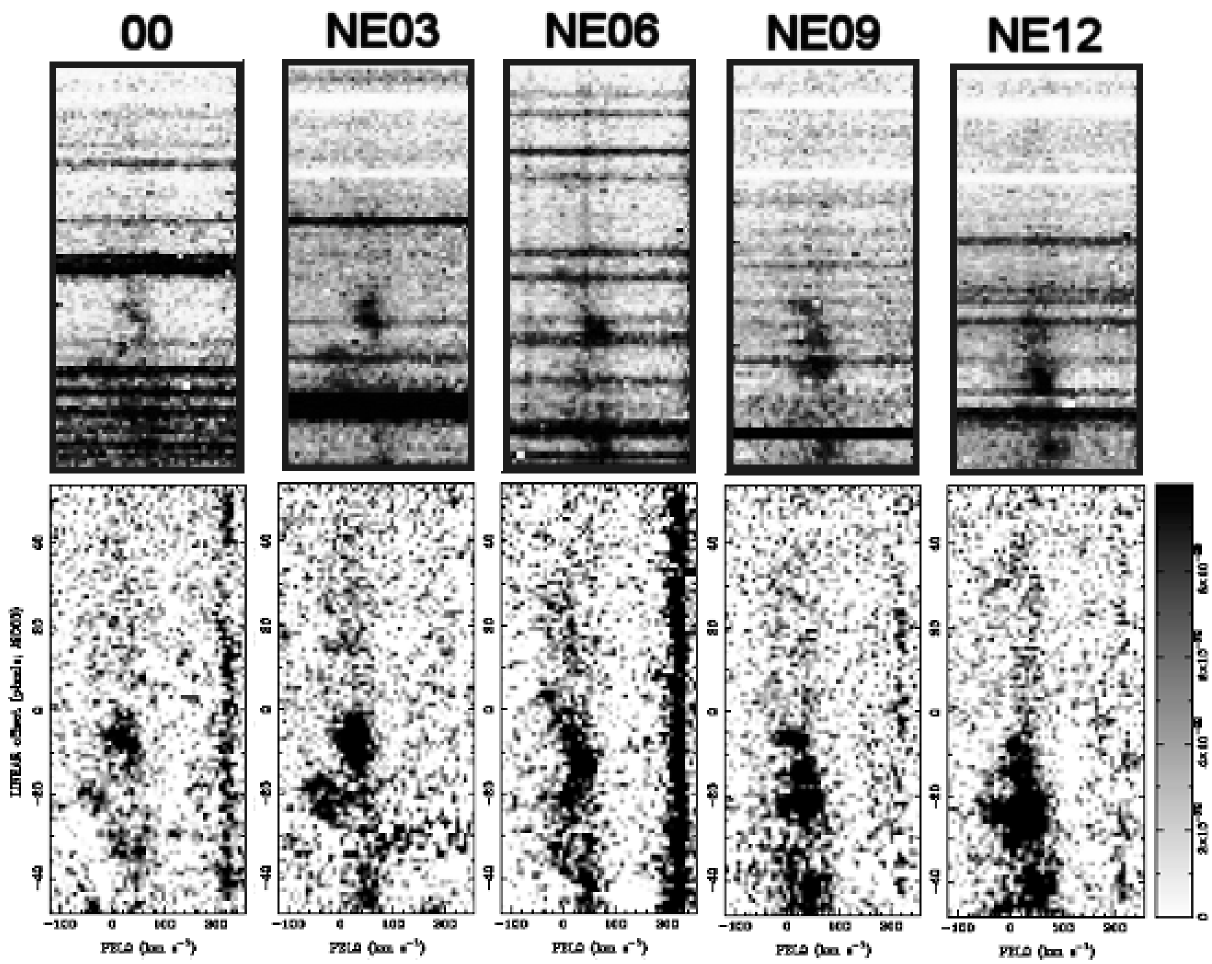

FIG. 3.17: Results of data reduction of the 2-D spectral images in field W (part I). The same as in Figure 3.8.

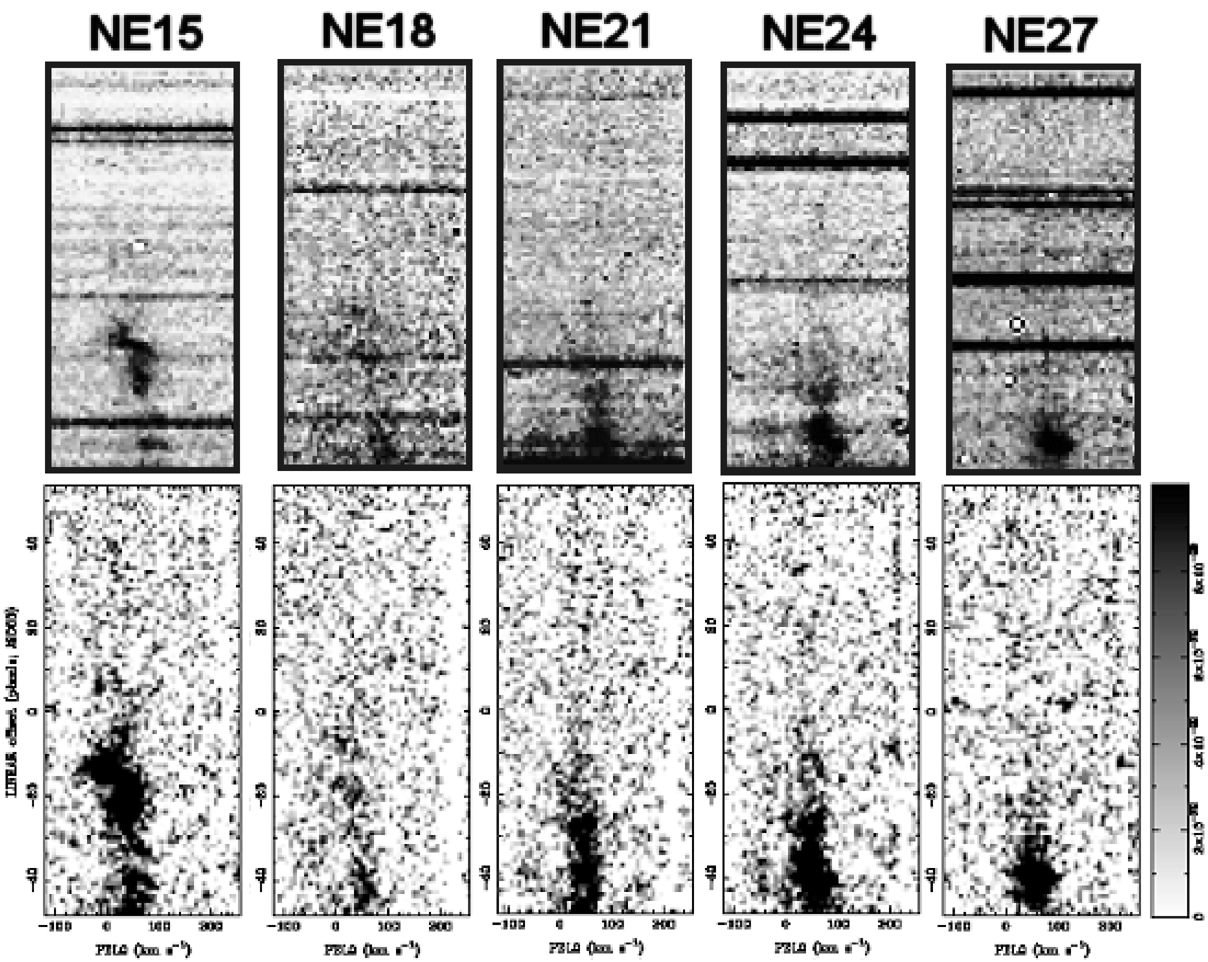

FIG. 3.18: Results of data reduction of the 2-D spectral images in field W (part II). The same as in Figure 3.8.

3.2 3-Dimensional Data Reduction Using MIRIAD

By unifying the high dispersion 2-D spectral images into a 3-D data cube, we can investigate the structure and kinematics of the H_2 emitting gas simultaneously. There are a few examples for handling 3-D data which are observed with low spectral dispersions (e.g., Burton & Allen 1992; Lee et al. 2005; see Figure 1.13). From these low dispersion 3-D data, we can extract images at various wavelengths (e.g. emission line images) but cannot get any kinematic information.

In the wavelengths shorter than infrared (IR), it is thought that there have been few cases of 3-D observations with such a high spectral dispersion as our observations using echelle grating. However, in radio observations, it is not unusual to map a large area with a very high resolution in frequency (or so called channel). Thus there are excellent tools for reducing and handling 3-D data including the Multichannel Image Reconstruction, Image Analysis and Display (MIRIAD; Sault, Teuben, & Wright 1995; Hoffman et al. 1996).

MIRIAD is a radio interferometry data reduction package, in the form of an environment with a large set of moderate-sized program which perform individual tasks, involving calibration, mapping, deconvolution and image analysis of interferometric data. However, MIRIAD can also be used for the general reduction of continuum and spectral line data in various formats (including FITS) through to the image analysis and display stages (publication quality output). Hence we use MIRIAD for our near-IR 3-D data.

First, we have to transform the FITS data reduced by IRAF into the MIRIAD format. This transformation of data format is easily achieved by the MIRIAD task FITS. This task also translate some standard information contained in the header of the FITS files into a MIRIAD-readable format (called 'item'). However, the FITS task cannot understand all the 'fields' in the FITS header which are often different between observatories or instruments. Thus we have to translate by hand some necessary, but abnormal, FITS fields into MIRIAD items.

Then we use the MIRIAD task IMCAT to stack the 2-D spectral images into a single 3-D data (or data cube). We built data cubes separately for each slit-scanning block (e.g. field NE-1, field NE-2, field NE-3...; see Table 2.3) since the spectral images are common in dimension and have common base position and slit angle within every single slit-scanning block. Consequently we have 11 data cubes with different dimensions, positions, and inclination angles for 11 different slit-scanning blocks.

However, in order to investigate the large-scale structure in the central 10 pc, we need to unify the data cubes into a big, single, data cube. For this purpose, every pixels in each unit of data cube should know its exact position on the sky; i.e. we give a coordinate information to each data cube. The sequence of this process is presented in Figure 3.19. As seen in the figure, the simply stacked data cubes have two spatial axes; one along the slit length and the other along the direction of the slit-scanning. If the position angle of slit were simply a multiple of right angle (i.e. $0°$, $90°$, $180°$, and $270°$), each of these two axes could be directly projected on Right Ascension (R.A.) and Declination (Dec), respectively, or vice versa. However, in our observations with various slit-position angles, the coordinating process becomes slightly more complicated. First, we make a template cube which contains no data value but is defined to have celestial coordinates (R.A. and Dec) along two spatial axes. Second, we rotate the template by the position angle of slit. Third, we merge the data cube with this rotated template cube. Finally, we de-rotate the merged cube then each data pixel is located in its exact position on the sky now.

Before the process of coordinating above, we re-sampled the data cube along all its axes using the MIRIAD task REGRID. Since the original pixel is not regular-square ($0\farcs9 \times 3''$ along the slit and perpendicular to it, respectively), the intensity distribution can become biased after the rotation of cube. We divided each pixel into much smaller, regular-square, pixels with a scale of $0\farcs3 \times 0\farcs3$ to decrease this bias effect (see Figure 3.20 for an example). Additionally, the higher sampling resolution has a merit of more accurate matching when we combine the different data cubes into one single cube. For this unification, we also re-sampled and unified the velocity axes of all the data cubes into a common definition (68 pixels with a scale of $7.3\ \mathrm{km\ s^{-1}}$ in the range from -200 to +300 $\mathrm{km\ s^{-1}}$).

MIRIAD have a few tasks for mosaicking data cubes (not 2-D images). Among these tasks LINMOS is most appropriate for non-radio data like ours. However, using LINMOS for mosaicking our data cubes, we found serious problems in overlapped regions (see Figure 3.21 for an example). Since the data values in an overlapped region are averaged, when an observed position in one cube is overlapped with a blank position in another cube, the resulting value in a combined cube is halved. The blank regions are un-avoidable results from the cube rotation. We hope that MIRIAD just ignore the blanks when combining the overlapped regions but it understands that the pixel values in the blanks are zero.

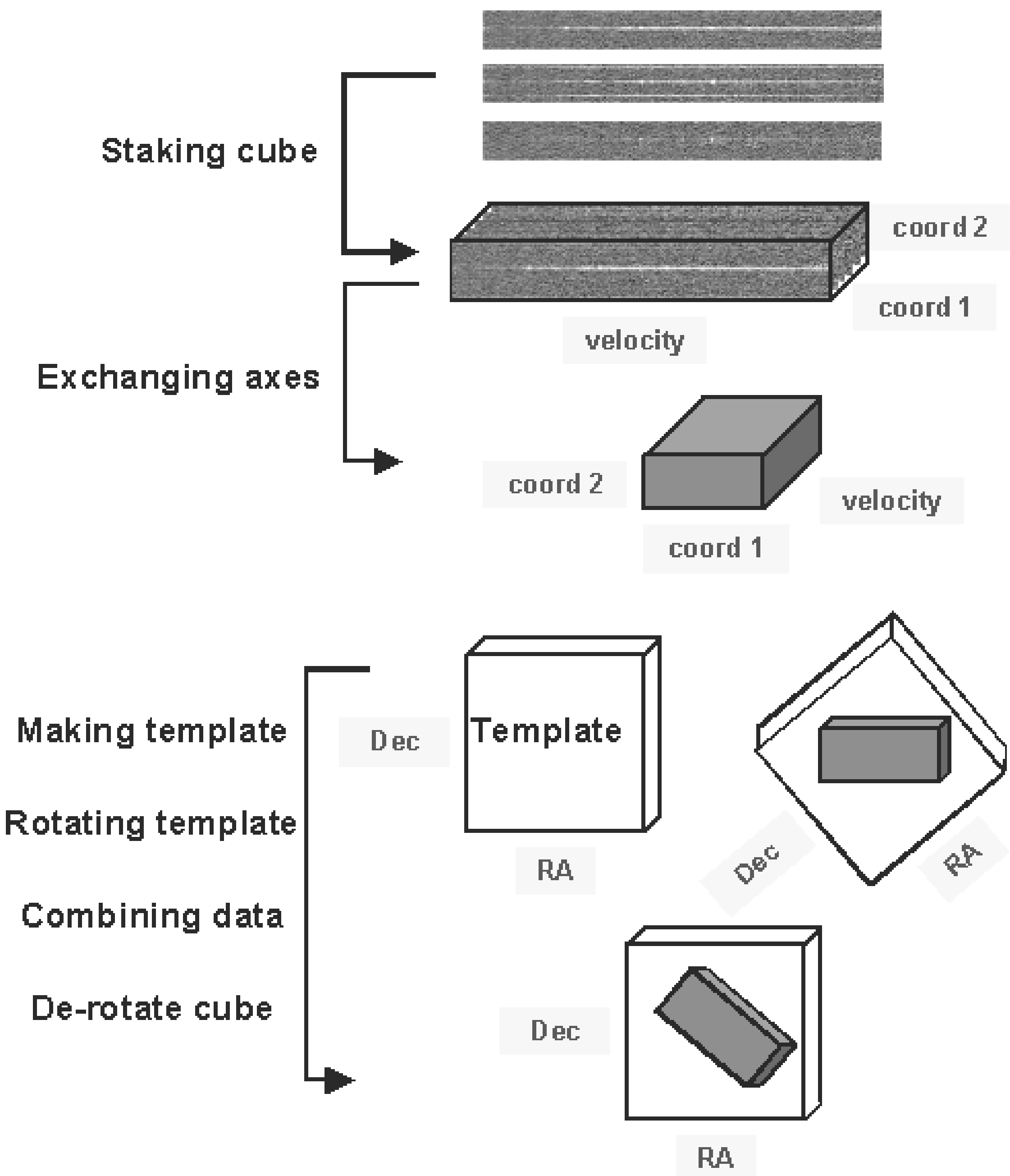

FIG. 3.19: Sequence of making a data cube (see text for the details). Note that coord1 and coord2 in the first half of the process is not celestial coordinates but with respect to the slit axes; coord2 is along the slit length and coord1 is along the direction of the slit-scanning.

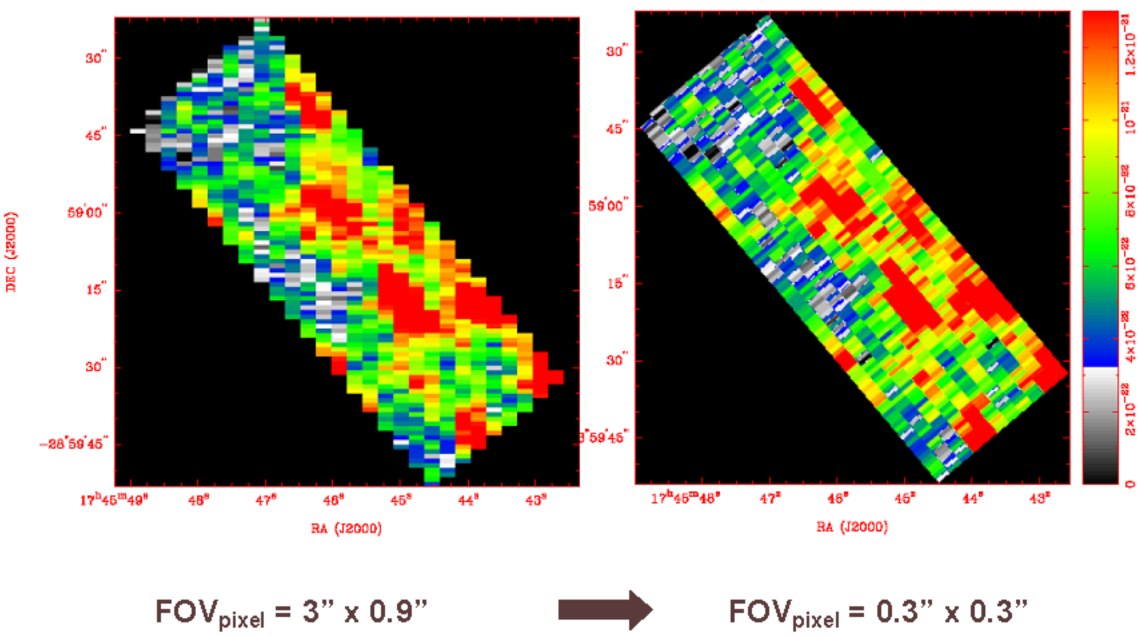

FIG. 3.20: Example of re-sampling a data cube (the velocity-averaged $\mathrm{H_2}$ $1-0$ $\mathrm{S}(1)$ map of field NE-1). The color-scaled intensity level is indicated by the right-side wedge in units of $\mathrm{W\ m^{-2}\ arcsec^{-2}\ km^{-1}\ s}$.

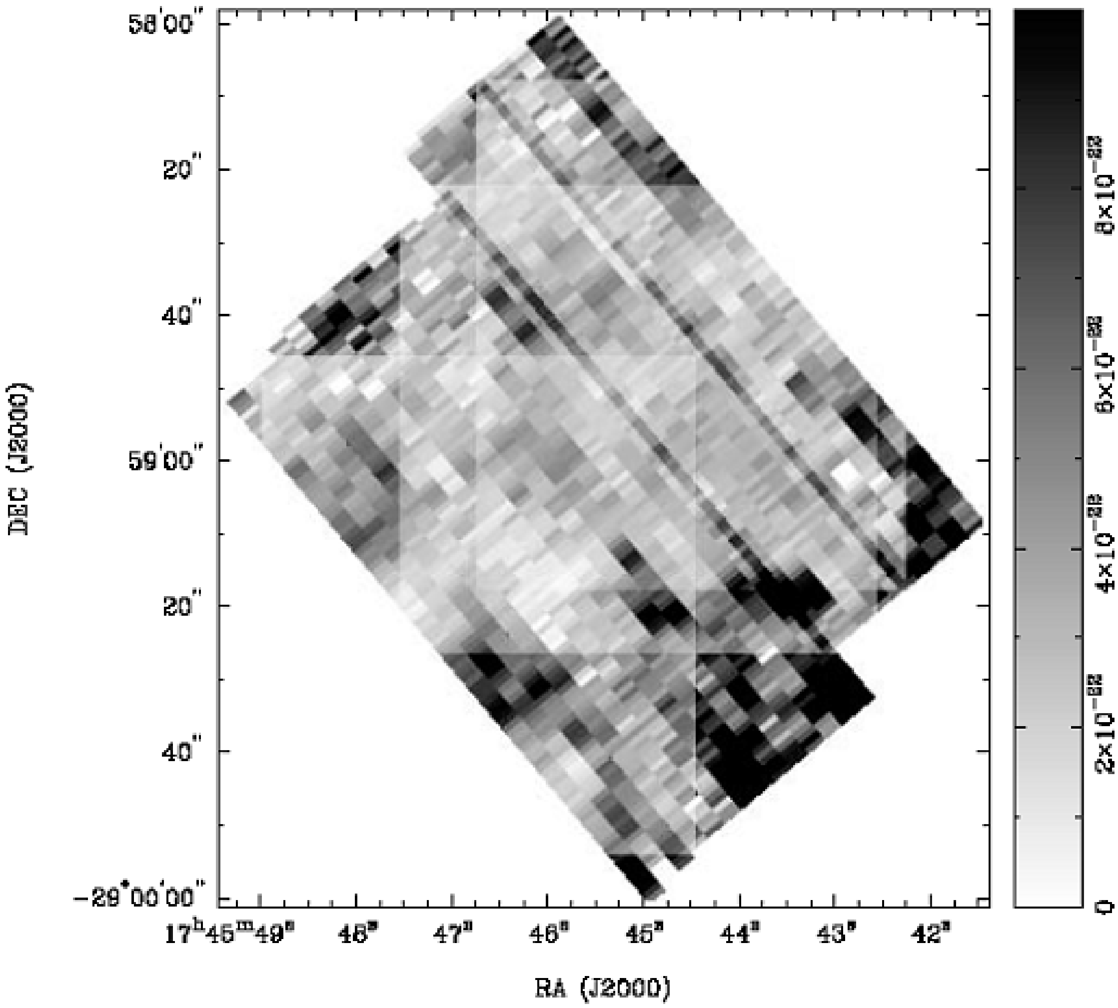

FIG. 3.21: Example of mosaicking data cubes using the MIRIAD task LINMOS. The velocity-averaged H_2 $1-0$ $S(1)$ map of field NE from the combined data cube. The gray-scaled intensity level is indicated by the right-side wedge in units of $\mathrm{W\ m^{-2}\ arcsec^{-2}\ km^{-1}\ s}$.

Thus we implement the 'weighted mosaicking' for our data cubes;

$$\mathrm{cube_A} + \mathrm{cube_B} = \frac{\mathrm{cube_{A'}} \times \mathrm{cube_{A,W}} + \mathrm{cube_{B'}} \times \mathrm{cube_{B,W}}}{\mathrm{cube_{A,W}} + \mathrm{cube_{B,W}}} \tag{3.7}$$

when $\mathrm{cube_{A,W}} > 0$ or $cube_{B,W} > 0$. Here 'cube' means each pixel in a cube, $\mathrm{cube_{A'}}$ and $\mathrm{cube_{B'}}$ are extended cubes from the original data cubes to the dimension for the combining cube, and $\mathrm{cube_{A,W}}$ and $\mathrm{cube_{B,W}}$ are the template cubes containing weight information (see Figure 3.22).

We present the results of mosaicking in Figures 3.23–3.27. Four figures for each field are presented for viewing in detail. Throughout the following chapters, we only use the cube for the entire region (Figure 3.27) for all the various analyses including the extracted spectra and the channel maps in Chapter 4, the position-velocity diagrams in Chapter 5, and the direct comparison with radio data in both Chapters. A smoothed version of the entire-region cube, which is convolved with a Gaussian of FWHM = $3''$ and has a higher S/N ratio, is also presented in Figure 3.28.

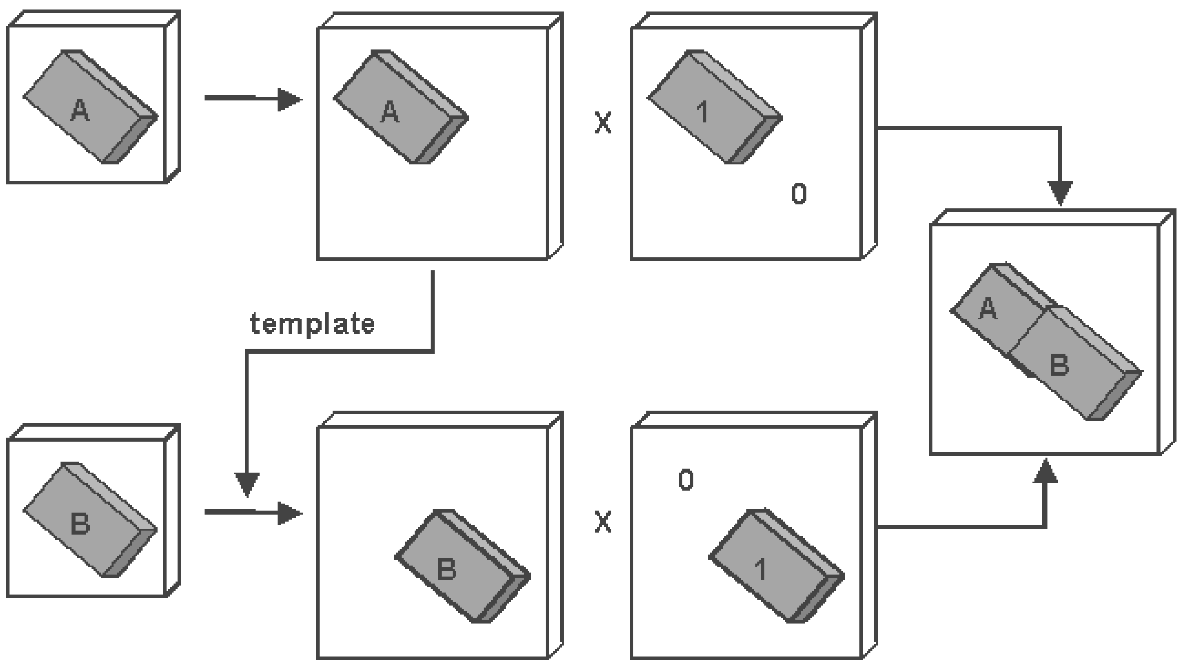

FIG. 3.22: Schematic diagram of weighted mosaicking. Note that the extended cube A is used as a template when extending cube B for two cubes to have the same dimension and format.

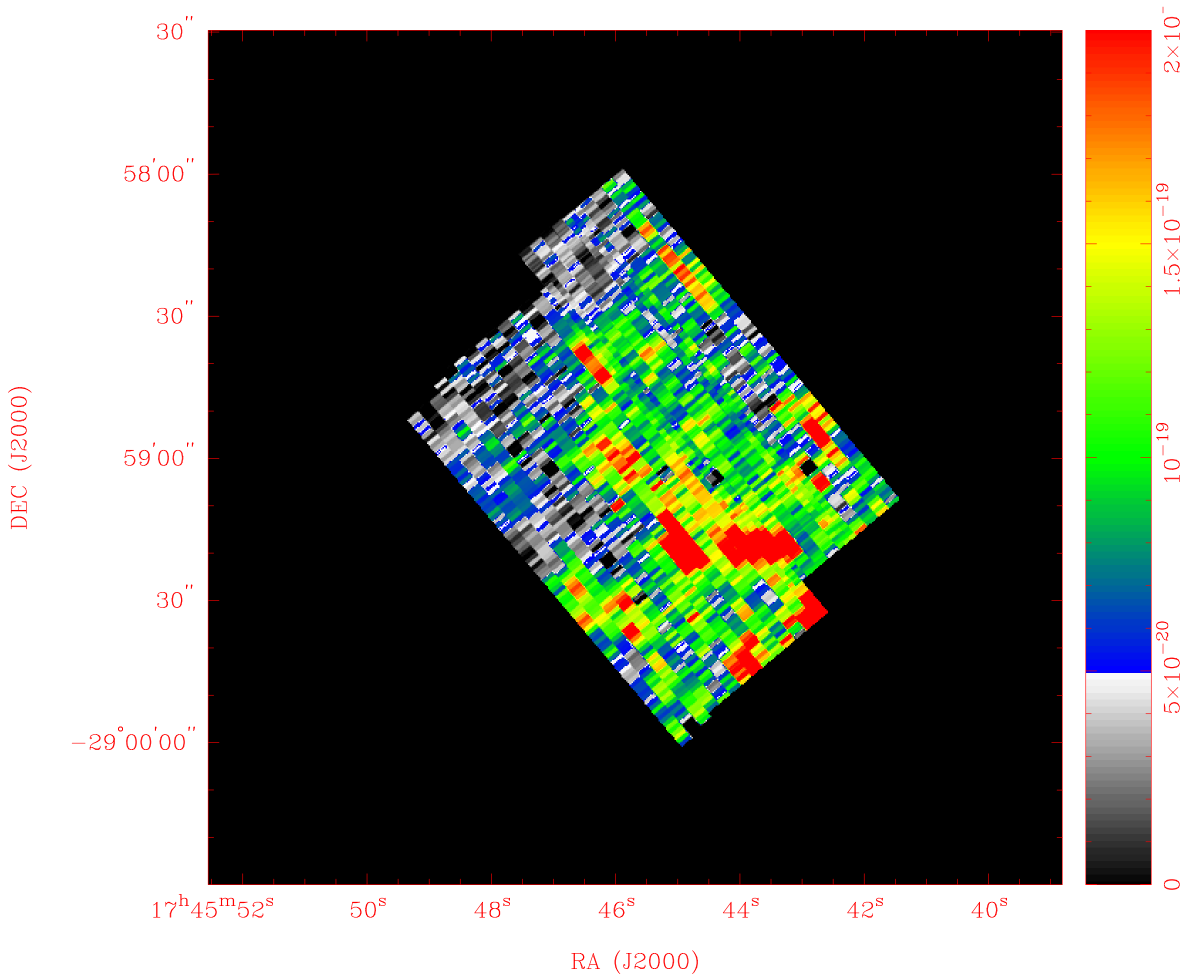

FIG. 3.23: The velocity-integrated H_2 $1-0$ $S(1)$ map of field NE from the combined data cube. The color-scaled intensity level is indicated by the right-side wedge in units of W m^{-2} $arcsec^{-2}$.

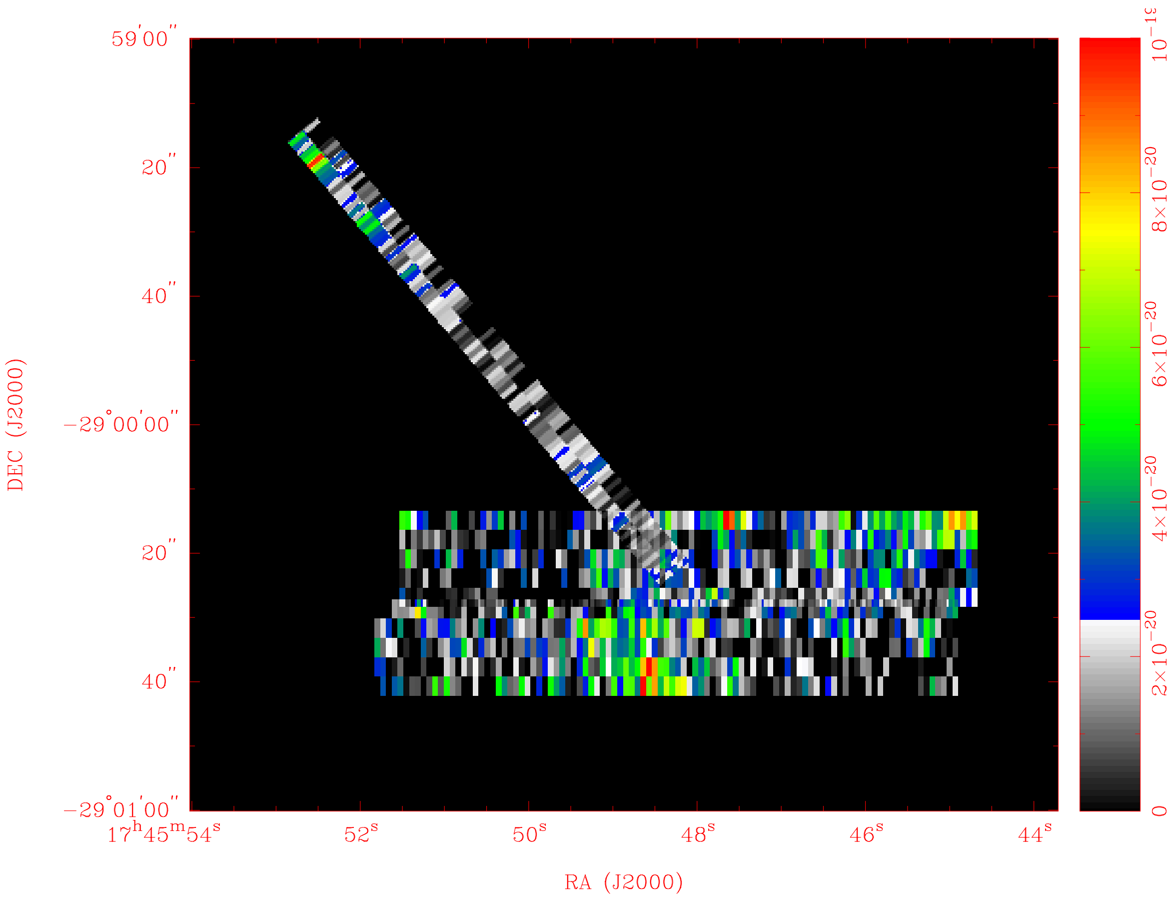

FIG. 3.24: The velocity-integrated H_2 $1-0$ S(1) map of field E from the combined data cube. The color-scaled intensity level is indicated by the right-side wedge in units of W m^{-2} $arcsec^{-2}$.

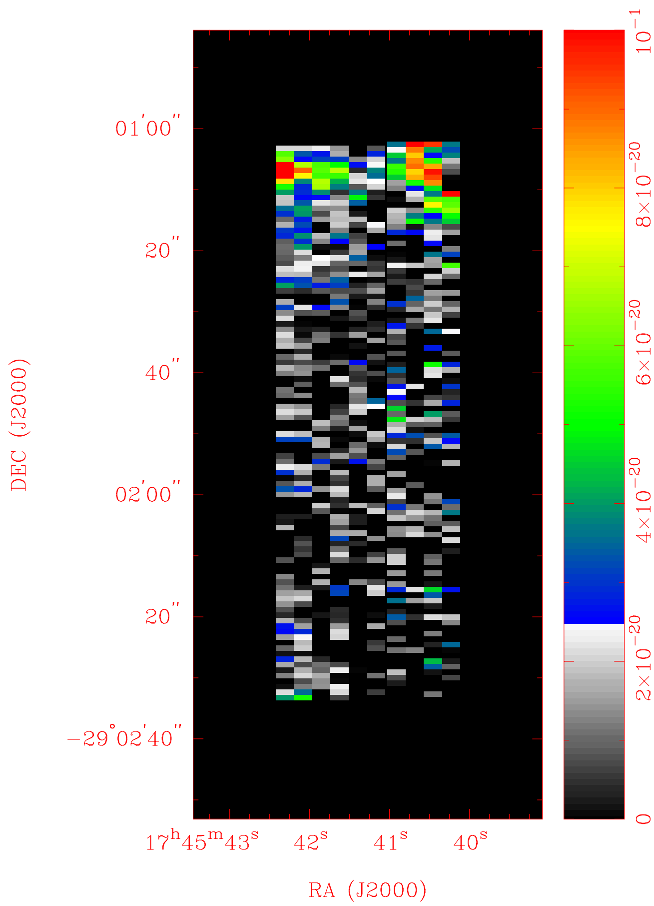

FIG. 3.25: The velocity-integrated $\mathrm{H_2}$ $1-0$ $\mathrm{S(1)}$ map of field S from the combined data cube. The color-scaled intensity level is indicated by the right-side wedge in units of $\mathrm{W\ m^{-2}\ arcsec^{-2}}$.

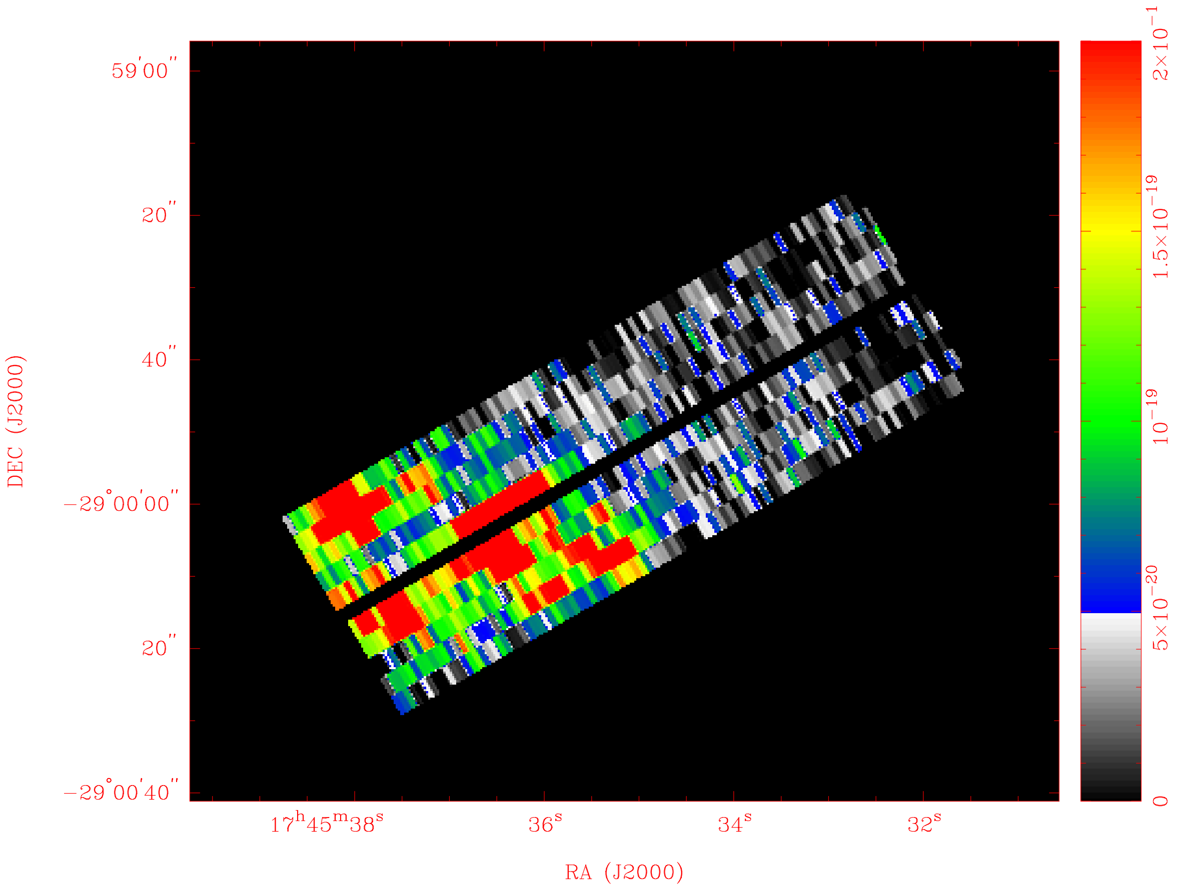

FIG. 3.26: The velocity-integrated $\mathrm{H_2}$ $1-0$ $\mathrm{S(1)}$ map of field W from the combined data cube. The color-scaled intensity level is indicated by the right-side wedge in units of $\mathrm{W\ m^{-2}\ arcsec^{-2}}$.

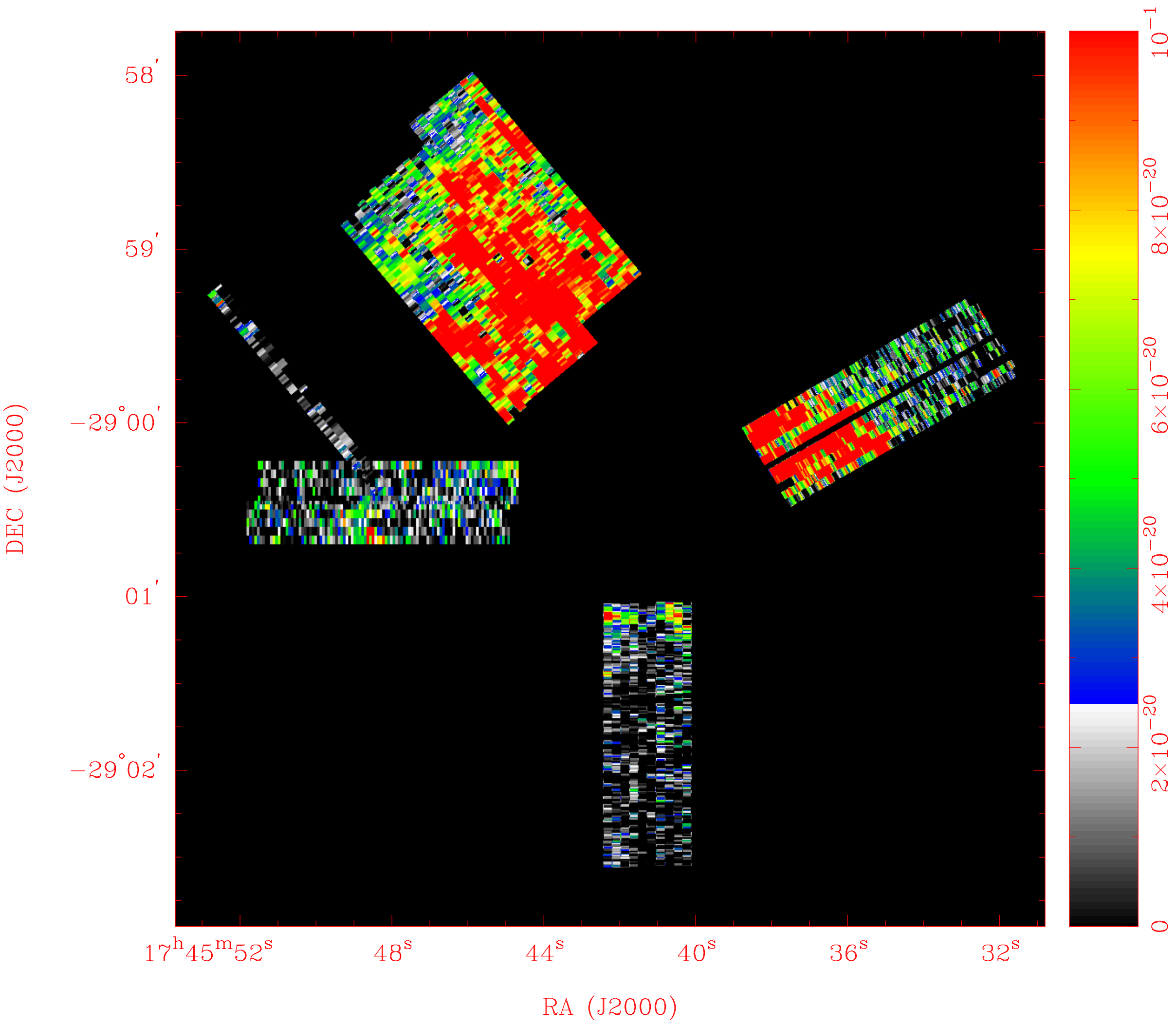

FIG. 3.27: The velocity-integrated H_2 $1-0$ $S(1)$ map of the entire surveyed region from the combined data cube. The color-scaled intensity level is indicated by the right-side wedge in units of $\mathrm{W\ m^{-2}\ arcsec^{-2}}$.

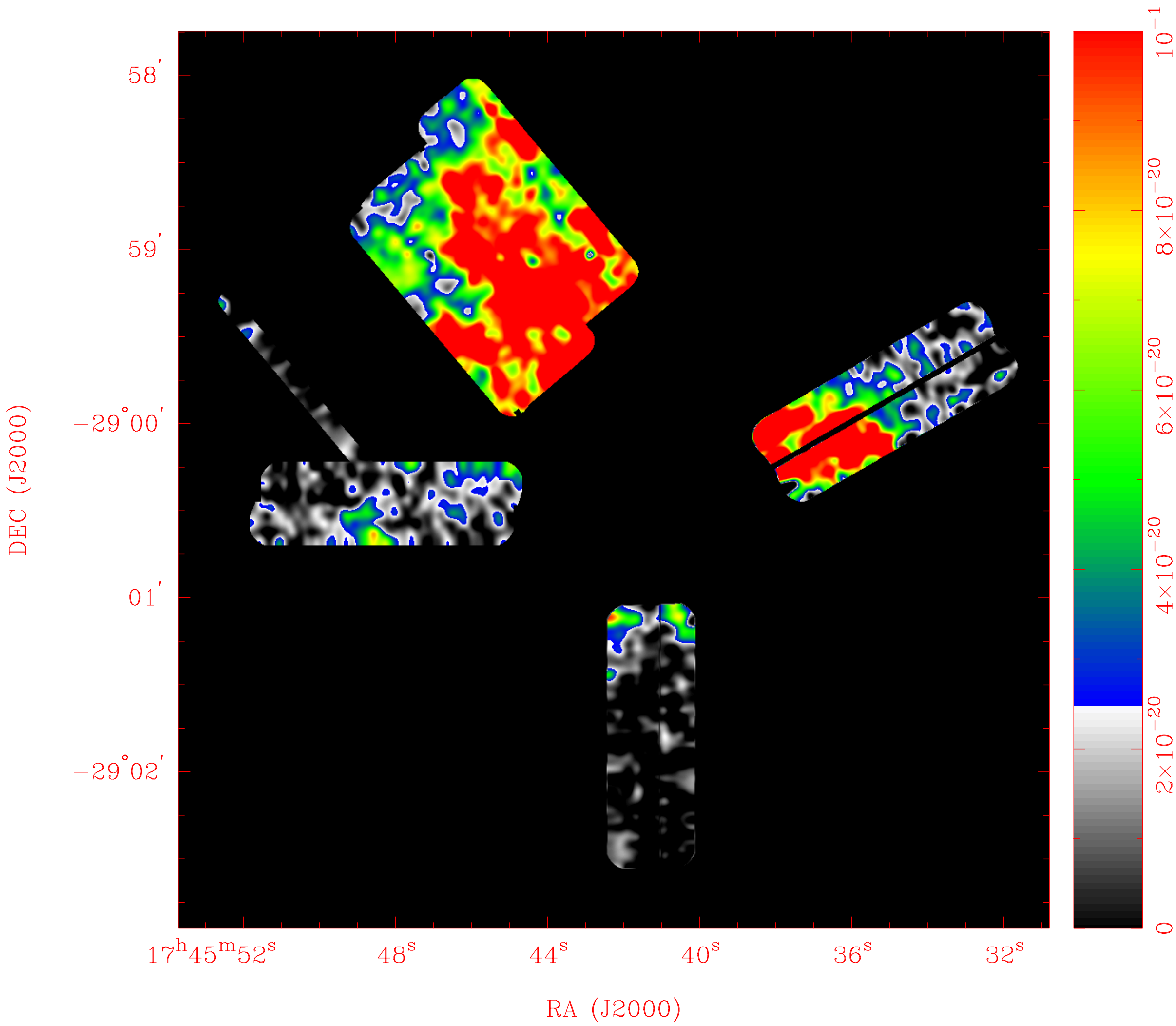

FIG. 3.28: The velocity-integrated $\mathrm{H_2}$ 1–0 $\mathrm{S(1)}$ map of the entire surveyed region: smoothed by $3''$-FWHM. The color-scaled intensity level is indicated by the right-side wedge in units of $\mathrm{W\ m^{-2}\ arcsec^{-2}}$.

REFERENCES

Burton M., & Allen D., 1992, Proc. Ast. Soc. Australia, 10, 55

Cox A.N., 2000, Allen's astrophysical quantities (4th ed.). AIP press, New York

Eyres S.P.S., Evans A., Geballe T.R., Salama A., & Smalley B., 1998, MNRAS, 298, L37

Hoffman W., Hudson J., Sharpe R.K., Grossman A.W., Morgan J.A., & Teuben P.J., 1996, in Jacoby G.H. & Barnes J., eds, PASP Conf. Ser. Vol. 101, Astronomical Data Analysis Software and Systems V, p. 436

Lee S., Pak S., Lee S.-G., Davis C.J., Kaufman M.J., Mochizuki K., & Jaffe D.T., 2005, MNRAS, in press (astro-ph/0410572)

McLean I., 1997, Electronic Imaging in Astronomy: Detectors and Instrumentation. Praxis publishing Ltd., Chichester

Rousselot P., Lidman C., Cuby J.-G., Moreels G., & Monnet G., 2000, A&A, 354, 1134

Sault R.J., Teuben P.J., & Wright M.C.H., 1995, in Shaw R.A., Payne H.E., & Hayes J.J.E., eds, PASP Conf. Ser. Vol. 77, Astronomical Data Analysis Software and Systems IV, p. 433

Chapter 4

Physical Properties from Emission Lines of Molecular Hydrogen‡

4.1 Introduction

In most cases H_2 line emission arises either from thermal excitation (e.g., by shock heating) or from non-thermal excitation by far-ultraviolet (hereafter far-UV) absorption (e.g., in photo-dissociation regions; PDRs). One can in principle distinguish between these two mechanisms by comparing near-infrared (near-IR) emission line intensities from different level populations. For example, the $\mathrm{H_2}\ 2-1\ \mathrm{S(1)}\ (\lambda = 2.2477\mu\mathrm{m})$ / $1-0\ \mathrm{S(1)}\ (\lambda = 2.1218\mu\mathrm{m})$ ratio has been an effective discriminant (Burton 1992). Fluorescent emission in a low-density PDR ($n_{H_2} < 5 \times 10^4\ \mathrm{cm}^{-3}$) should yield a ratio of about 0.6 because the UV-exited H_2 molecules de-excite solely by photon emission cascading down the vibrational in steps ladder, so lines from different vibrational levels are roughly the same intensity. A lower ratio is expected in a denser PDR environment, where collisions populate the energy levels (i.e. more thermalized; Black & van Dishoeck 1987; Sternberg & Dalgarno 1989; Lee

‡Part of this chapter was published;
Lee S., Pak S., Davis C.J., Herrnstein R.M., Geballe T.R., Ho P.T.P., & Wheeler J.C., 2003, MNRAS, 341, 509;
Lee S., Pak S., Davis C.J., Herrnstein R.M., Geballe T.R., Ho P.T.P., & Wheeler J.C., 2003, Astronomische Nachrichiten, 324, S1, 189

et al. 2005), or in a shock.

There are two basic types of shock; 'jump shock' or J-shock and 'continuous shock' or C-shock (see Hollenbach, Chernoff, & McKee 1989 and Draine & McKee 1993 for a review). A J-shock is formed in a highly ionized or weakly magnetized gas. Fluid parameters such as density and temperature undergo a discontinuous change (jump) at the shock front where the molecules may be dissociated. J-shocks (with velocities greater than about 24 $\mathrm{km\ s^{-1}}$) will completely dissociate the molecules (Kwan 1977); H_2 emission occurs from a warm, recombination plateau in the post-shock region. However, J-shocks typically produce low line intensities compared to C-shocks and $\mathrm{H_2\ 2{-}1\ S(1)\ /\ 1{-}0\ S(1)}$ line ratios as large as 0.5 are possible because of re-formation pumping (Hollenbach & McKee 1989). At lower shock velocities, below the H_2 dissociation speed limit, J-shocks may yield much lower line ratios; < 0.3 (Smith 1995). In a C-shock, where the magnetic field softens the shock front via ion-magnetosonic wave propagation so that the fluid parameters change continuously across the shock front, the H_2 dissociation speed limit is much higher ($\sim$ 45 $\mathrm{km\ s^{-1}}$; depending on the density and magnetic field strength in the pre-shock gas; Smith, Brand, & Moorhouse 1991). Smaller line ratios of about 0.2 are then predicted (Smith 1995; Kaufman & Neufeld 1996). In many astronomical sources the situation is more complicated, however, and a observed ratio may result from a mixture of shocks and PDRs (see e.g. Fernandes, Brand, & Burton 1997; Pak et al. 2004).

Kinematic information may also constrain the H_2 excitation mechanisms. In a pure PDR environment where the H_2 line emission generally arises from the stationary gas at the edges of neutral clouds illuminated by far-UV photons from early-type stars, the line profile has a narrow width (e.g. Lee et al. 2005). J-shocks also produce narrow lines since much of the IR emission is produced sufficiently far downstream that the gas has attained a velocity close to its final value. On the other hand, C-shocks produce much broader lines, broadened by the velocity range of emission with a significant contribution from velocities $<< v_{shock}$, since these shocks are non-dissociative and the gas radiates copiously before significant acceleration occurs (see Figure 4.1; Hollenbach, Chernoff, & McKee 1989). Table 4.1 summarizes the observable properties of each excitation mechanism.

To the Galactic center, Gatley et al. (1984) observed near-IR H_2 emission from the circum-nuclear disk (CND) and concluded that the H_2 molecules are mostly excited by collisions, while the results for larger regions (about 2×2 deg^2) by Pak, Jaffe, & Keller (1996a,b) are consistent with non-thermal excitation. The interpretation of Wardle, Yusef-

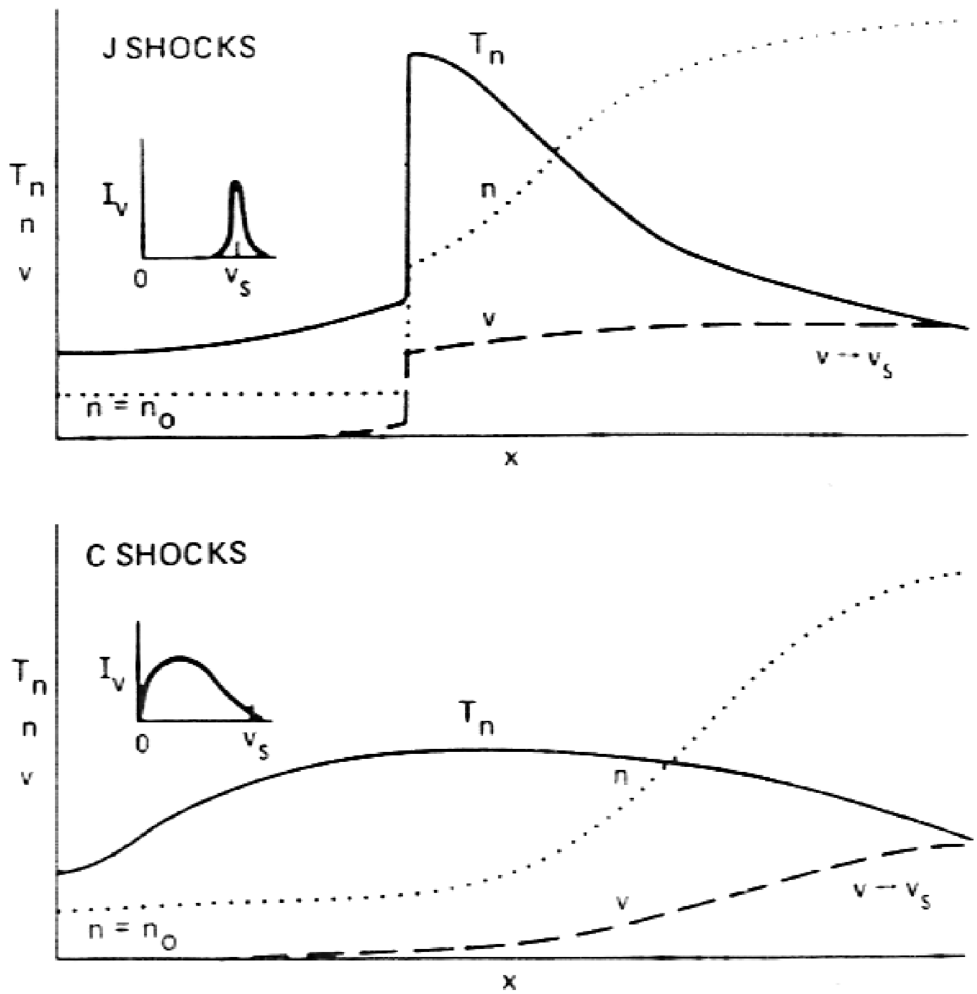

FIG. 4.1: J vs C shock structure and line profile (from Figure 1 of Hollenbach, Chernoff, & McKee 1989). T_n is the temperature of the neutral gas, n is the local hydrogen density, v is the flow velocity, and v_s is the shock velocity, in the frame of the ambient gas.

TABLE 4.1: Properties of H_2 Excitation Mechanisms

Excitation mechanism	Line width	Velocity shift (km s^{-1})	$2-1$ S(1) / $1-0$ S(1)
low density UV	narrow	0	0.6
high density UV	narrow	0	< 0.6
fast J-shock	narrow	> 24	< 0.5
slow J-shock	narrow	10–20	< 0.3
C-shock	broad	0–50	0.2

Zadeh, & Geballe (1999) and Yusef-Zadeh et al. (1999, 2001) that the H_2 line emission in Sgr A East is thermal is supported by the presence of the 1720 MHz OH masers. Several 1720 MHz OH masers, which have been found to be a good diagnostic of C-shock excitation (Frail et al. 1996; Wardle, Yusef-Zadeh, & Geballe 1999) have been detected to the south of Sgr A East and to the north of the CND (Yusef-Zadeh et al. 1996). It is therefore likely that Sgr A East is indeed driving shocks into the adjacent giant molecular clouds (GMCs) to the south and into the CND. However, the fields observed by Wardle, Yusef-Zadeh, & Geballe (1999) and Yusef-Zadeh et al. (1999, 2001) are restricted to the vicinity of the CND and cover only some of the regions where interaction of the Sgr A East shell with surrounding material is expected. Thus, more extensive observations are required to test their interpretations. In this chapter we report on measurements of the H_2 2–1 S(1) / 1–0 S(1) line ratio and simultaneously present velocity-resolved, near-IR H_2 line profiles at many positions along the boundary between Sgr A East and its surrounding molecular clouds to study the excitation mechanism of H_2 molecules and to understand the physical environment of the Galactic Center.

The observed H_2 emission lines can be used to estimate important physical parameters by comparing them with theoretical models. In a case of PDR, we can derive gas density and the strength of the incident UV field from the absolute line intensities and relative line ratios (e.g. Lee et al. 2005). Kinematic information from line shifts and line widths can make it possible to estimate shock velocities and determine the shock type, as discussed earlier.

4.2 Excitation Environment of Hydrogen Molecules

In this section, we examine the excitation mechanisms of H_2 emission from the inner 10 pc of the Galaxy. First, we investigate the velocity-integrated intensity of the $1-0$ S(1) line and the $2-1$ S(1) / $1-0$ S(1) line ratio from the northeastern part of the inner 10 pc. Sgr A East is believed to be interacting with its surrounding molecular clouds in this region and the H_2 $1-0$ S(1) emission is so bright (Pak, Jaffe, & Keller 1996a) that the probability of detection of weak H_2 $2-1$ S(1) lines is expected to be high. We assume that the line ratios in this region are representative of the ratios elsewhere.

Kinematics is also studied, over the whole regions of the central 10 pc, by comparing the H_2 line profiles with those of ammonia (NH_3) emission, which are observed by McGary, Coil, & Ho (2001). H_2 line profiles trace hot (~ 2000 K) gas and NH_3 cool ($\lesssim 100$ K; cool in the standard of the Galactic center) gas. Thus, in a case of shock environment, we can assume that the H_2 emission traces post-shocked gas and the NH_3 pre-shocked gas in the molecular clouds.

4.2.1 Integrated Line Intensity and H_2 $2-1$ S(1) / $1-0$ S(1) Line Ratio

We observed both the H_2 $1-0$ S(1) and the H_2 $2-1$ S(1) spectra at the position of Slit NW12 in the northern field (see Figure 4.2). "NW12" means the relative position of the slit (12 arcsec towards the north-west) from the base position of the slit-scanning observations to the northern field. Slit NW12 is one of the slit positions which is possibly brightest in the H_2 $2-1$ S(1) line. We did not scan the other positions in the H_2 $2-1$ S(1) emission since it takes much more observing time than the H_2 $1-0$ S(1) scan. As in Figure 4.3, bright H_2 $1-0$ S(1) emission lines are observed along the slit and also H_2 $2-1$ S(1) lines are detected at some positions although they are much weaker than the $1-0$ S(1) lines and so were averaged over 3.4 arcsec (4 pixels) along the slit to improve the signal-to-noise (S/N) ratios.

Integrated line intensities are calculated by fitting the lines with one or two Gaussian profiles and the results are shown in Table 4.2. Near-IR emission from the Galactic centre is attenuated by interstellar material in the foreground (mostly 4 – 8 kpc from the Galactic centre) and by material in the Galactic centre itself. Since we believe that the H_2 line emission originates from the surface of the cloud, we ignore the latter (Pak, Jaffe, & Keller 1996a,b) and correct only for foreground extinction; which we assume to be $A_K = 2.5$ mag

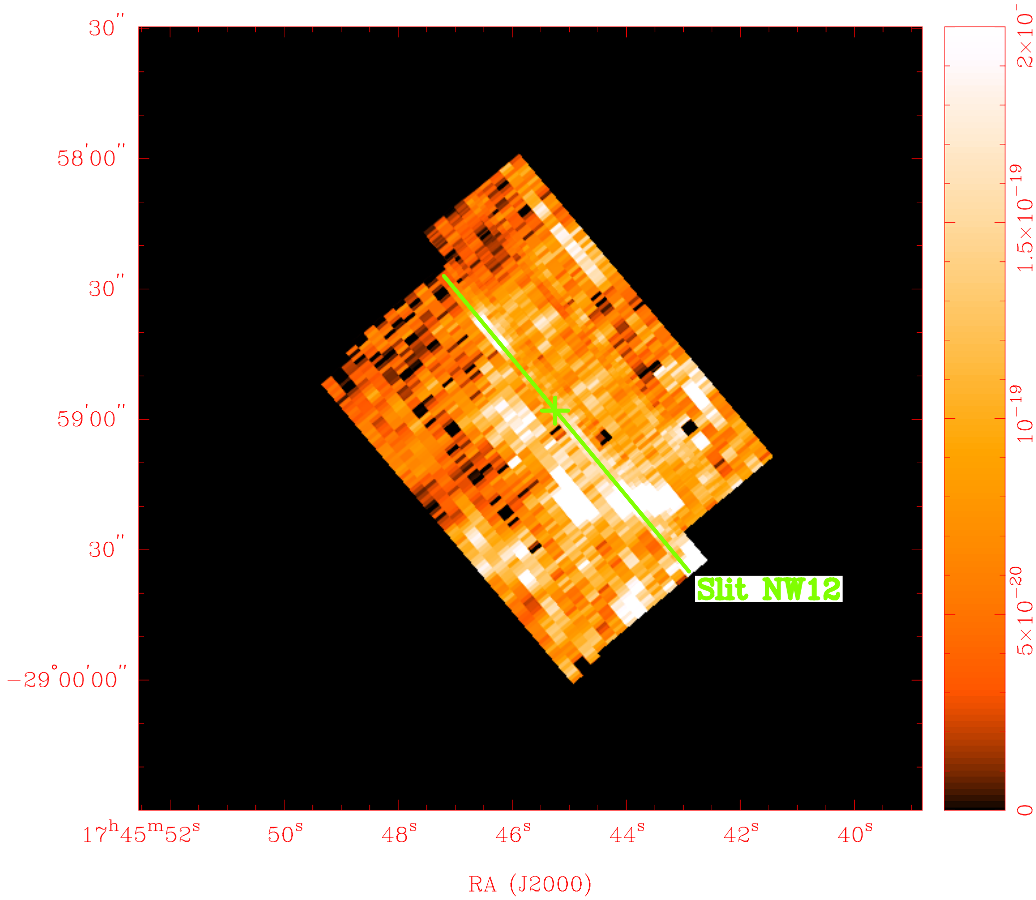

FIG. 4.2: Position of Slit NW12 in the north-eastern field. Integrated intensity map of $\mathrm{H_2}$ 1–0 S(1) line is presented with the intensity scale at the right of the figure. Slit position NW12 is indicated by a solid line. The reference position ($\alpha = 17^{\mathrm{h}}45^{\mathrm{m}}45\overset{\mathrm{s}}{.}3$, $\delta = -28^\circ58'58''$; J2000) is marked by a cross.

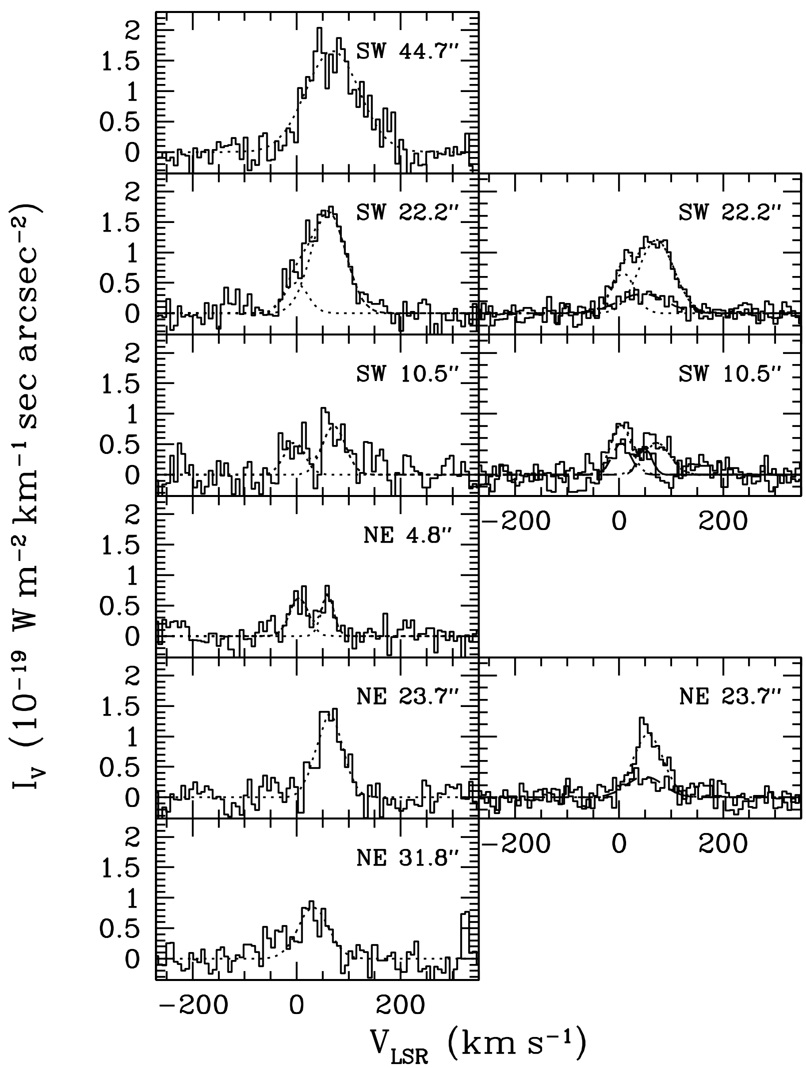

FIG. 4.3: H_2 $1-0$ S(1) and H_2 $2-1$ S(1) spectra from six positions along Slit NW12. Indicated positions are relative to $\alpha = 17^h45^m45\overset{s}{.}3$, $\delta = -28°58'58''$ (J2000), which is marked in Figure 4.2. Left panels show the H_2 $1-0$ S(1) spectra. The right three panels present both the H_2 1–0 S(1) and H_2 2–1 S(1) spectra from the positions where H_2 2–1 S(1) emission is detected; these are averaged over 3.4 arcsec on the sky to improve the S/N ratios. The dotted lines are Gaussian fits to the observed line profiles. The spectra are not corrected for instrumental broadening.

TABLE 4.2: H_2 Line Intensities and Ratios Measured along Slit NW12

Position[a]	$I_{\mathrm{H_2\ 1\text{–}0\ S(1)}}$ [b]	$I_{\mathrm{H_2\ 2\text{–}1\ S(1)}}$ [b,c]	$2-1$ S(1) / $1-0$ S(1)[c]
	($\mathrm{W\ m^{-2}\ arcsec^{-2}}$)		
SW $44.7''$	2.14 ($\pm$0.18) $\times 10^{-17}$	...	$< 0.1^d$
SW $22.2''$	1.66 ($\pm$0.34) $\times 10^{-17}$	2.99 ($\pm$0.83) $\times 10^{-18}$	0.27 ($\pm$0.07)
SW $10.5''$	7.01 ($\pm$1.84) $\times 10^{-18}$	3.70 ($\pm$1.12) $\times 10^{-18}$	0.51 ($\pm$0.17)
NE $4.8''$	4.82 ($\pm$0.89) $\times 10^{-18}$	...	$< 0.6^d$
NE $23.7''$	8.80 ($\pm$1.08) $\times 10^{-18}$	3.67 ($\pm$0.89) $\times 10^{-18}$	0.40 ($\pm$0.12)
NE $31.8''$	6.18 ($\pm$1.10) $\times 10^{-18}$	...	$< 0.5^d$

[a] Positions are relative to $\alpha = 17^{\mathrm{h}}45^{\mathrm{m}}45\overset{\mathrm{s}}{.}3,\ \delta = -28°58'58''$ (J2000), which is marked in Figure 4.2.

[b] Corrected for the interstellar extinction assuming A_K = 2.5 mag (see text).

[c] Averaged over 3.4 arcsec on the sky to improve the S/N ratios.

[d] $\mathrm{H_2}$ $2-1$ S(1) line is not detected with our sensitivity. A 3-σ upper limit is presented.

(Catchpole, Whitelock, & Glass 1990).

The $\mathrm{H_2}$ 2–1 S(1) line was detected in slit NW12 at regions centered 23.7 arcsec north-east (NE $23\overset{''}{.}7$), 10.5 arcsec south-west (SW $10\overset{''}{.}5$), and 22.2 arcsec south-west (SW $22\overset{''}{.}2$) relative to the reference position ($\alpha = 17^{\mathrm{h}}45^{\mathrm{m}}45\overset{\mathrm{s}}{.}3,\ \delta = -28°58'58''$; J2000). From these data we measured line ratios ($\mathrm{H_2}$ $2-1$ S(1) / $1-0$ S(1)) of 0.40 ± 0.12, 0.51 ± 0.17, and 0.27 ± 0.07, respectively (see Table 4.2). At other locations along the slit only the $\mathrm{H_2}$ $1-0$ S(1) line was detected, with 3σ upper limits to the ratio of 0.5, 0.6, and 0.1 at offsets of 31.8 arcsec north-east (NE $31\overset{''}{.}8$), 4.8 arcsec north-east (NE $4\overset{''}{.}8$), and 44.7 arcsec south-west (SW $44\overset{''}{.}7$) along Slit NW12, respectively.

As mentioned in Section 4.1, a $\mathrm{H_2}$ 2–1 S(1) / 1–0 S(1) line ratio of about 0.6 is expected in a low-density PDR ($\mathrm{n(H_2)} < 5 \times 10^4\ \mathrm{cm^{-3}}$) and a lower ratio in a denser PDR (Black & van Dishoeck 1987). In a shocked environment, line ratios as large as 0.5 are possible in J-shocks (Hollenbach & McKee 1989) although at lower shock velocities, below the $\mathrm{H_2}$ dissociation speed limit (about 24 $\mathrm{km\ s^{-1}}$), J-shocks may yield much lower line ratios; < 0.3 (Smith 1995). In a case of C-shocks, however, smaller line ratios of about 0.2 are predicted (Smith 1995; Kaufman & Neufeld 1996).

From the observed line ratios (as shown in Table 4.2) alone we are not able to unambiguously distinguish between excitation mechanisms. Our results in general can either be explained by fast J-shocks or a dense PDR, or by a combination of fluorescence and either C-shocks or slow J-shocks, since the higher line ratios associated with fluorescence will be tempered by the low $\mathrm{H_2}$ $2{-}1$ $\mathrm{S(1)}$ intensities associated with collisional excitation in shocks. Even with the exceptional ratio, < 0.1, at position SW $44\farcs7$, either a very dense PDR or very cool (far downstream) post-shock gas is possible.

We cannot reach a conclusion about the excitation mechanism based only on the observed line ratios. However, we can constrain the mechanism by 'excluding' improbable candidates, based on all of the observed facts (including the kinematic information in the next section). First, each of a pure PDR with low density, slow J-shocks, and C-shocks is excluded by the observed, moderate, $2-1$ $\mathrm{S(1)}$ / $1-0$ $\mathrm{S(1)}$ ratios. Also the scenario of fast J-shocks should be excluded since J-shocks typically produce lower $\mathrm{H_2}$ $1-0$ $\mathrm{S(1)}$ line intensities ($\lesssim 10^{-4}$ $\mathrm{ergs\ s^{-1}\ cm^{-2}\ sr^{-1}}$ or $\lesssim 3 \times 10^{-18}$ $\mathrm{W\ m^{-2}\ arcsec^{-2}}$) than our observed results (5 – 20 $\times 10^{-18}$ $\mathrm{W\ m^{-2}\ arcsec^{-2}}$; Table 4.2), except at very high gas densities of $\gtrsim 10^6 \mathrm{cm^{-3}}$ (Hollenbach & McKee 1989).

4.2.2 Line Profile: Comparing H_2 and NH_3

To distinguish between the H_2 excitation mechanisms, we can also consider the kinematic information obtained from the observed line profiles. In a pure PDR or in a J shock the H_2 line profiles are narrow, but in a PDR the line is un-shifted with respect to the cloud velocity, whereas in a J-shock it is shifted by up to $\sim 20\ \mathrm{km\ s^{-1}}$. In a C-shock the profiles are broad extending from the ambient cloud velocity to the shock velocity.

To investigate the kinematic properties of both hot gas and cool gas at the same time, we compare the high resolution $\mathrm{H_2}$ $1{-}0$ $\mathrm{S(1)}$ line profiles obtained from our observations with the NH_3(3,3) line profiles observed by McGary, Coil, & Ho (2001) using the National Radio Astronomy Observatory (NRAO)'s Very Large Array (VLA) telescope (their data are seen in Figure 4.4), at eight representative positions where both the H_2 and NH_3 measurements were made and bright emission lines of both molecules are detected (Figure 4.5). Since our H_2 data have much higher angular resolution ($\sim$ 2 arcsec in FWHM depending on seeing condition) than the NH_3 data (with a beam size of $\sim 15'' \times 13''$), the spectra in Figure 4.6 are convolved with a circular Gaussian beam with a FWHM of $30''$ for both H_2 and NH_3 to

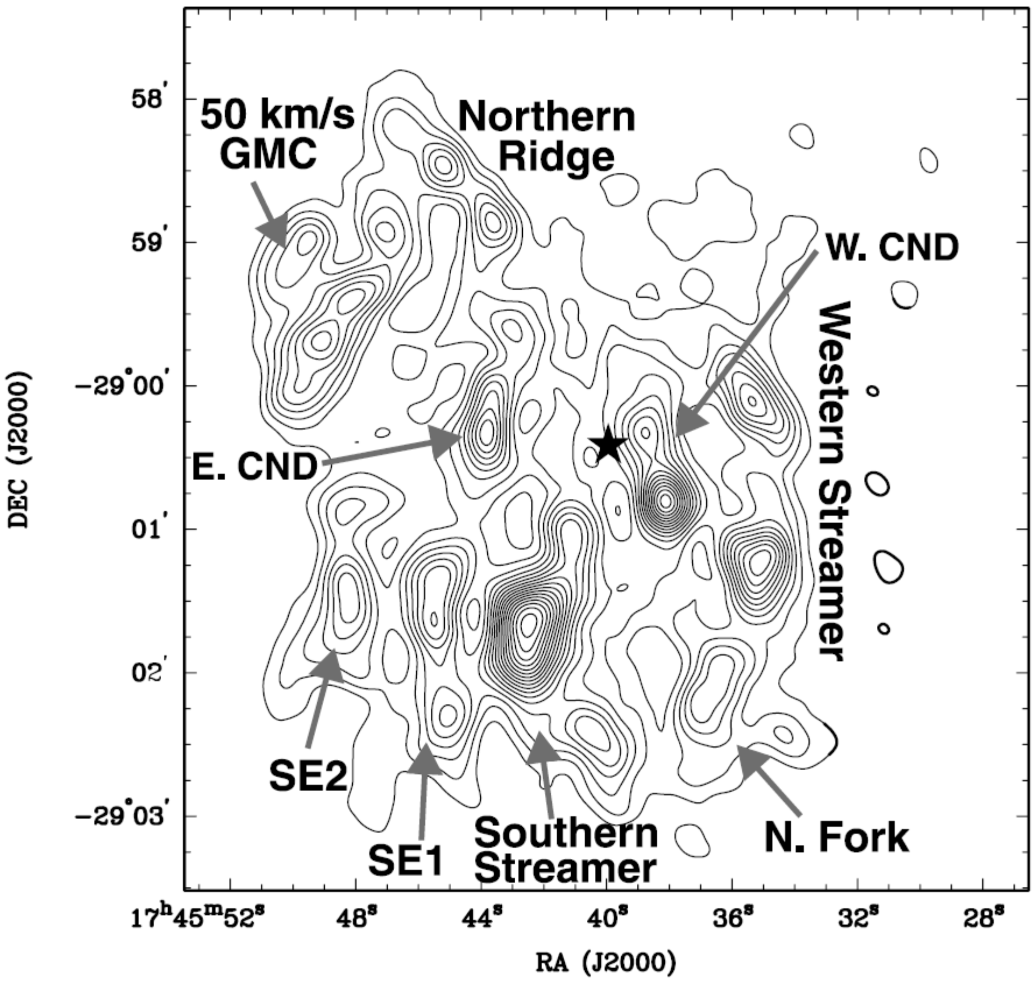

FIG. 4.4: Velocity-integrated map of NH_3(3,3) with labels of main molecular features in the central 10 pc (from McGary, Coil, & Ho 2001 and Herrnstein & Ho 2005). Contours are in steps of $1.32\ \mathrm{Jy\ beam^{-1}\ km\ s^{-1}}$ and the RMS noise $\sigma = 0.33\ \mathrm{Jy\ beam^{-1}\ km\ s^{-1}}$ (the beam size is $\sim 15'' \times 13''$). The position of Sgr A* is indicated by a star. Note that SE2 is also known as the molecular ridge.

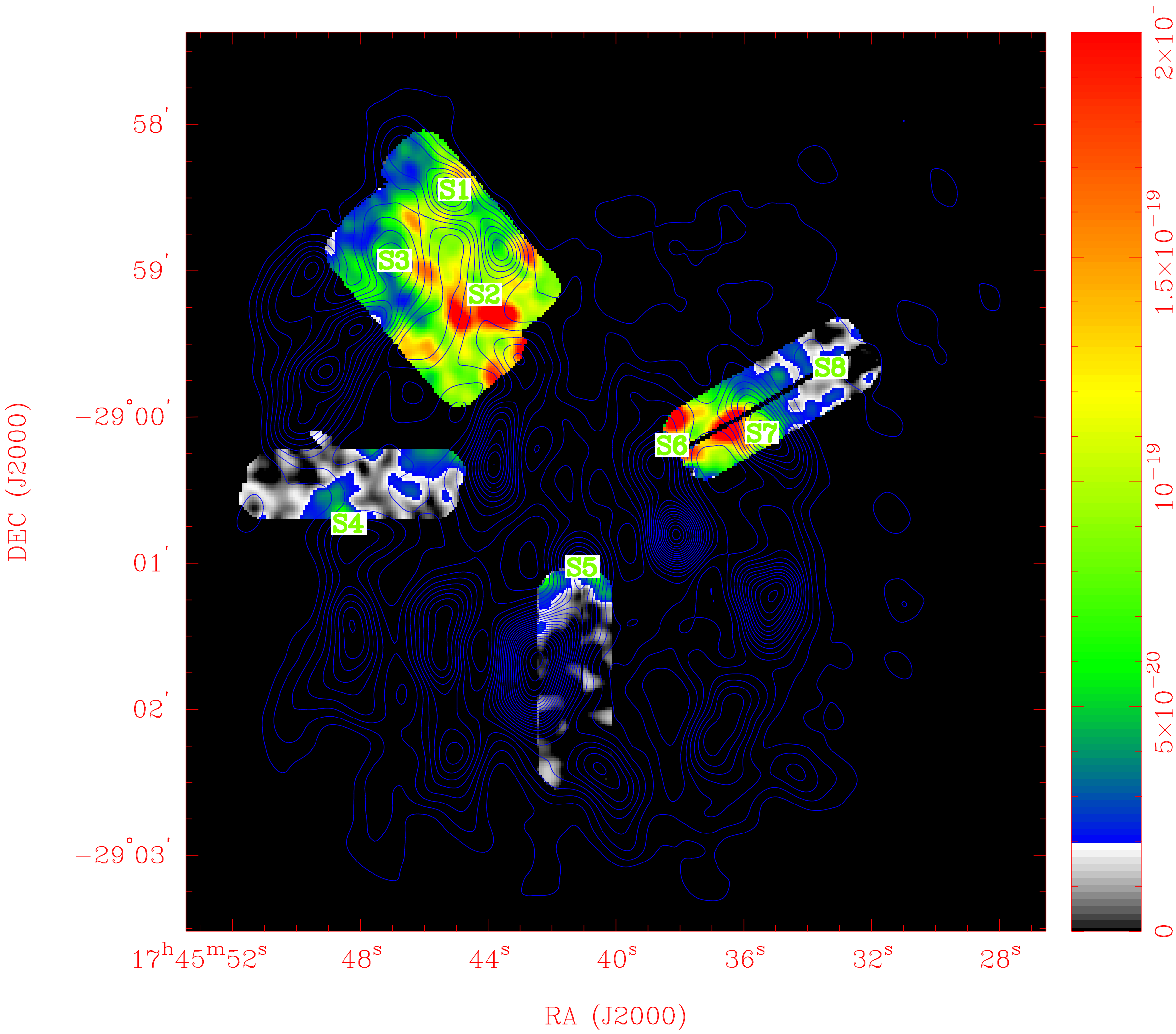

FIG. 4.5: Positions of the spectra of H_2 $1-0$ $S(1)$ and NH_3(3,3) in Figure 4.6. 8 positions are marked on the integrated intensity map of H_2 $1–0$ $S(1)$ line emission, which is smoothed by Gaussian with FWHM = 5″ and the color-scaled intensity level is indicated by the right hand bar in units of $\mathrm{W\ m^{-2}\ arcsec^{-2}}$. The overlaid contours show the velocity-integrated NH_3(3,3) emission map from (McGary, Coil, & Ho 2001), which has a beam size of $\sim 15'' \times 13''$ with a position angle of $-0.12°$ from north to east. The contour levels are in intervals of 3-σ (the RMS noise $\sigma = 0.33$ Jy beam^{-1} km s^{-1}).

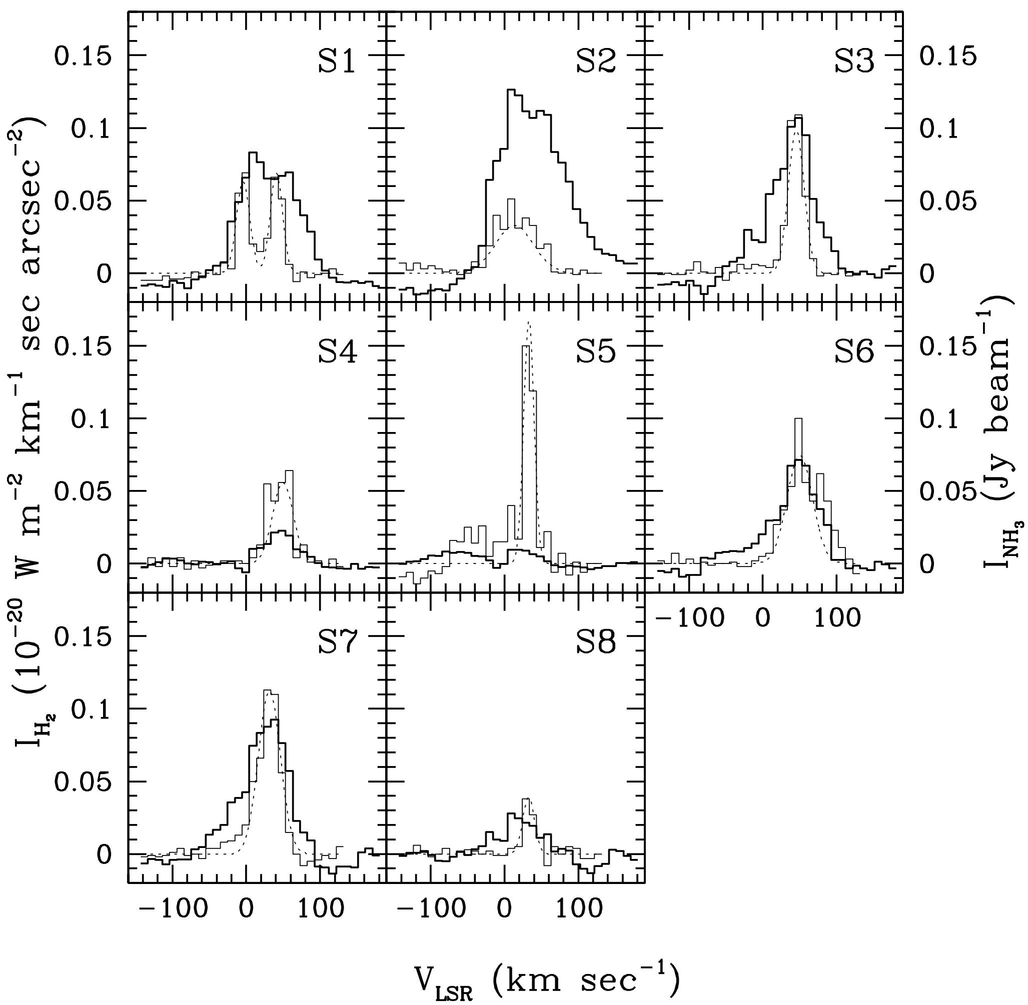

FIG. 4.6: Spectra of H_2 $1-0$ $S(1)$ and NH_3(3,3) at the positions marked in Figure 4.5. Thick solid lines are the H_2 $1-0$ $S(1)$ spectra, for which the intensity scale is indicated on the left-side, and thin solid lines NH_3(3,3), of which the scale is on the right-side. The dotted lines are Gaussian fits to the NH_3(3,3) line profiles. The spectra are convolved of circular Gaussian beam with a FWHM of $30''$ and not corrected for instrumental broadening in velocity.

eliminate any difference in beam dilution effect. The convolved beam size ($30''$) corresponds to 1.2 pc at a distance of 8.0 kpc (Reid 1993) and is the typical size of NH_3 clumps in the Galactic center molecular clouds.

For most spectra in Figure 4.6, the H_2 line widths are much larger (typically 50 – 100 $\mathrm{km\ s^{-1}}$) than the NH_3 line widths (typically 20 – 40 $\mathrm{km\ s^{-1}}$). Instrumental broadening, however, should be corrected for a more reliable comparison. We can calculate an intrinsic line width $\sigma_0 = \sqrt{\sigma_{obs}^2 - \sigma_{instrument}^2}$ assuming both the intrinsic line profile and the instrumental profile are Gaussian (see Sohn et al. 2001 for example). In the case of the $\mathrm{H_2}\ 1{-}0\ \mathrm{S(1)}$ lines, because the velocity resolution ($\sim 18\ \mathrm{km\ s^{-1}}$) is much less than the observed line width, correction for the instrumental broadening is only a few $\mathrm{km\ s^{-1}}$. On the other hand in the case of NH_3 lines, according to McGary & Ho (2002), the observed line widths may greatly overestimate the intrinsic line widths depending on the intrinsic line width (in a range of 1 – 15 $\mathrm{km\ s^{-1}}$) because of a blending of five hyperfine lines. They recovered the intrinsic line widths using the observed line width and intensity of two NH_3 rotation inversion transitions and the resulting mean width is about 15 $\mathrm{km\ s^{-1}}$. We can see an example of this hyperfine lines in Figure 4.6; for the NH_3 spectrum S5, small peaks around the highest one are satellite hyperfine lines, and the measured line width of the main line is 17 $\mathrm{km\ s^{-1}}$ which is consistent with the mean value of McGary & Ho (2002). Thus we can conclude that, intrinsically, the H_2 line widths are much larger than the NH_3 line widths, by as much as 30 – 80 $\mathrm{km\ s^{-1}}$.

This suggests shock excitation and turbulent motions in the H_2 gas and tends to exclude the pure fluorescence models. As an example of a pure PDR, the H_2 spectra observed by Lee et al. (2005) from Hubble V (HII region) of NGC 6822 (dwarf irregular galaxy in the Local group) using the echelle grating in the Cooled Grating Spectrometer 4 (CGS4) at the United Kingdom Infrared Telescope (UKIRT) are presented in Figure 4.7. Observed line profiles are very narrow (FWHM $\lesssim 20\mathrm{km\ s^{-1}}$) and cannot be resolved by the instrumental resolution of 17 and 20 $\mathrm{km\ s^{-1}}$ for $\mathrm{H_2}\ 1-0\ \mathrm{S(1)}$ and $\mathrm{H_2}\ 2-1\ \mathrm{S(1)}$, respectively. This is consistent with the intrinsic H_2 profiles being identical to the CO profiles (FWHM = 4–9 $\mathrm{km\ s^{-1}}$) observed by Wilson (1994) and Israel et al. (2003). The velocities of the H_2 line centers (between -36 and -48 $\mathrm{km\ s^{-1}}$ in V_{LSR}) also show no significant shift from those of the CO lines (about -41 $\mathrm{km\ s^{-1}}$; Wilson 1994; Israel et al. 2003). Hence, the kinematic data support a non-thermal excitation mechanism for H_2 molecules in NGC 6822 Hubble V.

The H_2 emission traces hot (~ 2000 K) gas and the NH_3 cool ($\lesssim\ 100$ K) gas. Thus, if we assume that shocks are driven by Sgr A East into cold molecular gas, whose velocities

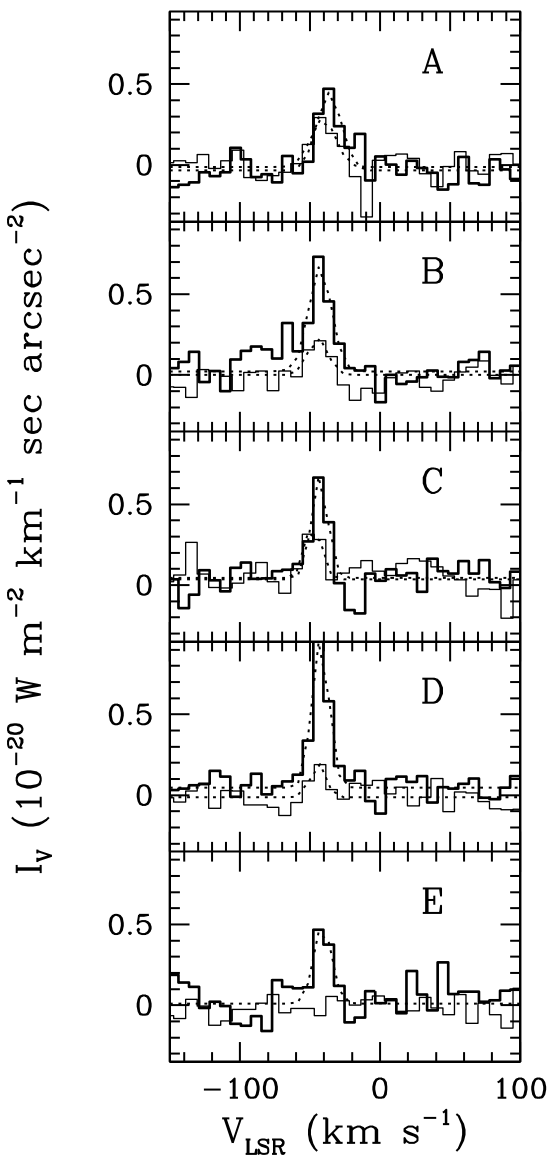

FIG. 4.7: Sample spectra of pure PDR H_2 emission: NGC 6822 Hubble V (from Lee et al. 2005). Thick lines are H_2 $1-0$ $S(1)$ and thin lines H_2 $2-1$ $S(1)$ spectra from their high resolution echelle observations. The position of each spectrum labelled by A–E is indicated in Lee et al. (2005). Each spectrum is averaged over 1.8 arcsec on the sky to improve the S/N ratios. The dotted lines are Gaussian fits to the observed line profiles. It should be noted that the spectra are not corrected for instrumental broadening of ~ 17 km s^{-1} for H_2 $1-0$ $S(1)$ and ~ 20 km s^{-1} for H_2 $2-1$ $S(1)$, respectively. In each region, the lines are therefore spectrally unresolved.

are given by the NH_3 data, then fast J-shocks seem to be inconsistent with our results, due to the low peak velocities of the H_2 lines relative to the molecular clouds (see Figure 4.6). Instead, the wide line profiles and low peak velocities indicate C-shock excitation. However, the high values of the line ratio at some positions along Slit NW12 (see Table 4.2) point to a fluorescent component to the excitation in some locations. A combination of C-shocks and fluorescence (see e.g. Fernandes, Brand, & Burton 1997) is therefore a more reasonable explanation for the H_2 excitation.

The measured line widths (50 – 100 $\mathrm{km\ s^{-1}}$), however, may be too large to be broadened by C-shocks which have breakdown velocities of $\lesssim 50\mathrm{km\ s^{-1}}$ in typical molecular clouds (Draine, Roberge, & Dalgarno 1983; Hollenbach, Chernoff, & McKee 1989; Smith & Brand 1990). If a C-shock were to be non-dissociative with such a high shock velocity, a very strong ($\gtrsim$ a few mG) magnetic field should be needed (Smith, Brand, & Moorhouse 1991). Alternatively, a mixture of C-shocks and multiple J-shocks with various shock velocities may explain the unusually broad line widths. For example, in the case of the supernova remnant (SNR) IC443, very broad ($\gtrsim 50\mathrm{km\ s^{-1}}$) CO lines are observed and van Dishoeck, Jansen, & Phillips (1993) suggested a mixture of slow C-shocks and fast J-shocks which have various shock velocities in an inhomogeneous medium due to different decelerations and deflection of shock directions; many different shocked emission lines are then blended into a single, very broad, line. The co-existence of C-shocks and J-shocks in IC443 are also suggested by some other authors like Burton et al. (1990); Wang & Scoville (1992); Inoue et al. (1993). In the scenario of a mixture of C-shocks and J-shocks, we may need no fluorescence since the differences in shock properties can explain the moderate $2{-}1\ \mathrm{S}(1)$ / $1{-}0\ \mathrm{S}(1)$ line ratios and the spatial variation in the ratio as mentioned at the end of Section 4.2.1. As a matter of fact, we cannot establish whether nearby stars are the source of the UV flux due to the lack of information on where or how many early type stars there are in the region.

Out of the bright synchrotron emission shell of Sgr A East, a weak extended halo of radio emission surrounds the shell (see the 6 cm continuum image in Figure 1.3). This diffuse halo is more evident in 20 cm emission and believed to be non-thermal (Yusef-Zadeh & Morris 1987; Pedlar et al. 1989). In Figure 1.4, we can see this halo also in X-ray. These radio and X-ray observations imply that a fraction of gas in the halo is ionized although the amount of the ionized gas should be much smaller than in the synchrotron shell. As we will see in the next chapter, the shocked H_2 emission extends out of the synchrotron shell and further into the surrounding molecular clouds with a similar extent with the diffuse halo. If the radio and

X-ray emitting gas in the halo is ionized by the shocks which also excite H_2 molecules, then our second model of shock may be more preferred since this model includes J-shocks which can dissociate and even ionize gas. However, it is also possible that the gas in the halo is ionized by UV photons from the hot gas in the Sgr A East shell or from massive stars in the central parsecs.

In summary, no single H_2 excitation mechanism (UV in low-density gas, UV in dense gas, fast J-shock, slow J-shock, or C-shock) can explain all of the observational results (integrated H_2 1–0 $S(1)$ line intensity, 2–1 $S(1)$ / 1–0 $S(1)$ line ratios, very broad H_2 line profiles, and low peak velocities relative to those of NH_3). Instead a combination of them can be a more reasonable interpretation; a combination of fluorescence and C-shocks in very strong magnetic fields, or a mixture of C-shocks and fast J-shocks. In any case, we can conclude that shocks play a major role in the H_2 excitation in the central 10 pc of the Galaxy.

4.3 Shock Velocity of Sgr A East from Line Profile

In this section, we derive the velocities of shocks driven by Sgr A East into the surrounding molecular clouds based on the H_2 $1-0$ $S(1)$ line profiles. Following the conclusions on the H_2 excitation mechanism in the previous section, two different models are assumed for the shock properties; a planar C-shock in a very strong magnetic field and a mixture of C-shocks and J-shocks.

4.3.1 Density and Clumpiness of the Molecular Clouds

At first, we need to know the density conditions of pre-shock gas in the molecular clouds. Shock velocities depend on the density given a constant ram pressure, $\rho\, v_{shock}^2$, over the whole shock front of Sgr A East assuming a symmetric explosion.

There are many observational studies on the gas density of molecular clouds in the Galactic center. Various density-sensitive molecular species such as CS, H_2CO, and HC_3N were observed to derive a mean number density of $n_{H_2} \sim 10^4$ cm^{-3} (see Güsten & Philipp 2004 for a review). However, some observations, particularly with high spatial resolutions (less than a few parsecs), reported higher density of $\sim 10^5$ cm^{-3} (e.g. Güsten & Henkel 1983; Paglione et al. 1998; Herrnstein & Ho 2005), and clumpy structures of molecular clouds may reconcile the differences (Güsten & Philipp 2004). For example, Walmsley et al. (1986) observed the GMC M-0.13-0.08 (also known as the '$+20\ \mathrm{km\ s^{-1}}$ cloud') in HC_3N and found that 20 per cent of the cloud mass is contained in compact clumps with high density of $n_{clump} \sim 10^5\ \mathrm{cm^{-3}}$ which are scattered in a low density medium with $n_{inter-clump} \sim 5 \times 10^3\ \mathrm{cm^{-3}}$.

As seen in Figure 4.5, the sizes of NH_3 clumps in the molecular clouds are about 20 – 50 arcsec (0.8 – 2 pc). The bright patches in H_2 emission are much smaller than NH_3; about 10 – 20 arcsec (0.4 – 0.8 pc). However, the angular resolutions of the observations seem not to be able to resolve the smallest clumps, of which the sizes are expected to be still smaller as discussed in the followings.

The north-eastern field shown in Figures 4.2 & 4.5 is a region where two different molecular clouds are superimposed along the line-of-sight (the GMC M-0.02-0.07 and the northern ridge; McGary, Coil, & Ho 2001). The spectrum S1 in Figure 4.6 is a representative example of them; the NH_3 peak at $v_{LSR} \simeq +50\ \mathrm{km\ s^{-1}}$ is from the GMC M-0.02-0.07 (also known as the '$+50\ \mathrm{km\ s^{-1}}$ cloud') and the other peak at $v_{LSR} \simeq 0\ \mathrm{km\ s^{-1}}$ is from the northern ridge. The H_2 line profile of S1 also show two peaks, each of which is emitted from the surfaces of two different clouds, but shocked by the same source, Sgr A East. We can see two-peaks H_2 profiles like this also in Figure 4.3, especially at the positions SW $10''\!.5$ and NE $4''\!.8$ on Slit NW12. It should be noted that the H_2 spectra in the left column of Figure 4.3 are not averaged over some area larger than the angular resolution of the observations (about 2 arcsec depending on the seeing condition).

The fact that the two H_2 velocity components overlap along the line-of-sight with roughly equal brightness seems somewhat unlikely, since one must be attenuated by the foreground molecular cloud. The equality might be explained by clumpiness of the foreground cloud, regardless of which one is in the foreground, where a small filling factor of high density clumps are embedded within a less dense medium (Burton, Hollenbach, & Tielens 1990). The size of such clumps should be smaller than our resolution of ~ 2 arcsec (~ 0.1 pc at the distance of 8.0 kpc to the Galactic center).

These expected size scales of H_2 clumps in the Galactic center agree with other observations to the SNRs IC443 (0.02 – 0.07 pc; Burton et al. 1988; Richter, Graham, & Wright 1995) or 3C 391 (~ 0.1 pc; Reach et al. 2002). Theoretically, size of a warm zone (with temperature of a few 10^3 K) in shocked H_2 gas is predicted to be $\lesssim 0.02$ pc in models (van Dishoeck, Jansen, & Phillips 1993). The smallest dense cores in molecular clouds are reported to be be 10^{-4} – 10^{-3} pc (Garay, Moran, & Reid, 1987; Churchwell et al., 1987).

4.3.2 Model I: A Planar C-shock in a Strong Magnetic Field

The simplest assumption is that a planar C-shock is driven by Sgr A East into the surrounding molecular clouds with a mean density of 10^4 cm^{-3}. As seen in Figure 4.1, a C-shock produces a broad line profile which extends up to the shock velocity. In C-shocks the radiation is emitted as the gas is being heated in the shock front, while in J-shocks it is given off after the impulsive heating event. These C-shocks are non-dissociative and molecular cooling is available and sufficiently intense. Therefore the neutral gas radiates copiously before significant acceleration or neutral compression occurs. An observer of an approaching or receding C-shock (with respect to the pre-shock gas) sees relatively low excitation lines, broadened by the velocity range of emission with a significant contribution from velocities much lower than V_s (Hollenbach, Chernoff, & McKee 1989 and references therein).

Therefore the speed of a C-shock can be determined from the velocity corresponding to the edge of the line profile, hereafter denoted by V_{max}. According to detailed models for the line profiles of C-shocks (e.g. Smith & Brand 1990), the full-width-at-zero-intensity (FWZI) of a line is 90 per cent of the shock velocity. Because line profiles from different regions are often superimposed, the low velocity edge of the profile of an individual shock, which is essentially the pre-shock velocity, is not always obvious. Thus, instead of using the FWZI to determine the speed of the C-shock, we use V_{max,H_2} of a post-shock H_2 profile and V_{0,NH_3}, the velocity of the pre-shock gas as traced by the NH_3 emission. Thus we determine the line-of-sight velocity of the C-shock ($V_{s,LOS}$) as follows.

$$V_{s,LOS} = (V_{max,H_2} - V_{0,NH_3})/0.9 \tag{4.1}$$

In the Galactic center, large turbulent motions in the pre-shock gas are evident in the NH_3 line profiles, whose widths are typically 15 km s^{-1} (McGary & Ho 2002). This results in significant uncertainties to the measurements. If we assume that the pre-shock molecular cloud is composed of gas blobs in random motions with a maximum velocity of V_b as in Figure 4.8, a relative shock velocity ($V_s{}'$) in the frame of each of the example gas blobs, A and B, is given by $V_{s,A}{}' = V_s + V_b$ and $V_{s,B}{}' = V_s - V_b$, respectively. Then, in the frame of the mean velocity of the pre-shock cloud, V_{max} of a post-shock line is given for gas blob A,

$$V_{max,A} = V_{s,A}{}' - V_b = V_s \tag{4.2}$$

and for gas blob B,

$$V_{max,B} = V_{s,B}{}' + V_b = V_s. \tag{4.3}$$

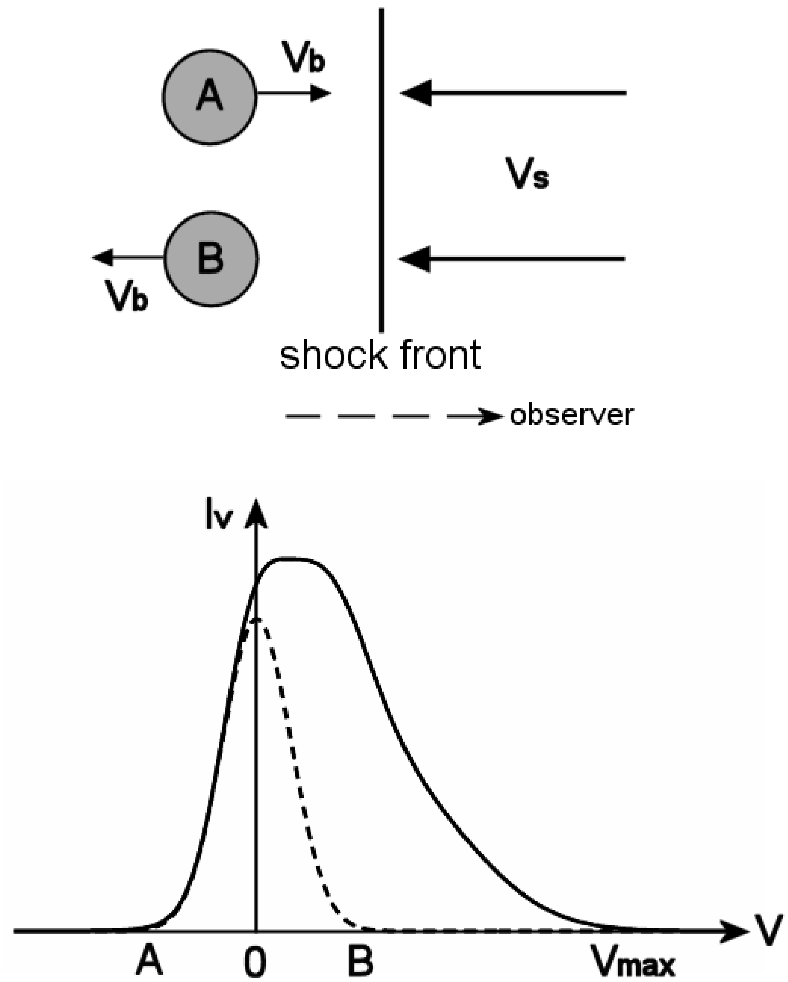

FIG. 4.8: Schematic diagrams for a planar C-shock. A planar shock front is driven into a molecular cloud, receding from an observer with a velocity of V_s. The molecular cloud is composed of gas blobs in random motions with a maximum velocity of V_b; blob A is approaching to and blob B is receding from the observer. In the line profiles, the dashed line is for pre-shock gas (e.g. NH_3 line) and the solid line is for post-shock gas (e.g. H_2 line). $V_{max} = V_s$ in a C-shock regardless of the velocity dispersion of the pre-shock gas (see text).

Thus, if V_{0,NH_3} is the center of the NH_3 line, we can still use equation (4.1) regardless of how the internal gas motion is in the pre-shock cloud.

We present the H_2 $1\text{–}0\ \mathrm{S}(1)$ and NH_3(3,3) spectra from Figure 4.6 again in Figure 4.9, but now with the intensities arbitrarily scaled for equal comparisons of the line profiles (while the velocity axes are fixed). Clear evidence of shock acceleration is found from the different velocity profiles between the H_2 and NH_3 lines. For example, in spectrum S2, the blue shoulders of the two lines are nearly coincident, while the redshifted H_2 line extends to much higher velocities. This is most easily interpreted as a receding shock which is sweeping up gas from the northern ridge, whose original velocity was $\sim 0\ \mathrm{km\ s^{-1}}$ (LSR). Conversely, in S6 the red shoulders of NH_3 and H_2 are nearly identical but the H_2 is much more extended to negative velocities. The most natural explanation is that an approaching shock is accelerating and heating gas in the northwestern part of the CND. The shocks are receding from us in spectra S1 and S2 and approaching to us in S4, S5, S6, and S8. In S3 and S7 approaching and receding shocks appear to overlap along the line of sight.

Spectrum S5 is different from others; it has two separate H_2 peaks. The more positive velocity peak partially coincides with the NH_3 velocity but extends $\sim 20\ \mathrm{km\ s^{-1}}$ further to the blue. The other peak is much more blue-shifted than this and is separated from the NH_3 line. The only possible explanations are that (1) it results from a J-shock of the gas associated with the positive velocity NH_3 emission or (2) it results from a C-shock of the gas associated with the marginally detected NH_3 emission at $-60 < V_{LSR} < -20\ \mathrm{km\ s^{-1}}$ which traces the CND (see Section 5.3.1). Avoiding ambiguity, we exclude S5 from the estimation of the mean velocities of the Sgr A East shocks assuming a planar C-shock in this section.

The resulting estimates of shock velocities using equation (4.1) are presented in Table 4.3. The velocity of NH_3 line center (V_{0,NH_3}) is measured from a Gaussian fit. V_{max,H_2} is determined from the deconvolved observed profile (using a Gaussian of FWHM = $18\ \mathrm{km\ s^{-1}}$ to approximate the instrumental resolution; see Appendix B for more details) and, in order to reduce the effect of noise, corresponds to the velocity at which the line intensity is 10 percent of the peak. Since the velocity in this definition is slightly less than the original V_{max,H_2}, the derived $V_{s,LOS}$ is underestimated by an unknown but probably small factor. V_s in the last column in Table 4.3 is the shock velocity which is corrected for a geometrical projection effect assuming an oblate shell for the Sgr A East shock front (see Appendix C).

Spectrum S8 is from a position beyond the Sgr A East boundary (see Chapter 5) and shows a much larger shock velocity than expected from a nearly perpendicular shock at the

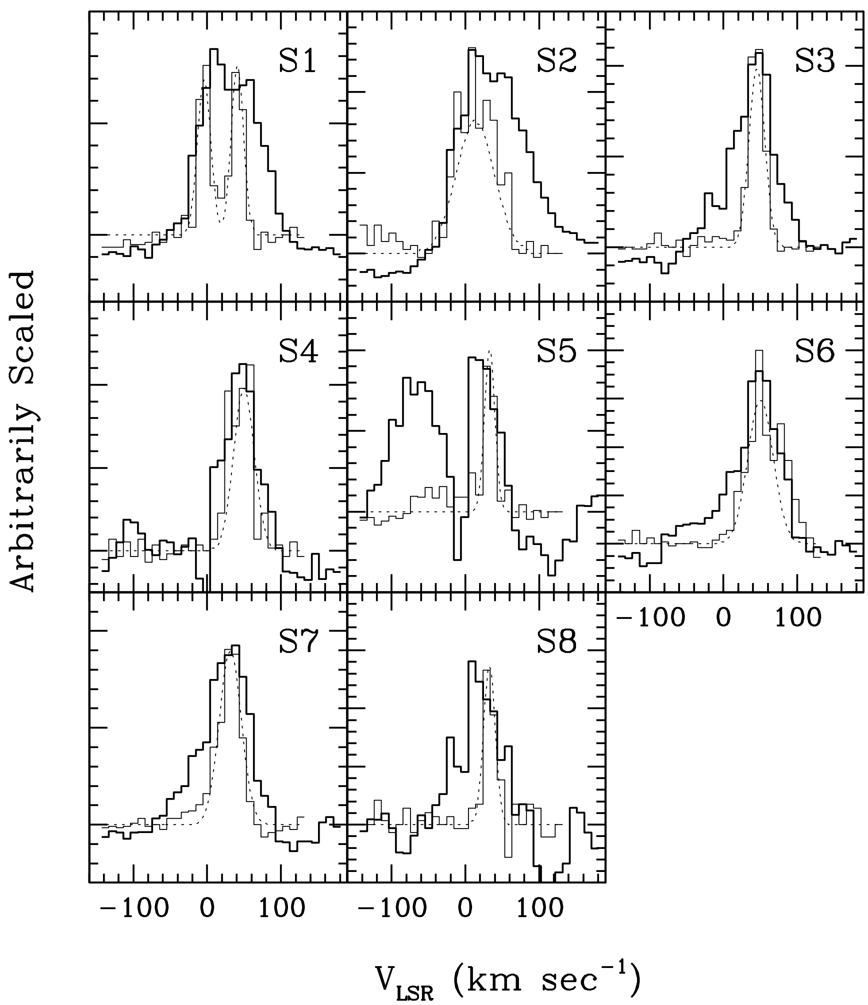

FIG. 4.9: Spectra of H_2 $1-0$ $S(1)$ and $NH_3(3,3)$ from the Galactic center, the same as Figure 4.6, but intensities are scaled differently to allow better comparison of line profiles.

TABLE 4.3: Shock Velocities Measured from Line Profiles Assuming a Planar C-shock

Spectrum[a]	Molecular cloud	Shock direction[b]	$V_{0,NH_3}{}^c$	$V_{max,H_2}{}^d$ (km s^{-1})	$V_{s,LOS}{}^e$	$\lvert V_s\rvert^f$
S1	$+50$ km s^{-1} cloud	R	+41 ($\pm$1.4)	+94	+60 ($\pm$20)	101 ($\pm$34)
S2	Northern Ridge (south)	R	+13 ($\pm$5.2)	+129	+128 ($\pm$21)	146 ($\pm$24)
S3	$+50$ km s^{-1} cloud	A	+45 ($\pm$1.1)	-28	-82 ($\pm$20)	114 ($\pm$28)
		R		+95	+56 ($\pm$20)	78 ($\pm$28)
S4	Molecular Ridge	A	+50 ($\pm$2.2)	+10	-44 ($\pm$20)	77 ($\pm$35)
S5	Southern Streamer	A[g]	+33 ($\pm$0.5)	-61	...	...
S6	CND (north-west)	A	+50 ($\pm$1.9)	-18	-76 ($\pm$20)	85 ($\pm$22)
S7	Western Streamer	A	+31 ($\pm$1.1)	-49	-89 ($\pm$20)	171 ($\pm$38)
		R		+79	+53 ($\pm$20)	101 ($\pm$38)
S8	Beyond Sgr A East	A	+33 ($\pm$2.4)	-29	-69 ($\pm$20)	...
Mean shock velocity of Sgr A East[h]						109 ($\pm$34)

[a] Presented in Figure 4.9.

[b] A = approaching, R = receding.

[c] From Gaussian fits.

[d] Defined at a specific intensity of 10 per cent of the peak value for each H_2 profile after the deconvolution of instrumental broadening. Uncertainty in the velocity is supposed to be 18 km s^{-1}, the instrumental resolution.

[e] Line-of-sight component of shock velocity; $(V_{max,H_2} - V_{0,NH_3})/0.9$.

[f] Absolute value of intrinsic shock velocity corrected for projection assuming a spherically symmetric outflow.

[g] A J-shock associated with the southern streamer or C-shocks associated with the southern streamer and the CND.

[h] Excluding S5 and S8 (see text).

edge of the Sgr A East shell. Thus we conclude that the emission seen in S8 originates elsewhere than Sgr A East and exclude it from calculation of the mean velocity of the Sgr A East shocks. The derived shock velocities seem to be too large to be acceptable by typical C-shock models which have breakdown velocities of $\lesssim 50 \text{ km s}^{-1}$. Above the breakdown velocity, all of the H_2 molecules are dissociated and the shock has many of the properties of a high velocity J-shock (Draine, Roberge, & Dalgarno 1983; Hollenbach, Chernoff, & McKee 1989; Smith & Brand 1990). Therefore it seems a contradiction that we obtained shock velocities of $\sim 100 \text{ km s}^{-1}$ assuming C-shocks for interpreting the line profiles.

The breakdown velocity of C-shock, however, depends on the density and magnetic field strength in the pre-shock gas. In order to explain very wide ($\sim 140 \text{ km s}^{-1}$) H_2 emission lines observed from the most powerful young stellar object (YSO) outflows OMC-1 and DR21 (Garden 1987; Brand 1989), Smith, Brand, & Moorhouse (1991) extended the parameter space of C-shocks up to very high gas densities and magnetic field strengths (B/n = 1 – 60 mG/10^6 cm^{-3}). Molecular dissociation in a C-shock via neutral-neutral collisions depends critically on the maximum temperature and the maximum streaming speed within the wave. The streaming speed is the relative speed of the ions and neutrals. Furthermore the maximum temperature is a strong function of the streaming speed. In very strong magnetic fields or with very high Alfvén speeds (when the Alfvén Mach number is of order unity), the upstream propagation of ion magnetosonic waves is very effective in cushioning the shock and greatly widening the transition. The neutrals are dragged along at similar speed to the ions, which means low streaming speed and consequently low temperature, unlike the case of the high Alfvén Mach numbers (Smith, Brand, & Moorhouse 1991).

There is a consensus that a magnetic field of a few milli-Gauss exists throughout the Galactic Center region (see Morris & Serabyn 1996; Güsten & Philipp 2004 for reviews). In equipartition (the kinetic energy density of material orbiting in the gravitational potential well of the Galaxy equals the magnetic energy density), with obvious uncertainties, field strengths of a few mG are deduced in the molecular clouds within 10 pc of the Galactic center (Chuss et al. 2003). Killeen, Lo, & Crutcher (1992) and Plante, Lo, & Crutcher (1995) measured Zeeman splitting of OH and HI absorption lines, respectively, against the background radio continuum and reported the magnetic field strengths along the line-of-sight of $\sim$ 2 – 3 mG towards the CND and $\sim$ 1 – 3 mG towards other Galactic center clouds. Therefore, for a mean cloud density of 10^4 cm^{-3}, $B/n \sim 100$ mG/10^6 cm^{-3}, similar to the conditions considered by Smith, Brand, & Moorhouse (1991), and the breakdown velocity is increased to $\gtrsim 200$ km s^{-1}. Thus we can conclude that the estimation of shock velocities in this section is reasonable.

4.3.3 Model II: A Mixture of C-shocks and J-shocks

Figures 4.10–4.17 show channel maps of H_2 1–0 S(1) and NH_3(3,3) emission for each of the molecular clouds in the central 10 pc of the Galaxy, whose locations are shown in Figure 4.4. For a direct comparison, we unified the velocity axes of two different emission data cubes with the same range (from -138.0 km s^{-1} to $+175.9$ km s^{-1}), resolution (9.8 km s^{-1}) and number (33) of pixels (or channels). In Figures 4.10–4.17, each channel map has a different velocity range with each other since the velocity range in which emission is detected is different from cloud to cloud. However, all the channel maps have the same resolution of 19.6 km s^{-1} (2 channels) which is similar with the resolution of our H_2 observations.

At most locations where NH_3 emission is seen it occupies only one or two channels spanning a velocity range of 20 – 40 km s^{-1}, while H_2 emission continues much farther out to either red-shifted or blue-shifted velocities from the NH_3 velocity as much as ~ 100 km s^{-1}. For example, in Figure 4.10, the northern ridge is seen in NH_3 emission at velocities of -5.7 km s^{-1} and $+14.0$ km s^{-1} and the related H_2 emission continues to much larger (red-shifted) velocities of $+92.5$ km s^{-1} or $+112.1$ km s^{-1}. The southern streamer in Figure 4.14 is seen in NH_3 emission at velocities from $+14.0$ km s^{-1} to $+53.2$ km s^{-1} and the related H_2 emission continues to much smaller (blue-shifted) velocities of -84.1 km s^{-1} or -103.7 km s^{-1}. In Figure 4.12, the $+50$ km s^{-1} cloud is seen in NH_3 emission at velocities of $+33.6$ km s^{-1} and $+53.2$ km s^{-1} and the related H_2 emission continues both towards red-shifted velocities up to $+112.1$ km s^{-1} and towards blue-shifted velocities up to -20.4 km s^{-1}.

The circles or ellipses in each channel map indicate the brightest peaks of NH_3 emission which correspond to dense cores in each molecular cloud. In most channel maps, H_2 emission is bright within the circles or ellipses at the velocities where also NH_3 emission is seen, but at more red-shifted or blue-shifted velocities H_2 emission is brighter along the outsides of circles or ellipses. In fact often the red-shifted or blue-shifted bright H_2 patches exist just outside the circles or ellipses frequently continuously to the most extreme velocities mapped, and sometimes when no H_2 emission at high velocities is seen in the cores. For example, in Figure 4.11 the brightest H_2 peaks coincide with NH_3 emission at $+14.0$ km s^{-1}, but

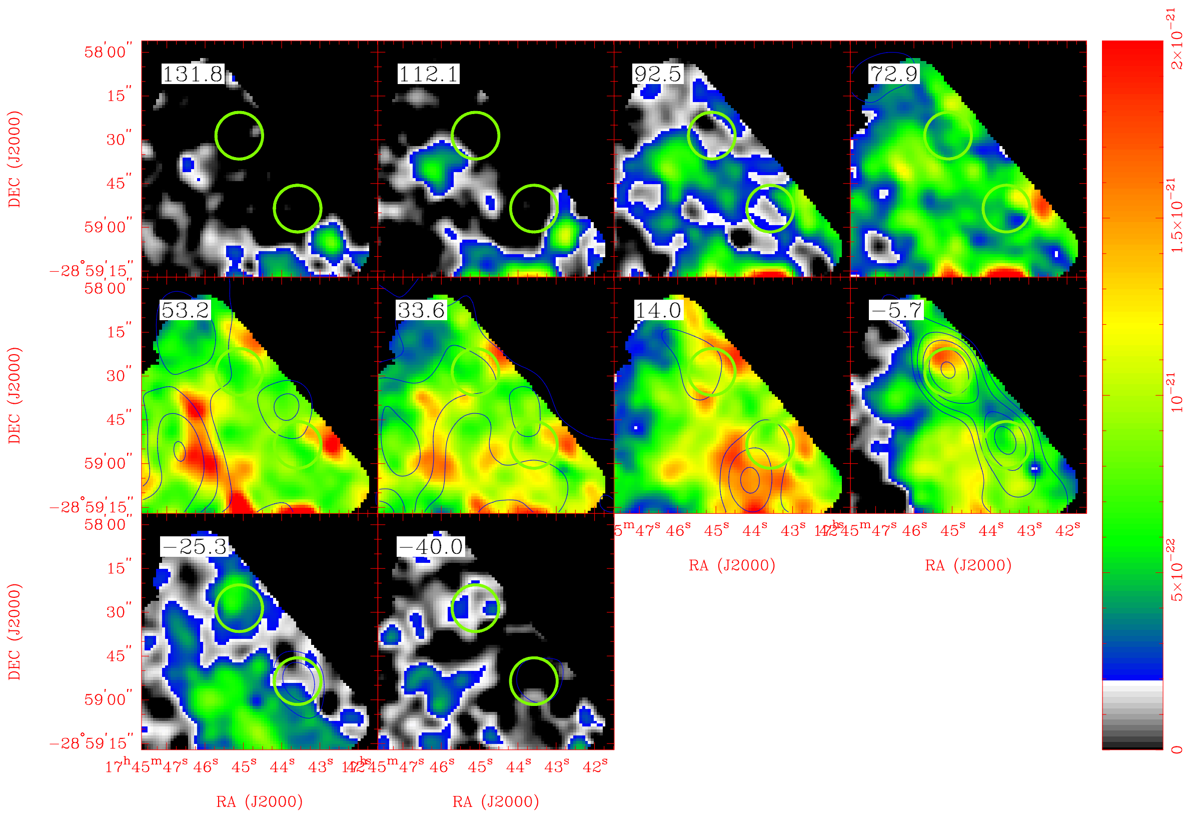

FIG. 4.10: Channel maps of H_2 $1-0$ S(1) and NH_3(3,3) emission for the northern ridge (northern part) with the mean velocity labeled in each map in units of $\mathrm{km\ s^{-1}}$. The color maps are for H_2 $1-0$ S(1) emission, which is smoothed by Gaussian with FWHM = $5''$, and the intensity level is indicated by the right hand bar in units of $\mathrm{W\ m^{-2}\ arcsec^{-2}\ km^{-1}\ s}$ (the RMS noise $\sigma_{H_2} = 1.5 \times 10^{-22}$ $\mathrm{W\ m^{-2}\ arcsec^{-2}\ km^{-1}\ s}$). The overlaid contours show NH_3(3,3) emission from McGary, Coil, & Ho (2001) and the contour levels are 3, 6, 10, 15, 23, 30, 40, 55, 70, and 90-σ_{NH_3} where the RMS noise $\sigma_{NH_3} = 0.01$ Jy beam^{-1} (the beam size is $\sim 15'' \times 13''$). Location of the northern ridge in the Galactic center is shown in Figure 4.4. The two circles or ellipses in each map indicate the brightest peaks in NH_3 emission in the molecular cloud.

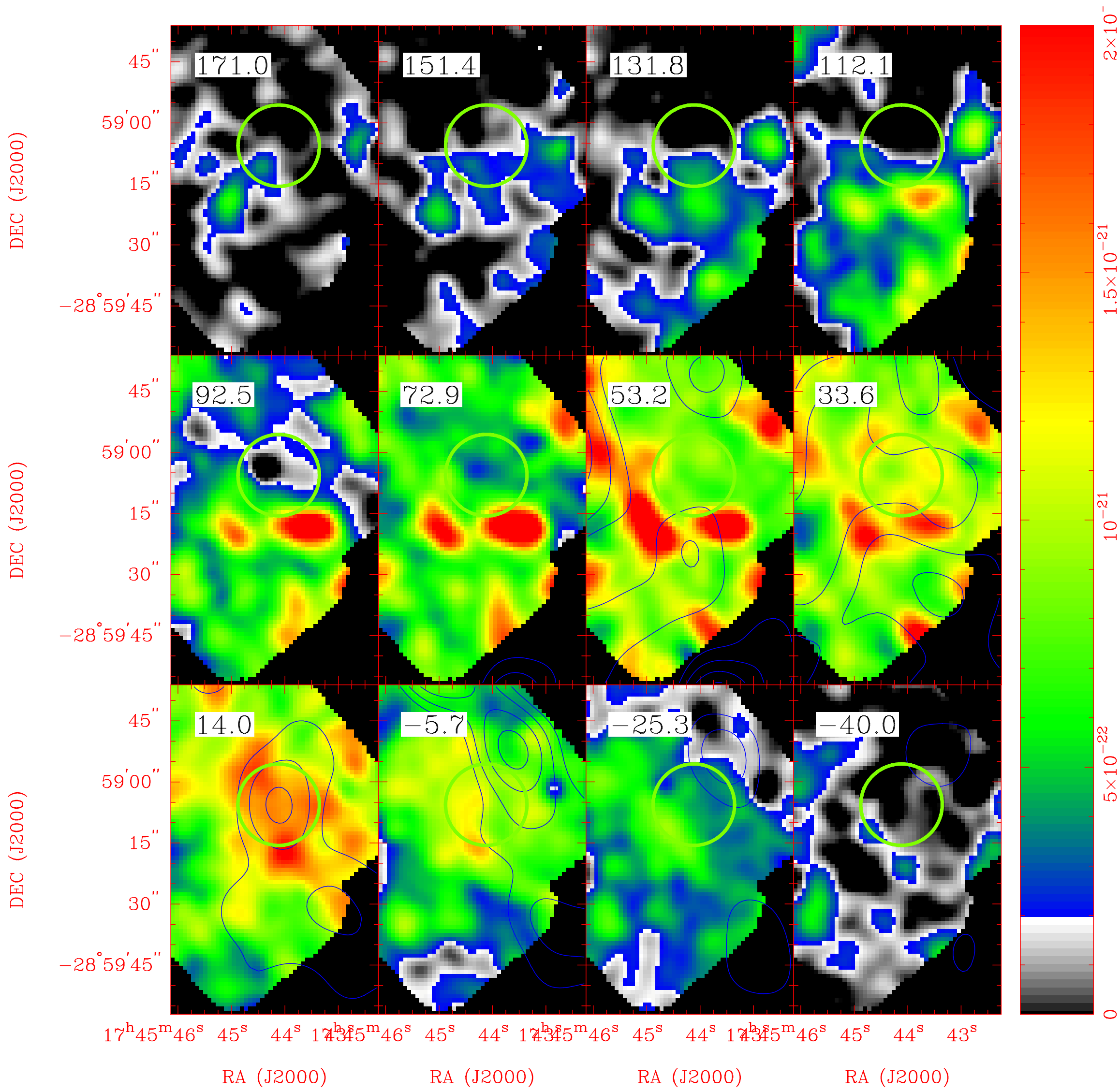

FIG. 4.11: Channel maps of H_2 $1-0$ $S(1)$ and NH_3(3,3) emission for the northern ridge (southern part). The other aspects are the same as Figure 4.10.

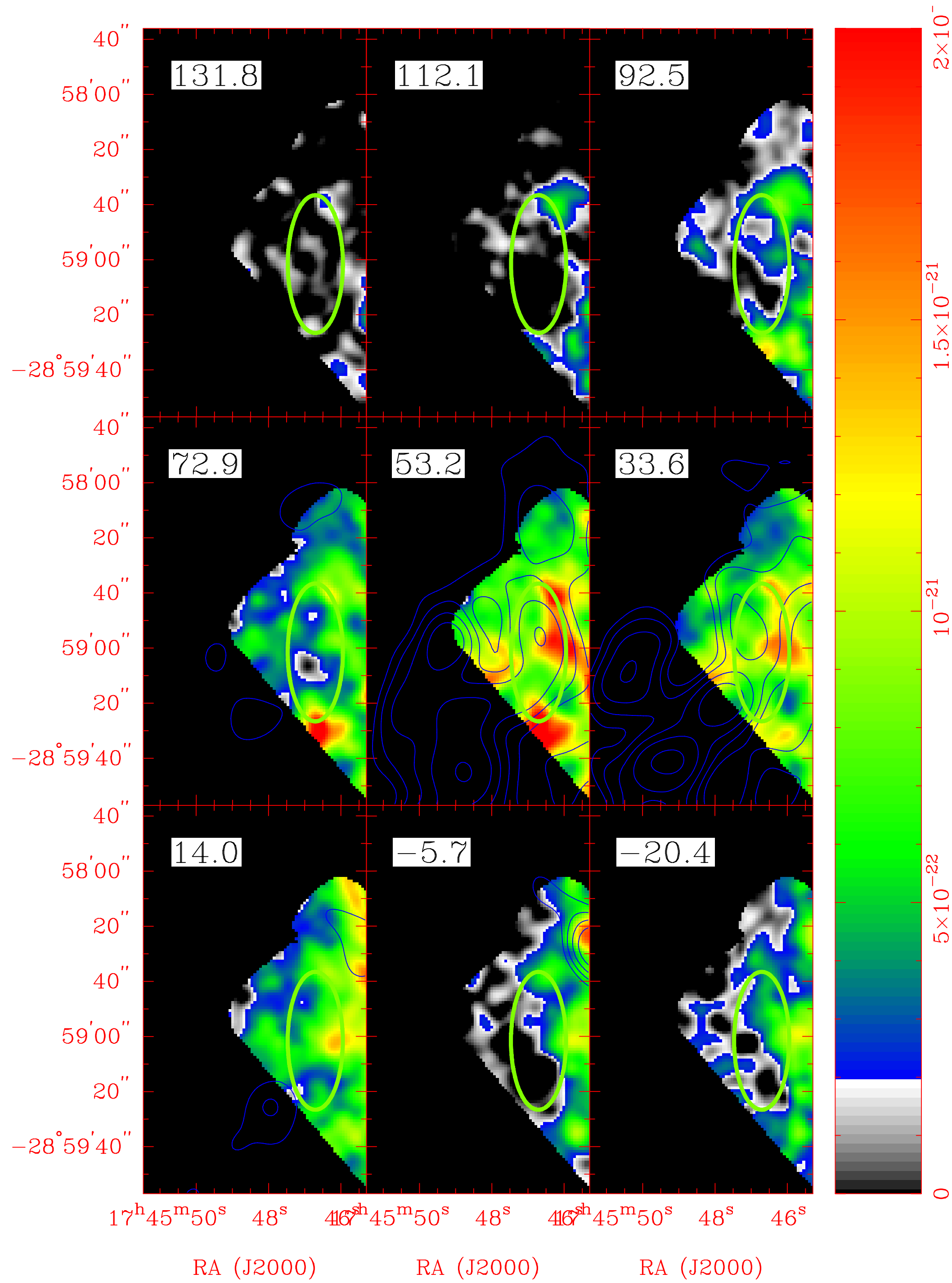

FIG. 4.12: Channel maps of H_2 $1{-}0\ S(1)$ and NH_3(3,3) emission for the $+50\ \mathrm{km\ s^{-1}}$ cloud. The other aspects are the same as Figure 4.10.

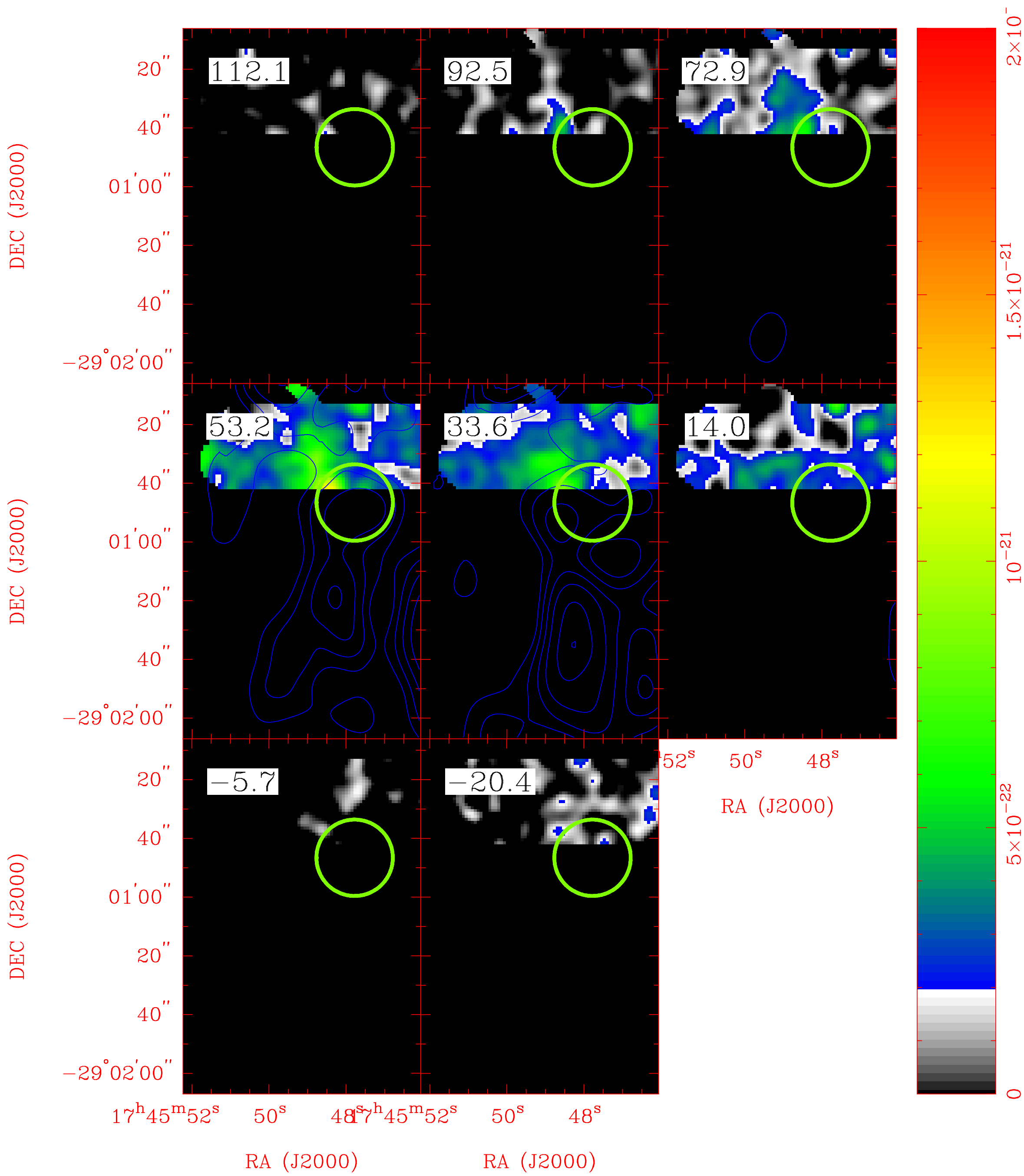

FIG. 4.13: Channel maps of H_2 $1-0$ S(1) and NH_3(3,3) emission for the molecular ridge. The other aspects are the same as Figure 4.10.

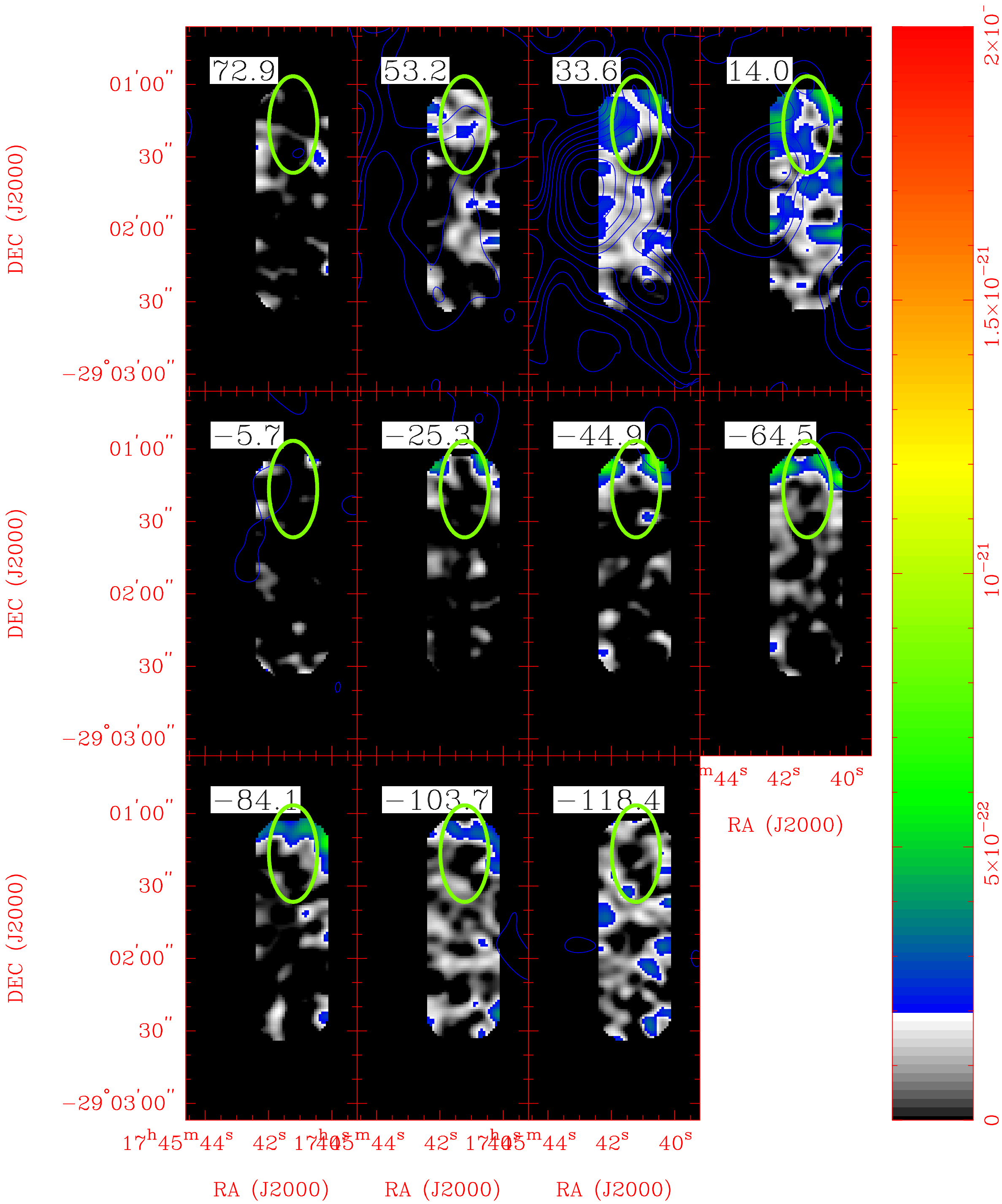

FIG. 4.14: Channel maps of H_2 $1-0$ S(1) and NH_3(3,3) emission for the southern streamer. The other aspects are the same as Figure 4.10.

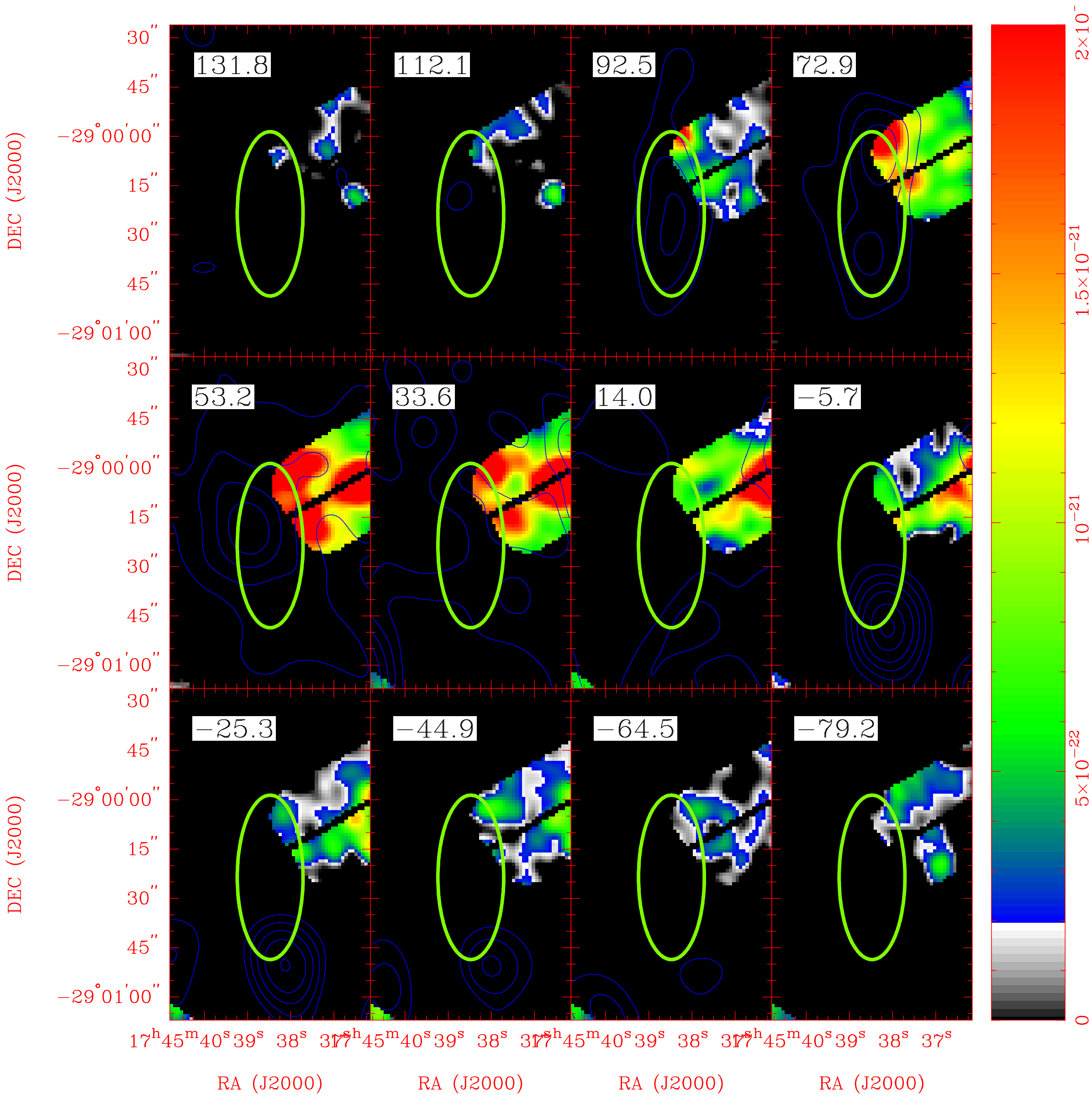

FIG. 4.15: Channel maps of H_2 $1-0$ $S(1)$ and NH_3(3,3) emission for the circum-nuclear disk (CND). The other aspects are the same as Figure 4.10.

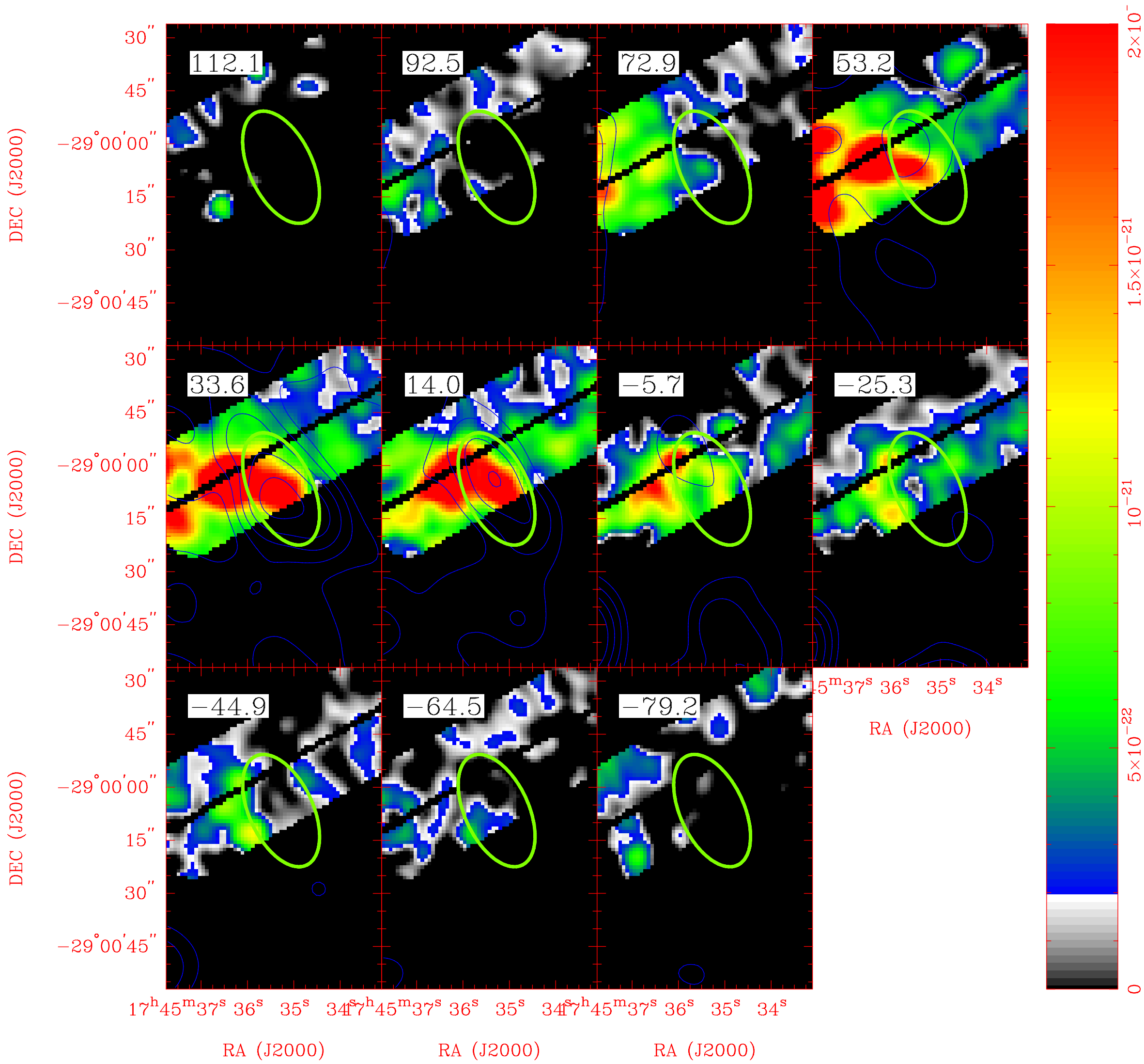

FIG. 4.16: Channel maps of H_2 $1-0$ S(1) and NH_3(3,3) emission for the western streamer. The other aspects are the same as Figure 4.10.

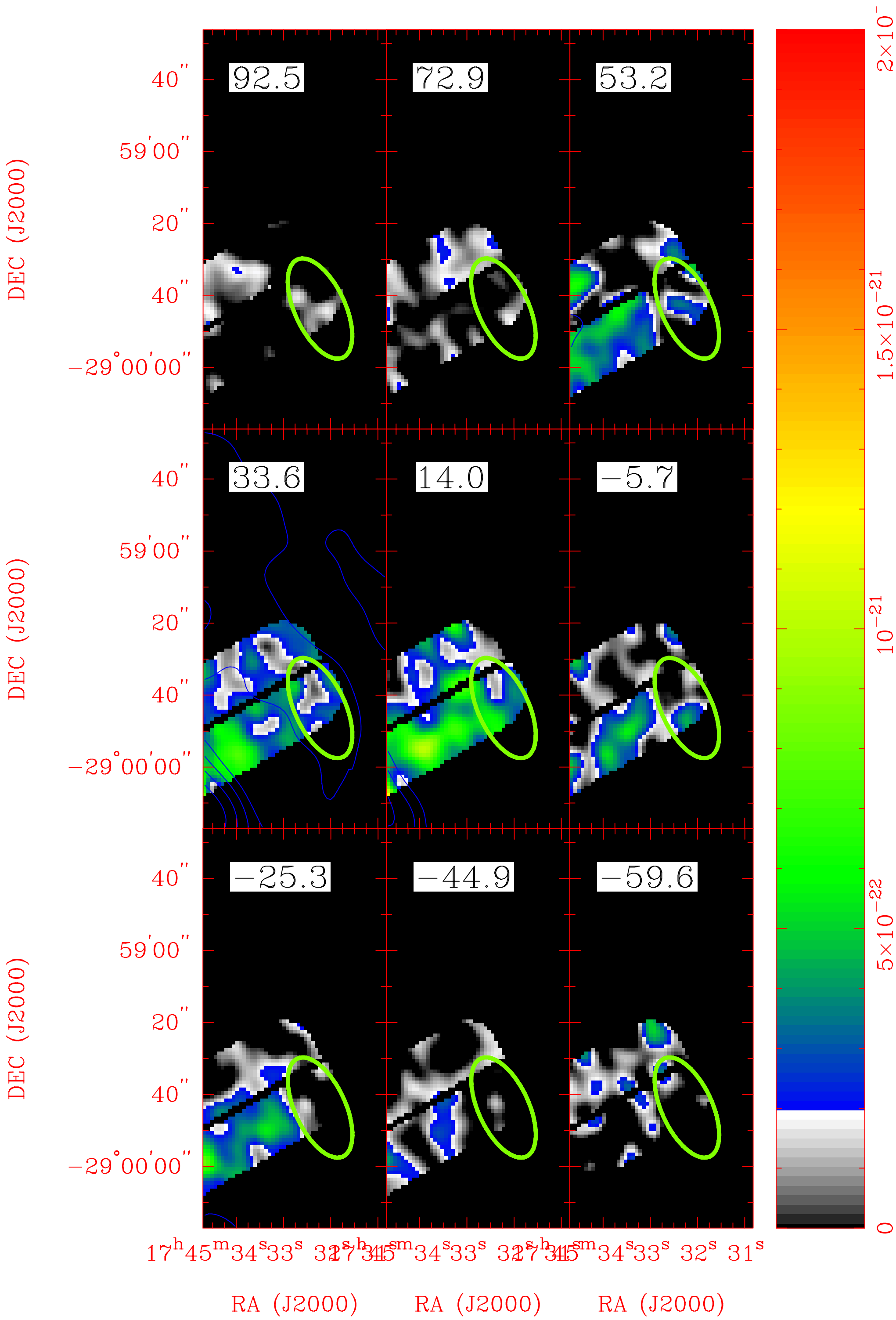

FIG. 4.17: Channel maps of H_2 $1-0$ $S(1)$ and NH_3(3,3) emission for a cloud beyond the western streamer. The other aspects are the same as Figure 4.10.

at the velocities from $+33.6\ \mathrm{km\ s^{-1}}$ to $+131.8\ \mathrm{km\ s^{-1}}$ two bright H_2 patches just outside the circle to the south exist consistently at the same positions, while the H_2 emission within the circle fades out above $+92.5\ \mathrm{km\ s^{-1}}$. For the western streamer (in Figure 4.16), there is bright H_2 emission within the ellipse between $+53.2\ \mathrm{km\ s^{-1}}$ and $+14.0\ \mathrm{km\ s^{-1}}$, but at the velocities less than $+14.0\ \mathrm{km\ s^{-1}}$ three bright H_2 patches exist continuously along the eastern boundary of the ellipse.

The different morphologies of the NH_3 and H_2 emission regions can be explained by a mixture of C-shocks and J-shocks such as van Dishoeck, Jansen, & Phillips (1993)'s model which assumes that shocks are propagating into a medium with an inhomogeneous density distribution. Assuming a constant ram pressure ($\rho\, v^2$) along the large scale shock front, the velocities of shocks propagating into the dense core of a gas clump are smaller than those of shocks into the outer-layers of the clump where density is much lower than in the core. Then slow C-shocks towards the center of the clump produce relatively narrow H_2 line profiles with velocities similar to that of the pre-shock gas (traced by a NH_3 line), and fast J-shocks towards the outer-layers produce H_2 lines with relatively large velocity shifts. Emission lines from individual J-shocks are not broad enough to explain the very broad wings of the observed H_2 line profiles from the Galactic center. However, the J-shocks should have various velocity shifts due to the inhomogeneous density distribution and deflection of shock directions (van Dishoeck, Jansen, & Phillips 1993), and so a composite line of multiple J-shock lines should be much broader than a line from a single shock (see Figure 4.18).

The resulting estimates of shock velocities are presented in Table 4.4. Here we assume that V_{max,H_2} corresponds to the velocity of the fastest J-shock which is propagating into a region of the lowest density (the out-most layer of the molecular clump where the density is similar to the inter-clump density $\sim 5000\ \mathrm{cm^{-3}}$). As in Table 4.3 in Section 4.3.2, the velocity of NH_3 line center (V_{0,NH_3}) is measured from a Gaussian fit. V_{max,H_2} is determined from the deconvolved observed profile using a Gaussian of FWHM = $18\ \mathrm{km\ s^{-1}}$ and corresponds to the velocity at which the line intensity is 10 per cent of the peak. V_s is the shock velocity which is corrected for a geometrical projection effect.

Spectrum S5 in Figure 4.9 can be best explained by this model of a composite profile. There are two separate H_2 profiles in S5; the relatively narrow one at $\sim +20\ \mathrm{km\ s^{-1}}$, which overlaps the NH_3 line, and the broad one at $\sim -70\ \mathrm{km\ s^{-1}}$. The blue shifted portion of the $+20\ \mathrm{km\ s^{-1}}$ component extends beyond the NH_3 line by $27\ \mathrm{km\ s^{-1}}$, and can be explained by a C-shock. On the other hand, the negative velocity component is separated from the bright

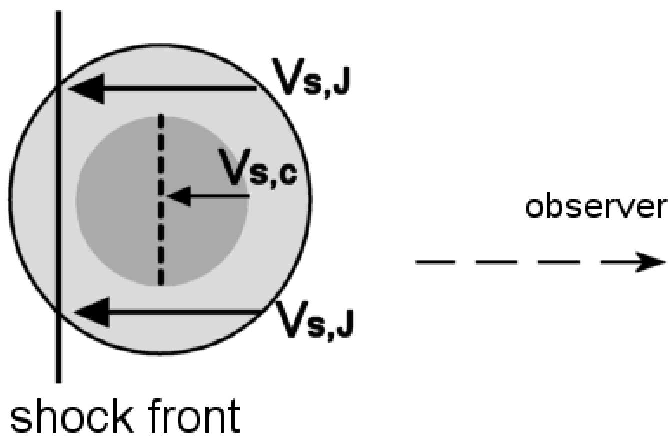

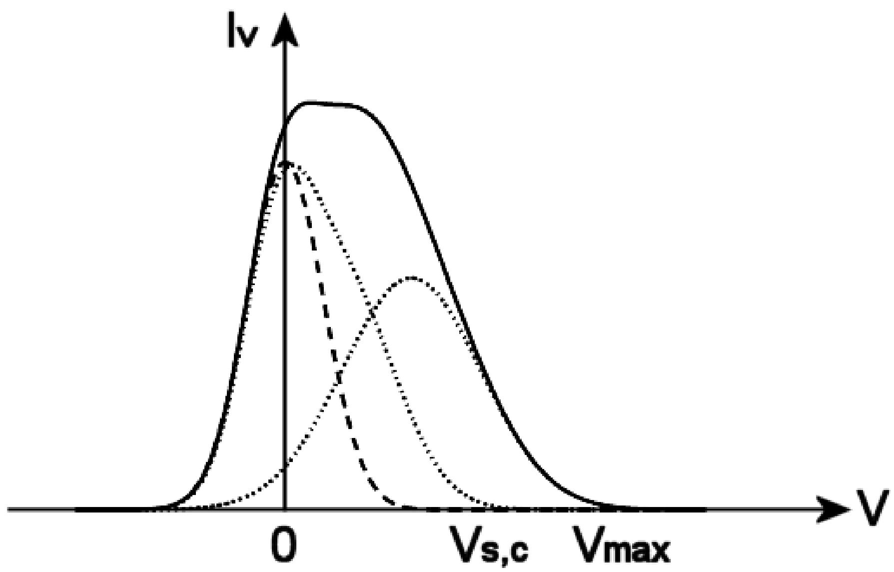

FIG. 4.18: Schematic diagrams for a mixture of C-shocks and J-shocks. A planar shock front, receding from an observer, is driven into a molecular cloud; slow C-shocks with a velocity of $V_{s,C}$ into the dense core and fast J-shocks with $V_{s,J}$ into the outer-layer of a molecular clump. In the line profiles, the dashed line is for pre-shock gas (e.g. NH_3 line) and the solid line is a composite profile for post-shock gas (e.g. H_2 line). Two dotted lines are for each component of two different shock types. The left one is a profile of C-shock with a maximum velocity shift of $V_{s,C} \lesssim 50 \text{ km s}^{-1}$ and the right one is a composite profile of multiple J-shocks with various line shifts due to density inhomogeneity and deflection of shock directions. $V_{max} \simeq V_{s,J,max}$, the velocity of the fastest J-shocks which is propagating into a region of the lowest density ($\simeq$ the inter-clump density; see text).

TABLE 4.4: Shock Velocities Measured from Line Profiles Assuming a Mixture of C & J Shocks

Spectrum[a]	Molecular cloud	Shock direction[b]	${V_{0,NH_3}}^c$	${V_{max,H_2}}^d$	${V_{s,LOS}}^e$	$\lvert V_s\rvert^f$
				(km s^{-1})		
S1	$+50$ km s^{-1} cloud	R	+41 (±1.4)	+94	+54 (±18)	91 (±31)
S2	Northern Ridge (south)	R	+13 (±5.2)	+129	+115 (±19)	131 (±21)
S3	$+50$ km s^{-1} cloud	A	+45 (±1.1)	-28	-74 (±18)	103 (±25)
		R		+95	+50 (±18)	70 (±25)
S4	Molecular Ridge	A	+50 (±2.2)	+10	-40 (±18)	70 (±32)
S5	Southern Streamer	A	+33 (±0.5)	-100	-133 (±18)	146 (±20)
S6	CND (north-west)	A	+50 (±1.9)	-18	-69 (±18)	76 (±20)
S7	Western Streamer	A	+31 (±1.1)	-49	-80 (±18)	154 (±35)
		R		+79	+47 (±18)	91 (±35)
S8	Beyond Sgr A East	A	+33 (±2.4)	-29	-62 (±18)	...
Mean shock velocity of Sgr A East[g]						104 (±33)

[a] Presented in Figure 4.9.

[b] A = approaching, R = receding.

[c] From Gaussian fits.

[d] Defined at a specific intensity of 10 per cent of the peak value for each H_2 profile after the deconvolution of instrumental broadening. Uncertainty in the velocity is supposed to be 18 km s^{-1}, the instrumental resolution.

[e] Line-of-sight component of shock velocity; $V_{max,H_2} - V_{0,NH_3}$.

[f] Absolute value of intrinsic shock velocity corrected for projection assuming a spherically symmetric outflow.

[g] Excluding S8 which is located beyond the Sgr A East boundary.

NH_3 line emission, and its blue-shifted edge is shifted by $133\ \mathrm{km\ s^{-1}}$ from that component. This requires an array of J-shocks. If we consider the difference in density between a dense core ($10^5\ \mathrm{cm^{-3}}$) and an outer-layer ($5000\ \mathrm{cm^{-3}}$) of a clump, a factor of 20 which is similar to the situation in IC 443 (a factor of 30; van Dishoeck, Jansen, & Phillips 1993), the difference in shock velocity of $133\ \mathrm{km\ s^{-1}}/27\ \mathrm{km\ s^{-1}} \simeq 4.9$ is consistent with the ratio of ~ 4.5 for a constant ram pressure;

$$\frac{v_{s,core}}{v_{s,outer-layer}} = \sqrt{\frac{n_{outer-layer}}{n_{core}}}. \tag{4.4}$$

As mentioned in Section 4.3.2, however, it is also possible that the H_2 component at negative velocity is not associated with the southern streamer at all but corresponds to the weak NH_3 emission from -20 to $-60\ \mathrm{km\ s^{-1}}$, in which case C-shocks can explain the data. If we excluded the shock velocity derived from this spectrum, the mean value would be changed to $98 \pm 30\ \mathrm{km\ s^{-1}}$; this change hardly affects our conclusions.

Since the intensity of a J-shock line is known to be much lower than that of a C-shock line (Hollenbach & McKee 1989), it may seem to be difficult to explain the observed H_2 profiles which have as bright wings as the line peaks. Although the optical depths of H_2 lines by themselves are extremely low, near-IR H_2 emission is absorbed by interstellar dust. In molecular clouds, near-IR H_2 emission is radiated from the surfaces of dense clumps and absorbed by other clumps along the line-of-sight. Dickman et al. (1992) suggested that the outer-layers of a cloud are stripped and fragmented into small clumps by shocks and subsequent gas flows from their CO observations to IC 443, and their argument is supported by the numerical models of Klein, McKee, & Colella (1994) and Mac Low et al. (1994) for interactions between shocks and clouds. Hence, for a given beam-size, outer-layers of a molecular cloud are expected to have lower area-filling factors for dust and lower "effective" optical depths than those of the dense core of the cloud. Consequently the column density in H_2 emission is higher at the outer-layers and, although H_2 emission from each J-shock is weaker than that from a C-shock, the strength of a composite line by J-shocks from the outer-layers can be competitive with the C-shock line from the surface of the core.

On the other hand, it should be questioned whether the reforming time scale of H_2 molecules in J-shocks is sufficiently short that J-shock emission can be observed simultaneously with C-shock emission at the same place after the large-scale shock front has passed through. According to the J-shock models of Hollenbach & McKee (1989), reformation of once-dissociated H_2 molecules and consequent emitting of IR lines occur at hydrogen column densities of $N(H) \simeq 10^{20.5} - -10^{21.5}\ \mathrm{cm^{-2}}$. In a medium with density of $n(H_2) = 5000\ \mathrm{cm^{-3}}$, these column densities can be reached after a shock has traveled a distance of about 0.01 – 0.1 pc which will take about 100 – 1000 yr for a shock velocity of $100\ \mathrm{km\ s^{-1}}$. A C-shock with a velocity of $50\ \mathrm{km\ s^{-1}}$ will pass the half of the distance J-shock traveled, so a gap between the emitting regions by C-shock and J-shock should be no larger than 0.005 – 0.05 pc, which corresponds 0.13 – 1.3 arcsec at a distance (8 kpc) to the Galactic center. Therefore we cannot distinguish positions of the H_2 emitting regions by two different shocks (along the line of shock propagation) with the angular resolution of ~ 2 arcsec in our observations.

4.3.4 Bulk Motion of Sgr A East?

In Tables 4.3 & 4.4, we measured two different shock velocities in opposite directions with each other (approaching vs. receding) for the $50\ \mathrm{km\ s^{-1}}$ cloud (from spectrum S3) and for the western streamer (from spectrum S7), respectively. If these clouds are at rest in the frame of Sgr A East, the absolute values of these two velocities should be the same with each other for each cloud assuming an isotropic expansion of Sgr A East. However, the measured absolute velocities along the line-of-sight (i.e. $|V_{s,LOS}|$) are different by as much as $\sim 25\ \mathrm{km\ s^{-1}}$ for the $50\ \mathrm{km\ s^{-1}}$ cloud and $\sim 35\ \mathrm{km\ s^{-1}}$ for the western streamer.

If there are non-zero bulk velocities of Sgr A East ($V_{SgrAEast}$) as well as the clouds (V_{cloud}), these differences can be explained by

$$|V_{s,a}| = V_s + (V_{cloud} - V_{SgrAEast}) \tag{4.5}$$

$$|V_{s,r}| = V_s - (V_{cloud} - V_{SgrAEast}) \tag{4.6}$$

$$\Delta V_s = |V_{s,a}| - |V_{s,r}| = 2(V_{cloud} - V_{SgrAEast}) \tag{4.7}$$

where $V_{s,a}$ is the velocity of an approaching shock and $V_{s,r}$ is of a receding one. Since we know the bulk velocities of the molecular clouds are $\sim +50\ \mathrm{km\ s^{-1}}$ and $\sim +30\ \mathrm{km\ s^{-1}}$ for the $50\ \mathrm{km\ s^{-1}}$ cloud and the western streamer, respectively, we can calculate the needed bulk velocity of Sgr A East from the last equation above.

$$V_{SgrAEast} = V_{cloud} - \frac{\Delta V_s}{2} \tag{4.8}$$

Then the estimated velocity of the bulk motion of Sgr A East is $\sim +40\ \mathrm{km\ s^{-1}}$ for the $50\ \mathrm{km\ s^{-1}}$ cloud and $\sim +10\ \mathrm{km\ s^{-1}}$ for the western streamer. Not surprisingly, the results are highly uncertain, because of the uncertainties of the measured velocities themselves and the possibilities of different cloud densities, in different directions, an anisotropic component to the expansion, other motions of Sgr A East (e.g. rotation), etc. In spite of this high uncertainty, we conclude that Sgr A East is in a bulk motion receding from us with a velocity of a few tens $\mathrm{km\ s^{-1}}$.

What influence does this bulk motion of Sgr A East have on our measurements of shock velocities? If the radial velocity of a cloud is zero, the receding motion of Sgr A East will cause us to underestimate the velocity of an approaching shock and overestimate the velocity of a receding one. In our sample, however, all the molecular clouds are in receding motions with velocities of about 10 – 50 $\mathrm{km\ s^{-1}}$, which are probably similar with the bulk velocity of Sgr A East, and the numbers of measurements are also nearly equal in shock directions. Hence, statistically, we expect no significant influence on the mean value of the measured shock velocities.

4.4 Conclusions

In this chapter, we investigate the physical conditions of H_2 line-emitting regions in the central 10 pc of the Galaxy based on our spectroscopic H_2 data and the NH_3 data observed by McGary, Coil, & Ho (2001).

From the observational results (integrated $\mathrm{H_2}$ 1–0 $\mathrm{S(1)}$ line intensity, 2–1 $\mathrm{S(1)}$ / 1–0 $\mathrm{S(1)}$ line ratios, very broad H_2 line profiles, and low peak velocities relative to those of NH_3), we conclude that the excitation of H_2 molecules in this region cannot be explained by any single mechanism (low-density PDR, dense PDR, fast J-shock, slow J-shock, or C-shock) alone. However, shocks and not fluorescence, play a major role in the H_2 excitation in the central 10 pc of the Galaxy. There are two models for H_2 excitation which can explain all of our observational results; a combination of fluorescence and C-shocks in very strong magnetic fields, or a mixture of slow C-shocks and fast J-shocks.

Assuming each of two shock models, we derive shock velocities of Sgr A East by comparing H_2 line profiles, which should trace post-shock gas, with those of NH_3, which are assumed to trace pre-shock gas in molecular clouds. The results from two different assumptions are consistent with each other as the mean velocity of about $100\ \mathrm{km\ s^{-1}}$ for the Sgr A East shocks propagating into the surrounding molecular clouds.

REFERENCES

Black J.H., & van Dishoeck E.F., 1987, ApJ, 322, 412

Brand P.W.J.L., Toner M.P., Geballe T.R., & Webster A.S., 1989, MNRAS, 237, 1009

Burton M.G., 1992, Aust. J. Phys., 45, 463

Burton M.G., Geballe T.R., Brand P.W.J.L., & Webster A.S., 1988, MNRAS, 231, 617

Burton M.G., Hollenbach D.J., Haas M.R., & Erickson E.F., 1990, ApJ, 355, 197

Burton M.G., Hollenbach D.J., & Tielens A.G.G.M., 1990, ApJ, 365, 620

Catchpole R.M., Whitelock P.A., & Glass I.S., 1990, MNRAS, 247, 479

Churchwell E., Wood D.O.S., Felli M., & Massi M., 1987, ApJ, 321, 516

Chuss D.T., Davidson J.A., Dotson J.L., Dowell C.D., Hildebrand R.H., Novak G., & Vaillancourt J.E., 2003, ApJ, 599, 1116

Dickman R.L., Snell R.L., Ziurys L.M., & Huang Y.L., 1992, ApJ, 400, 203

Draine B.T., & McKee C.F., 1993, ARA&A, 31, 373

Draine B.T., Roberge W.G., & Dalgarno A., 1983, ApJ, 264, 485

Fernandes A.J.L., Brand P.W.J.L., & Burton M.G., 1997, MNRAS, 290, 216

Frail D.A., Goss W.M., Reynoso E.M., Green A.J., & Otrupcek R., 1996, AJ, 111, 1651

Garay G., Moran J.M., & Reid M.J., 1987, ApJ, 314, 535

Garden R.P., 1987, in Peimbert M. & Jugaku J., eds, IAU Symp. No. 115, Star Forming Regions, Reidel, Dordrecht, p. 325

Gatley I., Jones T.J., Hyland A.R., Beattie D.H., & Lee T.J., 1984, MNRAS, 210, 565

Güsten R., & Henkel C., 1983, A&A, 125, 136

Güsten R., & Philipp S.D., 2004, in Pfalzner S., Kramer C., Staubmeier C., & Heithausen A., eds, Springer proceedings in physics, Vol. 91, Proc. of the 4th Cologne-Bonn-Zermatt Symp., The Dense Interstellar Medium in Galaxies, Berlin, Heidelberg: Springer, p. 253

Herrnstein R.M., & Ho P.T.P., 2005, ApJ, 620, 287

Hollenbach D.J., Chernoff D.F., & McKee C.F., 1989, in Kaldeich B.H., ed., Proc. of the 22nd Eslab Symp., Infrared Spectroscopy in Astronomy, ESA SP-290, European Space Agency, p. 245

Hollenbach D., & McKee C.F., 1989, ApJ, 342, 306

Inoue M.Y., et al., 1993, PASJ, 45, 539

Israel F.P., Baas F., Rudy R.J., Skillman E.D., & Woodward C.E., 2003, A&A, 397, 87

Kaufman M.J., & Neufeld D.A., 1996, ApJ, 456, 611

Killeen N.E.B., Lo K.Y., & Crutcher R.M., 1992, ApJ, 385, 585

Klein R.I., McKee C.F., & Colella P., 1994, ApJ, 420, 213

Kwan J., 1977, ApJ, 216, 713

Lee S., Pak S., Lee S.-G., Davis C.J., Kaufman M.J., Mochizuki K., & Jaffe D.T., 2005, MNRAS, in press (astro-ph/0410572)

Mac Low M.-M., McKee C.F., Klein R.I., Stone J.M., & Norman M.L., 1994, ApJ, 433, 757

McGary R.S., Coil A.L., & Ho P.T.P., 2001, ApJ, 559, 326

McGary R.S., & Ho P.T.P., 2002, ApJ, 577, 757

Morris M., & Serabyn E., 1996, ARA&A, 34, 645

Paglione T.A.D., Jackson J.M., Bolatto A.D., & Heyer M.H., 1998, ApJ, 493, 680

Pak S., Jaffe D.T., & Keller L.D., 1996a, ApJ, 457, L43

Pak S., Jaffe D.T., & Keller L.D., 1996b, in Gredel R., ed., ASP Conf. Ser. Vol. 102, The Galactic Center. Astron. Soc. Pac., San Francisco, p. 28

Pak S., Jaffe D.T., Stacey G.J., Bradford C.M., Klumpe E.W., & Keller L.D., 2004, ApJ, 609, 692

Pedlar A., Anantharamaiah K.R., Ekers R.D., Goss W.M., van Gorkom J.H., Schwarz U.J., & Zhao J.-H., 1989, ApJ, 342, 769

Plante R.L., Lo K.Y., & Crutcher R.M., 1992, ApJ, 385, 585

Reach W.T., Rho J., Jarrett T.H., & Lagage P.-O., 2002, ApJ, 564, 302

Reid M.J., 1993, ARA&A, 31, 345

Richter M.J., Graham J.R., & Wright G.S., 1995, ApJ, 454, 277

Sternberg A., & Dalgarno A., 1989, ApJ, 338, 197

Smith M.D., 1995, A&A, 296, 789

Smith M.D., & Brand P.W.J.L., 1990, MNRAS, 242, 495

Smith M.D., & Brand P.W.J.L., 1990, MNRAS, 243, 498

Smith M.D., Brand P.W.J.L., & Moorhouse A., 1991, MNRAS, 248, 730

Sohn J., Ann H.B., Pak S., & Lee H.M., 2001, JKAS, 34, 17

van Dishoeck E.F., Jansen D.J., & Phillips T.G., 1993, A&A, 279, 541

Wang Z., & Scoville N.Z., 1992, ApJ, 386, 158

Walmsley C.M., Güsten R., Angerhofer P., Churchwell E., & Mundy L., 1986, A&A, 155, 129

Wardle M., Yusef-Zadeh F., & Geballe T.R., 1999, in Falcke H. et al., eds, ASP Conf. Ser. Vol. 186, The Central Parsecs of the Galaxy. Astron. Soc. Pac., San Francisco, p. 432

Wilson C.D., 1994, ApJ, 434, L11

Yusef-Zadeh F., & Morris M., 1987, ApJ, 320, 545

Yusef-Zadeh F., Roberts D.A., Goss W.M., Frail D.A., & Green A.J., 1996, ApJ, 466, L25

Yusef-Zadeh F., Stolovy S.R., Burton M., Wardle M., & Ashley M.C.B., 2001, ApJ, 560, 749

Yusef-Zadeh F., Stolovy S.R., Burton M., Wardle M., Melia F., Lazio T.J.W., Kassim N.E., & Roberts D.A., 1999, in Falcke H. et al., eds, ASP Conf. Ser. Vol. 186, The Central Parsecs of the Galaxy. Astron. Soc. Pac., San Francisco, p. 197

Chapter 5

3-Dimensional Spatial and Kinematic Structure of the Central 10 Parsecs

5.1 Introduction

The inner 10 pc of the center of our Galaxy contains several principal components; a candidate of a super-massive black hole (SMBH; Sgr A*), a surrounding cluster of stars (the Central cluster), molecular and ionized gas clouds (the circum-nuclear disk (CND), Sgr A West, gas streamers, and giant molecular clouds), and a powerful supernova-like remnant (Sgr A East). The interactions between these components are responsible for many of the phenomena occurring in this complex and unique part of the Galaxy. Developing a consistent picture of the relationships and interactions between these components is essential to understand the nature of the Galactic center.

5.1.1 2-Dimensional Morphology in the Central 10 Parsecs

Since the discovery of Sgr A in the early 1950's, dramatic progress of radio technology made detailed, high resolution observations possible and the multiple natures of this bright radio source became evident in the early 1970's. The eastern part of Sgr A (Sgr A East), which is now known to nearly surround Sgr A West in projection (see Figure 1.10), has a non-thermal spectrum, while Sgr A West is predominantly a thermal source. Balick & Brown (1974) discovered a compact VLBI radio source, Sgr A*, within Sgr A West (see Goss et al. 1983 and references therein), now known to be the site of a $\sim 4 \times 10^6$ $M_\odot$ SMBH at the dynamical center of the Galaxy (see Ghez et al. 2003; Schödel et al. 2003 and references therein).

In addition to the two giant molecular clouds (GMCs) M-0.02-0.07 and M-0.13-0.08, (also known as the '50 km s^{-1} cloud' and the '20 km s^{-1} cloud', respectively; see Figures 1.9 & 5.1), recent accurate radio observations have resolved several dense and filamentary molecular features around the Sgr A complex; the 'molecular ridge', the 'southern streamer', the 'northern ridge', and the 'western streamer' (see Figures 1.10 & 5.1). These molecular features are believed to play important roles in feeding the central massive black hole (e.g. Coil & Ho 1999, 2000; McGary, Coil, & Ho 2001).

5.1.2 Previous Suggestions on the 3-D Spatial Structure

As the complicated morphology of the central 10 pc, which is composed of many different features in projection, is being unveiled, a lot of efforts are being made to reveal whether these features are really in the Galactic center or just along the line-of-sight in that direction, and to determine the relative positions of them along the line-of-sight, that is to say, the three-dimensional (3-D) spatial structure of the Galactic center.

Mezger et al. (1989) proposed a 3-D structure for the Sgr A complex (Figure 5.2) based on the following arguments.

(i) 327 MHz absorption towards Sgr A West definitely places Sgr A East behind Sgr A West (Yusef-Zadeh & Morris 1987).

(ii) A ring-shaped dense molecular feature across the GMCs M-0.02-0.07 (the $50 \, \text{km s}^{-1}$ cloud) and M-0.13-0.08 (the $20 \, \text{km s}^{-1}$ cloud), which is traced by 1.3 mm dust emission and many other tracers (see references therein), surrounds Sgr A East. This suggests that Sgr A East have expanded into the molecular clouds.

(iii) The two GMCs with $N_H \sim 5 \times 10^{22} \; cm^{-2}$ and $A_v = 90$ mag extend smoothly across Sgr A West based on their 1.3 mm observations, but are neither seen as extinction towards Sgr A West nor appear in OH absorption. This places them behind Sgr A West and Sgr A East.

(iv) The fact that the dust ring is seen in OH absorption (Sandqvist et al. 1987) shows that part of the dust ring is in front of the synchrotron source, Sgr A East.

Based on these arguments, they conclude that the event which created Sgr A East and the associated dust shell did not occur deep within the GMCs but close to their surfaces facing

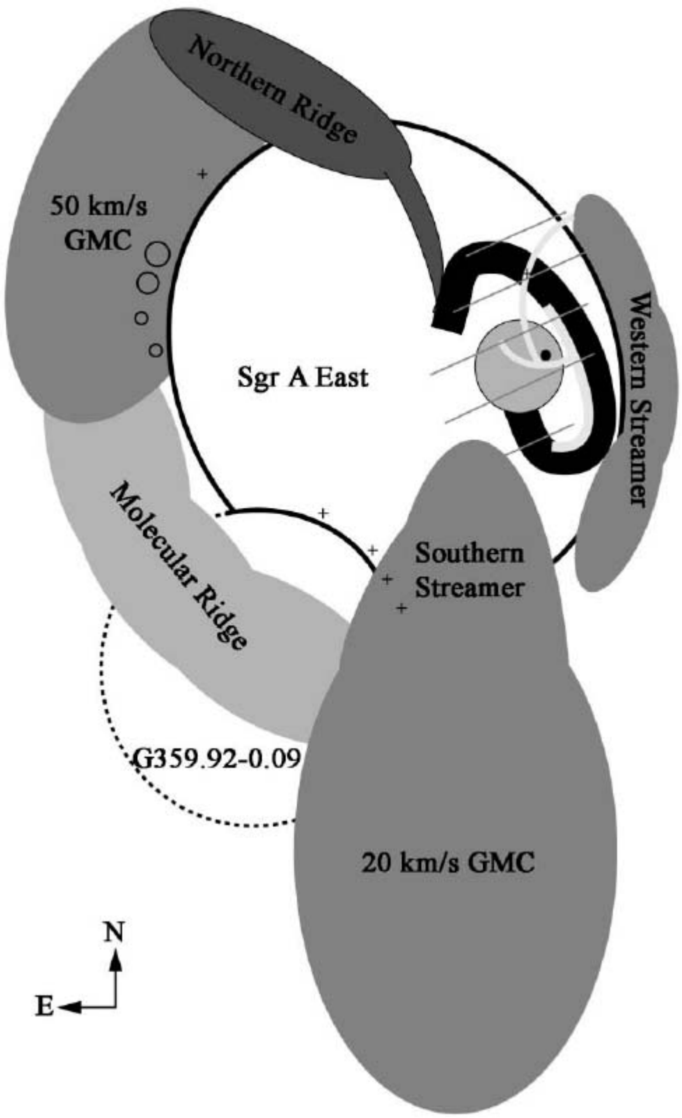

FIG. 5.1: Schematic drawing of the Galactic center as seen in the plane of the sky (from Figure 14 of Herrnstein & Ho 2005). The mini-spirals of Sgr A West and the gray sphere of 'high line ratio' gas (designated for NH_3 gas with $S_\nu(6,6) > S_\nu(3,3)$ by Herrnstein & Ho 2005) which contains Sgr A* (black dot), is surrounded by the partial ring of the CND. Hatched lines extending northward from the southern streamer indicate the faint extension of this cloud to the north of Sgr A*. Crosses indicate the positions of the 1720 MHz OH masers from Yusef-Zadeh et al. (1999a) and four small circles lying along the western edge of the 50 $\mathrm{km\ s^{-1}}$ GMC denote compact H II regions (see Yusef-Zadeh & Morris 1987). G 359.92-0.09 is a supernova remnant (SNR) which is believed to be interacting with the molecular ridge and Sgr A East (Coil & Ho 2000).

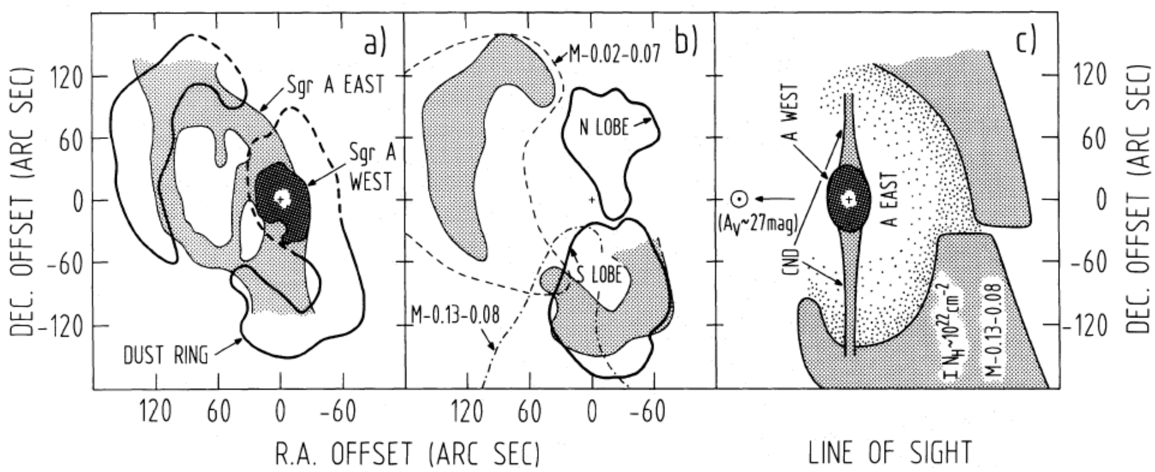

FIG. 5.2: Illustration of the 3-D structure of the Sgr A complex (from Figure 7 of Mezger et al. 1989). Crosses indicate the position of Sgr A*. (a) Views on the sky of the dust ring, the synchrotron source Sgr A East (based on the 18 cm continuum observations by Sandqvist et al. 1987) and the H II region Sgr A West; and (b) of the GMCs M-0.02-0.07 and M-0.13-0.08, dust ring and of the northern and southern lobes of the CND. (c) A simplified possible spatial arrangement in the line-of-sight direction drawn as a cross section in declination through the position of Sgr A*. The thickness of the neutral gas components is an indication of the hydrogen column density observed in this direction. Note that the CND is actually not seen edge-on (inclination angle $i = 90°$) but at an angle of $i \sim 70°$ (see Güsten 1987 and references therein).

the sun.

However, Geballe, Bass, & Wade (1989) reports CO absorption toward a few Galactic center IR sources and draws some limited conclusions about the relative positions of Sgr A West and the two GMCs that the location of the 20 km s^{-1} cloud is in front of Sgr A West. They also finds some evidence that the 50 km s^{-1} cloud is in front of part of Sgr A West.

Using the Very Large Array (VLA), Coil & Ho (1999, 2000) observed the (1,1) and (2,2) line emission of NH_3 from the molecular ridge, the southern streamer, and the 20 km s^{-1} cloud, and put the following constraints on the line-of-sight relationships in order to build a 3-D model of the Galactic center (Figure 5.3).

(i) The positive velocity gradient with declination along the southern streamer, which is believed to transport gas from the 20 km s^{-1} cloud to the CND, places the CND (and the nuclear region) behind the southern streamer (and the 20 km s^{-1} cloud).

(ii) Sgr A East is behind Sgr A West (and the nuclear region), as Sgr A West is seen in absorption against Sgr A East at 90 cm (Pedlar et al. 1989).

(iii) The 50 km s^{-1} cloud, or the northern part of the molecular ridge, is slightly behind Sgr A East since there is redshifted emission from the region where an interaction is expected with Sgr A East but no corresponding blueshifted emission in the NH_3 position-velocity diagrams (PVDs).

(iv) The supernova remnant (SNR) G 359.92-0.09, which can be seen in 20 cm radio continuum images (Yusef-Zadeh & Morris 1987; Pedlar et al. 1989), to the south of Sgr A East is interacting with the southern part of the molecular ridge and with the eastern edge of the 20 km s^{-1} cloud, while the northern part of the molecular ridge is impacted by Sgr A East, considering the NH_3 morphology and kinematics in these regions.

(v) The SNR is also interacting with the southern edge of Sgr A East which is supported by the inversely-curved shape of the southern edge of Sgr A East and several 1720 MHz OH masers observed in this location (Yusef-Zadeh et al. 1996, 1999a). The angular size of the SNR is $\sim 3\overset{\prime}{.}5$, which corresponds to ~ 8.4 pc, so Sgr A East and the 20 km s^{-1} cloud have to be within 8.4 pc of each other along the line-of-sight.

Herrnstein & Ho (2005) updated and modified Coil & Ho (2000)'s 3-D model based on their additional NH_3 line data and the more recent results in the published literature as follows (see Figure 5.4).

(i) The nuclear region (Sgr A*, Sgr A West, and the CND) is placed just inside the leading edge of Sgr A East according to Maeda et al. (2002) and references therein.

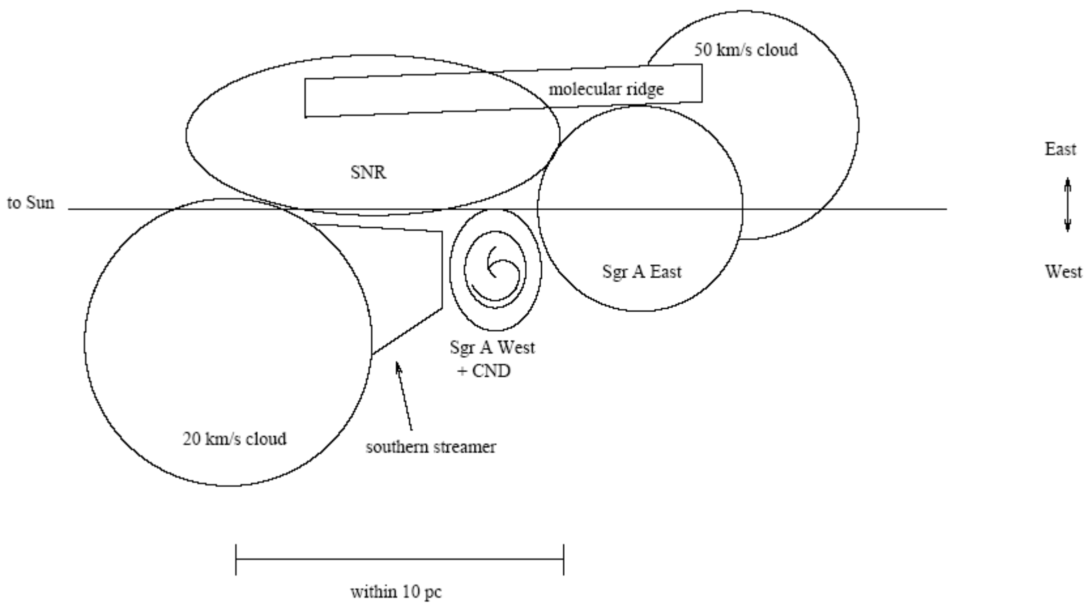

FIG. 5.3: Schematic drawing of the large-scale features in the central 15 pc showing positions along the line-of-sight from the sun with east being up (from Figure 13 of Coil & Ho 2000).

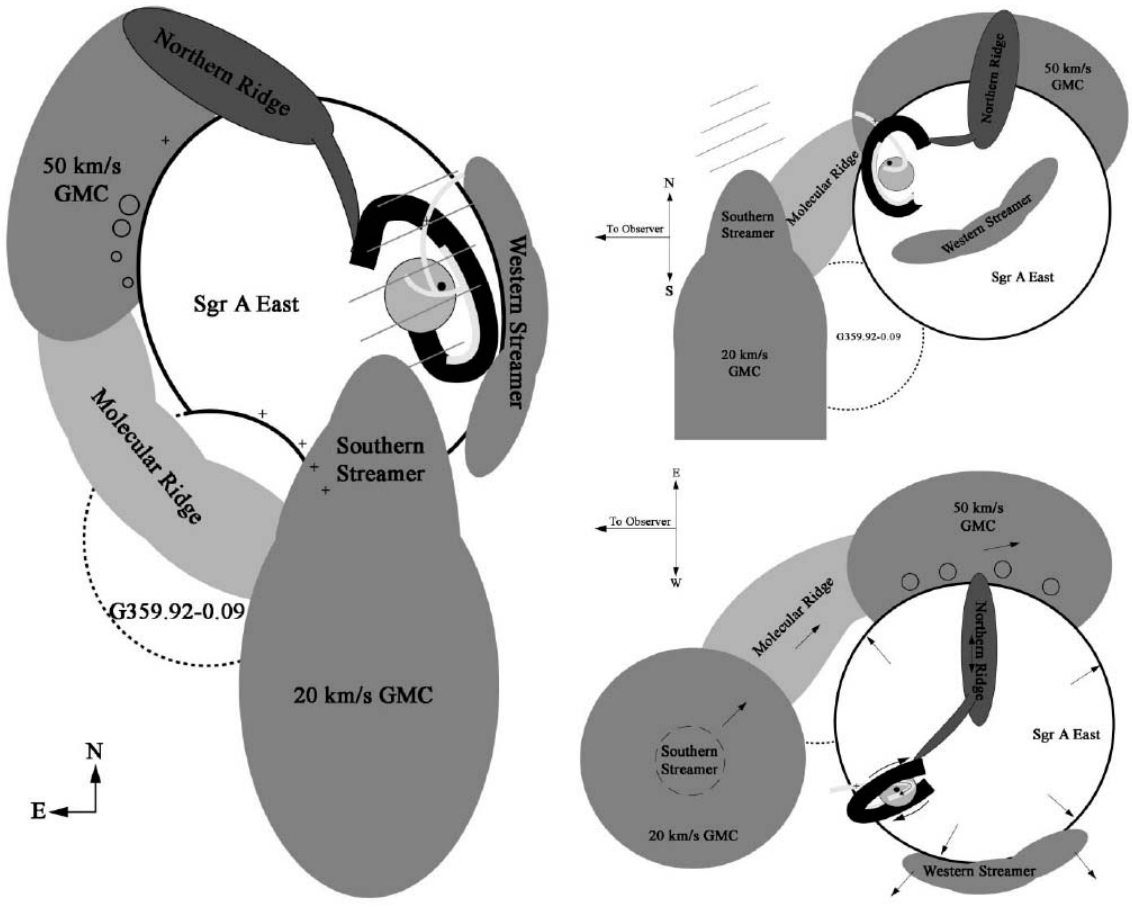

FIG. 5.4: Schematic drawing of the 3-D structure of the Galactic center from Herrnstein & Ho (2005). Arrows show the inferred motions of the main features based on the Doppler-shifted velocities. Refer to Figure 5.1 for other indicators.

(ii) The line-of-sight positions of the mini-spirals of Sgr A West and the CND are added to the 3-D model based on the observational results on H92α and Brγ emission and starlight absorption from Roberts & Goss (1993).

(iii) The 50 km s^{-1} cloud is located predominately to the east of Sgr A East but not in front of the Galactic center along the line-of-sight since X-ray emission from the central 10 pc is not observed to be strongly absorbed (Park et al. 2004).

(iv) Observations of formaldehyde (HCHO) absorption (Güsten & Downes 1980) and 2–10 keV X-ray absorption (Park et al. 2004) towards the 20 km s^{-1} cloud indicate that this GMC lies in front of the nucleus along the line-of-sight.

(v) The velocity gradient of the western streamer in NH_3 emission indicates that the streamer is highly inclined to the line-of-sight and expanding outward with Sgr A East.

(vi) The northern ridge is placed along the northern edge of Sgr A East with an orientation roughly in the plane of the sky based on its bulk motion with a velocity of -10 km s^{-1} which is consistent with an expansion perpendicular to the line-of-sight.

(vii) Based on the apparent continuation of the streamer to the north of Sgr A* and smaller velocity gradient than that expected for infalling gas to the SMBH, the southern streamer extends northward from the 20 km s^{-1} cloud, but does not interact with the nucleus.

(viii) An X-ray filament associated with the south-western edge of the SNR G 359.92-0.09, which is recently detected by *XMM-Newton* and *Chandra* (Sakano et al. 2003; Park et al. 2004), supports the argument of Coil & Ho (2000) on this SNR.

These models of the spatial structure of the central 10 pc have the following features in common.

(i) Galactic nucleus including Sgr A West and the CND lies in front of Sgr A East but behind the southern streamer and a part of the 20 km s^{-1} cloud along the line-of-sight.

(ii) Sgr A East is expanding into the 50 km s^{-1} cloud (M-0.02-0.07), the northern ridge, and the western streamer.

(iii) The SNR G 359.92-0.09 is interacting with the southern part of the molecular ridge, with the eastern edge of the 20 km s^{-1} cloud, and with the southern edge of Sgr A East.

On the other hand, the contradictions between the previous models raise the following questions.

(i) Is the nucleus in contact with or contained within Sgr A East?

(ii) Is the southern streamer falling into or interacting with the nucleus?

(iii) Has Sgr A East expanded into the 50 km s^{-1} cloud significantly, or just started to contact it?

(iv) Is Sgr A East interacting with the northern part of the molecular ridge?

(v) Is Sgr A East interacting with the $20\ \mathrm{km\ s^{-1}}$ cloud (M-0.13-0.08)?

(vi) Is the $20\ \mathrm{km\ s^{-1}}$ cloud located only in front of Sgr A East, or also extended further to the backside of it along the line-of-sight?

It should be noted that the models above are all based on indirect evidence like morphology, kinematics of molecular clouds, or absorption of background radiation by these clouds, not based on direct, physical, interactions between the objects. To answer the above questions, more robust evidence is needed.

5.1.3 Sgr A East as a Base Object for Determining the 3-D Structure

Sgr A East surrounds the Sgr A* complex (including Sgr A West and the CND) in projection as seen in the previous sections (see Figures 1.10 & 5.1). Along the line of sight, it seems obvious from the radio observations of absorption of non-thermal radiation that the Sgr A* complex lies in front of the Sgr A East shell (Yusef-Zadeh & Morris 1987; Pedlar et al. 1989). However, a number of arguments suggest that Sgr A* is in physical contact with or possibly embedded within the hot cavity of the Sgr A East shell (see Morris & Serabyn 1996; Yusef-Zadeh, Melia, & Wardle 2000; Maeda et al. 2002 and references therein).

For example, although the ionized gas associated with Sgr A West is absorbing most of the non-thermal emission from Sgr A East, there is still faint non-thermal emission detected at 90 cm toward the thermally ionized gas. This may be radiated from the front side of the Sgr A East shell in which Sgr A West is embedded but lies toward the front-most edge (Yusef-Zadeh, Melia, & Wardle 2000).

There is also observational support for suggestion that Sgr A East is in physical contact with and driving shocks into the CND. In their near-IR observations, Yusef-Zadeh et al. (1999b) found a linear filament of H_2 emission located at the western edge of the CND running parallel to the Sgr A East shell. The morphology of this feature, the association with a source of 1720 MHz OH maser, and the lack of evidence for UV heating in the form of thermal radio continuum or Brγ emission imply that this H_2 feature is shock-heated. Additionally, a north-south ridge outlining the eastern half of the CND can be seen in 20 cm continuum emission (Yusef-Zadeh, Melia, & Wardle 2000). This elongated ridge is also noted at 90 cm (Pedlar et al. 1989; Yusef-Zadeh et al. 1999b), suggesting that it is a non-thermal feature related to Sgr A East. On the other hand, highly negative radial velocity (about $-190\ \mathrm{km\ s^{-1}}$) absorption features of H_2CO, OH, HI, and HCO^+ have been observed toward Sgr A West (Marr et al. 1992; Pauls et al. 1993; Yusef-Zadeh, Lasenby, & Marshall 1993; Yusef-Zadeh, Zhao, & Goss 1995; Zhao, Goss, & Ho 1995). The kinematic and spatial distribution of this gas place it at the Galactic center and Yusef-Zadeh, Melia, & Wardle (2000) interpret its highly negative velocity as a result of acceleration by Sgr A East.

In fact we saw, through the comparison between the H_2 and NH_3 data in Chapter 4 (e.g. see Figure 4.15), that Sgr A East is driving strong shocks into the north-western part of the CND and accelerating the cloud toward negative velocities. This result of ours supports Yusef-Zadeh, Melia, & Wardle (2000)'s argument that the H_2 filament detected along the western edge of the CND is shock-heated. Thus we conclude that Sgr A East is situated within the central 10 pc and that physical interaction between it and the central few parsecs is inevitable.

As seen in the previous chapter, Sgr A East is also actively interacting with the molecular clouds in the central 10 pc. Because Sgr A East is expanding and driving shocks into clouds, we can determine the relative locations along the line of sight of Sgr A East and the clouds based on the relative radial velocities of the shocked and unshocked gas. Therefore Sgr A East can be used as a base object for determining the arrangements of the molecular clouds along the line-of-sight and consequently understanding the 3-D structure around the nucleus of our Galaxy.

5.2 Projected Morphology of Sgr A East in H_2 Emission

Before addressing the 3-D structure, it is worthwhile to investigate the 2-D morphology of the Sgr A East boundary which is imaged in H_2 emission in this study for the first time.

Figure 5.5 shows our model of the Sgr A East boundary in projection based on the intensity map of H_2 emission. As discussed in Chapter 4, Sgr A East is actively interacting with and driving strong shocks into the surrounding molecular clouds. There is intense H_2 emission from the interaction regions related to the $50\ \mathrm{km\ s^{-1}}$ cloud and the northern ridge in the north-eastern field and from the regions related to the CND and the western streamer in the western field. In the eastern and southern fields, the H_2 emission is weaker than in other fields, but it is still significantly bright considering the RMS noise of $5 \times 10^{-21}\ \mathrm{W\ m^{-2}\ arcsec^{-2}}$ (then the blue color means about 4-σ detection).

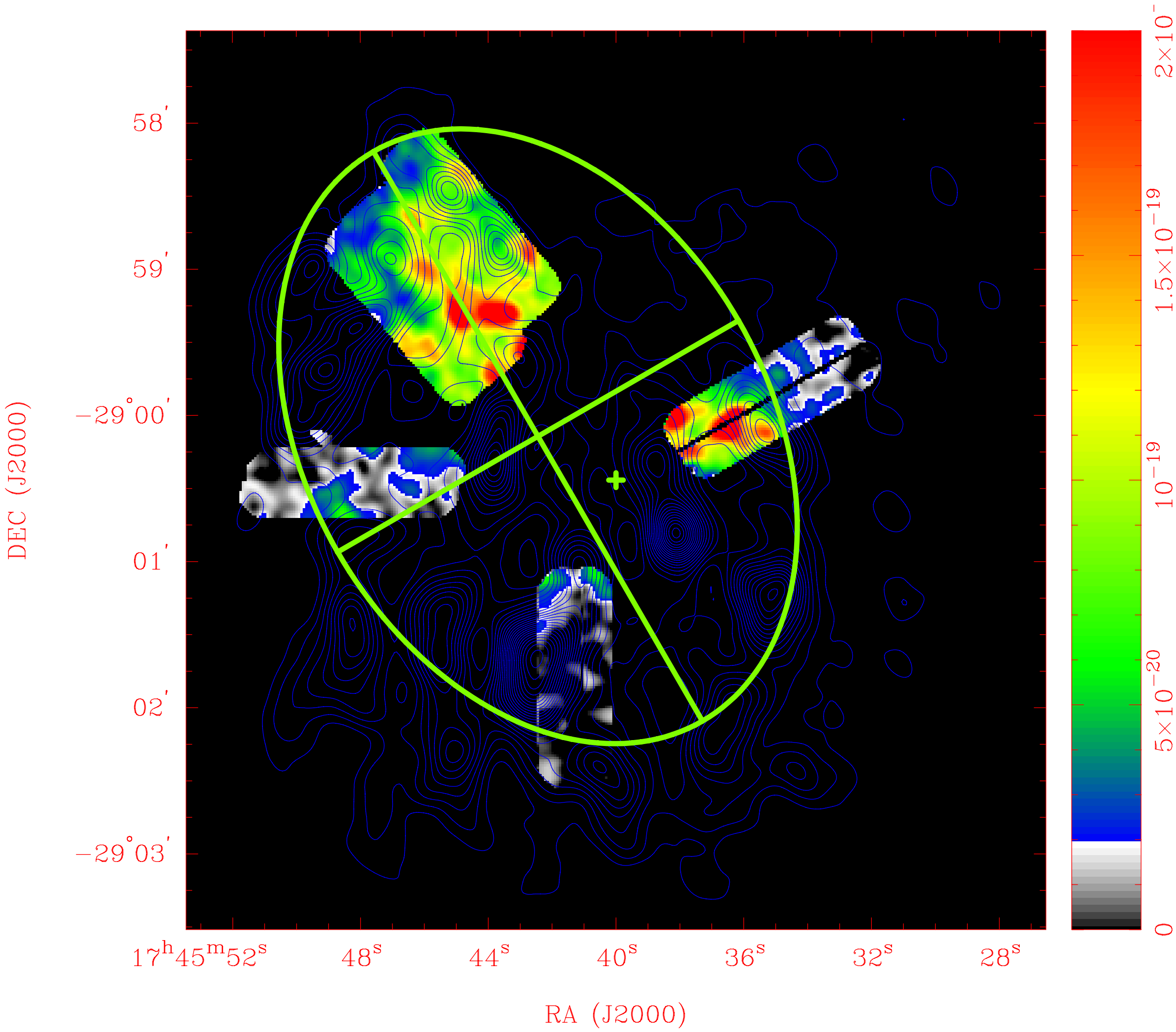

FIG. 5.5: Definition of the Sgr A East boundary in H_2 emission. An ellipse defining the outer boundary of Sgr A East is overlaid on the integrated intensity map of $\mathrm{H_2}\ 1{-}0\ \mathrm{S(1)}$ line emission (smoothed by Gaussian with FWHM = $5''$) with contours for NH_3 (3,3) emission from McGary, Coil, & Ho (2001). The color-scaled intensity level is indicated by the right-side bar in units of $\mathrm{W\ m^{-2}\ arcsec^{-2}}$ and the contour levels are in interval of 3-σ (the RMS noise $\sigma = 0.33\ \mathrm{Jy\ beam^{-1}\ km\ s^{-1}}$ where the beam size is $\sim 15'' \times 13''$). Major and minor axes of the ellipse are also indicated and the cross at the center of the image represents the position of Sgr A*.

An elliptical boundary is defined to trace the outer edges of the H_2 emitting regions with a center at $\alpha = 17^{\rm h}45^{\rm m}42\overset{\rm s}{.}13,\ \delta = -29°0'8\overset{''}{.}6$ (J2000), which is offset from Sgr A* by ($+32''$, $+18''$) or ~ 1.5 pc at the distance of 8.0 kpc to the Galactic center (Reid 1993). The ellipse has a semi-major radius of $a = 135''$ ($= 2\overset{'}{.}25 = 5.4$ pc), a semi-minor radius of $b = 95''$ ($= 1\overset{'}{.}58 = 3.8$ pc), and a position angle of $30°$ from north to east, which is almost parallel to the Galactic plane whose position angle is $\simeq 34°$.

The only conflict with this model is the southern field where the H_2 emission is situated well inside of the synchrotron shell in projection (see Figure 1.10). We believe that this southern H_2 emission is not radiated from the southern-most edge of the Sgr A East shell but from a position where the tilted surface of the shell contacts a molecular cloud (i.e. the southern streamer) in front of or behind it. Alternatively, the H_2 emission may be extended more to the south from the detected position but severely diminished and not detected due to a very high extinction toward the southern part of the southern streamer. In Figure 1.9, we can see the dust emission is significantly higher in this direction and the NH_3 opacity in this region is much higher ($\tau_{NH_3\ (1,1)}$ = 2–5) than in the region where H_2 is detected ($\tau_{NH_3\ (1,1)} \simeq 0$; see Figure 2 of Herrnstein & Ho 2005). The 1720 MHz OH masers detected at several positions around this region by Yusef-Zadeh et al. (1996, 1999a) may support this hypothesis because those authors interpreted these masers as indicators of shocks from Sgr A East toward its nearby molecular cloud, although Coil & Ho (2000) and Herrnstein & Ho (2005) argued that they originate from the interaction between Sgr A East and the SNR G 359.92-0.09. A similar interpretation is also possible for the $50\ \rm km\ s^{-1}$ cloud. In the north-eastern field of our H_2 observation, the H_2 intensity decreases toward the center of the $50\ \rm km\ s^{-1}$ cloud (Figure 5.5), where the dust emission is the strongest in Figure 1.9 and the NH_3 opacity is as high as in the southern streamer (Herrnstein & Ho 2005). Thus it is possible that, even though Sgr A East has expanded deeply into this cloud, the shock-excited H_2 emission is highly obscured.

Sgr A East is historically first identified and is traditionally and most frequently defined in the 6 cm synchrotron radiation (Ekers et al. 1983; Yusef-Zadeh & Morris 1987; Pedlar et al. 1989; see the red image in Figure 1.10 and the shaded area in Figure 5.6). Assuming the same center and the same position angle as our H_2 boundary, the projected 6 cm continuum shell can be fitted with an ellipse with $a_{6\ cm} = 1\overset{'}{.}7 = 4.2$ pc and $b_{6\ cm} = 1\overset{'}{.}3 = 3.0$ pc. These dimensions are smaller than those of the H_2 boundary by about 20 per cent.

The boundary of Sgr A East defined by H_2 emission is more consistent with the dust ring

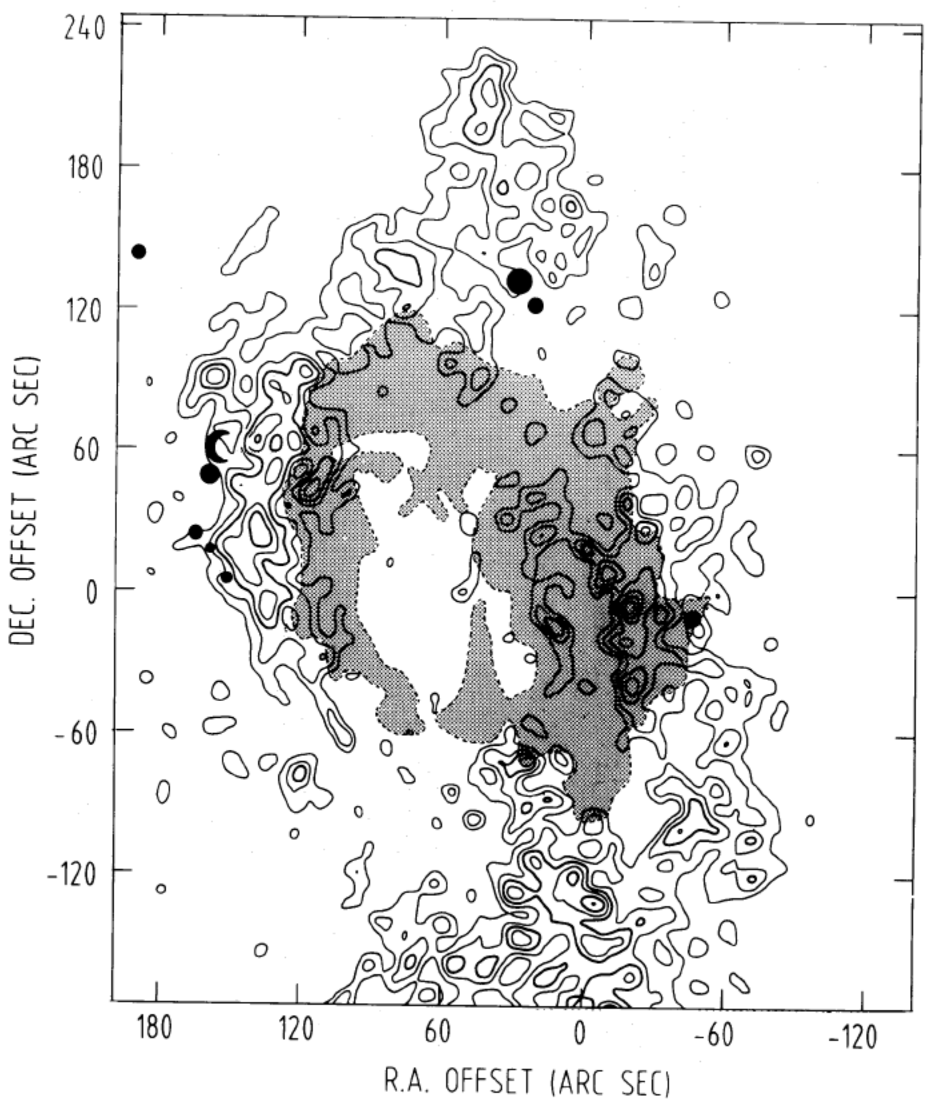

FIG. 5.6: 1.3 mm emission and 6 cm continuum maps of the central 10 pc from Mezger et al. (1989). The contours (90, 160 ... 930, 1230, 1530 ... 3330 mJy beam^{-1} where the beam size is $11''$) are 1.3 mm emission with emission from Sgr A* and Sgr A West subtracted. Shaded areas are defined by the second lowest contour of the 6 cm map of Ekers et al. (1983) pertaining to the synchrotron emission from Sgr A East. Black dots mark the positions of H II regions as observed by Yusef-Zadeh & Morris (1987). The coordinates are offset from the position of Sgr A*.

observed by Mezger et al. (1989) than is the outer edge of the 6 cm shell. Figure 5.6 shows the partial ring of 1.3 mm dust emission which surrounds the 6 cm synchrotron emission. This dust ring is well identified with the molecular clouds seen in NH_3 in Figure 1.10; the $50\ \mathrm{km\ s^{-1}}$ cloud, the northern ridge, the western streamer, and the southern streamer in NH_3 emission are easily matched with the dust ridges. Assuming again the same center and the same position angle with our H_2 boundary, the dust ring is fitted with an ellipse with $a_{dust} = 2\rlap{.}'5 = 6.0$ pc and $b_{dust} = 1\rlap{.}'5 = 3.7$ pc, which is nearly identical with the H_2 ellipse although the major axis of the dust ring is slightly (about 10 per cent) longer.

In the comparison between their 1.3 mm map and the 6 cm map, Mezger et al. (1989) argued that the magnetic field in the synchrotron source is created in regions of the shell well down-stream of the blast wave. This argument, together with the fact that the dust ring coincides well with the outer boundary of the H_2 emission implies that the H_2 boundary defined here traces the shock front from Sgr A East.

5.3 Sgr A East and Molecular Clouds

As seen so far, Sgr A East is physically in contact with and expanding into all of the surrounding molecular clouds; the $50\ \mathrm{km\ s^{-1}}$ cloud, the northern ridge, the molecular ridge, the southern streamer, the north-western part of the CND, and the western streamer. Since the hot cavity of Sgr A East is driving shocks into these clouds as discussed in Chapter 4, based on the directions of shock propagation, we can determine the arrangements of the clouds along the line-of-sight with respect to Sgr A East.

5.3.1 Shock Directions and Spatial Relationships

In addition to the spectra and the channel maps of H_2 and NH_3 emission in Chapter 4 (e.g. Figures 4.6, 4.9, and 4.10–4.16), we can also investigate the large scale spatial and kinematic structure of Sgr A East and the molecular clouds effectively by comparing the position-velocity diagrams (PVDs) of the H_2 and NH_3 emission. For six cuts indicated in Figure 5.7, the PVDs of the H_2 data we observed and the NH_3 data from McGary, Coil, & Ho (2001) are superimposed for direct comparisons (Figures 5.8–5.13).

In Figure 5.8, most of the NH_3 emission contours trace the $50\ \mathrm{km\ s^{-1}}$ cloud (the GMC M-0.02-0.07) and extend to the northern end of the molecular ridge (at positions $< -100''$).

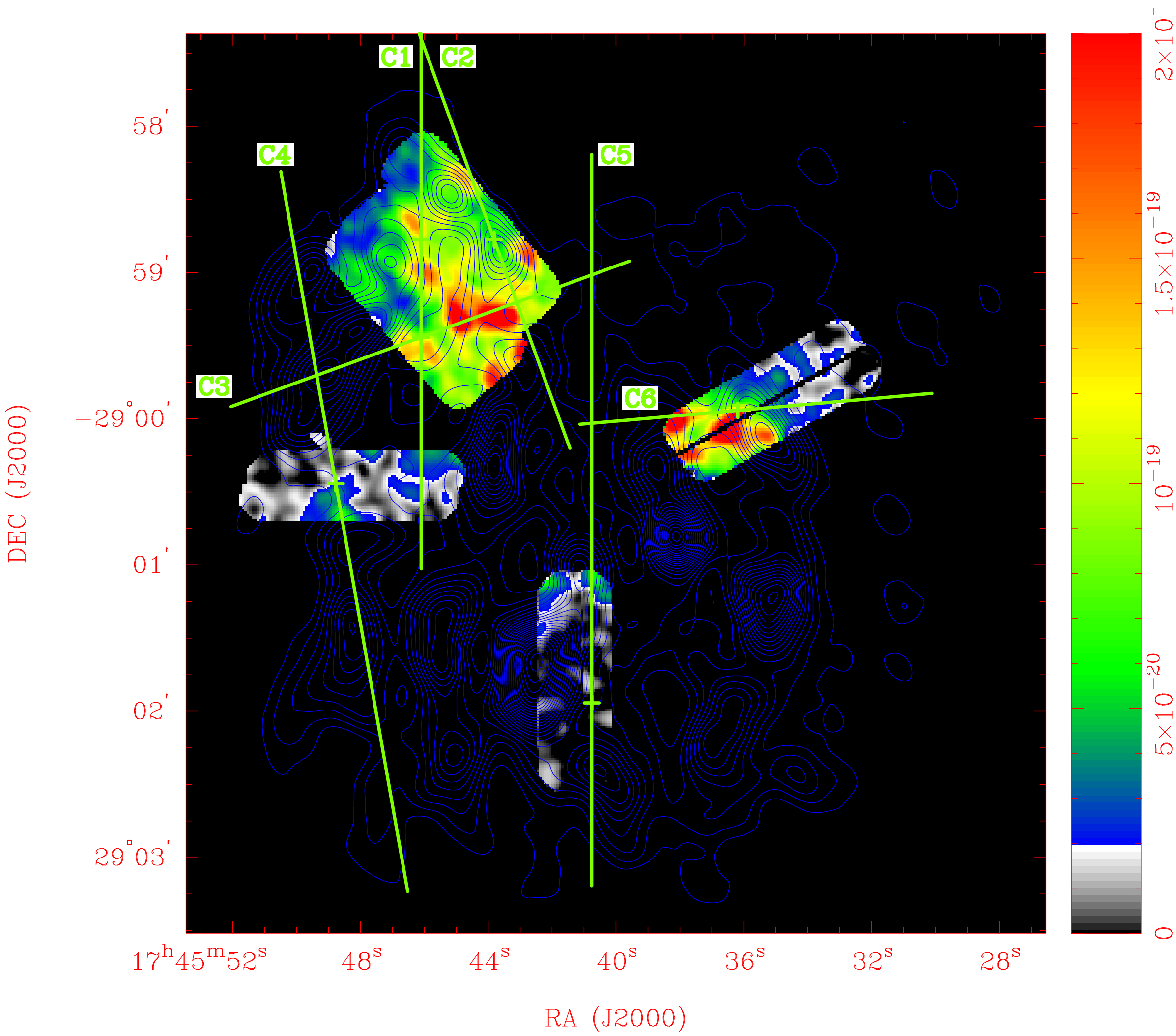

FIG. 5.7: Positions of the cuts for the position-velocity diagrams (PVDs) of $\mathrm{H_2}$ 1–0 $\mathrm{S(1)}$ and NH_3 (3,3) emission in Figures 5.8–5.13. For each cut, the labeled end indicates the direction of positive offset and the small cross corresponds to the reference (0) position in each PVD. The $\mathrm{H_2}\ 1-0\ \mathrm{S(1)}$ map was smoothed by Gaussian with FWHM = $5''$. The intensity scale and contour levels are the same as Figure 5.5.

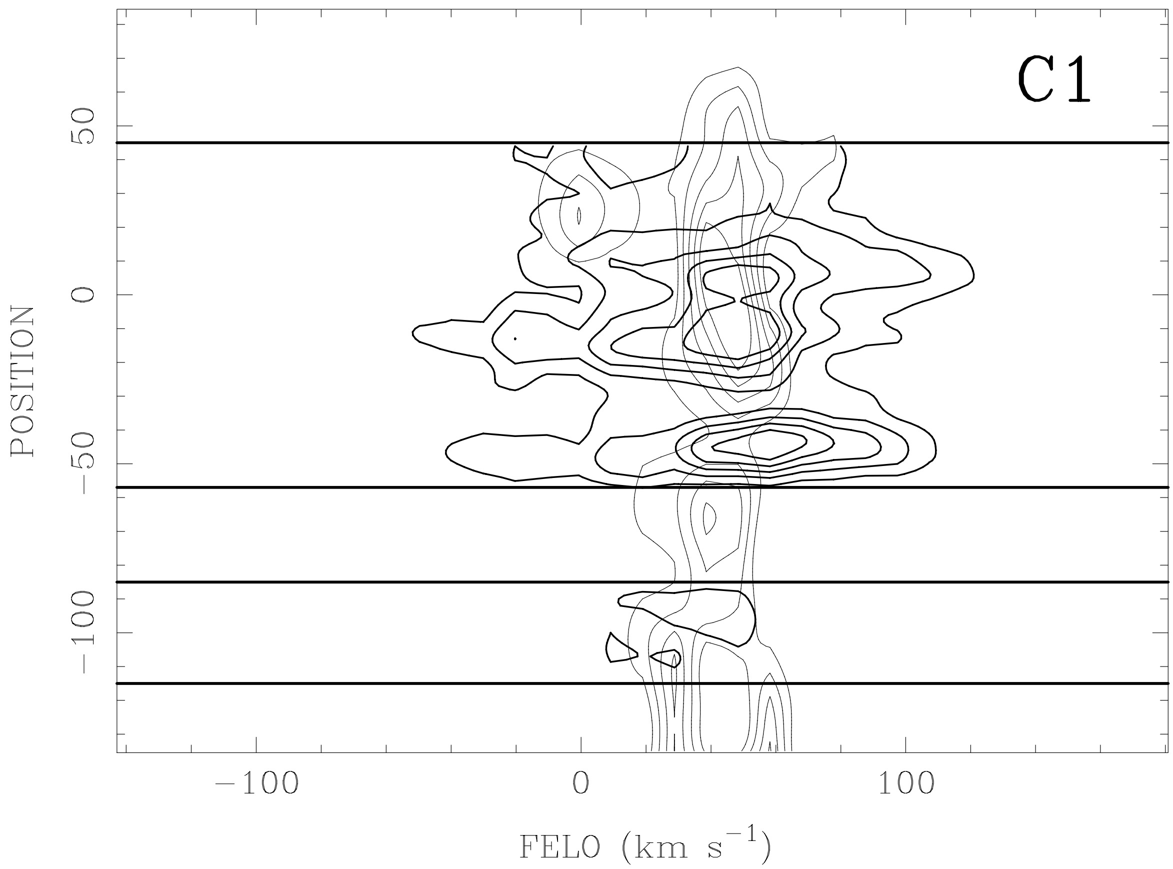

FIG. 5.8: Position-velocity diagram for H_2 $1-0$ $S(1)$ and NH_3 (3,3) emission at cut C1. Thick contours are for H_2 emission and thin contours are for NH_3. The contour levels are 2, 4, 6, 8, 10, 20, 40, 60, 80, and 100-σ for both contours where $\sigma_{H_2} = 1.5 \times 10^{-22}$ W m^{-2} arcsec^{-2} km^{-1} s and $\sigma_{NH_3} = 0.01$ Jy beam^{-1} (the beam size is $\sim 15'' \times 13''$). Positions in unit of arcsec are relative to the reference position which is marked on the cut in Figure 5.7. "FELO" of the horizontal axis means the radial velocity calculated using the approximation $c(\lambda^2 - \lambda_0^2)/(\lambda^2 + \lambda_0^2) = c(\lambda - \lambda_0)/\lambda_0$ in MIRIAD. Thick horizontal lines indicate the boundaries of the fields in which we performed the H_2 observations.

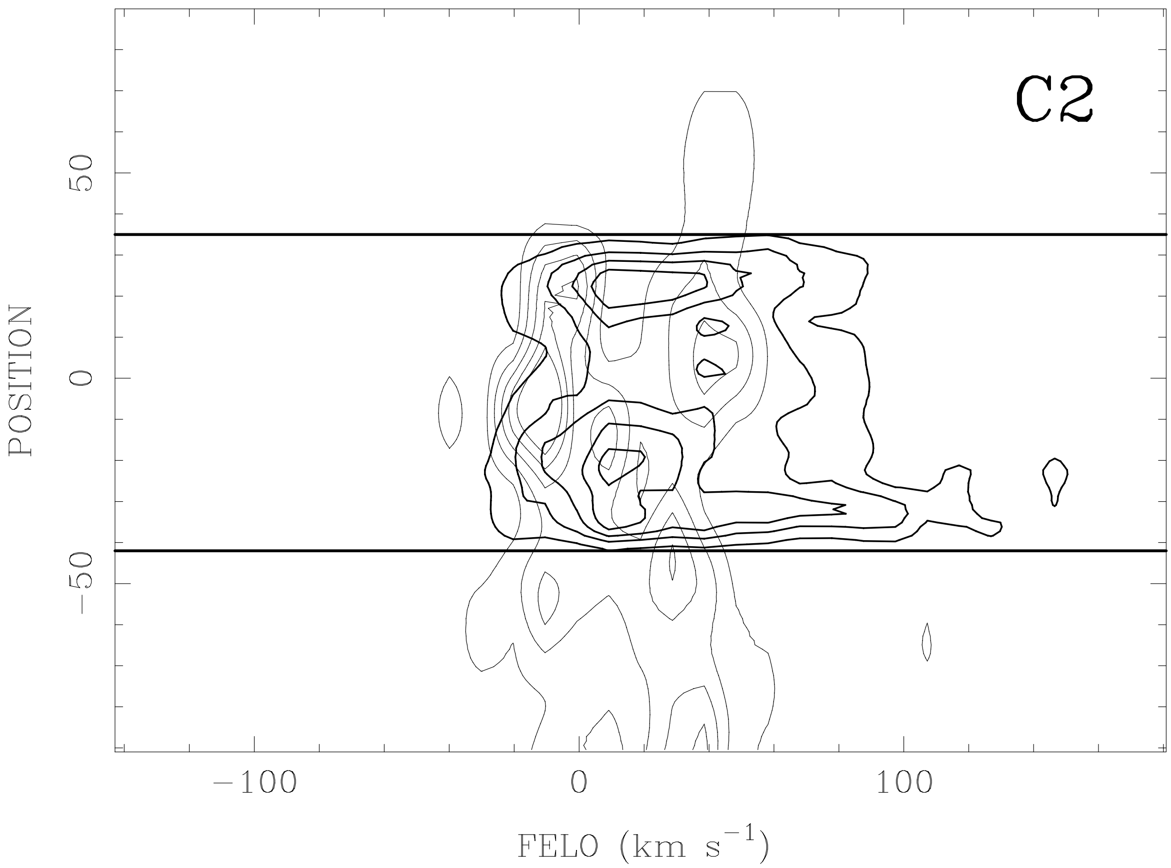

FIG. 5.9: Position-velocity diagram for H_2 1−0 S(1) and NH_3 (3,3) emission at cut C2. The other aspects are the same as Figure 5.8.

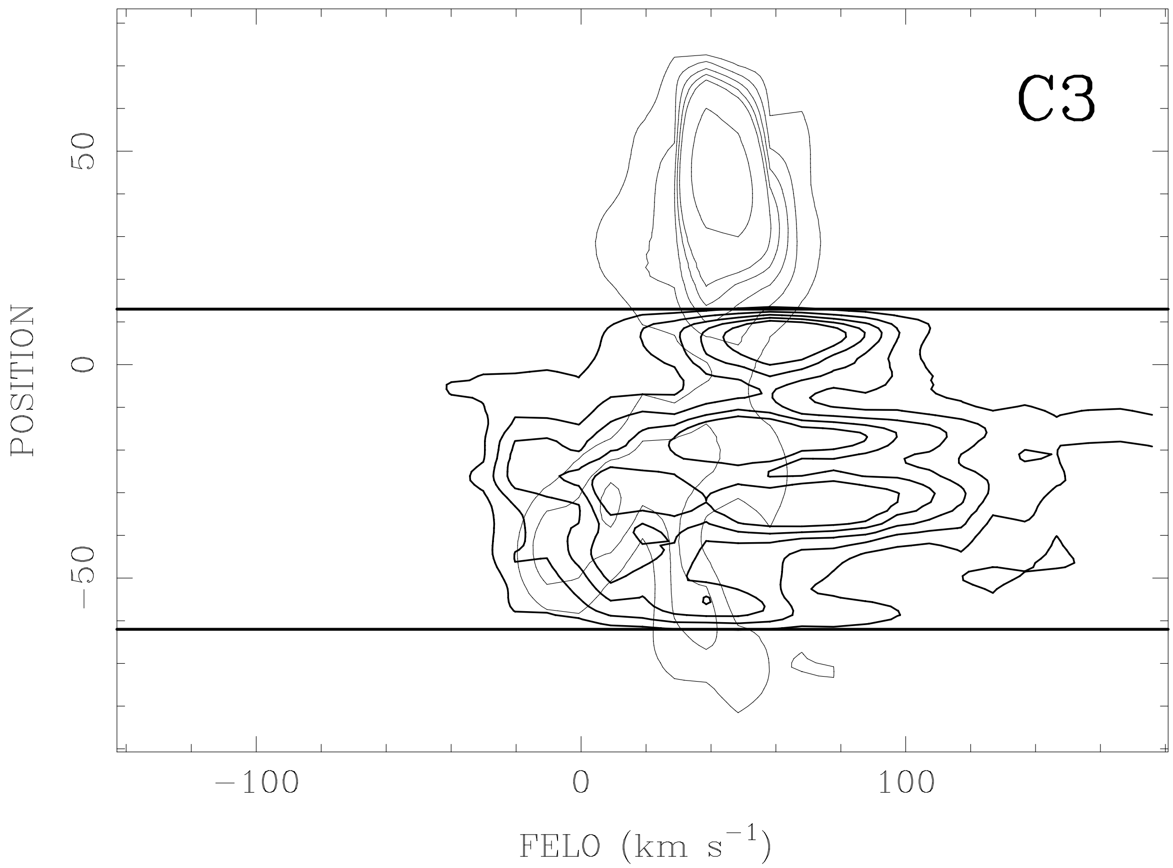

FIG. 5.10: Position-velocity diagram for H_2 $1-0$ $S(1)$ and NH_3 (3,3) emission at cut C3. The other aspects are the same as Figure 5.8.

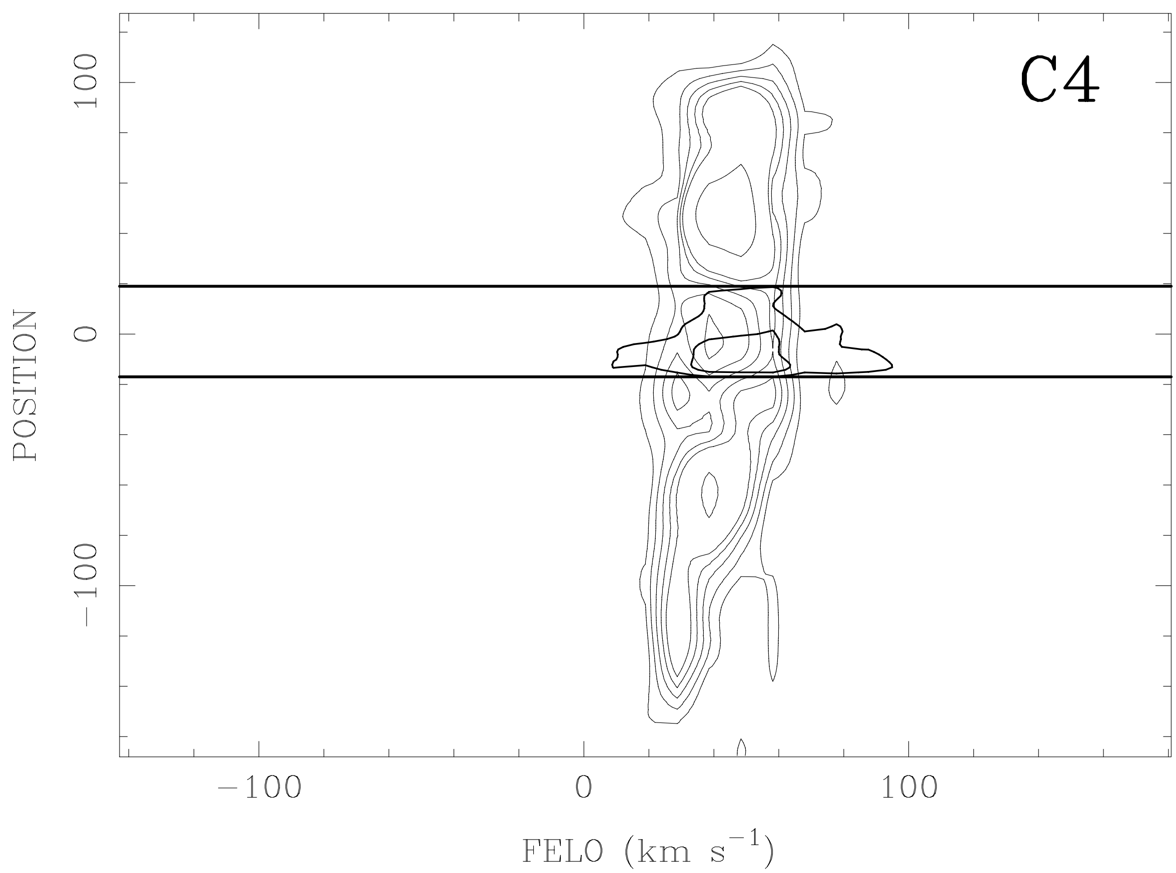

FIG. 5.11: Position-velocity diagram for H_2 $1-0$ S(1) and NH_3 (3,3) emission at cut C4. The other aspects are the same as Figure 5.8.

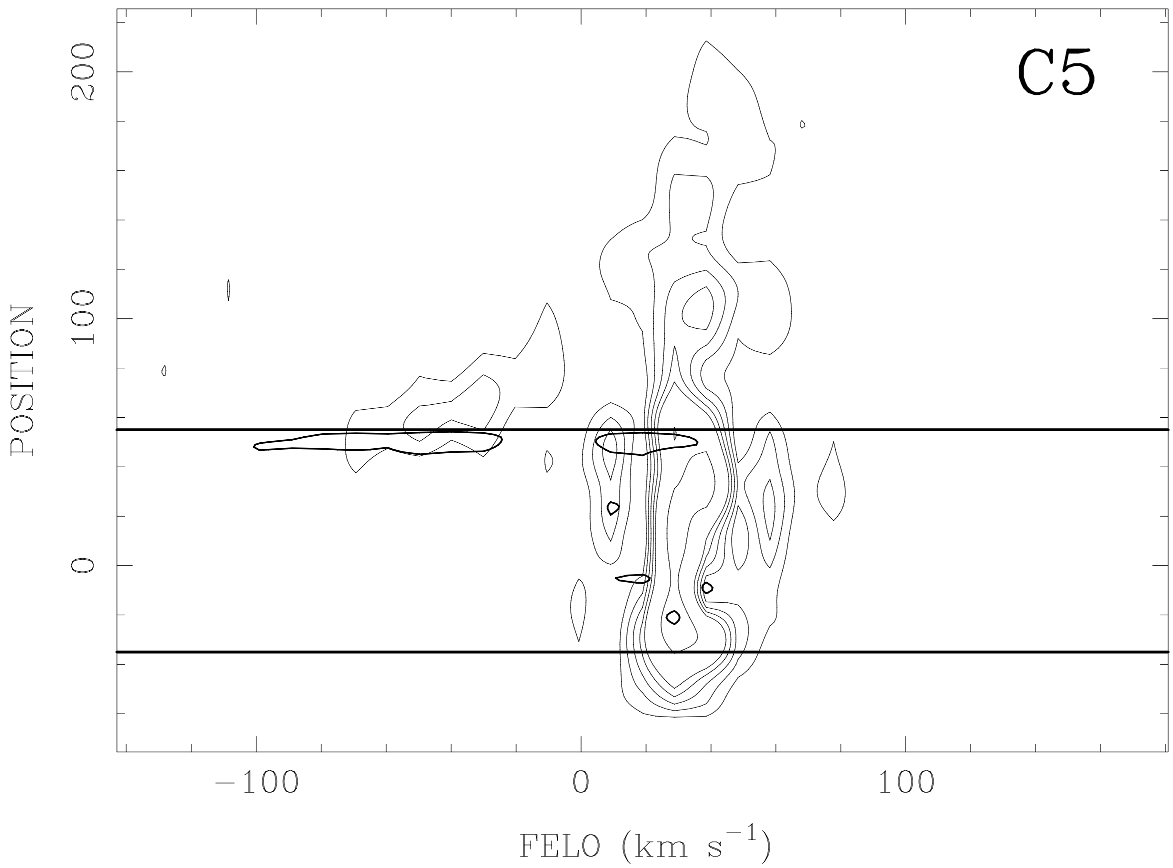

FIG. 5.12: Position-velocity diagram for H_2 $1-0$ S(1) and NH_3 (3,3) emission at cut C5. The other aspects are the same as Figure 5.8.

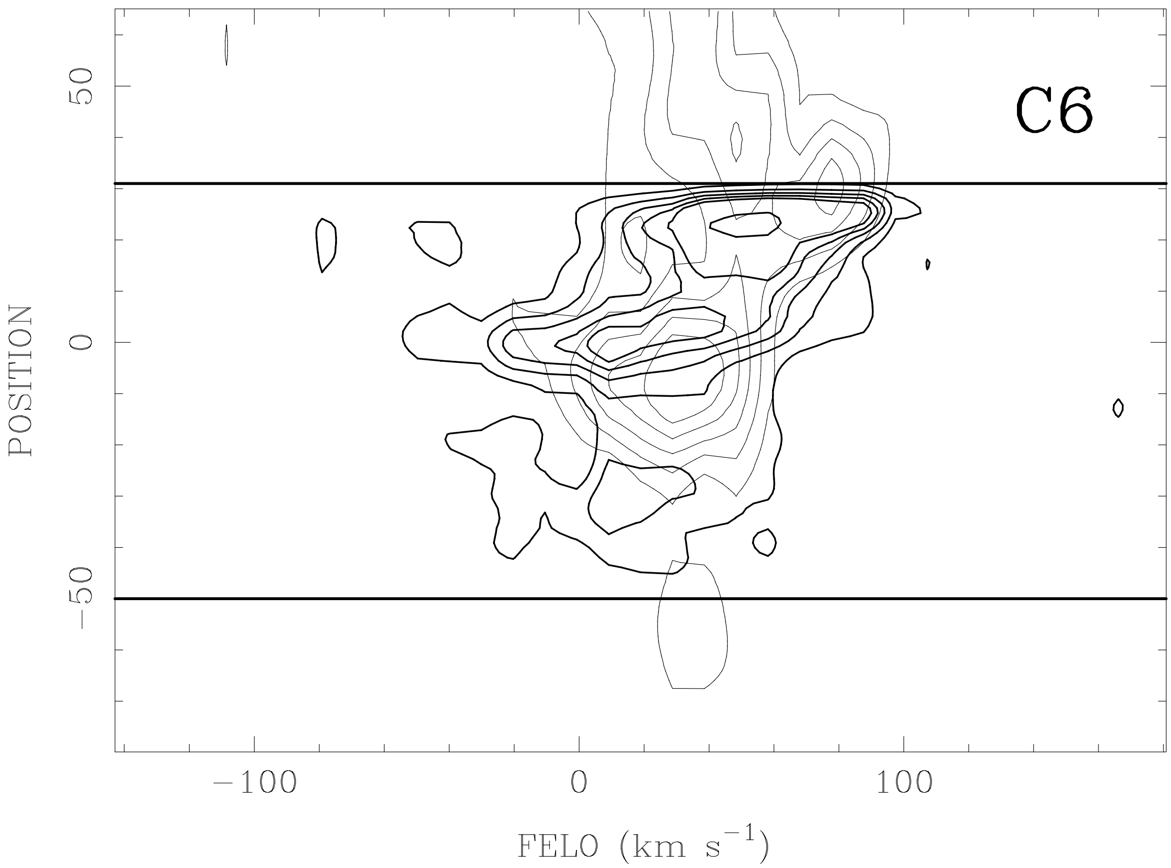

FIG. 5.13: Position-velocity diagram for H_2 $1-0$ S(1) and NH_3 (3,3) emission at cut C6. The other aspects are the same as Figure 5.8.

The small patch of emission at positions $10''$–$40''$ and velocity of about 0 km s^{-1} corresponds the northern end of the northern ridge. The H_2 emission observed in our north-eastern field (at positions between $-50''$ and $50''$) has similar velocities as but shows much broader velocity extension than NH_3; by as much as 60 km s^{-1}, both to positive and negative velocities. This implies that strong shocks are propagating both towards us and in the opposite direction along the line-of-sight, within the 50 km s^{-1} cloud. We can understand this if the western portion of the 50 km s^{-1} GMC actually envelops Sgr A East, which is expanding into it at both its front and back surfaces.

On the other hand, the H_2 emission from the northern end of the molecular ridge has a narrow and very similar velocity distribution as the NH_3 emission. H_2 from fluorescence could explain this. However, in the PVD for cut C4 (Figure 5.11) which more exactly passes through the center of the molecular ridge along its length, we can see that the H_2 contours are broader in velocity and extend farther to the red side than NH_3. Thus we are certain that Sgr A East is in physical contact with and driving shocks into the molecular ridge too, at least into its northern part (this is confirmed in the channel map, Figure 4.13). The velocity shift of H_2 here is about $+20 \text{ km s}^{-1}$ which is much smaller than in the 50 km s^{-1} cloud. However, considering that the molecular ridge is located at the outermost edge of the Sgr A East boundary and that its projected width is only about 1 pc, shocks from Sgr A East would propagate into the cloud nearly perpendicular to the line-of-sight and consequently the radial component of velocity shift of the shocked gas must be small. Nevertheless, we expect that the northern end of the molecular ridge is tipped slightly to the backside of Sgr A East since the H_2 emission there is red-shifted, i.e. the hot cavity of Sgr A East is located in front of the ridge and pushing its material farther away from us.

As for the small emission patch of the northern ridge in Figure 5.8, it is difficult to distinguish the H_2 emission that originated from this cloud from that from the 50 km s^{-1} cloud since two molecular clouds overlap along the line-of-sight. This problem is similar to the other PVDs related to the northern ridge (Figures 5.9 & 5.10 for cuts C2 and C3, respectively). However, there is a common aspect in these PVDs; there is no H_2 emission more blue-shifted than the NH_3. This implies either that Sgr A East is located in front of the northern ridge along the line-of-sight or that the H_2 emission does not originate from shocked gas. The latter interpretation is not likely; in Figure 5.9, the positions of the bright peaks of broad (as much as 100 km s^{-1}) H_2 line emission are more closely coincident with two NH_3 peaks of the northern ridge (at $\sim 0 \text{ km s}^{-1}$) than with the single peak of the 50 km s^{-1} cloud.

Evidence for red-shifted H_2 emission in the northern ridge can also be found in Chapter 4 (see spectrum S2 in Figure 4.9 and the channel map Figure 4.10). Therefore we conclude that it is the northern ridge that is located to the rear of Sgr A East and is being accelerated to larger, positive, velocities.

Cut C5 follows the southern streamer (see Figure 5.12). The NH_3 at $\sim 30\ \mathrm{km\ s^{-1}}$ is presented between $-60''$ and $+80''$, continues through the nuclear region (between $+90''$ and $+140''$) and reaches beyond the northern boundary of the CND. The weak NH_3 features at both sides of the southern streamer (at 10, 60, and 80 $\mathrm{km\ s^{-1}}$) are the satellite hyperfine lines of the strong main line (McGary & Ho (2002); Herrnstein & Ho (2005)), so have no additional kinematic meaning. The NH_3 feature with a very high velocity gradient between $+40''$ and $+100''$ is thought to be associated with the CND. The H_2 emission along the cut C5 is neither as bright (the signal-to-noise (S/N) ratio is between 2 and 4) nor as extended (only seen at $\sim 50''$). In spite of that, the H_2 emission is clearly blue-shifted from NH_3 by at least $20\ \mathrm{km\ s^{-1}}$ for both clouds. Hence we conclude that Sgr A East is located behind the southern streamer and the southern part of the CND, respectively.

Figure 5.13 includes emission from three different molecular features. One is the north-western part of the CND at position $> 20''$. The NH_3 emission from this cloud has a very broad velocity distribution ($\sim 100\ \mathrm{km\ s^{-1}}$) reflecting very complicated and energetic gas motions in the nuclear region. The related H_2 contours from $40''$ to $60''$ are as wide in velocity. The NH_3 emission contours here peak at $\sim 80\ \mathrm{km\ s^{-1}}$ and are skewed toward positive velocities while the H_2 emission is peaked at $\sim 50\ \mathrm{km\ s^{-1}}$ and is also bright toward lower velocities. This indicates that this part of the CND is located in front of Sgr A East.

The second feature is the northern half of the western streamer at $-30''$ to $10''$. The H_2 contours from the shocked gas at $\sim 0''$ are as wide as $\sim 130\ \mathrm{km\ s^{-1}}$ and extended slightly farther (by $\sim 30\ \mathrm{km\ s^{-1}}$) both to the blue side and the red side than the NH_3. Thus it is likely that this part of the western streamer actually surrounds the western part of Sgr A East and is being swept up by both the front and back of the expanding shell.

The third feature is the H_2 emission at $\sim -35''$, which must certainly originate in shocked gas considering its wide velocity distribution of $\sim 80\ \mathrm{km\ s^{-1}}$. However, it is not clear from which molecular cloud it arises. Since its position is beyond the boundary of Sgr A East comparing Figure 5.5 and Figure 5.7, we cannot determine its line-of-sight position with respect to Sgr A East. This H_2 feature beyond Sgr A East may be associated with another phenomenon or accelerating source. For example, it might be a manifestation of the bipolar streamers or outflows from the Galactic nucleus which are suggested by radio and X-ray observations (Yusef-Zadeh & Morris 1987; Maeda et al. 2002). However, the nature and origin of this H_2 feature is out of the scope of this study.

5.3.2 3-D Spatial Structure of the Central 10 Parsecs

In Section 5.1.2, we found a few points of agreement among the previous studies from the literature (Mezger et al. 1989; Coil & Ho 2000; Herrnstein & Ho 2005) on the 3-D structure of the inner 10 pc of the Galaxy.

(i) The Galactic nucleus including Sgr A West and the CND lies in front of Sgr A East but behind the southern streamer and a part of the $20~\mathrm{km~s^{-1}}$ cloud along the line-of-sight.

(ii) Sgr A East is expanding into the $50~\mathrm{km~s^{-1}}$ cloud (M-0.02-0.07), the northern ridge, and the western streamer.

(iii) The SNR G 359.92-0.09 is interacting with the southern part of the molecular ridge, with the eastern edge of the $20~\mathrm{km~s^{-1}}$ cloud, and with the southern edge of Sgr A East.

We can now add to them our conclusions in section 5.3.1 on the positional relationships between Sgr A East and the molecular clouds along the line-of-sight which are derived from the physical, in contact, interactions between them as follows.

(i) Sgr A East is expanding deeply into the western edge of the $50~\mathrm{km~s^{-1}}$ GMC which envelops it both at the front and rear of the ionized shell.

(ii) The molecular ridge is approximately at the same distance as the center of Sgr A East but the northern end of the ridge is tilted slightly to the back of it.

(iii) The northern ridge is located behind Sgr A East.

(iv) The northern-most end of the southern streamer and the CND lie in front of Sgr A East and are being pushed toward us by it.

(v) The northern part of the western streamer is located at the same distance with the center of Sgr A East and barely envelops the western edge of it.

Based on the measured outer boundary of the Sgr A East cavity defined by H_2 line emission and on all of the above conclusions, a revised model for the 3-D structure of the central 10 pc is suggested here as Figure 5.14.

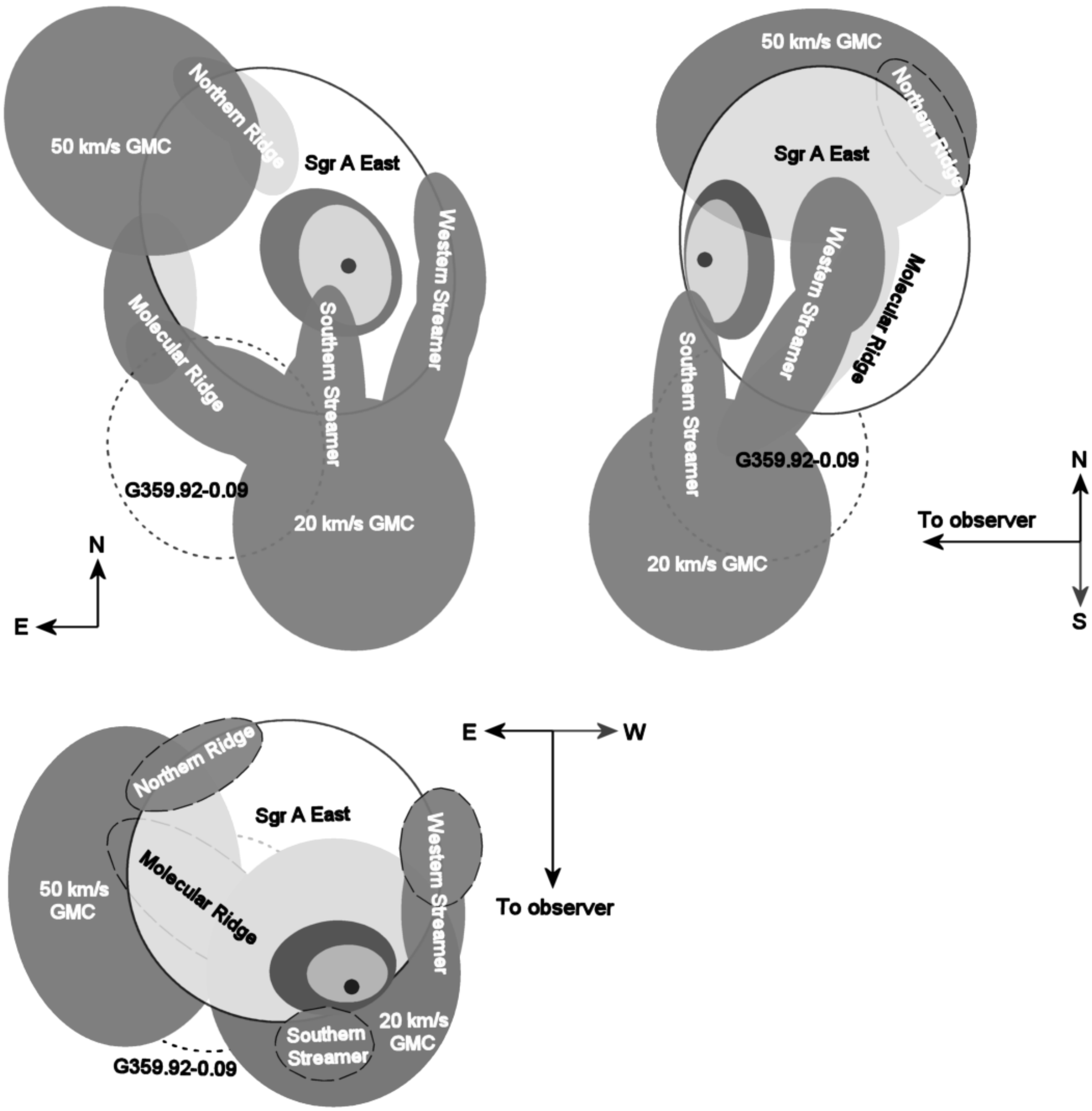

FIG. 5.14: Schematic drawing of the 3-D structure of the central 10 pc suggested by this study. Black dots indicate Sgr A*. Sgr A West and the CND are simplified as ellipses surrounding it.

5.4 Conclusions

Based on the H_2 emission map, we determined the outer boundary of Sgr A East where it is interacting and driving shocks into the surrounding molecular clouds, to be approximately an ellipse with a center at ($+32''$, $+18''$) or ~ 1.5 pc offset from Sgr A*, a major axis of 10.8 pc length, which is nearly parallel to the Galactic plane, and a minor axis of 7.6 pc length. This boundary is significantly larger than the synchrotron emission shell (Ekers et al. 1983; Yusef-Zadeh & Morris 1987; Pedlar et al. 1989) but is closely consistent with the dust ring suggested by Mezger et al. (1989).

Since, as shown in chapter 4 by the strong shock-excited H_2 emission, Sgr A East is in physical contact with all of its nearby molecular clouds (the $50\ \mathrm{km\ s^{-1}}$ cloud, the northern ridge, the molecular ridge, the southern streamer, the CND, and the western streamer), we are able to determine the positional relationships between Sgr A East and the molecular clouds along the line-of-sight using the shock directions as indicators. Based on the determined relationships and the strong evidence that Sgr A East is located in the Galactic center and in contact with the nucleus, we have suggested a revised model for the 3-D spatial structure of the central 10 pc of our Galaxy modifying the previous models of Mezger et al. (1989), Coil & Ho (2000), and Herrnstein & Ho (2005).

Our conclusions on the 3-D structure resolve most of the debates from the previous studies in the literature, which were summarized in Section 5.1.2, as follows.

(i) Is the nucleus in contact with or contained within Sgr A East?
– The Galactic nucleus is in physical contact with Sgr A East since the CND is pushed away toward us by the expanding hot cavity of Sgr A East.

(ii) Is the southern streamer falling into or interacting with the nucleus?
– It is highly probable that the southern streamer is falling into the nuclear region considering that Sgr A East is driving shocks to the northern-most part of this cloud where it meets the CND in projection.

(iii) Has Sgr A East expanded into the $50\ \mathrm{km\ s^{-1}}$ cloud significantly, or just started to contact it?
– In the H_2 data of the north-eastern field, we can see most of this region is filled with shocked gas from the $50\ \mathrm{km\ s^{-1}}$ cloud. This area corresponds to at least one third of that of the entire cloud. Thus Sgr A East has significantly penetrated the cloud.

(iv) Is Sgr A East interacting with the northern part of the molecular ridge?

– Yes, we detected shocked H_2 emission from the northern-most part of this cloud.

Among the questions from Section 5.1.2, we cannot answer those related to the $20\ \mathrm{km\ s^{-1}}$ cloud. We know the branches (the southern streamer and the western streamer) from this GMC are interacting with Sgr A East but the main body of this cloud is located far to the south, beyond the scope of our observations. Therefore it should be noted that the position and extent along the line-of-sight of this GMC in Figure 5.14 is uncertain.

REFERENCES

Balick B., & Brown R.L., 1974, ApJ, 194, 265

Coil A.L., & Ho P.T.P., 1999, ApJ, 513, 752

Coil A.L., & Ho P.T.P., 2000, ApJ, 533, 245

Ekers R.D., van Gorkom J.H., Schwarz U.J., & Goss W.M., 1983, A&A, 122, 143

Gatley I., Jones T.J., Hyland A.R., Beattie D.H., & Lee T.J., 1984, MNRAS, 210, 565

Geballe T.R., Bass F., & Wade R., 1989, A&A, 208, 255

Ghez A.M., et al., 2003, ApJ, 586, L127

Goss W.M., Schwarz U.J., Ekers R.D., & van Gorkom J.H., 1983, in Danziger J., Gorenstein P., eds, Proc. IAU Symp. 101, Supernova Remnants and Their X-Ray Emission. Dordrecht, Reidel, p. 65

Güsten R., 1987, in Backer D.C., ed., AIP Conf. Proc. Vol. 155, The Galactic Center, American Institute of Physics (AIP), New York, p. 19

Güsten R., & Downes D., 1980, A&A, 87, 6

Herrnstein R.M., & Ho P.T.P., 2005, ApJ, 620, 287

Maeda Y. et al., 2002, ApJ, 570, 671

Marr J.M., Rudolph A.L., Pauls T.A., Wright M.C., & Backer D.C., 1992, ApJ, 400, L29

Mezger P.G., Zylka R., Salter C.J., Wink J.E., Chini R., Kreysa E., & Tuffs R., 1989, A&A, 209, 337

McGary R.S., Coil A.L., & Ho P.T.P., 2001, ApJ, 559, 326

McGary R.S., & Ho P.T.P., 2002, ApJ, 577, 757

Morris M., & Serabyn E., 1996, ARA&A, 34, 645

Pak S., Jaffe D.T., & Keller L.D., 1996a, ApJ, 457, L43

Pak S., Jaffe D.T., & Keller L.D., 1996b, in Gredel R., ed., ASP Conf. Ser. Vol. 102, The Galactic Center. Astron. Soc. Pac., San Francisco, p. 28

Park S., Muno M.P., Baganoff F.K., Maeda Y., Morris M., Howard C., Bautz M.W., & Garmire G.P., 2004, ApJ, 603, 548

Pauls T.A., Johnston K.J., Wilson T.L., Marr J.M., & Rudolph A.L., 1993, ApJ, 403, L13

Pedlar A., Anantharamaiah K.R., Ekers R.D., Goss W.M., van Gorkom J.H., Schwarz U.J., & Zhao J.-H., 1989, ApJ, 342, 769

Reid M.J., 1993, ARA&A, 31, 345

Roberts D.A., & Goss W.M., 1993, ApJS, 86, 133

Sakano M., Warwick R.S., Decourchelle A., & Predehl P., 2003, MNRAS, 340, 747

Sandqvist Aa., Karlsson R., Whiteoak J.B., & Gardner F.F., 1987, in Backer D.C., ed., AIP Conf. Proc. Vol. 155, The Galactic Center, American Institute of Physics (AIP), New York, p. 95

Schödel R., Ott T., Genzel R., Eckart A., Mouawad N., & Alexander T., 2003, ApJ, 596, 1015

Yusef-Zadeh F., Lasenby A., & Marshall J., 1993, ApJ, 410, L27

Yusef-Zadeh F., Melia F., & Wardle M., 2000, Science, 287, 85

Yusef-Zadeh F., & Morris M., 1987, ApJ, 320, 545

Yusef-Zadeh F., Roberts D.A., Goss W.M., Frail D.A., & Green A.J., 1996, ApJ, 466, L25

Yusef-Zadeh F., Roberts D.A., Goss W.M., Frail D.A., & Green A.J., 1999a, ApJ, 512, 230

Yusef-Zadeh F., Stolovy S.R., Burton M., Wardle M., Melia F., Lazio T.J.W., Kassim N.E., & Roberts D.A., 1999b, in Falcke H. et al., eds, ASP Conf. Ser. Vol. 186, The Central Parsecs of the Galaxy. Astron. Soc. Pac., San Francisco, p. 197

Yusef-Zadeh F., Zhao J.H., & Goss W.M., 1995, ApJ, 442, 646

Zhao J.H., Goss W.M., & Ho P.T.P., 1995, ApJ, 450, 122

Chapter 6

Nature of Sgr A East

6.1 Introduction

As discussed in the previous chapters, Sgr A East plays an essential role in the large-scale structure and kinematics in the central 10 pc of our Galaxy. Since this object is situated between the Galactic nucleus and the surrounding molecular clouds in three dimensional (3-D) space as in Figure 5.14 and pushing out the clouds by its pressure of hot gas, Sgr A East is also thought to have a significant influence on the mass inflow to the Galactic nucleus as an obstructor. However, the nature of Sgr A East is still in controversy; we have not reached any consensus even on the origin of this important object yet.

In the early days after its discovery, Sgr A was often related to the violent phenomena observed in active galactic nuclei (AGNe) and quasi-stellar objects (QSOs) because its position is coincided with the center of the Galaxy as estimated from optical observations, i.e. it is apparently located in the Galactic nucleus (e.g. Downes & Maxwell 1966). Since Sgr A East was resolved from Sgr A in the early 1970's, however, it has frequently been interpreted as a supernova remnant (SNR) due to its shell structure and non-thermal spectrum (Jones 1974; Goss et al. 1983 and references therein; and see more recent references in Maeda et al. 2002). Some recent works, however, have suggested that the energy, size, and elongated morphology of Sgr A East cannot have been produced by a typical supernova (Yusef-Zadeh & Morris 1987; Mezger et al. 1989).

Mezger et al. (1989) estimate the required energy to produce Sgr A East in the dense environment of the Galactic center ($\sim 10^4\ \mathrm{cm}^{-3}$) to be more than 4×10^{52} ergs. Modeling of the entire spectrum of Sgr A East by Fatuzzo et al. (1999), which fits very well with the observations of the non-thermal radio emission of Sgr A East and *EGRET* γ-ray sources, supports the energy estimate by Mezger et al. (1989). Those authors concluded that a single supernova explosion could explain the existence of Sgr A East only if it occurred within the cavity formed by the stellar wind from a progenitor star. In that scenario, however, the formation of the cavity takes too much time ($\sim 10^6$ yr) compared with the orbital period ($\sim 10^5$ yr) of matter circling around the Galactic centre (Mezger et al. 1989).

Yusef-Zadeh & Morris (1987) suggested that a different kind of event which is related to the Galactic nucleus could create Sgr A East. For example, they hypothesize a strong and steady wind of $\sim 10^{-3}\ \mathrm{M_\odot}$ yr^{-1} emanating from the nucleus, the possible existence of which was suggested by Hall, Kleinmann, & Scoville (1982) and Geballe et al. (1984). In this case, it takes $\sim 10^5$ yr to make a cavity like Sgr A East and this period is enough to account for the displacement (~ 2 pc) between Sgr A* and the center of the Sgr A East shell with a proper motion at a velocity of $50\ \mathrm{km\ s^{-1}}$ which is typical near the Galactic nucleus. This pure wind hypothesis, however, has severe difficulties in accounting for the synchrotron emission of Sgr A East and needs some other process for generation of relativistic electrons within the shell.

On the other hand, Khokhlov & Melia (1996) hypothesize that Sgr A East may be the remnant of a solar mass star tidally disrupted by a $10^6\ \mathrm{M_\odot}$ super massive black hole (SMBH) of which Sgr A* is the most probable candidate. Their model can explain the elongated shape of Sgr A East as well as the extreme energetics ($\sim 4 \times 10^{52}$ ergs).

However, from the observation with the *Chandra X-ray Observatory*, Maeda et al. (2002) suggest that Sgr A East should be classified as a metal-rich 'mixed morphology' SNR. They argue that the model of Khokhlov & Melia (1996) cannot reproduce the metal-rich abundance observed at the centre of Sgr A East. They also conclude that a single Type II supernova explosion with an energy of 10^{51} ergs into a homogeneous ambient medium with a density of $10^3\ \mathrm{cm^{-3}}$ can most simply explain the results of both radio and X-ray observations, and thus that the extreme energy of $\sim 10^{52}$ ergs is not required.

Herrnstein & Ho (2005) estimated the energy of the progenitor explosion of Sgr A East based on their NH_3 data (McGary, Coil, & Ho 2001). Using the mass and kinematics of the western streamer, which have the strongest evidence for an interaction with Sgr A East (e.g. its long, filamentary structure, its curvature closely matching the western edge of Sgr A East, and the high velocity gradient of $25\ \mathrm{km\ s^{-1}\ pc^{-1}}$ along its length), they calculated an explosion energy of 2–9 $\times 10^{51}$ ergs and concluded that Sgr A East was produced by a single supernova.

The energy required to make the Sgr A East shell is the key parameter which constrains these hypotheses, but estimates of this energy are still controversial as seen above. In principle, the energy of the explosive event can be directly measured by studying regions where Sgr A East is colliding with ambient interstellar material. The physical properties of interaction such as shock velocity, which is estimated in this study, can constrain the various hypothesis on the origin of the Sgr A East.

6.2 Initial Energy of the Sgr A East Explosion

In this section, we estimate the explosion energy of Sgr A East using the shock velocities measured (in Chapter 4) from the interacting regions between this hot cavity and its surrounding molecular clouds. We use the model of Shull (1980) for the evolution of a SNR in a molecular cloud of uniform density as Herrnstein & Ho (2005) did in their estimations. We also followed the calculations of Mezger et al. (1989) using the model of Wheeler, Mazurek, & Sivaramakrishnan (1980). Both calculations did not make any meaningful difference in the results. Sgr A East is thought to be in a pressure driven radiative phase (or snow-plow phase) in which the timescale for radiative cooling becomes less than the dynamical timescale and a thin, dense shell is driven outward by thermal pressure from a hot interior with the shock front (e.g. see Mezger et al. 1989; Maeda et al. 2002; Herrnstein & Ho 2005).

The current kinetic energy of the expanding shell is given by

$$E_{shell} = \frac{2\pi}{3} \, R_{shell}^3 \, n_0 \, m_H \, V_{shell}^2 \tag{6.1}$$

where R_{shell} is the current radius of the shell, n_0 is the mean initial H number density of the pre-shock gas, m_H is the proton mass, and V_{shell} is the expansion velocity of the shell material (e.g. Mezger et al. 1989). In the snow-plow phase, the energy of the initial explosion, E_0, is related to the current kinetic energy of the shell by

$$\left(\frac{E_0}{E_{shell}} \right) = \left(\frac{R_{shell}}{R_{sg}} \right)^2 \tag{6.2}$$

where R_{sg} is the radius at the time of shell generation, t_{sg}. The shell radius at time t is given by

$$R_{shell} = 0.329 \left(\frac{E_0}{10^{51}\ \mathrm{ergs}}\right)^{1/4} \left(\frac{n_0}{10^4\ \mathrm{cm}^{-3}}\right)^{-1/2} \left(\frac{t}{t_{sg}}\right)^{2/7} \quad [\mathrm{pc}]. \qquad (6.3)$$

Then substituting $R_{sg} = R_{shell}(t = t_{sg})$ from equation 6.3 into equation 6.2,

$$E_0 = 4.3 \times 10^{51} \left(\frac{E_{shell}}{10^{51}\ \mathrm{ergs}}\right)^{2/3} \left(\frac{R_{shell}}{1\ \mathrm{pc}}\right)^{4/3} \left(\frac{n_0}{10^4\ \mathrm{cm}^{-3}}\right)^{2/3} \quad [\mathrm{erg}] \qquad (6.4)$$

where E_{shell} is calculated from equation 6.1.

R_{shell} and V_{shell} are assumed to be the same as the mean of the major and minor radii of the elliptical boundary (defined in Chapter 5) and the shock velocity, V_{shock} (measured in Chapter 4), respectively, and we can use the values obtained from the observations for these parameters. We need a hypothesis, however, for n_0 and suppose two extreme cases for the density conditions under which the explosion of Sgr A East occurred; in a dense giant molecular cloud (scenario I) and in a low density halo (scenario II). For each scenario of density condition, we use both estimates of shock velocity from Chapter 4; C-shocks propagating through molecular clouds (case A) and C & J-shocks through dense clumps and inter-clump medium, respectively (case B).

6.2.1 Scenario I: Explosion in a Giant Molecular Cloud

If Sgr A East exploded in a giant molecular cloud (GMC) that is very similar to the $50\ \mathrm{km\ s}^{-1}$ cloud (M-0.02-0.07) or the $20\ \mathrm{km\ s}^{-1}$ cloud (M-0.13-0.08), we can directly use the density condition in the environment where shocked H_2 emission is currently observed.

In case A, shocks with a mean velocity of $V_{shock,A} = 109\ \mathrm{km\ s}^{-1}$ are propagating through molecular clouds with a mean H_2 density of $n_{H_2,A} = 10^4\ \mathrm{cm}^{-3}$ (see Section 4.3.2). Thus $V_{shell,I-A} = V_{shock,A} = 109\ \mathrm{km\ s}^{-1}$ and $n_{0,I-A} = 2\ n_{H_2,A} = 2 \times 10^4\ \mathrm{cm}^{-3}$. Since the mean radius of $R_{shell,I} = 4.6$ pc, which is derived from the elliptical boundary of 5.4 pc $\times$ 3.8 pc (see Section 5.2), the kinetic shell energy calculated from equation 6.1 is $E_{shell,I-A} = 2.3 \times 10^{52}$ ergs and the initial explosion energy $E_{0,I-A} = 4.2 \times 10^{53}$ ergs from equation 6.4.

In case B, J-shocks have a mean velocity of $V_{shock,B} = 104\ \mathrm{km\ s}^{-1}$ in a inter-clump medium with $n_{H_2,B} = 5 \times 10^3\ \mathrm{cm}^{-3}$ (see Section 4.3.3). Since according to Walmsley et al. (1986) eighty per cent of the cloud mass exists as the inter-clump medium within a GMC in the Galactic center, we assume $V_{shell,I-B} = V_{shock,B} = 104\ \mathrm{km\ s}^{-1}$ and $n_{0,I-B} = 2\ n_{H_2,B} = 10^4\ \mathrm{cm}^{-3}$. Then we obtain $E_{shell,I-B} = 1.0 \times 10^{52}$ ergs and $E_{0,I-B} = 1.5 \times 10^{53}$ ergs, which are lower limits since twenty per cent of the cloud mass confined in the dense clumps are ignored in the calculations.

In this scenario of an explosion in a GMC, we estimate an explosion energy of 2–4 $\times 10^{53}$ ergs depending on the assumptions of shock properties in the outer boundary regions of Sgr A East. The explosion energy estimated here is an upper limit since it is more likely that the explosion occurred in an inhomogeneous environment. If it had happened in a homogeneous medium, a mostly perfect shell or ring in projection should be made as a result. Observations on the surrounding molecular material, however, report a partial ring or fragmented shell-like structure composed of several molecular clouds (e.g. Mezger et al. 1989; McGary, Coil, & Ho 2001; see our structure model in Chapter 5).

6.2.2 Scenario II: Explosion in a Low Density Halo

In their observations of radio continuum from the whole region of the Sgr A complex in various wavelengths (6, 20, and 90 cm), Pedlar et al. (1989) reported a low-frequency turnover in the non-thermal spectrum of Sgr A East, which means the spectral index between 20 cm and 90 cm is flatter (-0.3 to 0.0) than that between 20 cm and 6 cm (-1.1 to -0.9). They concluded that it indicates a presence of an ionized gas halo and its free-free absorption extending over the Sgr A East. Anantharamaiah, Pedlar, & Goss (1999) further suggest that this halo has an extent of ~ 9 pc and a density of 10^2–$10^3\ \mathrm{cm}^{-3}$ from their observations of recombination lines.

On the other hand, Uchida et al. (1998) suggested that Sgr A East is likely to be in the region of non-solid-body rotation near the gravitational center of the Galaxy, where the rotation time scale is $\sim 4 \times 10^4\ R^{1.5}$ yr at Galactocentric radius R in pc (Lugten et al. 1986). Differential rotation shears the ISM and smoothes it out into a homogeneous medium in a few rotation cycles ($\sim 10^5$ yr). The range of the non-solid-body rotation region is supposed to be $R = 1$–10 pc.

From the fact that the ionized gas halo with a size of ~ 9 pc can be included within the non-solid-body rotation region in projection, in their discussion on the evolution of Sgr A East, Maeda et al. (2002) assumed that the ionized gas halo is filling the non-solid-body rotation region with a nearly homogeneous density of $10^3\ \mathrm{cm}^{-3}$ (due to the shearing), and that Sgr A East exploded in this ionized gas halo.

We regard the assumption of Maeda et al. (2002) as the other extreme case for the ambient gas density, scenario II. This density condition must be the lower limit since there is no evidence that the ionized gas halo occupies the non-solid-body rotation region along the line-of-sight. On the contrary, there exist many dense molecular clouds at $R < 10$ pc. Therefore explosion energy of Sgr A East estimated in this scenario is a lower limit.

In this scenario, we assume a situation that the shock front of Sgr A East has just started to contact its surrounding molecular clouds and the shocks are slowed down by dense gas in the clouds. Since the measured shock velocities from the H_2 lines are for these slowed shocks, we use instead the velocities of fast shocks having propagated through the low density gas halo before they contact the molecular clouds. The velocity of the fast ambient shocks in the halo can be derived by

$$\frac{v_{s,halo}}{v_{s,cloud}} = \sqrt{\frac{n_{cloud}}{n_{halo}}} \tag{6.5}$$

where $n_{halo} = 10^3\ \mathrm{cm}^{-3}$. On the other hand, as for the compressed shell, it is reasonable to regard it as the synchrotron shell which contacts the inner edge of the dust ring observed by Mezger et al. (1989) in scenario II. Hence we use $R_{shell,II} = 3.7$ pc, which is smaller by 80 per cent than the size determined from the H_2 emission, in the calculations of this section.

In case A for the shock velocity, using $V_{s,cloud,A} = 109\ \mathrm{km\ s}^{-1}$ and $n_{cloud,A} = 2 \times 10^4\ \mathrm{cm}^{-3}$, we calculate $V_{shell,II-A} = V_{s,halo,A} = 487\ \mathrm{km\ s}^{-1}$ and $n_{0,II} = n_{halo} = 10^3\ \mathrm{cm}^{-3}$ from equation 6.5. Then the kinetic shell energy calculated from equation 6.1 is $E_{shell,II-A} = 1.2 \times 10^{52}$ ergs and the initial explosion energy $E_{0,II-A} = 2.7 \times 10^{52}$ ergs from equation 6.4.

In case B, using $V_{s,cloud,B} = 104\ \mathrm{km\ s}^{-1}$ and $n_{cloud,B} = 10^4\ \mathrm{cm}^{-3}$ for the inter-clump medium in a molecular cloud, we calculate $V_{shell,II-B} = V_{s,halo,B} = 329\ \mathrm{km\ s}^{-1}$ and $n_{0,II} = n_{halo} = 10^3\ \mathrm{cm}^{-3}$ from equation 6.5. Then we obtain $E_{shell,II-B} = 5.1 \times 10^{51}$ ergs and $E_{0,II-B} = 1.6 \times 10^{52}$ ergs.

6.2.3 Comparison with Other Studies

In Table 6.1 we summarize the results of the estimations on the explosion energy of Sgr A East in the previous sections. As we mentioned above we regard the energies estimated under the conditions of scenario I as upper limits and those from scenario II as lower limits.

Mezger et al. (1989) estimated the required energy to produce Sgr A East within a GMC with a density of $10^4\ \mathrm{cm}^{-3}$ (as our scenario I) to be more than 4×10^{52} ergs. Their lower limit is a few times smaller than ours from scenario I (1.5×10^{53}). Considering that they assumed

TABLE 6.1: Estimations on the Explosion Energy and Age of Sgr A East

Case[a]	n_0 (cm^{-3})	$R_{shell}{}^b$ (pc)	$V_{shell}{}^c$ (km s^{-1})	E_0 (erg)	Age (yr)
I-A	2×10^4	4.6	109	4.2×10^{53}	2.5×10^4
I-B	10^4	4.6	104	1.5×10^{53}	2.7×10^4
II-A	10^3	3.7	487	2.7×10^{52}	4.6×10^3
II-B	10^3	3.7	329	1.6×10^{52}	6.8×10^3

[a] I = explosion in a GMC. II = explosion in a low density halo. A = fast C-shocks in a strong magnetic field. B = composition of C & J-shocks. (see text for more detailed descriptions.)

[b] Mean of the major and minor radii of an elliptical boundary.

[c] Assumed to be the same as a shock velocity.

a lower limit of shock velocity as $\sim 50~\mathrm{km~s^{-1}}$ which is needed to ionize the ambient hydrogen gas ($\frac{1}{2} m_H V_{shock}^2 \geq$ 13.6 eV) in order to explain the radio continuum emission within Sgr A East, their estimate is consistent with ours using the measured shock velocities of $\sim 100~\mathrm{km~s^{-1}}$; then their lower limit increases by a factor of 2.4 and becomes 1×10^{53} ergs.

Based on the small gas mass and thermal energy of 10^{49} ergs inferred from *Chandra* X-ray observations of hot gas associated with Sgr A East, Maeda et al. (2002) suggested that their results are consistent with the ejecta by a single Type II supernova explosion with an energy of 10^{51} ergs into a homogeneous ambient medium with a density of $10^3~\mathrm{cm^{-3}}$. Assuming these conditions of explosion and adopting the age of $\sim 10^4$ yr which is estimated by Uchida et al. (1998) for Sgr A East, which is consistent with other studies (e.g. Mezger et al. 1989; Herrnstein & Ho 2005), they predicted current velocities of $\sim 20~\mathrm{km~s^{-1}}$ for the shocks driven by Sgr A East into the $50~\mathrm{km~s^{-1}}$ cloud. As seen in Chapter 4, however, the velocities of shocks currently propagating into the $50~\mathrm{km~s^{-1}}$ cloud are measured to be $\sim 100~\mathrm{km~s^{-1}}$. Therefore we conclude that Maeda et al. (2002)'s estimate on the explosion energy of Sgr A East is significantly underestimated.

Herrnstein & Ho (2005) estimated an energy of 2–9 $\times 10^{51}$ ergs for the Sgr A East explosion using the mass and kinematics of molecular clouds obtained from their $\mathrm{NH_3}$ observations. They estimated the current kinetic energy of the expanding molecular shell as 0.4–2 $\times 10^{51}$ ergs and the initial gas density of ambient medium as 600–1000 cm^{-3} assuming that only the western streamer ($M \simeq 4 \times 10^3$ $\mathrm{M_\odot}$) has been swept out by the expansion of Sgr A East. However, they missed the northern ridge ($M \simeq 2 \times 10^3$ $\mathrm{M_\odot}$) out of their assumptions although they stated that this cloud is also highly possibly affected by the impact of Sgr A East like the western streamer. In addition to this, as seen in the previous chapters, our study has shown that the CND ($M > 10^4$ $\mathrm{M_\odot}$; Yusef-Zadeh, Melia, & Wardle 2000) and a significant portion, at least one third, of the $50\ \mathrm{km\ s^{-1}}$ cloud ($M \simeq 5 \times 10^4$ $\mathrm{M_\odot}$) have been expanded by Sgr A East as well. Thus it is possible that Herrnstein & Ho (2005)'s estimate on the explosion energy of Sgr A East is underestimated by several times and consequently a corrected energy would certainly exceed that a single supernova can generate.

6.3 Age of Sgr A East

According to Shull (1980), the time of shell generation is given by

$$t_{sg} = 114 \ \left(\frac{E_0}{10^{51}\ \mathrm{ergs}}\right)^{1/8} \ \left(\frac{n_0}{10^4\ \mathrm{cm}^{-3}}\right)^{-3/4} \quad [\mathrm{yr}]. \tag{6.6}$$

Substituting this equation into equation 6.3 and solving for t, we can calculate the age of Sgr A East with

$$t = 114 \ \left(\frac{R_{shell}}{0.329\ \mathrm{pc}}\right)^{7/2} \ \left(\frac{E_0}{10^{51}\ \mathrm{ergs}}\right)^{-3/4} \ \left(\frac{n_0}{10^4\ \mathrm{cm}^{-3}}\right) \quad [\mathrm{yr}], \tag{6.7}$$

using the estimated explosion energy, E_0, in the previous section.

We present our estimates on the age of Sgr A East in Table 6.1, which are $\sim 3 \times 10^4$ yr in the case of scenario I and 5000–7000 yr for scenario II. Our results for both scenarios of the Sgr A East evolution satisfy the constraint of the non-solid-body rotation in the central 10 pc of the Galaxy; i.e. any structure would be sheared and eventually smoothed out by differential rotation in $\sim 10^5$ yr (e.g. see Maeda et al. 2002).

The derived age of $\sim 3 \times 10^4$ yr in scenario I is well consistent with the estimation of Uchida et al. (1998) who modeled the shearing effect in detail and used the elongated shape of Sgr A East to constrain its expansion time scale as a few 10^4 yr. Our result is also consistent with Mezger et al. (1989)'s calculation of $\sim 5 \times 10^4$ yr for a strong explosion with an energy of $\sim 6 \times 10^{52}$ ergs deep inside a dense molecular cloud with $n_H = 10^4\ \mathrm{cm}^{-3}$.

On the other hand, the estimated age of (5–7) $\times 10^3$ yr for scenario II is similar to the age of 7500 yr derived by Mezger et al. (1989) for a model in which an explosion occurred within a low-density bubble, which is supposed to be blown by the wind from a massive progenitor or from the Galactic center, inside a dense GMC. Although Mezger et al. (1989)'s model of bubble is excluded by the constraint of the differential rotation, this consistency shows our calculations under the low density condition are reasonable.

6.4 Candidates for the Sgr A East Explosion

There are several different hypotheses for the origin of Sgr A East; e.g., a single explosion of typical supernova with an energy of 10^{51} ergs (e.g. Jones 1974; Goss et al. 1983; Maeda et al. 2002; Herrnstein & Ho 2005), a supernova within a bubble blown by some winds (e.g. Yusef-Zadeh & Morris 1987; Mezger et al. 1989), and a different kind of explosive event with an extreme energy of $\gtrsim 10^{52}$ ergs like a tidal disruption by the SMBH in the Galactic center (Khokhlov & Melia 1996).

The explosion energy of Sgr A East is estimated to be 2×10^{52} ergs $< E_0 < 4\times10^{53}$ ergs in this study. This extremely high energetics excludes the hypothesis of a single, typical, supernova for the origin of Sgr A East. On the other hand, we exclude the models with wind-bubble which expect a time required for the bubble formation to be 10^5–10^7 yr (Yusef-Zadeh & Morris 1987; Mezger et al. 1989) since this time scale is much larger than that of differential rotation in the non-solid-body rotation region near the Galactic center (Uchida et al. 1998).

Among the previously considered hypothesis, only the model of tidal disruption suggested by Khokhlov & Melia (1996) is consistent with the energy constraint. We suggest, however, that the extreme energy required to make Sgr A East could be associated with another hypotheses like several tens of multiple supernova explosions or a single, extremely energetic explosion, so called hypernova (Paczyński 1998). In this section, we examine each of these candidates for Sgr A East based on the observational constraints known so far.

6.4.1 Tidal Disruption of a Star by the SMBH

It has been thought that the tidal disruption of stars by a massive black hole can result in flare-like activity in the central regions of AGNs and even in normal galaxies. The flare results from the rapid release of gravitational energy as the debris from the disrupted star accretes into the black hole (Rees 1990; Shlossman, Begelman, & Frank 1990; and references therein).

Recently, Komossa et al. (2004) observed the non-active galaxy RX J1242.6-1119A using the X-ray observatories *Chandra* and *XMM-Newton* and measured a factor of ~ 200 drop in its X-ray luminosity, which is one of the most extreme variability ever recorded among galaxies, compared with that measured by $ROSAT$ in 1992 (Komossa & Greiner 1999). They concluded that the inferred black hole mass, the amount of liberated energy, and the duration of the event favor an accretion event expected from the tidal disruption of a star.

On the other hand, Khokhlov & Melia (1996) pointed out that only half of the stellar mass is expected to be captured and the other half will be ejected with extremely high velocity during this catastrophic event. They suggested a model in which approximately half of the stellar mass is ejected with an energy of

$$E \simeq 3.8 \times 10^{54} \left(\frac{M_*}{M_\odot}\right)^2 \left(\frac{R_\odot}{R_*}\right) \left(\frac{M_h}{10^6 M_\odot}\right) \left(\frac{R_*}{R_p}\right)^2 \;\; \mathrm{ergs} \tag{6.8}$$

within a solid angle of

$$\Omega \gtrsim 16 \left(\frac{R_*}{R_p}\right)^{1/2} \left(\frac{M_*}{M_h}\right)^{1/2} \;\; \mathrm{radians}^2, \tag{6.9}$$

where $R_*, R_p, M_*,$ and M_h are the stellar radius, pericentric distance of the orbit, stellar mass and the black hole mass, respectively. As a result, the impact of the disrupted matter efflux on the surrounding ISM may be like that of a supernova, although with considerably greater energy and with an anisotropy in the expanding shell structure.

For the conditions in the Galactic center (e.g. $M_h \sim 10^6$ M$_\odot$ and the stellar number density near the black hole is about 10^6 pc^{-3}), they predicted that this sort of events occur roughly once every 10^4–10^5 yr. They suggested that Sgr A East may be the remnant of a solar mass star disrupted by the SMBH in the Galactic nucleus at a pericentric distance $R_p \simeq 10 R_\odot$, which results in an explosion with energy of $\sim 4 \times 10^{52}$ ergs (or as much as $\sim 4 \times 10^{53}$ ergs when relativistic effects are taken into account). They also argued that the fact that the shell structure of Sgr A East is elongated with a significantly offset centroid from the likely source of the explosion (i.e., Sgr A*) can be understood as being due to the strongly directed ejection of matter in their model.

The predicted energy and frequency of the event from Khokhlov & Melia (1996)'s model is well consistent with our estimates on the explosion energy and age of Sgr A East ((0.2–

4)$\times 10^{53}$ ergs and (0.5–3)$\times 10^4$ yr, respectively). However the anisotropic explosion is not likely according to more detailed studies on the evolution of the stellar debris after tidal disruption (see Figure 6.1 for example; Lee & Kim 1996; Kim, Park, & Lee 1999; Ayal, Livio, & Piran 2000; Bogdanović et al. 2004). Then the geometry of the Sgr A complex becomes very difficult to be explained by this hypothesis since Sgr A*, which is thought to be the source of explosion (i.e. the SMBH), is located at the edge of Sgr A East along the line of sight (see Figure 5.14); this structure needs a highly collimated eruption toward the far side from us.

On the other hand, Maeda et al. (2002) observed the X-ray emission from Sgr A East with the *Chandra* and reported that the X-ray-emitting plasma appears to be rich in heavy elements, over-abundant by roughly a factor of 4 with respect to solar abundances based on the spectrum showing strong lines from highly ionized ions of S, Ar, Ca, and Fe. They argued that the model of Khokhlov & Melia (1996) is not likely to reproduce the metal-rich plasma because the explosion is driven by gravity rather than by a nuclear reaction. Nevertheless, if the gas itself has been much more enriched in the Galactic center than normal interstellar gas by sustained star formation by gas inflow (Serabyn & Morris 1996; Najarro et al. 1999), the model of Khokhlov & Melia (1996) will not be excluded. A lot of observational studies have shown evidence that the abundance of heavy elements in the Galactic center is a few times higher than the solar value (e.g., Shaver et al. 1983; Sodroski et al. 1995; Mezger, Duschl, & Zylka 1996; Munn et al. 2004). However, some recent measurements of stellar metallicity in the Arches cluster (Najarro et al. 2004) and within the inner 2.5 pc (Ramírez et al. 2000) are reported to be near solar. Therefore the constraint of metallicity on the tidal disruption model seems still unclear.

6.4.2 Multiple Supernovae

Even the extremely large energy of the Sgr A East explosion can be explained by typical supernovae of $E \sim 10^{51}$ ergs (e.g. Woolsey & Weaver 1995) if a number of them exploded together. Multiple supernovae can produce heavy elements and may not be excluded by the constraint of metallicity from the X-ray observations. However, Maeda et al. (2002) pointed out that the hypothesis of near-simultaneous explosions of tens of supernovae may be strongly constrained by the short expansion time of the shell ($\sim 10^4$ yr) and by the absence of a residual stellar cluster near the center of the shell.

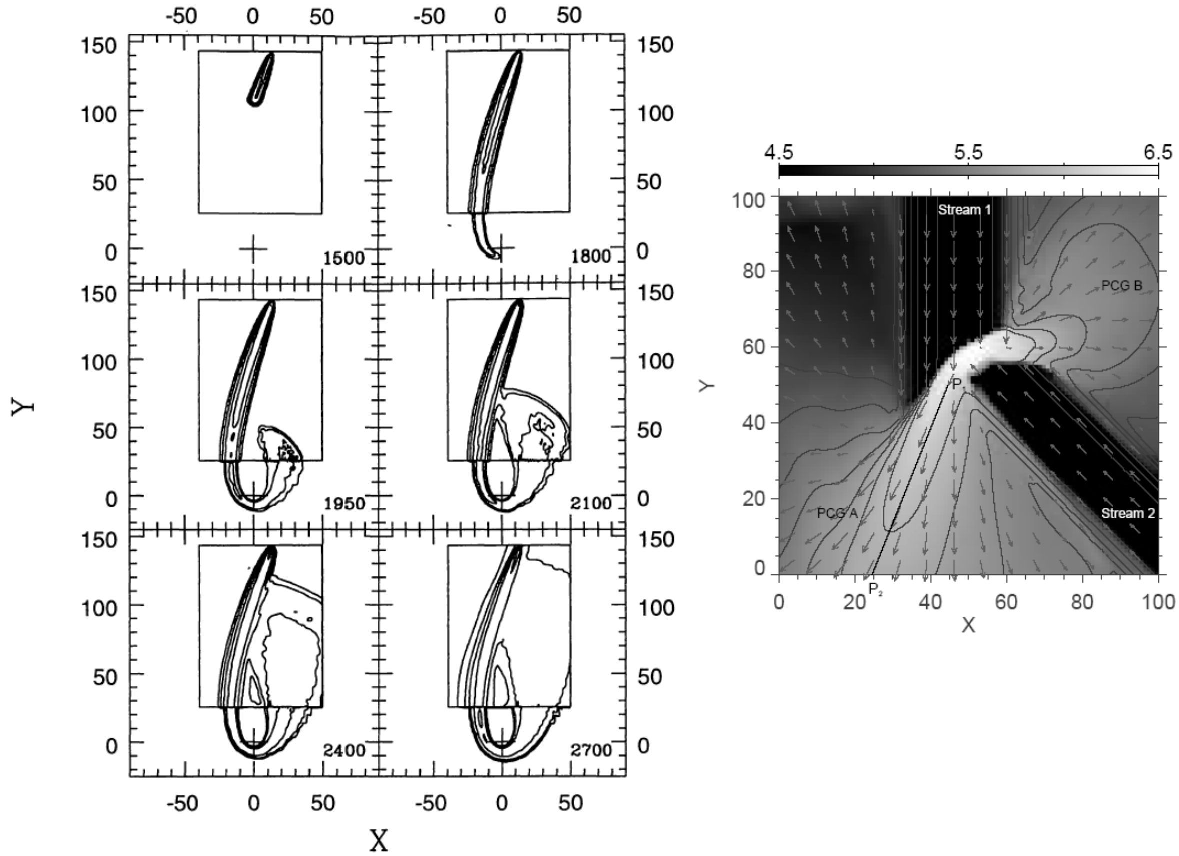

FIG. 6.1: Evolution of tidally disrupted stellar debris by a SMBH. (left) Density contour maps of the results of simulation by Lee & Kim (1996) (from their Figure 5). The length is in 1.48×10^{12} cm and total duration of this simulation is about 30 hours. (right) Density, temperature, and velocity vector plot at $t = 4 \times 10^4$ s of the simulation by Kim, Park, & Lee (1999) (from their Figure 2). Units of x and y are the grid size of the 3-D simulation, 5.93×10^{10} cm. The contour shows the density, the gray-scale map shows temperature, and arrows show velocity vectors projected onto the x-y plane. The logarithmic temperature scale in K is shown as a bar at the top of the figure. The head of stream of the stellar debris (stream 2), which already passes by the SMBH for the second time, is colliding with its tail (stream 1) at the center of the figure, and the thermalized post-collision gas (PCG) is expanding out.

TABLE 6.2: Properties of Massive Clusters in the Galactic Center

Cluster	log M ($M_\odot$)	Radius (pc)	log ρ ($M_\odot$ pc^{-3})	Age (Myr)	log L ($L_\odot$)
Center[a]	3.0–4.0	0.23	4.3–5.3	3–7	7.3
Arches[b]	3.7–4.8	0.19–0.23	5.0–6.3	2.5 ± 0.5	7.8
Quintuplet[c]	3.0–3.8	1.0	2.4–3.2	3–6	7.5

[a] Krabbe et al. 1995

[b] Serabyn, Shupe, & Figer 1998; Figer et al. 2002

[c] Figer, McLean, & Morris 1999b

Is it possible that about 10–100 supernova explosions occur in a short time scale of $\sim 10^4$ yr and satisfy the constraints of energy and age of Sgr A East (from Table 6.1)? This might happen in a large stellar cluster containing a huge number of massive stars. There could be many stars with such similar masses that their lifetimes before the ends as supernovae have a very small dispersion. In the Galactic center, there are three extraordinarily massive and dense young clusters of stars near Sgr A East (within 30 pc; see Figure 6.2); the Central, Arches, and Quintuplet clusters (see Table 6.2 for their properties).

From their observations using *HST* and Keck, Figer et al. (2002) expanded the identification of member stars in the Arches cluster (Figure 6.3) up to 196 and derived various properties of the stars including the initial masses, M_{init}, assuming the relation between mass and magnitude for the cluster age of 2.5 Myr from the Geneva models with solar metallicity and enhanced mass-loss rates (see Table 3 in Figer et al. 2002).

We calculate the lifetimes from their births (starting the hydrogen core burning) to deaths (finishing the silicon core burning) of these stars in the Arches cluster using a relation between initial mass and lifetime which we derive from the evolution models of massive stars by Woosley, Langer, & Weaver (1993) and Woosley, Heger, & Weaver (2002). In Figure 6.4, we plot the model results of initial mass, M_{init}, and lifetime, τ_{life}, which are least-square fitted by a relation of

$$\tau_{life} = 2.7 \times 10^5 \ M_{init}^{-1.1} \ \text{kyr} \quad (\text{for } M_{init} \leq 40 \ \text{M}_\odot) \tag{6.10}$$

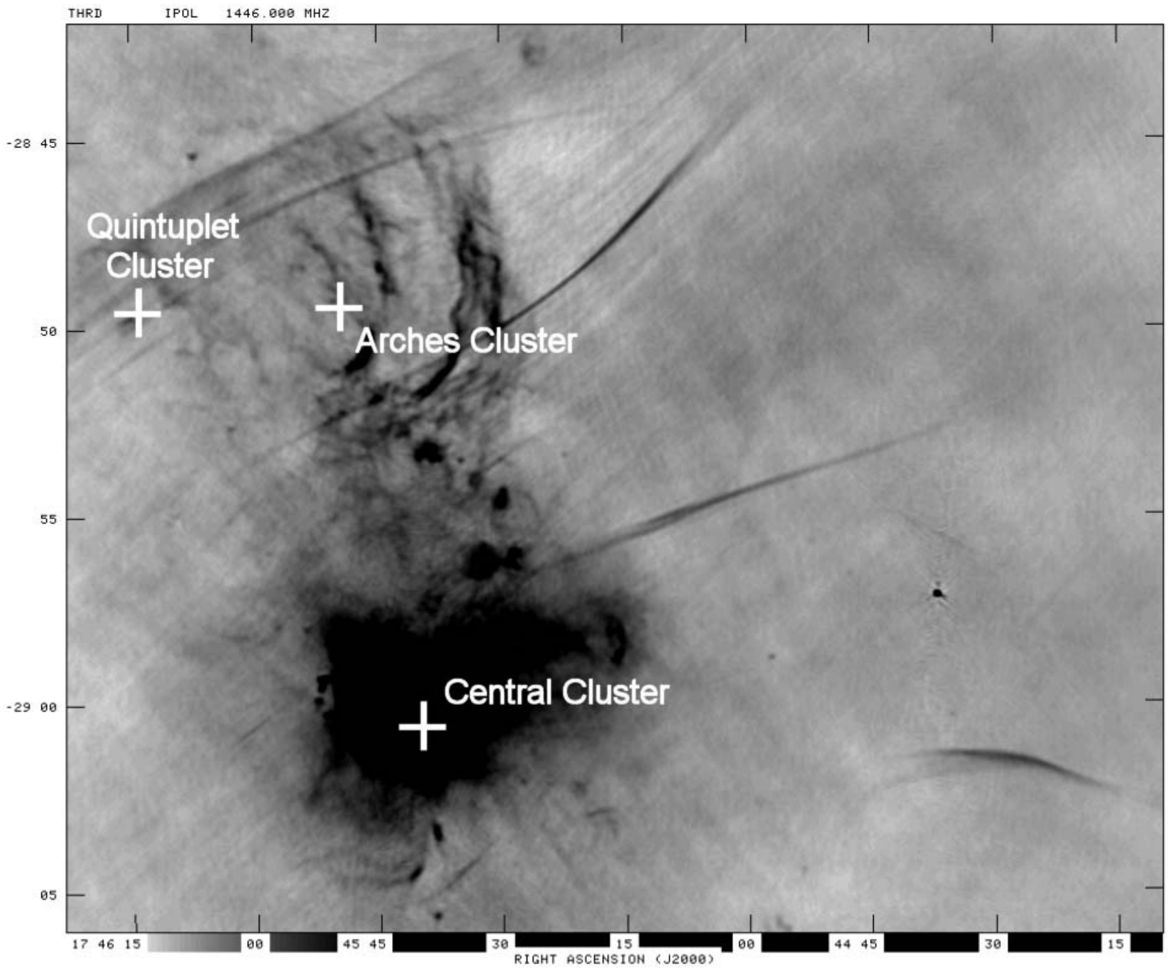

FIG. 6.2: Positions of massive stellar clusters (Figer et al. 1999a) are marked on the continuum image at 20 cm of a 60 pc region of the Galactic center (from Lang, Morris, & Echevarria 1999). The resolution of this image is $5.''90 \times 5.''5$ with PA$= 80^\circ$ and the RMS noise level is 0.5 mJy beam^{-1}. The bright, diffuse, emitting region at the lower-left quadrant is the Sgr A complex.

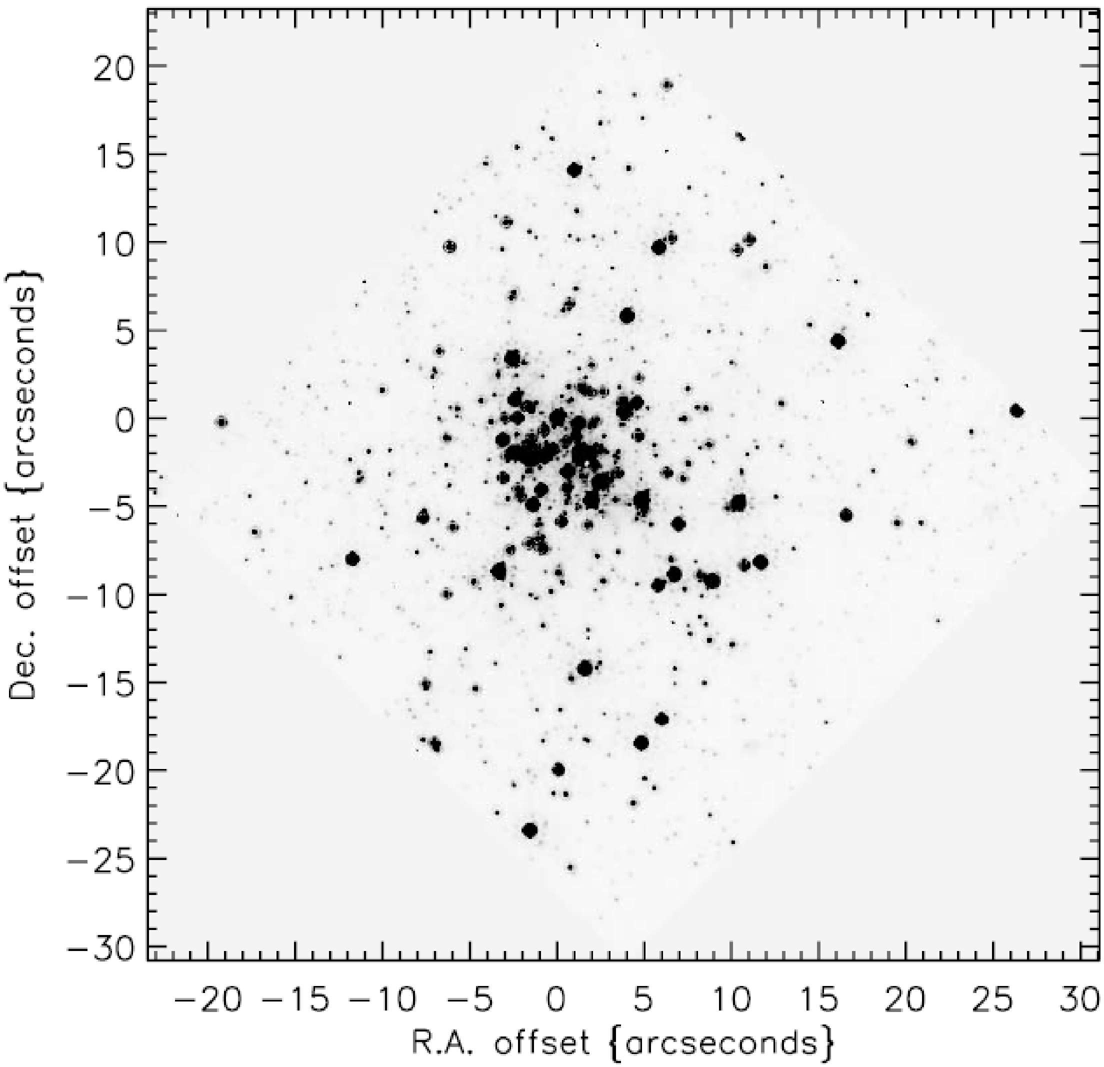

FIG. 6.3: *HST*/NICMOS image of the Arches Cluster (from Figer et al. 2002) in F205W ($\lambda_{center} = 2.05\mu\mathrm{m}$).

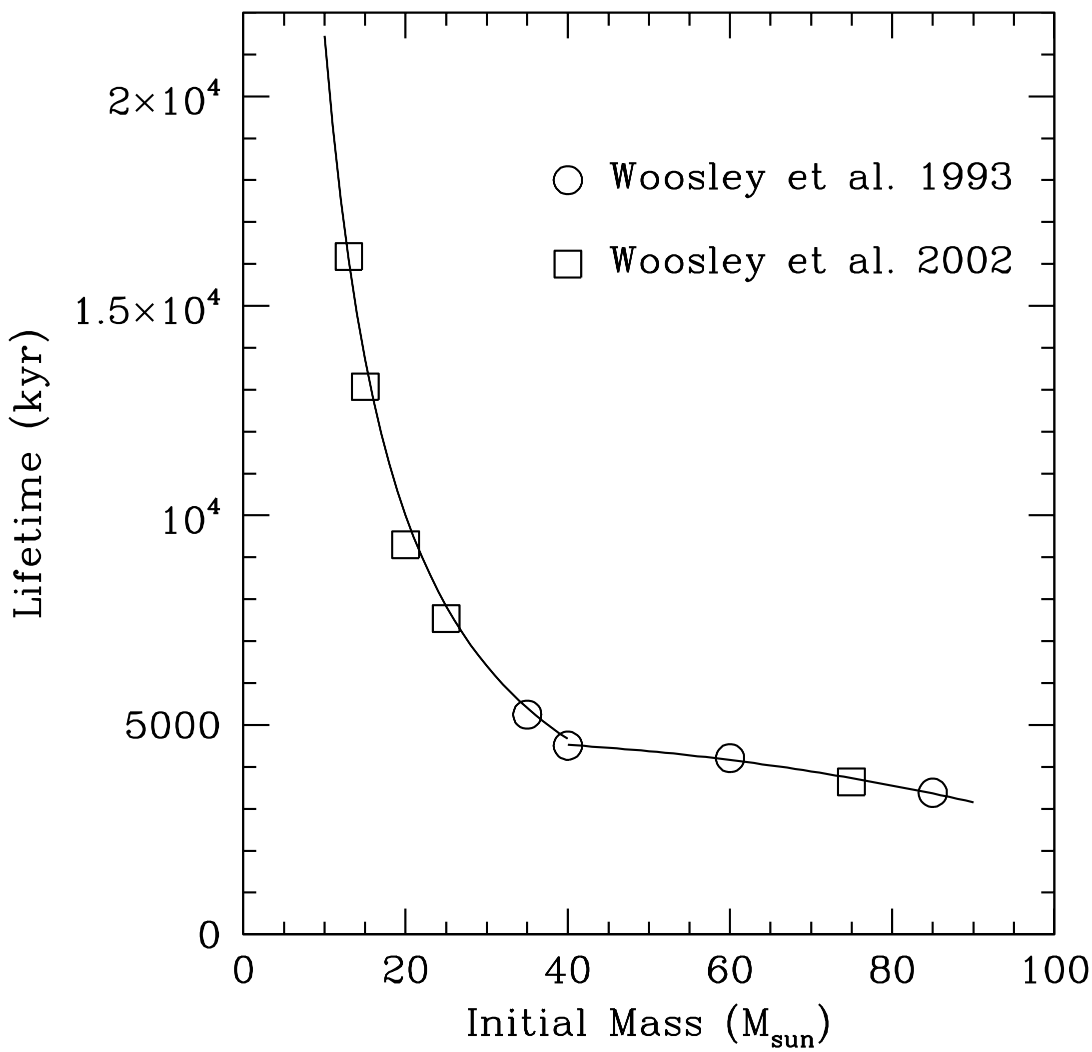

FIG. 6.4: Initial mass and lifetime relation of massive stars. Symbols are from the evolution models of massive stars by Woosley, Langer, & Weaver (1993) (open circles) and Woosley, Heger, & Weaver (2002) (open squares). The best fit to the data points are represented by a solid curve (see text for the the fitting equations).

and

$$\tau_{life} = -0.31\ M_{init}^2 + 13\ M_{init} + 4.5 \times 10^3\ \text{ kyr} \quad (\text{for } M_{init} > 40\ \mathrm{M}_\odot). \tag{6.11}$$

Figure 6.5 shows the distribution of masses and lifetimes of the members of Arches. We can see the initial masses are concentrated between 20–40 $\mathrm{M}_\odot$ while the lifetimes are around 4500 kyr which corresponds to $M_{init} \simeq 40$–70 $\mathrm{M}_\odot$. More than 20 supernovae in 10^5 yr seems not probable from Figure 6.5 (b). Then, statistically, only a few supernova explosions are expected within the age of Sgr A East ($\sim 10^4$ yr) even during the periods of the most frequent supernovae in the densest cluster like the Arches cluster. Therefore we conclude that the hypothesis of multiple supernovae cannot explain the origin of Sgr A East.

6.4.3 Hypernova: Collapsar or Jet-Powered Supernova

The term "hypernova" has been used to name the explosive phenomenon which is much more luminous and energetic ($\gtrsim 10^{52}$ ergs) than any supernova (Paczyński 1998; Nakamura et al. 2001b). SN 1998bw, which is believed to be associated with the gamma-ray burst (GRB) 980425, is a quite unusual supernova in its radio and optical properties. The light curve and spectra of SN 1998bw can be well reproduced by an extremely energetic explosion of a carbon+oxygen (C+O) star of 6–14 $\mathrm{M}_\odot$ (the core of a star with initial mass of $\sim 40\ \mathrm{M}_\odot$) with a kinetic energy of 2–6×10^{52} ergs (Iwamoto et al. 1998; Woosley, Eastman, & Schmidt 1999; Nakamura et al. 2001a). The spectra and the light curve of SN 1997ef have been well simulated by the explosion of a $10\ \mathrm{M}_\odot$ C+O star with $E \simeq 1 \times 10^{52}$ ergs (Iwamoto et al. 2000; Mazzali, Iwamoto, & Nomoto 2000). SN 1997cy is classified as a SN IIn but unusually bright. Its light curve has been simulated by a circum-stellar interaction model, which requires $E \sim 5 \times 10^{52}$ ergs (Turatto et al. 2000).

The extremely large energies of the hypernova explosions cannot be reproduced by normal core-collapse models of supernovae which are powered by neutron star formation. Thus new explosion mechanisms powered by black hole formation have been searched and the "collapsar" or "jet-powered supernova (JetSN)" model (initially referred to as the "failed supernova" model because the prompt supernova mechanism failed; see, e.g., Woosley 1993) has been suggested (see Woosley, Eastman, & Schmidt 1999; Woosley, Heger, & Weaver 2002; Heger et al. 2003 and references therein).

The term "collapsar" is used to describe all massive stars ($M_{init} \gtrsim 20\ \mathrm{M}_\odot$) whose cores collapse to black holes and that have sufficient angular momentum (rotation rate of about

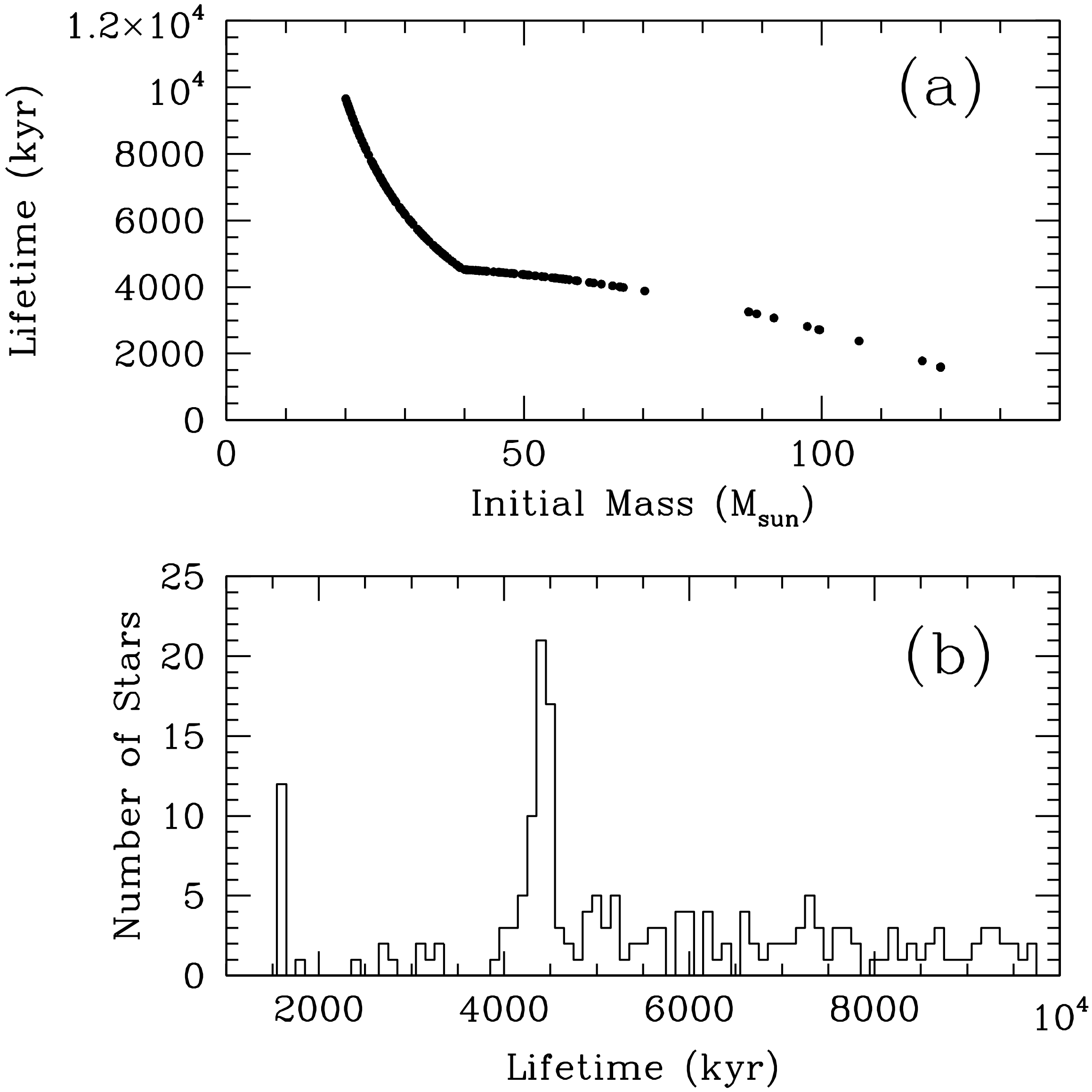

FIG. 6.5: Initial mass and lifetime distribution of the Arches cluster. (a) Distribution of initial mass (from Figer et al. 2002) and lifetime (calculated by equations 6.10 & 6.11) of the 196 member stars of the Arches cluster. (b) Histogram for the lifetimes of the stars in the Arches cluster. The data are binned by 10^5 yr for the lifetime.

sub-millisecond at the final stage of collapse) to form a disk (Heger et al. 2003 and references therein). This model is very similar to the "microquasar" model of Paczyński (1998) which was suggested as an engine of GRBs associated with hypernovae. At the end of its nuclear evolution, the inner iron core of a very massive star collapses into a few solar mass black hole. If the star is spinning rapidly, then its angular momentum prevents all matter from going down the drain, and a rotating, very dense torus forms around the rapidly spinning Kerr black hole. Then the largest energy reservoir is the rotational energy of the black hole (Paczyński 1998);

$$E_{rot,max} \simeq 5 \times 10^{54} \left(\frac{M_{BH}}{10\ \mathrm{M}_\odot}\right) \ \mathrm{erg}. \tag{6.12}$$

Based on both theory and observations of jets in active galactic nuclei, it seems likely that some fraction (about 1–10 per cent) of the mass that accretes through the disk will be converted into the energy of twin jets propagating along the rotational axes. The mechanism for converting disk energy to jet energy could be neutrino transport, magnetic-field dissipation in the disk, extraction of part of the black hole's rotational energy, or other more exotic processes. For 1 per cent efficiency, over 10^{52} ergs of jet energy would be provided by the accretion of only $1\ \mathrm{M}_\odot$ of mantle material. The accretion would take ~ 10 sec, the free-fall time scale for a mantle with average density $\sim 10^4$ g cm^{-3}. This jet would explode the rest of the star (i.e. JetSN). If it would still maintain a large fraction of its initial energy after breaking out, the interaction of this relativistic jet with the circum-stellar matter would produce a GRB. It is important in this GRB model that the star have lost its hydrogen envelope prior to iron core collapse, otherwise the jet dissipates its energy prior to breaking out. However, a star with an extended envelope might still make a very powerful, bright supernova (see Woosley, Heger, & Weaver 2002 and references therein).

This hypothesis of hypernova (the collapsar or JetSN model) can make such a powerful explosion that it satisfies the energy constraint of Sgr A East (2×10^{52} – 4×10^{53} ergs) suggested by us. The constraint of metallicity from the X-ray observations (Maeda et al. 2002) cannot exclude this model since it is the result from the nuclear evolution of a massive star like a supernova.

Moreover there are likely to be many potential candidates of hypernovae near Sgr A East in the Galactic center. Investigating how metallicity, and its effect on mass loss, affects the evolution and final fate of massive stars, Heger et al. (2003) mapped, as a function of mass and metallicity, where black holes and neutron stars are likely to form and where different types of supernovae are produced including the extremely energetic JetSNe (Figure 6.6).

At the metallicity in the Galactic center, which is reported to be similar to or higher than the solar value (see Section 6.4.1), JetSNe are possible in the range of $M_{init} \simeq 25$–$60\ \mathrm{M}_\odot$ (GRBs are also possible when $M_{init} \gtrsim 35\ \mathrm{M}_\odot$ because of the significant loss of the hydrogen envelope). In the Arches cluster, there are ~ 130 massive stars in the potential mass range of JetSNe and ~ 80 stars in the range of JetSNe+GRBs (Figer et al. 2002). These number of candidates may be doubled taking account of the other clusters in the Galactic center, the Central and Quintuplet clusters, which have similar properties to the Arches cluster (see Table 6.2).

A number of studies on angular momentum in massive stars found that the core can reach critical rotation for being a collapsar before the final central burning phases. However, there exist also arguments against this conclusion; e.g. magnetic torques (see Heger et al. 2003 and references therein). Therefore it seems that we need more understandings about stellar evolution before we can determine how many stars among the potential candidates can be collapsars or JetSNe at their ends of life.

6.5 Influence of Explosive Events like Sgr A East on the Mass Inflow to the Galactic Nucleus

According to studies on the mass inflow to the Galactic center, the time-average rate of total mass flow seems high enough for the nucleus to emit at the Eddington rate making the Milky Way a Seyfert galaxy (Morris & Serabyn 1996). However, the current accretion rate and luminosity of Sgr A* (the SMBH) are many orders of magnitude smaller than those of an AGN. On the other hand, such a large amount of mass inflow can cause massive star formation in the nuclear region. The massive young stars clustered within the inner 1 parsec are indicative of a substantial star formation event within the past 10^7 yr (Morris & Serabyn 1996). Therefore, if the mass inflow were favorable without any obstruction, the Galactic nucleus would be in its ‘active phase’ and our Galaxy might resemble an AGN galaxy or a starburst galaxy.

Explosive events such as Sgr A East could make important roles in the evolution of the nucleus. In general, they are expected to obstruct the mass inflow from surrounding material into the nuclear region and suppress the activity of the Galactic nucleus as a result. As we have seen in Chapter 5, Sgr A East is actually pushing away all the filamentary molecular

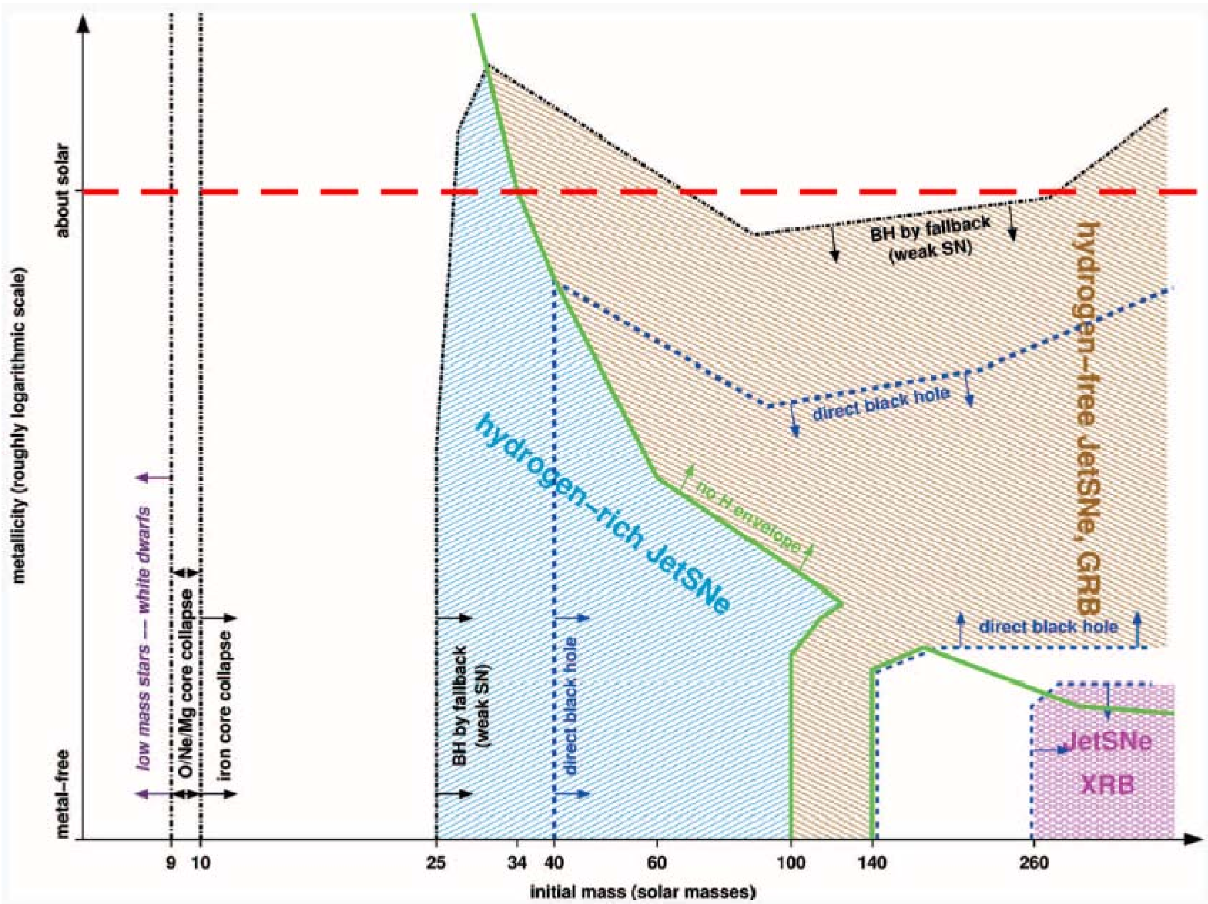

FIG. 6.6: Jet-powered supernova (JetSN) types as a function of initial metallicity and initial mass (from Heger et al. 2003). The regimes in which hydrogen-rich JetSNe are possible (below the thick green line indicating loss of the hydrogen envelope) is indicated by cyan hatching and that of hydrogen-free JetSNe by light brown hatching (above the thick green line) where GRBs may also be possible. The thick dashed red line indicates the solar metallicity which is a lower limit in the Galactic center. The dashed blue line indicates the border of the regime of direct black hole formation. This domain is interrupted by a strip of pair-instability supernovae that leave no remnant (white). Outside the direct black hole regime, at lower mass and higher metallicity, follows the regime of BH formation by fallback, and again outside of this, the formation of neutron stars. At even lower mass ($< 9\,\mathrm{M}_{\odot}$), the cores do not collapse and only white dwarfs are made.

features around it out of the Galactic nucleus (Figure 5.14). Considering the speculations of previous studies on the possible connections and relationships between the CND and the nearby molecular structures; the southern streamer (Coil & Ho 1999, 2000; McGary, Coil, & Ho 2001), the molecular ridge, the northern ridge (McGary, Coil, & Ho 2001), and the western streamer (Herrnstein & Ho 2005), it is highly probable that most of them existed very near and were really connected to the nuclear region in the past (before the explosion of Sgr A East) as passages of mass inflow to the SMBH from the surrounding GMCs, the $50\ \mathrm{km\ s^{-1}}$ cloud (M-0.02-0.07) and the $20\ \mathrm{km\ s^{-1}}$ cloud (M-0.13-0.08).

Then how effectively can the Sgr A East-like explosions obstruct the mass inflow? The main point in this question is whether the explosions are sufficiently strong and frequent that they can keep the continuous and inevitable mass inflow out of the nuclear region of the Galaxy. If the explosions are very strong and frequent, the Galactic nucleus might spend most of its life in quiescent phase (with occasional short periods of high activity). In the opposite case, the evolution of the Galactic nucleus could be dominated by active phase due to a high rate of mass inflow (with occasional breaks by infrequent explosions).

First, we investigate the question whether Sgr A East is powerful enough to obstruct the mass inflow that currently exist around it, by a simple comparison between the kinetic energy of the Sgr A East explosion and the gravitational potential energy of the mass inflow. There are four molecular structures suspected to be the inflow; the southern streamer, the molecular ridge, the northern ridge, and the western streamer. Total mass of these structures are $\sim 10^5\ \mathrm{M_\odot}$ (Herrnstein & Ho 2005). Here we assume that these clouds are located at a Galactocentric radius $R = 5$ pc, which is the approximate radius of Sgr A East, and the whole body of each cloud is in contact with Sgr A East. Actually, the latter assumption is not exactly the current situation but will be in the near future as Sgr A East goes on its expanding. Then, with the mass of the SMBH $\sim 10^6\ \mathrm{M_\odot}$, the total gravitational potential energy of these clouds is $\sim 2 \times 10^{51}$ ergs. We should consider that all the kinetic energy of Sgr A East will not transfer to these clouds since they will contact only some fraction of the whole surface of Sgr A East. Based on the solid angle ratio the western streamer, $\Omega_{WS}/4\pi \sim 0.1$ (Herrnstein & Ho 2005), we assume the total solid angle for the four clouds to be $\Omega_{total}/4\pi \sim 0.4$. Then, the transferable kinetic energy from Sgr A East to these clouds is calculated to be 1×10^{52} – 2×10^{53} ergs, which is much larger than the gravitational potential energy of the clouds. Hence we expect that these clouds can even be blown out of the central 10 pc by Sgr A East.

How about the nearby GMCs, M-0.02-0.07 and M-0.13-0.08? Since these GMCs are also located within the non-solid-body rotation region ($R < 10$ pc), they should be disturbed by differential rotation and lose their angular momentum to start to spiral into the Galactic nucleus in $\sim 10^5$ yr. The combined mass of the GMCs is $\sim 10^6$ $\mathrm{M}_\odot$ (e.g., see Güsten, Walmsley, & Pauls 1981; Herrnstein & Ho 2005) and the gravitational potential energy at $R = 5$ pc is calculated to be $\sim 2 \times 10^{52}$ ergs, which is similar to the lower limit of the explosion energy of Sgr A East estimated by us. This implies that Sgr A East can prevent even these GMCs from falling into the nuclear region.

Second question is whether the Sgr A East-like explosions occur frequently enough to resist against the succeeding mass inflow. Here we presume that the explosion of Sgr A East is a hypernova (JetSN), the hypothesis most favored by the observational constraints in the previous sections. The supernova (SN) rate in the Galaxy is known to be ~ 2.2 per 100 yr and the total mass of the Galaxy (within $R < 35$ kpc) is $\sim 4 \times 10^{11}$ $\mathrm{M}_\odot$ (Cox 2000 and references therein). Then SN rate per unit mass in the Galaxy, $r_{SN,Galaxy} \simeq 6 \times 10^{-14}$ ${\mathrm{M}_\odot}^{-1}$ yr^{-1}. Since the total mass in the central 10 pc is $\sim 6 \times 10^7$ $\mathrm{M}_\odot$ (Mezger et al. 1989), $r_{SN,10pc} \sim 4 \times 10^{-6}$ yr^{-1} is expected (i.e., 1 SN in $\sim 3 \times 10^5$ yr). GRBs are 10^4 – 10^5 times less common than SNe (Paczyński 1998) and the rate of JetSNe is expected to be about double rate of GRBs assuming that the mass function of the Arches cluster is typical in the central a few tens of parsecs (see Section 6.4.3). Thus the JetSN rate in the central 10 pc is probably 8×10^{-10} – 8×10^{-11} yr^{-1} (i.e., a JetSN in 10^9 – 10^{10} yr). According to Morris & Serabyn (1996), the time scale on which massive clouds in the Central Molecular Zone (CMZ) of about 200-pc radius spiral into the Galactic center is a few 10^8 yr, which is significantly shorter than the expected interval of JetSNe. Therefore we conclude that the Sgr A East-like explosions are not likely to be able to keep the mass inflow out of the Galactic center all the time, although the very recent one, which made Sgr A East, seems to be obstructing it effectively for now.

6.6 Cyclic Activity of the Galactic Nucleus

How would be the influence of normal SNe on the mass inflow into the nucleus? Although the energy of each SN ($\sim 10^{51}$ ergs) is much smaller than that of a Sgr A East-like explosion, normal SNe are certainly much more abundant (considering a large number of massive stars, at least in the Central cluster) and frequent(one per $\sim 10^5$ yr) in the central 10 pc. It is possible that hundreds of them make an explosion energy more than 10^{53} ergs in a time scale of $\sim 10^7$ yr which is much shorter than that of the mass inflow ($\sim 10^8$ yr). Thus normal SNe seem to be able to effectively cut the mass inflow from the nuclear region.

However, the huge concentration of massive stars in the nuclear region is thought to be the result of the mass accumulation. This implies that the mass inflow into the nucleus was successful at least for a while in the past although it is ceased now. Therefore we can imagine a scenario that un-obstructed mass inflow put the Galactic nucleus into its active phase by igniting the SMBH or stimulating a starburst every $\sim 10^8$ yr, but the massive star clusters newly born in this phase should result in a large number of SNe which will cease the mass supply effectively in a time scale of $\sim 10^7$ yr. That is to say, the Galactic nucleus may spend most of its life-time in quiescence, but occasionally (every $\sim 10^8$ yr) become active only with a short duration ($\sim 10^7$ yr).

In this scenario for the influence of SNe on the nuclear activity of the Galaxy, a number of normal SNe ought to be detectable maybe by the small shells and cavities that they created, although they cannot create the kinds of large energetic shells like Sgr A East. However, the explosion of Sgr A East may have erased out most of them and perhaps a new normal SN has not yet occurred, since Sgr A East itself is very young ($\sim 10^4$ yr). Nevertheless, we have at least one normal SNR in this region; G 359.92-0.09 to the south of Sgr A East. This SNR is thought to be interacting with the molecular ridge, the $20 \mathrm{~km~s^{-1}}$ cloud, and also with Sgr A East as Coil & Ho (2000) suggested. This SNR seems to have not yet seriously disturbed by Sgr A East but just became in contact with it recently. Also this SNR, however, would be destroyed sometime in the future if Sgr A East keeps expanding on.

Such a scenario about the cyclic nature of the nuclear activity was also suggested by Morris & Serabyn (1996). Based on the kinematics and mass of the CND and considering the radiation pressure and wind from an AGN and stellar winds from massive stars as the obstructors, Morris & Serabyn (1996) suggested that a brief active phase repeats every 10^5–10^6 yr. Their scenario is different from ours in a point that they are focusing on the mass infall within the nucleus itself and dealing with short time scale variation, while we are interested in the large scale mass inflow into the nuclear region from the outer GMCs over a large time scale.

This kind of brief activity was also suggested by Maeda et al. (2002) as follows. A dust ridge compressed by the Sgr A East shock reached Sgr A* $\sim 10^3$ yr ago. The passage of the dust ridge may have led to increased accretion onto the SMBH and triggered nuclear activity for $\lesssim 10^3$ yr. The remains of the activity are observed today as the ionized gas halo surrounding Sgr A* with a radial extent of ~ 10 pc and the fluorescent X-ray emission from cold iron atoms in the Sgr B2 molecular cloud.

Based on the discussions above, we also make a suggestion for the recent history of the central 10 pc as follows. The Galactic nucleus had long been in quiescence until sufficient mass inflow started so it entered into its active phase several 10^6 yr ago. Starburst around the nucleus during this period of active phase made massive star clusters like Central, Arches, and Quintuplet. The Galactic nucleus might be able to be in its active phase for a few 10^6 yr more, before the massive star clusters result in a huge number of SNe. However, the active phase was unexpectedly ceased much earlier than its usual schedule by a highly unusual event, Sgr A East, $\sim 10^4$ yr ago. From now on, the Galactic nucleus will be mostly in rest until the next active age begins after $\sim 10^8$ yr, but possibly with occasional, brief, waking ups as suggested by Morris & Serabyn (1996). This scenario for the recent history of the Galactic center is consistent with the small spread of formation times for the known young clusters and the relative lack of intermediate-age stars (ages of 10^7–$10^{7.3}$ yr) in this region (see Figer et al. 2002 and references therein).

6.7 Conclusions

In spite of its important role in the large-scale structure and kinematics in the central 10 pc of our Galaxy, the origin of Sgr A East has long been under debate. The most important clue to this puzzle is the energy required to make the current shell of Sgr A East. In this chapter, we estimated the initial explosion energy of Sgr A East from the shock velocities using a standard model of SNR evolution. The lower limit of the energy is (2–3) $\times 10^{52}$ ergs under the assumption that Sgr A East exploded in a low density halo, and the upper limit is (2–4) $\times 10^{53}$ ergs which is derived in the condition that the explosion occurred within a dense GMC.

This extremely high energy excludes the hypothesis of a single, typical, supernova for the origin of Sgr A East. Instead, another hypotheses, which can generate such a high explosion energy, were examined; tidal disruption of a star by the SMBH (Sgr A*), multiple supernovae, and a hypernova. We also considered other observational constraints like the age of Sgr A East, the metallicity and 3-D geometry in the region. We conclude that only the hypothesis of hypernova, which has theoretical backgrounds of collapsar (JetSN) or microquasar, can satisfy all the observational constraints.

As we have seen in the previous chapters, the hot cavity of Sgr A East is expanding and accelerating the surrounding molecular clouds away from the Galactic nucleus. Comparing the gravitational potential energy of these clouds and the kinetic energy of Sgr A East, we conclude that Sgr A East is effectively preventing the materials from falling into the nuclear region and it is responsible for the current quiescence of the SMBH in the Galactic nucleus. However, the occurrence frequency (per 10^9 – 10^{10} yr) of Sgr A East-like explosions (i.e. hypernovae) in the central 10 pc is so low compared with the time scale (a few 10^8 yr) of mass inflow from the larger scale structure, the CMZ. Therefore it may be possible that the nuclear activity of our Galaxy in the current age is temporarily suppressed owing to Sgr A East.

Instead normal SNe, which are much more abundant and frequent than a Sgr A East-like explosion, also make a total energy of $\sim 10^{53}$ ergs in a relatively short time scale of $\sim 10^7$ yr so can effectively cut the mass inflow from the nuclear region. Therefore we suggest a scenario that the continuous mass inflow into the Galactic nucleus makes it active by igniting the SMBH or stimulating a starburst every $\sim 10^8$ yr, but each active phase continues only $\lesssim 10^7$ yr since massive star clusters newly born in this age of abundant material result in a large number of SNe which will cease the mass supply in $\sim 10^7$ yr. Thus the Galactic nucleus is likely to spend only about $1/10$ of its life in active.

We also suggest a scenario for the recent history of the central 10 pc. The Galactic nucleus had long been in quiescence before the amount of mass inflow became large enough for the nucleus to enter into its active phase several 10^6 yr ago. In its usual schedule, the Galactic nucleus would continue its activity for a few 10^6 yr more before the a huge number of SNe occur. However, the last active phase was unexpectedly ceased $\sim 10^4$ yr ago by the highly unusual event, Sgr A East.

REFERENCES

Anantharamaiah K.R., Pedlar A., & Goss W.M., 1999, in Falcke H. et al., eds, ASP Conf. Ser. Vol. 186, The Central Parsecs of the Galaxy. Astron. Soc. Pac., San Francisco, p. 422

Ayal S., Livio M., & Piran T., 2000, ApJ, 545, 772

Bogdanović T., Eracleous M., Mahadevan S., Sigurdsson S., & Laguna P., 2004, ApJ, 610, 707

Coil A.L., & Ho P.T.P., 1999, ApJ, 513, 752

Coil A.L., & Ho P.T.P., 2000, ApJ, 533, 245

Cox A.N., 2000, Allen's astrophysical quantities (4th ed.). AIP press, New York

Downes D., & Maxwell A., 1966, ApJ, 146, 653

Fatuzzo M., Melia F., Yusef-Zadeh F., & Markoff S., 1999, in Falcke H. et al., eds, ASP Conf. Ser. Vol. 186, The Central Parsecs of the Galaxy. Astron. Soc. Pac., San Francisco, p. 560

Figer D.F., Kim S.S., Morris M., Serabyn E., Rich R.M., & McLean I.S., 1999a, ApJ, 525, 750

Figer D.F., McLean I.S., & Morris M., 1999b, ApJ, 514, 202

Figer D.F., et al., 2002, ApJ, 581, 258

Geballe T.R., Krisciunas K., Lee T.J., Gatley I., Wade R., Duncan W.D., Garden R., & Becklin E.E., 1984, ApJ, 284, 118

Goss W.M., Schwarz U.J., Ekers R.D., & van Gorkom J.H., 1983, in Danziger J., Gorenstein P., eds, Proc. IAU Symp. 101, Supernova Remnants and Their X-Ray Emission. Dordrecht, Reidel, p. 65

Güsten R., Walmsley C.M., & Pauls T., 1981, A&A, 103, 197

Hall D.N., Kleinmann S.G., & Scoville N.Z., 1982, ApJ, 260, L53

Heger A., Fryer C.L., Woosley S.E., Langer N., & Hartmann D.H., 2003, ApJ, 591, 288

Herrnstein R.M., & Ho P.T.P., 2005, ApJ, 620, 287

Iwamoto K., et al., 1998, Nature, 395, 672

Iwamoto K., et al., 2000, ApJ, 534, 660

Jones T.W., 1974, A&A, 30, 37

Khokhlov A., & Melia F., 1996, ApJ, 457, L61

Kim S.S., Park M.-G., & Lee H.M., 1999, ApJ, 519, 647

Komossa S., & Greiner J., 1999, A&A, 349, L45

Komossa S., Halpern J., Schartel N., Hasinger G., Santos-Lleo M., & Predehl P., 1999, ApJ, 603, L17

Krabbe A., et al., 1995, ApJ, 447, L95

Lang C.C., Morris M., & Echevarria L., 1999, ApJ, 526, 727

Lee H.M., & Kim S.S., 1996, JKAS, 29, 195

Lugten J.B., Genzel R., Crawford M.K., & Townes C.H., 1986, ApJ, 306, 691

Mazzali P.A., Iwamoto K., & Nomoto K., 2000, ApJ, 545, 407

McGary R.S., Coil A.L., & Ho P.T.P., 2001, ApJ, 559, 326

Maeda Y. et al., 2002, ApJ, 570, 671

Mezger P.G., Duschl W.J., & Zylka R., 1996, ARA&A, 7, 289

Mezger P.G., Zylka R., Salter C.J., Wink J.E., Chini R., Kreysa E., & Tuffs R., 1989, A&A, 209, 337

Morris M., & Serabyn E., 1996, ARA&A, 34, 645

Munn K.E., Dufton P.L., Smartt S.J., & Hambly N.C., 2004, A&A, 419, 713

Najarro F., Figer D.F., Hillier D.J., & Kudritzki R.P., 2004, ApJ, 611, L105

Najarro F., Hillier D.J., Figer D.F., & Geballe T.R., 1999, in Falcke H. et al., eds, ASP Conf. Ser. Vol. 186, The Central Parsecs of the Galaxy. Astron. Soc. Pac., San Francisco, p. 340

Nakamura T., Mazzali P.A., Nomoto K., & Iwamoto K., 2001a, ApJ, 550, 991

Nakamura T., Umeda H., Iwamoto K., Nomoto K., Hashimoto M., Hix W.R., & Thielemann F.-K., 2001b, ApJ, 555, 880

Paczyński B., 1986, ApJ, 308, L43

Paczyński B., 1998, ApJ, 494, L45

Pedlar A., Anantharamaiah K.R., Ekers R.D., Goss W.M., van Gorkom J.H., Schwarz U.J., & Zhao J.-H., 1989, ApJ, 342, 769

Ramírez S.V., Sellgren K., Carr J.S., Balachandran S.C., Blum R., Terndrup D.M., & Steed A., 2000, ApJ, 537, 205

Rees M.J., 1990, Science, 247, 817

Serabyn E., & Morris M., 1996, Nature, 382, 602

Serabyn E., Shupe D., & Figer D.F., 1998, Nature, 394, 448

Shlossman I., Begelman M.C., & Frank J., 1990, Nature, 345, 679

Shaver P.A., McGee R.X., Newton L.M., Danks A.C., & Pottasch S.R., 1983, MNRAS, 204, 53

Shull J.M., 1980, ApJ, 237, 769

Sodroski T.J., et al., 1995, ApJ, 452, 262

Turatto M., et al., 2000, ApJ, 534, L57

Uchida K.I., Morris M., Serabyn E., Fong D., & Meseroll T., 1998, in Sofue Y., ed., IAU Symp. Vol. 184, The Central Regions of the Galaxy and Galaxies, Kluwer, Dordrecht, p. 317

Walmsley C.M., Güsten R., Angerhofer P., Churchwell E., & Mundy L., 1986, A&A, 155, 129

Wheeler J.C., Mazurek T.J., & Sivaramakrishnan A., 1980, ApJ, 237, 781

Woosley S.E., 1993, ApJ, 405, 273

Woosley S.E., Eastman R.G., & Schmidt B.P., 1999, ApJ, 516, 788

Woosley S.E., Heger A., & Weaver T.A., 2002, Rev. Mod. Phys., 74, 1015

Woosley S.E., Langer N., & Weaver T.A., 1993, ApJ, 411, 823

Woolsey S.E., & Weaver T.A., 1995, ApJS, 101, 181

Yusef-Zadeh F., Melia F., & Wardle M., 2000, Science, 287, 85

Yusef-Zadeh F., & Morris M., 1987, ApJ, 320, 545

Chapter 7

Conclusions

We observed the H_2 $1-0$ $S(1)$ ($\lambda = 2.1218\mu m$) and H_2 $2-1$ $S(1)$ ($\lambda = 2.2477\mu m$) emission line spectra from the interaction regions between Sgr A East and the other members in central 10 pc of the Galaxy, the nucleus (Sgr A*, Sgr A West, and the circum-nuclear disk or CND) and the surrounding molecular clouds (the giant molecular cloud (GMC) M-0.02-0.07, the molecular ridge, the northern ridge, the southern streamer, and the western streamer). Using the Cooled Grating Spectrometer 4 (CGS4; Mountain et al. 1990) with a 31 l/mm echelle grating and 300 mm focal length camera optics at the 3.8 m United Kingdom Infrared Telescope (UKIRT), we scanned 56 positions in the interaction regions with a 90-arcsec-length slit in 2001 and 2003.

Data reduction of the two-dimensional (2-D) spectral images was implemented using IRAF including the cleaning of contaminations and the calibrations of wavelength and flux. Using MIRIAD, we constructed and analyzed a three-dimensional (3-D) data cube which has the information of the H_2 emission both in space (with a $\sim$ 2-arcsec resolution) and in velocity (with a ~ 18 km s^{-1} resolution). The H_2 $1-0$ $S(1)$ data cube was directly compared with the NH_3(3,3) data cube from McGary, Coil, & Ho (2001) to investigate the gas kinematics with various methods including line profiles, channel maps, and position-velocity diagrams (PVDs).

In chapter 4, we investigate the physical conditions of H_2 emitting regions. From the observational results including integrated H_2 $1-0$ $S(1)$ line intensities, the $2-1$ $S(1)$ / $1-0$ $S(1)$ line ratio, very broad H_2 line profiles, and low peak velocities relative to those of NH_3, we concluded that the excitation of H_2 molecules in this region cannot be explained by any single mechanism (low-density PDR, dense PDR, fast J-shock, slow J-shock, or C-shock) but shocks driven by Sgr A East play a major role. Two models for H_2 excitation can explain all of the observational results; a combination of fluorescence and C-shocks in very strong magnetic fields, or a mixture of slow C-shocks and fast J-shocks. For each of two shock models, we estimated shock velocities of Sgr A East by comparing H_2 line profiles, which trace post-shock gas, with those of NH_3, which trace pre-shock gas in molecular clouds. The results from two different assumptions are consistent with each other; the mean velocity of the shocks are about $100\ \mathrm{km\ s^{-1}}$.

From the distribution of the shocked H_2 emission which is the most direct evidence that Sgr A East is in physical contact with its surrounding molecular clouds, in chapter 5, we determined the interacting boundary of Sgr A East in projection as an ellipse with a center at ($+32''$, $+18''$) or ~ 1.5 pc offset from Sgr A*, a major axis of 10.8 pc length, which is nearly parallel to the Galactic plane, and a minor axis of 7.6 pc length (assuming the distance to the Galactic center as 8.0 kpc; Reid 1993). This boundary is significantly larger than the synchrotron emission shell (e.g. Yusef-Zadeh & Morris 1987) but well consistent with the dust ring suggested by Mezger et al. (1989).

Based on the shock directions, we determined the positional relationships between Sgr A East and the molecular clouds along the line-of-sight and suggested a model for the 3-D structure of the central 10 pc of the Galaxy in chapter 5. Our model is revised from the previous models of Mezger et al. (1989), Coil & Ho (2000), and Herrnstein & Ho (2005). Our conclusions on the 3-D structure resolve most of the unsolved questions as follows. (i) The Galactic nucleus is in physical contact with Sgr A East since the CND is being accelerated toward us by the shocks from Sgr A East. (ii) The southern streamer is highly probably falling into the nuclear region considering that Sgr A East is driving shocks to the northern-most part of this cloud where it meets the CND in projection. (iii) Sgr A East has expanded into the $50\ \mathrm{km\ s^{-1}}$ cloud significantly since at least one third of the cloud is filled with shocked gas. (iv) Sgr A East is interacting with the northern part of the molecular ridge considering the shocked H_2 emission detected in this region.

Finally in Chapter 6, we estimated the initial explosion energy of Sgr A East from the estimated shock velocities using a standard model for evolution of a supernova remnant (SNR). The lower limit of the energy is 2–3×10^{52} ergs under the assumption that Sgr A East exploded in a low density halo, and the upper limit is 2–4×10^{53} ergs in the condition that the explosion occurred within a dense GMC. This extremely high energy excludes the hypothesis of a single, typical, supernova for the origin of Sgr A East. We examined another hypotheses; tidal disruption of a star by the SMBH (Sgr A*), multiple supernovae, and a hypernova. Based on the observational constraints like the age, the metallicity, and the geometry as well as the energetics of Sgr A East, we suggested a hypernova, which has theoretical backgrounds of collapsar (Jet-powered SN; Heger et al. 2003) or microquasar (Paczyński (1998)), as the most probable origin of Sgr A East.

The hot cavity of Sgr A East is expanding and accelerating the surrounding molecular clouds away from the Galactic nucleus. Comparing the gravitational potential energy of these clouds and the kinetic energy of Sgr A East, we conclude that Sgr A East is effectively preventing the materials from falling into the nuclear region and it is responsible for the current quiescence of the SMBH in the Galactic nucleus. However, the expected frequency (per 10^9 – 10^{10} yr) of the Sgr A East-like events (i.e. hypernovae) in the central 10 pc is so low compared with the time scale (a few 10^8 yr; Morris & Serabyn 1996) of mass inflow from the outer regions that these explosions can only disturb the nuclear activity of the Galaxy for a while. Normal SNe, which are much more abundant and frequent than a Sgr A East-like explosion in the central 10 pc, can make a total energy of $\sim 10^{53}$ ergs in a time scale of $\sim 10^7$ yr which is longer than the need time of Sgr A East but still shorter than that of the mass inflow. Therefore we suggest a scenario that the continuous mass inflow into the Galactic nucleus makes it active by igniting the SMBH or stimulating a starburst every $\sim 10^8$ yr, but each active phase continues only $\lesssim 10^7$ yr since massive star clusters newly born in this age of abundant material result in a large number of SNe which will cease the mass supply in $\sim 10^7$ yr. Thus the Galactic nucleus is likely to spend only about $1/10$ of its life in active.

Based on the conclusions above, we also suggest a scenario for the recent history of the central 10 pc as follows. The Galactic nucleus had long been in quiescence before the mass inflow became efficient enough for the nucleus to enter into its active phase several 10^6 yr ago. In its usual schedule, the Galactic nucleus would continue its activity for a few 10^6 yr more before the a huge number of SNe occur. However, the last active phase was unexpectedly ceased $\sim 10^4$ yr ago by the highly unusual event, Sgr A East.

References

Coil A.L., & Ho P.T.P., 2000, ApJ, 533, 245

Heger A., Fryer C.L., Woosley S.E., Langer N., & Hartmann D.H., 2003, ApJ, 591, 288

Herrnstein R.M., & Ho P.T.P., 2005, ApJ, 620, 287

Mezger P.G., Zylka R., Salter C.J., Wink J.E., Chini R., Kreysa E., & Tuffs R., 1989, A&A, 209, 337

McGary R.S., Coil A.L., & Ho P.T.P., 2001, ApJ, 559, 326

Morris M., & Serabyn E., 1996, ARA&A, 34, 645

Mountain C.M., Robertson D.J., Lee T.J., & Wade R., 1990, in Crawford D.L., ed., Proc. SPIE Vol. 1235, Instrumentation in Astronomy VII. SPIE, Bellingham, p. 25

Paczyński B., 1998, ApJ, 494, L45

Reid M.J., 1993, ARA&A, 31, 345

Yusef-Zadeh F., & Morris M., 1987, ApJ, 320, 545

Appendix A

Correction for Slit Obscuration in Flux Calibration

Since only part of the flux from a standard star is detected due to a narrow slit (see Figure A.1), the measured signal must be corrected for proper flux calibration;

$$F_0 = C_{slit} \cdot F_{obs} \tag{A.1}$$

where F_0 is the original flux of the standard star, F_{obs} is the measured flux, and C_{slit} is the correction factor for the slit obscuration.

Assuming a circularly symmetric Gaussian point-spread-function (PSF) for the star, the intensity distribution is given by

$$I(r) = I_{max} \cdot \exp\left[-\frac{1}{2}\left(\frac{r}{\sigma}\right)^2\right] \tag{A.2}$$

where I_{max} is the peak intensity and $\sigma =$FWHM$/2.354$. Then the original flux,

$$F_0 = \int_0^{I_{max}} \pi r^2 \, dI(r). \tag{A.3}$$

Since from equation A.2

$$\ln I(r) - \ln I_{max} = -\frac{r^2}{2\sigma^2} \tag{A.4}$$

$$r^2 = 2\sigma^2(\ln I_{max} - \ln I(r)), \tag{A.5}$$

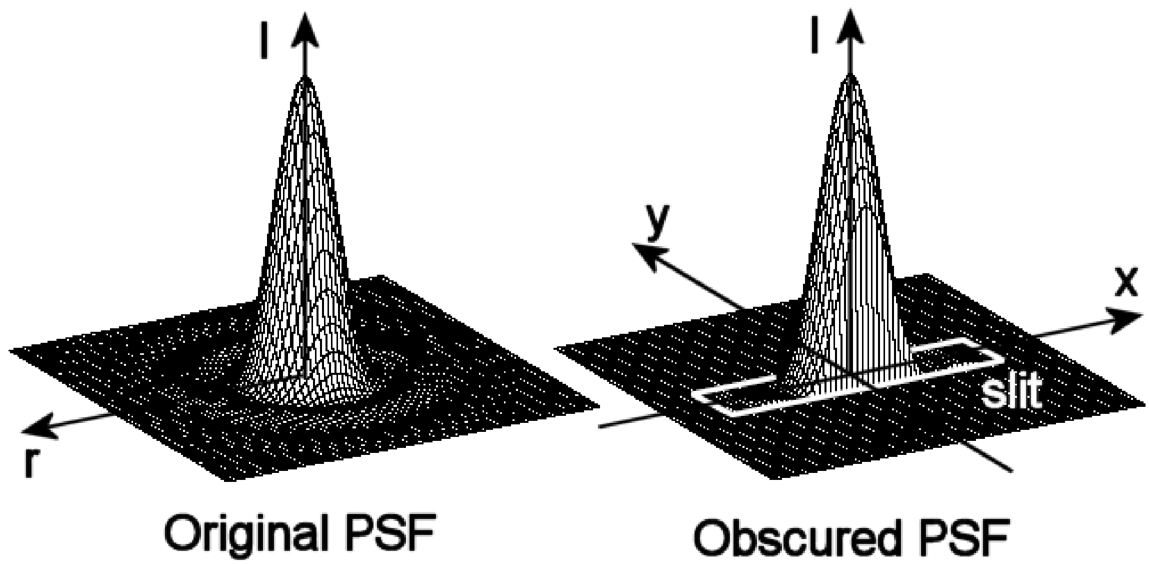

FIG. A.1: Obscuration of a point-spread-function (PSF) by a narrow slit. (left) A circularly symmetric PSF. (right) PSF obscured by a narrow slit. x-axis is along the slit length and y-axis is along the slit width.

$$\begin{aligned}
F_0 &= \pi \int_0^{I_{max}} 2\sigma^2 (\ln I_{max} - \ln I)\, dI \\
&= 2\pi\sigma^2 \left([\ln I_{max} \cdot I]_0^{I_{max}} - \int_0^{I_{max}} \ln I \, dI \right) \\
&= 2\pi\sigma^2 \left(I_{max} \ln I_{max} - [I \ln I - I]_0^{I_{max}} \right) \\
&= 2\pi\sigma^2 \left(I_{max} \ln I_{max} - I_{max} \ln I_{max} + I_{max} + 0 - 0 \right) \\
&= 2\pi\sigma^2 I_{max} \qquad \text{(A.6)}
\end{aligned}$$

where we use $\lim_{I->0}(I\ln I) = 0$.

Next we calculate the observed flux after the slit, F_{obs}. When we define x- and y-axis as in Figure A.1, since $r^2 = x^2 + y^2$, equation A.2 can be written as

$$I(x, y) = I_{max} \cdot \exp\left[-\frac{x^2 + y^2}{2\sigma^2} \right]. \qquad \text{(A.7)}$$

Given a slit width, $2Y$ (from $-Y$ to Y along the y-axis), the observed flux,

$$\begin{aligned}
F_{obs} &= \int_{-Y}^{+Y} \int_{-\infty}^{+\infty} I(x, y)\, dx\, dy \\
&= 4 \int_0^Y \int_0^\infty I_{max} \cdot \exp\left[-\frac{x^2 + y^2}{2\sigma^2} \right] dx\, dy \\
&= 4 I_{max} \int_0^Y \exp\left[-\frac{y^2}{2\sigma^2} \right] dy \int_0^\infty \exp\left[-\frac{x^2}{2\sigma^2} \right] dx \\
&= 4 I_{max} \frac{\sigma\sqrt{\pi}}{\sqrt{2}} \int_0^Y \exp\left[-\frac{y^2}{2\sigma^2} \right] dy \\
&= I_{max} \sigma \sqrt{8\pi} \left(\int_{-\infty}^Y \exp\left[-\frac{y^2}{2\sigma^2} \right] dy - \int_0^\infty \exp\left[-\frac{y^2}{2\sigma^2} \right] dy \right).
\end{aligned}$$

Here if we define $t = y/\sigma$ and $dt = dy/\sigma$,

$$\begin{aligned}
F_{obs} &= I_{max} \sigma \sqrt{8\pi} \left(\sigma \int_{-\infty}^{Y/\sigma} \exp\left[-\frac{t^2}{2} \right] dt - \sigma \int_0^\infty \exp\left[-\frac{t^2}{2} \right] dt \right). \\
&= I_{max} \sigma^2 \sqrt{8\pi} \left(\int_{-\infty}^{Y/\sigma} \exp\left[-\frac{t^2}{2} \right] dt - \sqrt{\frac{\pi}{2}} \right). \qquad \text{(A.8)}
\end{aligned}$$

Here

$$P \equiv \int_{-\infty}^{Y/\sigma} \exp\left[-\frac{t^2}{2}\right] \, dt \tag{A.9}$$

can be calculated from a table for the standard normal distribution if we know the slit width ($2Y$) and seeing (FWHM= $2.354 \cdot \sigma$).

Therefore, from equations A.1, A.6, A.8, and A.9, the correction factor, C_{slit}, for the missing flux is given by

$$\begin{aligned} C_{slit} &= \frac{F_0}{F_{obs}} = \frac{2\pi\sigma^2 I_{max}}{\sqrt{8\pi} sigma^2 I_{max}(P - \sqrt{\pi/2})} = \frac{\sqrt{\pi/2}}{P - \sqrt{\pi/2}} \\ &= \frac{1}{\sqrt{2/\pi}P - 1}. \end{aligned} \tag{A.10}$$

Appendix B

Deconvolution of Instrumental Line Broadening

We deconvolve the observed $\mathrm{H_2}\ 1-0\ \mathrm{S(1)}$ line profiles for the instrumental line broadening using the Interactive Data Language (IDL) procedure, MAX-LIKELIHOOD which was written by Frank Varosi at NASA/GSFC, 1992 and can be found at 'the IDL Astronomy User's Library' (http://idlastro.gsfc.nasa.gov).

MAX-LIKELIHOOD performs iteration based on the Maximum Likelihood solution for the restoration of a blurred image (or spectrum) with additive noise given the instrumental point spread response function or line profile (spatially/spectrally invariant). The maximum Likelihood solution is a fixed point of an iterative equation (derived by setting partial derivatives of Log(Likelihood) to zero). More details about this method and its performance are discussed by Lucy (1974, AJ, 79, 745).

Figures B.1 – B.6 show the results of deconvolution in which we assume a Gaussian function with FWHM = $18\ \mathrm{km\ s^{-1}}$, which is the measured mean width of arc lines and telluric OH lines, for the instrumental profile. We can see that reasonable results are from 3 or 5 iterations and the iterations more than 10 result in just meaningless amplifications of statistical fluctuations. In fact, according to Lucy (1974), best solutions are obtained in a few iterations and, after that, the iterations are merely fitting the statistical noise in data and the solution becomes worse. Therefore we choose 5 as an appropriate and enough number of iterations for our purpose.

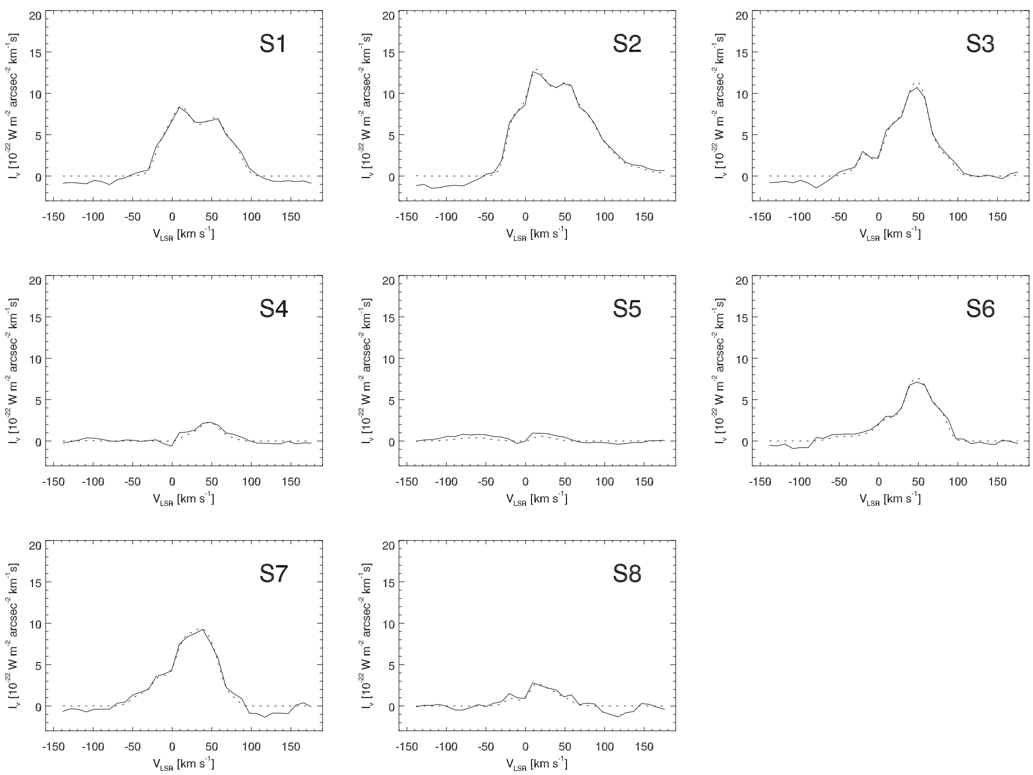

FIG. B.1: Deconvolution of instrumental line broadening: results after 3 iterations. Solid lines are the H_2 $1-0$ $S(1)$ line profiles which are the same as in Figure 4.6. Dashed lines are the deconvolved profiles with a Gaussian kernel with FWHM = 18 km s^{-1} for the instrumental profile.

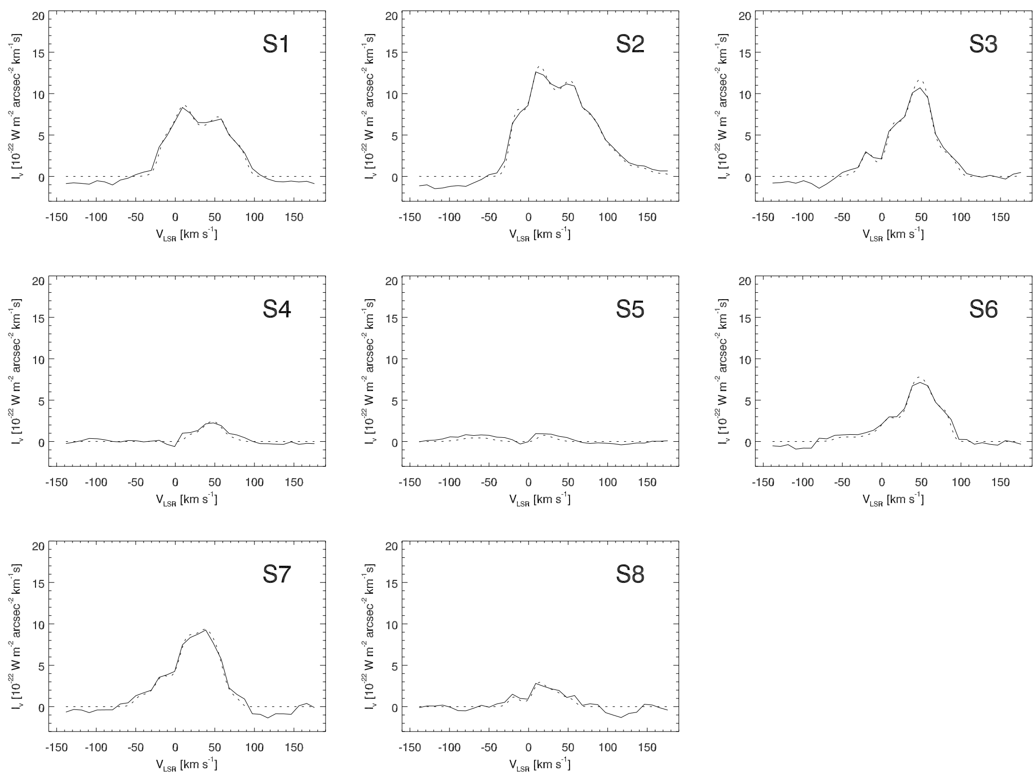

FIG. B.2: Deconvolution of instrumental line broadening: results after 5 iterations. The other aspects are the same as Figure B.1.

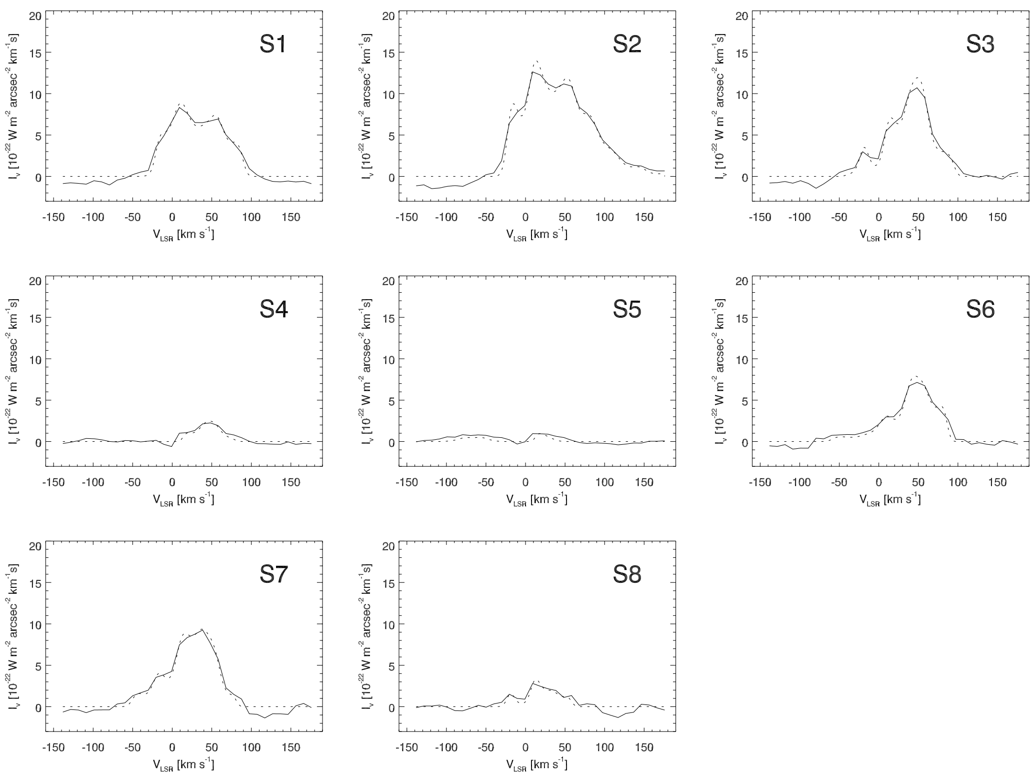

FIG. B.3: Deconvolution of instrumental line broadening: results after 10 iterations. The other aspects are the same as Figure B.1.

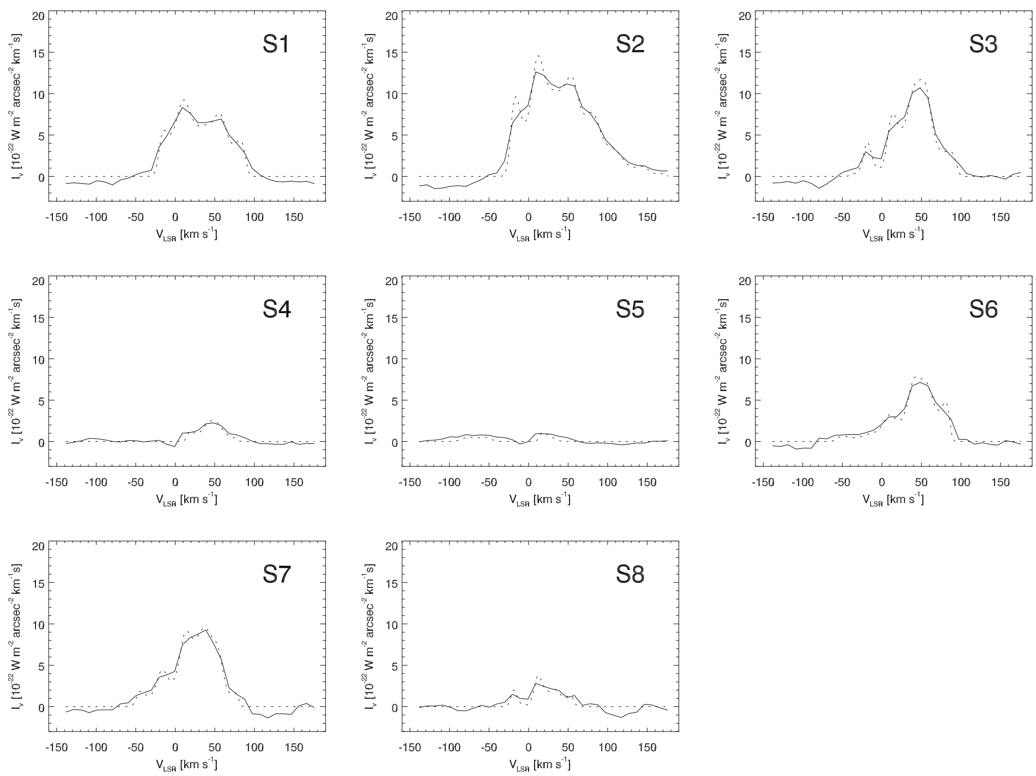

FIG. B.4: Deconvolution of instrumental line broadening: results after 20 iterations. The other aspects are the same as Figure B.1.

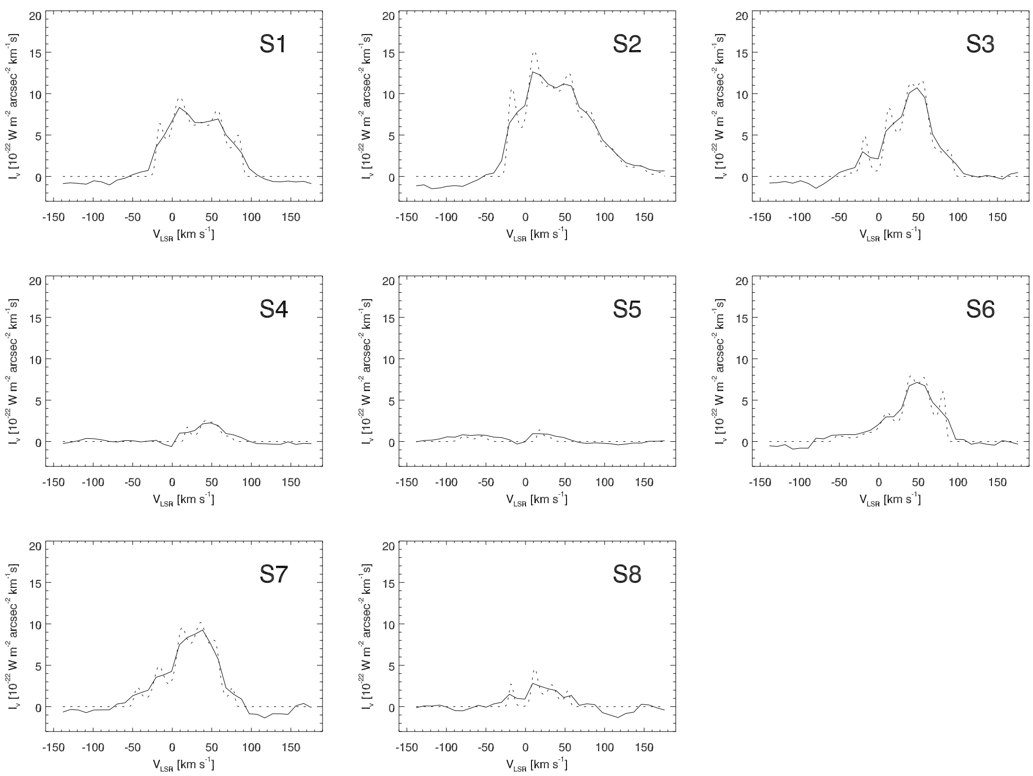

FIG. B.5: Deconvolution of instrumental line broadening: results after 50 iterations. The other aspects are the same as Figure B.1.

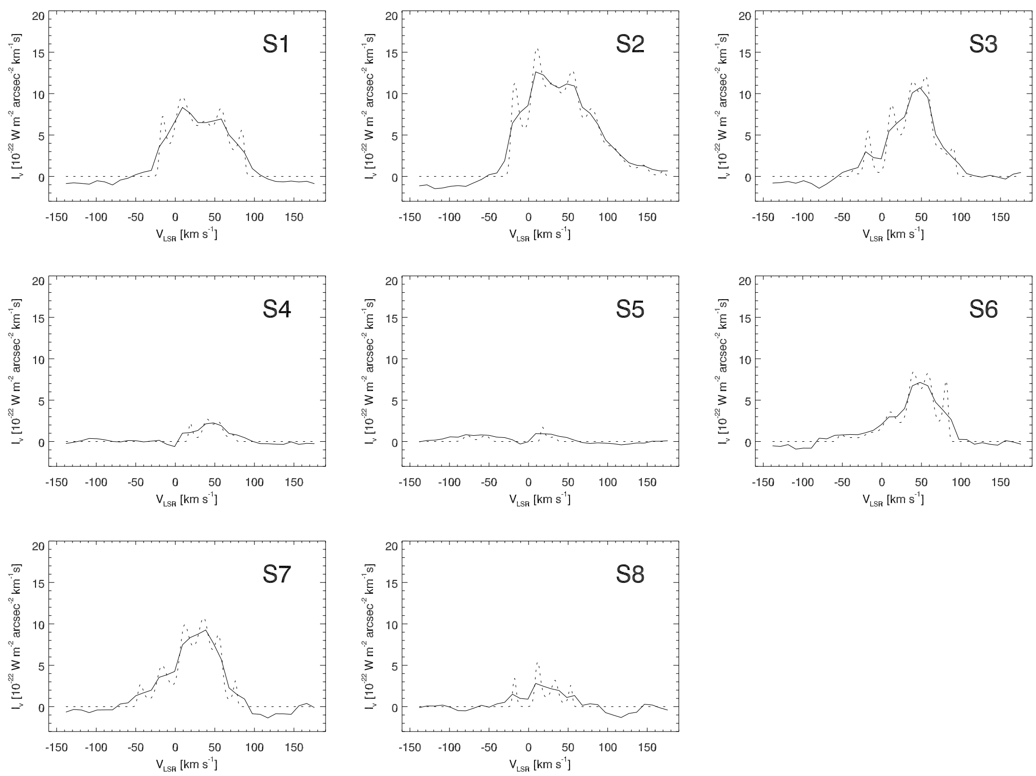

FIG. B.6: Deconvolution of instrumental line broadening: results after 100 iterations. The other aspects are the same as Figure B.1.

Appendix C

Correcting Shock Velocities for Projection Effects

Assuming the Sgr A East shell as an oblate like in Figure C.1 (a), a corrected shock velocity, v_s, is related with a observed line-of-sight (LOS) component, $v_{s,LOS}$, as follows,

$$\frac{v_s}{r_0} = \frac{v_{s,LOS}}{z_0} \tag{C.1}$$

where

$$r_0 = \sqrt{x_0^2 + y_0^2 + z_0^2} \tag{C.2}$$

$$\begin{aligned} x_0 &= r\,sin\theta \\ y_0 &= y_e = r\,cos\theta \end{aligned} \tag{C.3}$$

in Figure C.1 (b) and

$$z_0^2 = x_e^2 - x_0^2 = x_e^2 - r^2\,sin^2\theta \tag{C.4}$$

in Figure C.1 (c) (θ is defined to be $\leq \frac{\pi}{2}$).

Since, on the ellipse,

$$\frac{x_e^2}{a^2} + \frac{y_e^2}{b^2} = 1 \tag{C.5}$$

if equation (C.2) is substituted by equations (C.3), (C.4), and (C.5),

$$r_0 \;=\; \sqrt{r^2 sin^2\theta + y_e^2 + x_e^2 - r^2 sin^2\theta}$$

$$
\begin{aligned}
&= \sqrt{y_e^2 + a^2 - \frac{a^2}{b^2} y_e^2} \\
&= \sqrt{r^2 cos^2\theta (1 - \frac{a^2}{b^2}) + a^2} \\
&= \sqrt{a^2 + r^2 (cos^2\theta - \frac{a^2}{b^2} cos^2\theta)}. \qquad \text{(C.6)}
\end{aligned}
$$

Equation (C.4) can be re-written as follows,

$$
\begin{aligned}
z_0 &= \sqrt{x_e^2 - r^2 sin^2\theta} \\
&= \sqrt{a^2 - \frac{a^2}{b^2} y_e^2 - r^2 sin^2\theta} \\
&= \sqrt{a^2 - \frac{a^2}{b^2} r^2 cos^2\theta - r^2 sin^2\theta} \\
&= \sqrt{a^2 - r^2 (sin^2\theta + \frac{a^2}{b^2} cos^2\theta)}. \qquad \text{(C.7)}
\end{aligned}
$$

Then

$$
\frac{r_0}{z_0} = \sqrt{\frac{a^2 + r^2 (cos^2\theta - \frac{a^2}{b^2} cos^2\theta)}{a^2 - r^2 (sin^2\theta + \frac{a^2}{b^2} cos^2\theta}} \qquad \text{(C.8)}
$$

where a, b, r, and θ are measurable and we can calculate v_s from $v_{s,LOS}$ using equation (C.1).

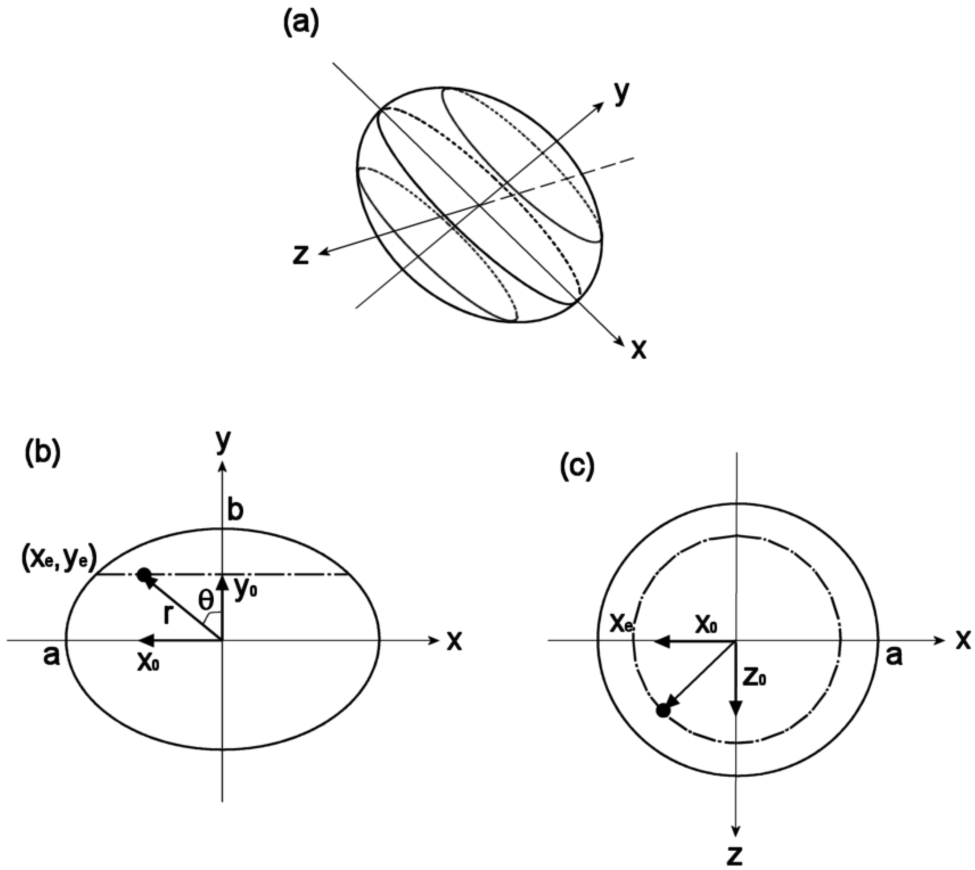

FIG. C.1: Schematic diagram for the Sgr A East shell, which is assumed as an oblate (a). y-axis is the axis of Galactic rotation and x-z plane is the Galactic plane where z-axis is along the line-of-sight. Black dot in each of (b) and (c) corresponds to the position where the line-of-sight component of a shock velocity ($v_{s,LOS}$) is estimated. In (b), the semi-major and semi-minor radius of the ellipse is a and b, respectively, and (x_e, y_e) is a point on the ellipse where the dot-dashed circle in (c) cuts across the oblate.

초 록

우리 은하의 중심부는 우리 은하의 현재 상태뿐만 아니라 그 탄생과 진화, 미래의 운명에까지 영향을 미친다. 우리 은하의 핵은 외부 은하 핵 연구의 표준이 되며 초거대 블랙홀 주변의 환경에 대한 자세한 연구를 가능케 한다. 우리 은하 중심으로부터 10 파섹 내의 Sgr A 영역은 초거대 블랙홀로 여겨지는 Sgr A*, 중심 성단, 은하핵 둘레 원반형 성운 (CND), 이온화 가스 영역인 Sgr A West, 강력한 폭발 현상의 잔해인 Sgr A East, 이 모든 천체들을 둘러싼 분자운들 등 다양한 종류의 주요한 천체들을 포함하고 있다. 우리 은하와 그 핵의 성질을 이해하기 위해서는 이러한 은하 중심 천체들 간의 상호작용에 대한 종합적인 이해가 필요하다. 은하 중심 천체들의 공간적 위치 관계와 역학적 상호작용에 관한 기존의 연구들은 대부분 간접적이고 정성적인 근거를 기반으로 했기 때문에 많은 미해결 문제들을 남겼으며 이러한 문제들을 해결하기 위해서는 보다 확실한 관측적 증거가 필요한 실정이다. 고밀도 분자운과 고온의 역동적인 천체 사이의 상호작용 지역들의 탐사와 연구에 널리 사용되고 있는 수소분자 (H_2) 방출선은 본 연구에 가장 적합한 관측 수단 중의 하나이다.

본 연구에서는 Sgr A East, CND, 주변 분자운들 간의 상호작용 지역에서 방출되는 H_2 1-0 S(1) (파장 = 2.1218㎛) 및 H_2 2-1 S(1) (파장 = 2.2477㎛) 스펙트럼을 관측하였다. 관측은 하와이 마우나케아 산 정상에 위치한 3.8 m United Kingdom Infrared Telescope (UKIRT)와 에셀 (echelle) 격자를 장착한 Cooled Grating Spectrometer 4 (CGS4) 긴슬릿 분광기를 사용하여 수행되었으며 총 56개 지점을 관측하였다. 2차원 스펙트럼 이미지는 IRAF를 사용하여 처리하였으며 3차원 데이터의 분석에는 MIRIAD를 사용하였다. 3차원 데이터는 관측된 수소분자 가스에 대한 약 2 각초 해상도의 공간 정보와 약 18 km s^{-1} 해상도의 속도 정보를 동시에 포함하고 있다. 상호작용 지역의 가스 운동을 분석하기 위해 H_2 1-0 S(1) 3차원 데이터를 McGary, Coil, & Ho (2001, ApJ, 559, 326)의 NH_3(3,3) 3차원 데이터와 직접 비교하였다.

관측된 상호작용 지역의 수소분자 가스의 방출 기작을 규명하기 위해 H_2 1-0 S(1) 및 H_2 2-1 S(1) 방출선의 세기와 가스 운동을 분석하였으며, 그 결과 (1) 매우 강한 자기장 환경에서의 C형 충격파와 자외선 복사에 의한 들뜸이 혼합된 기작 또는 (2) 느린 C형 충격파와 빠른 J형 충격파가 혼합된 기작의 두 가지 설명이 가능하다는 결론을 얻었다. Sgr A East에 의해 발생하는 충격파의 속도는 H_2 방출선 모양과 NH_3 방출선 모양의 비교로부터 약 100 km s^{-1} 으로 추정된다. 충격파로 인한 수소분자 방출광의 분포로부터 Sgr A East와 주변 분자운과의 상호작용의 경계면을 규정하였으며 투영된 2차원 경계는 중심이 Sgr A*로부터 약 1.5 파섹 떨어져 있고 크기가 10.8 파섹 × 7.6 파섹인 타원으로 근사된다. 또한 Sgr A East와 주변 분자운들의 시선방향에 대한 위치 관계를 규명하여 우리 은하 중심 10 파섹 영역의 3차원 구조에 대해 기존의 연구들보다 개선된 모델을 제시하였다. 본 연구에서 추정한 충격파의 속도로부터 Sgr A East의 초기 폭발 에너지를 계산하였으며 그 결과는 0.2-4 × 10^{53} ergs 이다. 이러한 폭발 에너지는 일반적인 단일 초신성으로는 설명할 수 없다. 본 연구에서는 Sgr A East의 기원에 관해 초거대 블랙홀의 조석력에 의한 별 붕괴설, 다중 초신성 폭발설, 극초신성 (hypernova) 폭발설의 가능성들을 검토하였으며, 그 결과 붕괴성 (collapsar) 또는 미니-퀘이사 (microquasar)의 이론적 배경을 가지고 있는 극초

신성 폭발설이 가장 유력하다는 결론을 얻었다.

Sgr A East의 기원인 극초신성 폭발과 일반적인 초신성 폭발이 우리 은하 핵으로의 물질 유입에 미치는 영향을 고찰하였으며 다음과 같은 가설을 제안한다. 우리 은하 핵으로의 지속적인 물질 유입은 약 10^8 년마다 초거대 블랙홀의 활동을 촉발하거나 대규모 별탄생을 유발하여 우리 은하 핵을 활동기에 접어들게 한다. 그러나 그 결과로 탄생하는 다수의 무거운 별들이 초신성 폭발을 일으킴에 따라 물질 유입은 차단되고 활동기는 약 10^7 년 이하의 기간 동안만 지속할 수 있다. 즉 우리 은하의 핵은 일생의 약 1/10의 기간만을 활동기로 보내게 되는 것이다. 가장 최근의 활동기는 약 10^8 년의 휴지기 이후에 수백만년 전에 본격적인 물질 유입과 함께 재개되었다. 통상적인 경우라면 최근의 활동기는 다수의 초신성 폭발이 일어나기 전까지 수백만년 동안 더 지속될 수 있었을 것이지만, 약 10^4 년 전에 매우 드물지만 강력한 Sgr A East 폭발이 발생함에 따라 과거의 활동기들에 비해 특별히 일찍 끝나게 되었다.

주요어: 우리 은하 중심, 성간물질, 적외선, 초신성, 초신성 잔해
학 번: 99304-804